HAL
open science

Control of AC/DC Microgrids with Renewables in the Context of Smart Grids : Including Ancillary Services and Electric Mobility

Filipe Perez

To cite this version:

Filipe Perez. Control of AC/DC Microgrids with Renewables in the Context of Smart Grids : Including Ancillary Services and Electric Mobility. Automatic. Université Paris-Saclay; Universidade federal de Itajuba. Brésil, 2020. English. NNT : 2020UPASG011 . tel-03050337

HAL Id: tel-03050337

https://theses.hal.science/tel-03050337

Submitted on 10 Dec 2020

HAL is a multi-disciplinary open access archive for the deposit and dissemination of scientific research documents, whether they are published or not. The documents may come from teaching and research institutions in France or abroad, or from public or private research centers.

L'archive ouverte pluridisciplinaire **HAL**, est destinée au dépôt et à la diffusion de documents scientifiques de niveau recherche, publiés ou non, émanant des établissements d'enseignement et de recherche français ou étrangers, des laboratoires publics ou privés.

Control of AC/DC Microgrids with Renewables in the Context of Smart Grids

Including Ancillary Services and Electric Mobility

Thèse de doctorat de l'Université Paris-Saclay et UNIFEI

École doctorale n° 580, Sciences and Technologies of Information and Communication (STIC)
Spécialité de doctorat: Automatique
Unité de recherche: Université Paris-Saclay, CNRS, CentraleSupélec, Laboratoire des signaux et systèmes, 91190, Gif-sur-Yvette, France
Référent: CentraleSupélec

Thèse présentée et soutenue en visioconférence totale, le 28 septembre 2020, par

Filipe PEREZ

Composition du jury:

Antonio Carlos Zambroni de Souza Professeur, Université Fédérale d'Itajubá	Président
Didier Georges Professeur, Grenoble INP Institut d'ingénierie (GIPSA)	Rapporteur & Examinateur
Glauco Nery Taranto Professeur, Université Fédérale de Rio de Janeiro (COPPE)	Rapporteur & Examinateur
William Pasillas-Lépine Chercheur (HDR), CNRS, Université Paris-Saclay (L2S)	Examinateur
Pedro Machado de Almeida Professeur, Université Fédérale de Juiz de Fora	Examinateur
Benedito Donizeti Bonatto Professeur, Université Fédérale d'Itajubá	Invité
Françoise Lamnabhi-Laguarrigue Directeur de recherche, Université Paris-Saclay (L2S)	Directrice
Paulo Fernando Ribeiro Professeur, Université Fédérale d'Itajubá	Directeur
Gilney Damm Maître de conférences, Université Paris-Saclay (IBISC)	Coencadrante

Thèse de doctorat

NNT: 2020UPASG011

Acknowledgments

First, I would like to thank God for giving me life, good experiences, and for giving me the ability to do this work.

I would like to thank my supervisors Dr. Françoise Lamnabhi-Lagarrigue, Dr. Gilney Damm and Dr. Paulo Ribeiro for the guidance and learning during the thesis period. Françoise, thank you for the opportunity to be part of this excellent team. Gilney, thank you for the excellent guidance in technical issues and personal friendship. Paulo, thank you again for helping me improve.

Thank you, the members of the jury for accepting this mission and spending your time to make this thesis much better, providing detailed and consistent recommendations, suggestions and corrections.

I want to thank L2S Laboratory for the thesis subject and for the people company during the first two years of the thesis, especially Paulo, Hidayet, Fernando, Abdelkrim, João, Janailson, Juan, Sabah, João Neto, Kuba, Raul and Maryvonne. Thank you Guacira for your friendship in the laboratory during working and resting days, and for your help with softwares and simulations.

I would like to thank Efficacity for the partnership during the thesis progression, specially to Alessio for the fruitful discussions and for mentoring in control area, and to Lilia for the support. I also would like to thank Erasmus Mundus Programme on SMART^2 Project for the scholarship.

I want to thank the friendships I made in Paris and for being with me in moments of relaxation. I also thank the power systems team from Lactec Institute for the support in the last years of the thesis.

Finally, to my wife Rafaela, I cannot describe how your support was important to me. Thank you for being there for me in all bad and great moments of my life. Also, I want to thank my family, especially my father Ulisses, my mother Ivani and my sister Talita, for the love and support, for helping me even with the distance and difficulties of life.

Filipe PEREZ
September, 2020

Contents

Acknowledgments **i**

Contents **iii**

List of Tables **vii**

List of Figures **ix**

Abstract **xix**

Résumé **xxi**

Resumo **xxiii**

1 General Introduction **1**
1.1 Context 1
1.1.1 Renewable energy sources 2
1.1.2 Energy storage systems 4
1.2 Microgrids 5
1.2.1 Hierarchical structure 8
1.3 Ancillary Services 10
1.4 Thesis Contribution 13
1.5 Thesis Outcomes 15

2 Microgrid Overview **17**
2.1 Introduction 17
2.1.1 General review 17
2.1.2 Supervision and optimal operation 19
2.1.3 Microgrid examples 22
2.2 Classification and Stability 25
2.3 DC Microgrids 31
2.3.1 Droop control strategies 34
2.4 AC Microgrids 36
2.5 Conclusions 43

3 The Microgrid Components **45**
3.1 Introduction 45
3.2 Microgrid Components 46
3.2.1 Photovoltaic panels 46

3.2.2 Energy storage systems . . . 52
3.2.3 Braking energy recovery system . . . 63
3.2.4 Local loads . . . 67
3.2.5 Grid-connection . . . 68
3.3 Proposed Microgrid Design . . . 68
3.3.1 Power converters configuration . . . 71
3.3.2 Sizing of DC/DC converters . . . 73
3.4 Conclusions . . . 74

4 Control Strategy **77**
4.1 Introduction . . . 77
4.1.1 Model introduction . . . 78
4.2 Supercapacitor Subsystem . . . 79
4.2.1 Supercapacitor model . . . 80
4.2.2 Non-minimum phase problem . . . 80
4.2.3 Control induced time-scale separation . . . 82
4.2.4 Supercapacitor control application . . . 86
4.2.5 Zero dynamics analysis . . . 87
4.2.6 Reference calculation . . . 89
4.3 Battery Subsystem . . . 91
4.3.1 Battery model . . . 92
4.3.2 Feedback linearization . . . 93
4.3.3 Zero dynamics analysis . . . 94
4.4 PV Array Subsystem . . . 95
4.4.1 PV array model . . . 96
4.4.2 Feedback linearization . . . 96
4.4.3 Zero dynamics analysis . . . 97
4.5 DC Load Subsystem . . . 98
4.5.1 DC load model . . . 98
4.5.2 Backstepping control . . . 99
4.5.3 Zero dynamics analysis . . . 101
4.6 Regenerative Braking Subsystem . . . 102
4.6.1 Regenerative braking model . . . 103
4.6.2 Regenerative braking control application . . . 104
4.6.3 Zero dynamics analysis . . . 105
4.6.4 Reference calculation . . . 106
4.7 AC Grid-Connection . . . 107
4.7.1 AC grid model . . . 107
4.7.2 Feedback linearization . . . 109
4.7.3 Zero dynamics analysis . . . 109
4.7.4 PLL synchronization . . . 110
4.8 System Interconnection . . . 111
4.8.1 The DC bus . . . 111
4.8.2 Hierarchical control structure . . . 112
4.8.3 Preliminaries . . . 113
4.8.4 Stability analysis . . . 113

4.9 Simulation Results . . . 120
4.9.1 The proposed nonlinear control . . . 121
4.9.2 A control comparison: Linear vs Nonlinear . . . 129
4.9.3 Robustness . . . 133
4.10 Different Approaches for DC Bus Control . . . 135
4.10.1 Fixed reference for V_{C_2} . . . 135
4.10.2 Simplification on C_2 dynamics . . . 142
4.10.3 DC bus generalization: Thévenin equivalent . . . 143
4.11 Conclusions . . . 148

5 Ancillary Services for AC Microgrids 151
5.1 Chapter Introduction . . . 151
5.2 Power System Stability . . . 151
5.2.1 Frequency stability and control . . . 153
5.2.2 Voltage stability and control . . . 160
5.3 Ancillary Services in Brazil . . . 164
5.4 Power Converters Issues . . . 168
5.4.1 Inertial response and low inertia issues . . . 171
5.4.2 Frequency problems in weak power systems . . . 172
5.5 Virtual Inertia . . . 173
5.5.1 Virtual inertia topologies . . . 176
5.5.2 Weak grid modelling . . . 182
5.5.3 Proposed virtual inertia . . . 183
5.5.4 Droop control strategy . . . 184
5.5.5 Stability analysis . . . 185
5.5.6 Simulation results . . . 187
5.5.7 Isolated operation . . . 189
5.5.8 Dynamics of the DC Microgrid . . . 193
5.6 Adaptive Virtual Inertia Formulation . . . 195
5.6.1 Stability analysis . . . 196
5.6.2 Simulation results . . . 198
5.6.3 Comparison with droop control . . . 201
5.6.4 Comparison of different inertia coefficients . . . 203
5.6.5 Additional simulation results . . . 204
5.7 VSM with Voltage and Current Control . . . 206
5.7.1 Active and reactive power control . . . 208
5.7.2 Virtual impedance . . . 208
5.7.3 Voltage and current control . . . 209
5.7.4 Simulation results . . . 211
5.7.5 Fixed voltage reference . . . 214
5.7.6 Parameters variation . . . 215
5.7.7 Control strategy comparison . . . 216
5.8 Conclusions . . . 218

6 General Conclusions 219
6.1 Main Results . . . 222

6.2 Future Works 223

Bibliography **225**

Appendix

G Appendix I **251**
G.1 Proportional Integral (PI) Controller 251
G.2 Park Transformation 256
G.3 Input-to-State Stability 257

H Appendix II - Résumé en Français **261**
H.1 Introduction 261
H.1.1 Sources d'énergie renouvelables 262
H.2 Microgrids 263
H.3 Services Système 267
H.4 Contribution de la Thèse 269
H.5 Conclusions Générales 271
H.6 Résultats Principaux 275
H.7 Travaux Futurs 276

List of Tables

1.1 Electric grid energy storage services. 4

2.1 Categories of Microgrid control from communication perspective. 26
2.2 Main issues in Control System Stability of Microgrids. 29
2.3 Main issues in Power Supply and Balance Stability of Microgrids. 30
2.4 Control techniques feature in DC Microgrids. 37
2.5 Different application of power converters for AC Microgrids. 38

3.1 Different topologies of grid-connected photovoltaic systems. 51
3.2 Energy storage systems classification according to the form of store energy. 53
3.3 Power converters configuration in the Microgrid. 74

4.1 Microgrid parameters 122
4.2 Gains' parameters for the nonlinear controller. 123

5.1 Microgrid operation standard for frequency levels. 173
5.2 Microgrid parameters 187
5.3 The AC load power demand. 188
5.4 The AC load power demand in isolated operation. 190
5.5 The power demand in the AC load, considering the DC Microgrid dynamics. 193
5.6 The AC load power demand for two synchronous machines scenario. 204

G.1 Parameter gains of the linear Proportional-Integral (PI) controller. 256

List of Figures

1.1 The transformation of the distribution grid from a centralized generation to a heterogeneous grid. 3
1.2 Relation between energy density and power density for different ESS. 5
1.3 A general DC Microgrid scheme. 8
1.4 The traditional hierarchical control structure for a Microgrid. The local and primary control generate the references for lower level power converters, while the secondary control deals with power flow regulation and the tertiary control covers the energy dispatch and energy market. 9
1.5 The effect of the inertia reduction according to the renewable integration levels in the network. 11
1.6 Network evolution towards power converters' systems. 11

2.1 A Microgrid composed of central control with hierarchical structure. 21
2.2 The classification of stability in Microgrids. 28
2.3 Conventional droop control scheme for multiple generations units in a DC Microgrid. 35
2.4 Local control loop in a Microgrid using VSC converter. 39
2.5 Power converter control of a Microgrid applying virtual output impedance loop. . . . 41

3.1 Simplified model of photovoltaic panel. 47
3.2 Characteristic curve of PV, and curves for different irradiance and temperature values. 48
3.3 Control scheme of the MPPT algorithm. 49
3.4 Incremental conductance scheme. 49
3.5 Parallel and series arrangement of PV arrays. 50
3.6 Characteristic curve of the entire PV system considering different irradiation and temperature levels. 52
3.7 Battery electrical model based on internal resistance. 56
3.8 Different HESS configurations among passive, active, cascaded and multi-level applications. 60
3.9 Power sharing of passive HESS where supercapacitor and battery time constant is highlighted. 61
3.10 Discharge curve of the Lithium-ion battery from Simulink model. 63
3.11 Supercapacitor charge characteristic. 63
3.12 The power and speed variation of a urban train between two stations. 64
3.13 Sankey diagram for DC railway station extracted from. 65
3.14 a) Traditional braking energy recovery. b) Braking energy recovery with energy storage system. 66
3.15 The general AC/DC hybrid Microgrid scheme. 70

4.1 The considered Microgrid framework. 78

4.2 The bidirectional boost converter of the supercapacitor subsystem. 80
4.3 The bidirectional boost converter of the battery subsystem. 92
4.4 The boost converter of the PV array subsystem. 96
4.5 The buck converter of the DC load subsystem. 99
4.6 The buck converter of the train (regenerative braking) subsystem. 103
4.7 Voltage Source Converter (VSC) to AC grid-connection. 108
4.8 Block diagram of SRF-PLL. 111
4.9 The PV incident irradiance and the demanded DC load current, respectively. 122
4.10 The power demand in the DC load in kW. 122
4.11 The voltages V_S, V_B, V_{PV}, V_T, of the supercapacitor, battery, PV array, and train, respectively. 123
4.12 The currents I_{L_3}, I_{L_6}, I_{L_9} and their references $I^e_{L_3}$, $I^*_{L_6}$, $I^*_{L_9}$. 124
4.13 The voltage V_{C_2} and its nominal reference $V^e_{C_2}$. 124
4.14 A zoom on V_{C_2} voltage dynamics, showing its convergence and settling times. 125
4.15 The DC bus voltage V_{dc} and its reference V^*_{dc}. 125
4.16 The DC load voltage $V_{C_{11}}$ and its reference $V^*_{C_{11}}$. 125
4.17 The currents $I_{L_{13}}$, $I_{L_{16}}$ and $I_{R_{17}}$ with their respective references $I^e_{L_{13}}$ and $I^e_{L_{16}}$. 126
4.18 The voltage $V_{C_{14}}$ and its reference $V^*_{C_{14}}$ ensuring the injection of power from the regenerative braking system. 126
4.19 The direct and quadrature currents I_{ld} and I_{lq} with their references I^*_{ld} and I^*_{lq}, respectively. 127
4.20 The AC bus voltage and the injected current into AC grid in $[p.u.]$. 127
4.21 The dynamics of V_{C_1}, V_{C_4} and V_{C_7}, respectively. 128
4.22 The output voltages V_{C_5}, V_{C_8}, $V_{C_{12}}$, $V_{C_{15}}$ and $V_{C_{17}}$ on the Microgrid converters (zero dynamics). 128
4.23 The computed (in red) and simulated (in blue) voltages V_{C_2} and $V_{C_{14}}$ with a zoom in the respective variables. 129
4.24 A comparison of the DC bus dynamics when the whole system is controlled by simple PI (blue curve) and by the introduced nonlinear technique (red curve). 130
4.25 A zoom on V_{dc} to compare PI and nonlinear control in the most critical transients. . 131
4.26 The controlled variables in the Microgrid, comparing the PI controller in red and the nonlinear controller in blue. 131
4.27 The stronger variations in the battery current. 132
4.28 The supercapacitor current variation to regulate the power mismatch in the DC bus. 132
4.29 The behavior of the DC bus voltage for the PI controller in red and nonlinear controller in blue, when strong variations takes place. 133
4.30 A zoom on V_{dc} to highlight the PI controller diverging towards the power imbalance caused by the battery. 133
4.31 The voltage V_{dc} when comparing PI and nonlinear control with parametric errors of $+20\%$ and -20%. 134
4.32 A zoom on V_{dc} of Figure 4.31 to compare PI and nonlinear control in the most critical transients. 134
4.33 The voltage V_{dc} in case of $+25\%$ higher parametric error than the nominal value. . . 135
4.34 A zoom of Figure 4.33 in the highest transients, showing the unstable behavior of PI control after the high peak transient due to the regenerative braking. 135

4.35 The considered DC Microgrid. 136
4.36 V_{C_2} voltage behavior for different values of R_2. 138
4.37 Calculated voltage V_{C_2} from equation (4.45) for different values of R_2. 138
4.38 Voltage V_{C_2} with the calculated value from equation (4.45) and the error between those variables. 138
4.39 DC bus voltage (V_{dc}) profile for different values of R_2. 139
4.40 Controlled current I_{L_3} on the supercapacitor subsystem for different values of R_2. . . 139
4.41 Voltage V_{C_2} with parameters uncertainties 10% and 20%. 140
4.42 Voltage on the DC bus with parameters uncertainties 10% and 20%. 140
4.43 Voltage V_{C_2} controlled by nonlinear control (in blue) and linear control (in red). . . . 141
4.44 A comparison on the DC bus voltage (V_{dc}) between the proposed nonlinear and linear control. 141
4.45 The controlled currents I_{L_3}, I_{L_6}, I_{L_9} and $I_{L_{12}}$. 144
4.46 The controlled voltages $V_{C_{11}}$ and V_{dc}. 144
4.47 Zero dynamics V_{C_2}, V_{C_5}, V_{C_8}, and $V_{C_{12}}$. 145
4.48 Thévenin equivalent circuit for the DC Microgrid. 146
4.49 The simplified electrical model of the DC Microgrid. 146
4.50 The equivalent Thévenin voltage (V_{th}) for the Microgrid part (battery, PV and DC load). 147
4.51 The controlled currents I_{L_3}, I_{L_6}, I_{L_9} and $I_{L_{13}}$ in the equivalent Thévenin approach. . 148
4.52 The controlled voltages V_{C_2}, V_{dc} and $V_{C_{11}}$. 149
4.53 Zero dynmics V_{C_5}, V_{C_8}, and $V_{C_{12}}$. 149

5.1 Power system stability classification. 152
5.2 Isochronous governor block diagram. 156
5.3 Frequency response in the isochronous mode. 156
5.4 Droop governor block diagram. 157
5.5 Power sharing scheme of droop control in steady-state. 157
5.6 Frequency response in the droop control mode. 158
5.7 Block diagram of a droop governor with load reference setpoint. 159
5.8 A generator connected to a load through a transmission line. 160
5.9 $P - V$ curve characteristics for different power factors. 161
5.10 Block diagram of the voltage regulator and exciter. 162
5.11 Different coefficients of the voltage droop control scheme. 164
5.12 Time-scale separation of power system dynamics considering conventional synchronous generators and power converters integration. 170
5.13 Inertial response scheme with a primary control. 172
5.14 The concept of virtual inertia. 174
5.15 Time range of frequency response stages. 175
5.16 Control diagram of a synchronverter. 177
5.17 General control scheme of ISE lab topology for virtual inertia. 178
5.18 General control scheme of Virtual Synchronous Generator (VSG) topology for virtual inertia. 180
5.19 Virtual Synchronous Machine (VSM) connected to an AC Microgrid based on diesel generation. 183
5.20 VSM general control scheme for a Microgrid integration. 184

5.21 The controlled active and reactive power in the VSC converter of the Microgrid. . . . 188
5.22 The active and reactive power supplied by the diesel generator. 189
5.23 The voltage amplitude profile on the PCC. 189
5.24 The controlled frequency from the VSM approach. 189
5.25 The frequency deviation (Δw) and RoCoF. 190
5.26 The active and reactive power from the VSM in the isolated operation. 191
5.27 The voltage profile and the grid frequency in the isolated operation. 191
5.28 Frequency deviation and RoCoF in isolated operation. 192
5.29 Voltage profile on PCC applying the integral term. 192
5.30 Frequency response with the integral term (secondary control). 192
5.31 Frequency deviation and RoCoF when the integral term is applied. 193
5.32 Active and reactive power injected by the VSC converter from the DC side of the grid. 194
5.33 The mechanical power in the diesel generator. 194
5.34 The voltage on the PCC and the frequency of the grid. 194
5.35 The DC bus voltage of the Microgrid considering the virtual inertia approach. 195
5.36 AC load profile in the Microgrid. 198
5.37 The injected power P into the grid and its desired power dispatch P^*. 199
5.38 The injected reactive power Q into the grid and its desired power dispatch Q^*. 199
5.39 Voltage profile on the PCC. 199
5.40 The $I_{d,q}$ currents of the VSM. 200
5.41 The mechanical power input of the synchronous machine. 200
5.42 Grid frequency ω_g with the angular speed on the VSM (ω_{vsm}) and frequency reference ω^*. 200
5.43 Inertia coefficient behavior varying during frequency transients. 201
5.44 Zoom in frequency deviation $\tilde{\omega}$ and in angular acceleration $\dot{\tilde{\omega}}$ during the largest transients. 201
5.45 Frequency of the grid considering different control approaches. 202
5.46 Zoom in the frequency tramsients to compare the control strategies. 203
5.47 Grid frequency on left and frequency deviation on right for different variation in the inertia coefficients. 203
5.48 Inertia coefficient on the left and angular acceleration on the right over different values of K_M. 204
5.49 Active and reactive power flow of the generator 1 ($2MVA$) and the inserted generator 2 ($1MVA$), respectively. 205
5.50 Controlled active and reactive power in the VSM. 205
5.51 Voltage on the PCC and grid frequency with two generators connected in the AC bus of the Microgrid. 205
5.52 The comparison between fixed inertia and adaptive inertia approach for the system in isolated operation. 206
5.53 Proposed virtual inertia control scheme for the Microgrid using virtual impedance. . 207
5.54 The controlled active and reactive power in the Voltage Source Converter (VSC) converter of the Microgrid. 212
5.55 The controlled active and reactive power in the diesel generator to allow power balance. 212
5.56 The controlled voltage of the grid in the Point of Common Coupling (PCC). 212
5.57 The controlled currents of the VSC converter. 213
5.58 Frequency of the grid and its reference. 213

5.59 Inertia coefficient behavior varying during frequency transients. 214
5.60 Zoom in frequency deviation $\tilde{\omega}$ and in angular acceleration $\dot{\tilde{\omega}}$ during the largest transients. 214
5.61 Zoom in frequency deviation $\tilde{\omega}$ and in angular acceleration $\dot{\tilde{\omega}}$ during the largest transients. 214
5.62 Comparison among different VSM parameters considering the response of the grid frequency. 216
5.63 Comparison among different Virtual Synchronous Machine (VSM) parameters considering the response of the grid frequency. 217
5.64 A comparison among different control approaches in the frequency behavior. 217
5.65 A zoom in the frequency for different control strategies. 218

G.1 Block diagram of the DC bus voltage control. 251
G.2 Block diagram of the current battery control. 252
G.3 Block diagram of the current PV control. 253
G.4 Block diagram of the DC load voltage control. 254
G.5 Block diagram of the DC load voltage control. 254
G.6 Block diagram of I_{ld} and I_{lq} current control, respectively. 255

Acronyms

AC Alternating Current.
AGC Automatic Generation Control.
AVR Automatic Voltage Regulator.
CPL Constant Power Load.
DC Direct Current.
DER Distributed Energy Resources.
EMS Energy Management System.
ESS Energy Storage System.
FACTS Flexible AC Transmission Systems.
HESS Hybrid Energy Storage System.
HVDC High-Voltage Direct Current.
ICT Information and Communication Technologies.
IEEE Institute of Electrical and Electronics Engineers.
ISS Input to State Stability.
LPF Low Pass Filter.
LQR Linear Quadratic Regulator.
MMC Modular Multilevel Converter.
MPC Model Predictive Control.
MPP Maximum Power Point.
MPPT Maximum Power Point Tracking.
MTDC Multi-Terminal DC system.
PCC Point of Common Coupling.
PI Proportional-Integral.
PID Proportional-Integral-Derivative.
PLL Phase Locked Loop.
PSP Pumped Storage Plants.
PSS Power System Stabilizer.
PV Photovoltaic Panel.
PWM Pulse Width Modulation.
rms root mean square.
RoCoF Rate of Change of Frequency.
SoC State of Charge.
SRF Synchronous Reference Frame.
TSO Transmission System Operator.
UPS Uninterruptible Power Supply.
VSC Voltage Source Converter.
VSG Virtual Synchronous Generator.
VSM Virtual Synchronous Machine.

Nomenclature

δ	Power angle
η	Dynamics related to the DC bus interconnection
μ	Controlled dynamics of the supercapacitor subsystem
ω_g	Grid frequency
ω_{vsm}	Frequency produced by the Virtual Synchronous Machine
θ	Phase angle
$\tilde{\omega}$	Frequency deviation
ξ_1	Dynamics controlled by feedback linearization
ξ_2	Dynamics controlled by dynamical feedback linearization
ζ	Zero dynamics
E	Generator's voltage magnitude
e	Per unit voltage magnitude on the power converter
E_k	Kinetic energy
E_k	Potential energy
$I_{c,dq}$	Synchronous reference frame currents in the output filter of the VSC converter
$I_{l,dq}$	Synchronous reference frame currents in the line of AC grid
I_{L_m}	Inductor current, $m = \{3, 6, 9, 13, 16\}$
I_L	Current on DC load
$K_{m.n}$	Control gains
$L_{f,g}$	Lie derivative
m_{dq}	Modulation indexes of the VSC converter
P	Measured active power
P_m	Active power input
P_{AC}	Power injected into AC grid
P_B	Battery power
P_{load}	Active power demand from AC load

P_L	Power demand from DC load
P_{PV}	PV generated power
P_S	Supercapacitor power
P_T	Regenerative train braking power
Q	Measured reactive power
Q_{load}	Reactive power demand from AC load
r	Reference vector
T_e	Electric torque
u_i	Control input, $i = \{1, 2, 3, 4, 5, 6, 7\}$
V	Voltage magnitude on the load side terminal
v_m	Additional control inputs
V_B	Voltage on battery
$V_{c,dq}$	Synchronous reference frame voltages in the output filter of the VSC converter
V_{C_n}	Voltage on the capacitor C_n, where $n = \{1, 2, 4, 5, 7, 8, 11, 12, 14, 15, 17\}$
V_{dc}	Voltage on the DC bus
$V_{l,dq}$	Synchronous reference frame voltages on AC grid
V_L	Voltage on DC load
V_{PV}	Voltage on PV array
V_S	Voltage on supercapacitor
V_T	Voltage on train system
W	Lyapunov function
x	Extended state variable
x^e	Equilibrium point of x
y	Output control
$z_{1,2}$	Variable transformation for $V_{C_{14}}$

Abstract

Microgrids are a very good solution for current problems raised by the constant growth of load demand and high penetration of renewable energy sources, that results in grid modernization through "*Smart-Grids*" concept. The impact of distributed energy sources based on power electronics is an important concern for power systems, where natural frequency regulation for the system is hindered because of inertia reduction. In this context, Direct Current (DC) grids are considered a relevant solution, since the DC nature of power electronic devices bring technological and economical advantages compared to Alternative Current (AC). The thesis proposes the design and control of a hybrid AC/DC Microgrid to integrate different renewable sources, including solar power and braking energy recovery from trains, to energy storage systems as batteries and supercapacitors and to loads like electric vehicles or another grids (either AC or DC), for reliable operation and stability. The stabilization of the Microgrid buses' voltages and the provision of ancillary services is assured by the proposed control strategy, where a rigorous stability study is made. A low-level distributed nonlinear controller, based on "*System-of-Systems*" approach is developed for proper operation of the whole Microgrid. A supercapacitor is applied to deal with transients, balancing the DC bus of the Microgrid and absorbing the energy injected by intermittent and possibly strong energy sources as energy recovery from the braking of trains and subways, while the battery realizes the power flow in long term. Dynamical feedback control based on singular perturbation analysis is developed for supercapacitor and train. A Lyapunov function is built considering the interconnected devices of the Microgrid to ensure the stability of the whole system. Simulations highlight the performance of the proposed control with parametric robustness tests and a comparison with traditional linear controller. The Virtual Synchronous Machine (VSM) approach is implemented in the Microgrid for power sharing and frequency stability improvement. An adaptive virtual inertia is proposed, then the inertia constant becomes a system's state variable that can be designed to improve frequency stability and inertial support, where stability analysis is carried out. Therefore, the VSM is the link between DC and AC side of the Microgrid, regarding the available power in DC grid, applied for ancillary services in the AC Microgrid. Simulation results show the effectiveness of the proposed adaptive inertia, where a comparison with droop and standard control techniques is conducted.

Index Terms: Microgrids, Nonlinear control, Power system stability, Voltage and frequency regulation, Lyapunov methods, Virtual inertia, Ancillary services.

Résumé

Les Microgrids sont une excellente solution aux problèmes actuels soulevés par la croissance constante de la demande de charge et la forte pénétration des sources d'énergie renouvelables, qui se traduisent par une modernisation du réseau grâce au concept de "*Smart-Grids*". L'impact des sources d'énergie distribuées basées sur l'électronique de puissance est une préoccupation importante pour les systèmes d'alimentation, où la régulation naturelle de la fréquence du système est entravée en raison de la réduction de l'inertie. Dans ce contexte, les réseaux à courant continu (DC) sont considérés comme une solution pertinente, car la nature DC des appareils électroniques de puissance apporte des avantages technologiques et économiques par rapport au courant alternatif (AC). La thèse propose la conception et le contrôle d'une Microgrid hybride AC/DC pour intégrer différentes sources renouvelables, y compris la récupération d'énergie solaire et de freinage des trains, aux systèmes de stockage d'énergie sous forme de batteries et de supercondensateurs et à des charges telles que les véhicules électriques ou d'autres réseaux (AC ou DC), pour un fonctionnement et une stabilité fiables. La stabilisation des tensions des bus du Microgrid et la fourniture de services systèmes sont assurées par la stratégie de contrôle proposée, où une étude de stabilité rigoureuse est réalisée. Un contrôleur non linéaire distribué de bas niveau, basé sur une approche "*System-of-Systems*", est développé pour un fonctionnement correct de l'ensemble du Microgrid. Un supercondensateur est appliqué pour faire face aux transitoires, équilibrant le bus DC du Microgrid et absorbant l'énergie injectée par des sources d'énergie intermittentes et possiblement très fortes comme celle provenant du freinage régénératif de trains ou metros, tandis que la batterie réalise le flux de puissance à long terme. Un contrôle de linéarisation par bouclage dynamique basé sur une analyse par perturbation singulière est développé pour les supercondensateurs et les trains. Des fonctions de Lyapunov sont construites en tenant compte des dispositifs interconnectés au Microgrid pour assurer la stabilité de l'ensemble du système. Les simulations mettent en évidence les performances du contrôle proposé avec des tests de robustesse paramétriques et une comparaison avec le contrôleur linéaire traditionnel. L'approche VSM (*Virtual Synchronous Machine*) est implémentée dans le Microgrid pour le partage de puissance et l'amélioration de la stabilité de fréquence. Une inertie virtuelle adaptative est proposée, puis la constante d'inertie devient une variable d'état du système qui peut être conçue pour améliorer la stabilité de fréquence et le support inertiel, où l'analyse de stabilité est effectuée. Par conséquent, le VSM est la connexion de liaison entre les côtés DC et AC du Microgrid, où la puissance disponible dans le réseau DC est utilisée pour les services système dans les Microgrids AC. Les résultats de la simulation montrent l'efficacité de l'inertie adaptative proposée, où une comparaison avec la solution de statisme et le contrôle standard est effectuée.

Mot Clés: Microgrids, Contrôle non-linéaire, Stabilité du système électrique, Régulation de tension et de fréquence, Méthodes de Lyapunov, Inertie virtuelle, Services système.

Resumo

As Microrredes são uma ótima solução para os problemas atuais gerados pelo constante crescimento da demanda de carga e alta penetração de fontes de energia renováveis, que resulta na modernização da rede através do conceito "*Smart-Grids*". O impacto das fontes de energia distribuídas baseados em eletrônica de potência é uma preocupação importante para o sistemas de potência, onde a regulação natural da frequência do sistema é prejudicada devido à redução da inércia. Nesse contexto, as redes de corrente contínua (CC) são consideradas um progresso, já que a natureza CC dos dispositivos eletrônicos traz vantagens tecnológicas e econômicas em comparação com a corrente alternada (CA). A tese propõe o controle de uma Microrrede híbrida CA/CC para integrar diferentes fontes renováveis, incluindo geração solar e frenagem regenerativa de trens, sistemas de armazenamento de energia como baterias e supercapacitores e cargas como veículos elétricos ou outras (CA ou CC) para confiabilidade da operação e estabilidade. A regulação das tensões dos barramentos da Microrrede e a prestação de serviços anciliares são garantidas pela estratégia de controle proposta, onde é realizado um rigoroso estudo de estabilidade. Um controlador não linear distribuído de baixo nível, baseado na abordagem "*System-of-Systems*", é desenvolvido para a operação adequada de toda a rede elétrica. Um supercapacitor é aplicado para lidar com os transitórios, equilibrando o barramento CC da Microrrede, absorvendo a energia injetada por fontes de energia intermitentes e possivelmente fortes como recuperação de energia da frenagem de trens e metrôs, enquanto a bateria realiza o fluxo de potência a longo prazo. O controle por *dynamical feedback* baseado numa análise de *singular perturbation* é desenvolvido para o supercapacitor e o trem. Funções de Lyapunov são construídas considerando os dispositivos interconectados da Microrrede para garantir a estabilidade de todo o sistema. As simulações destacam o desempenho do controle proposto com testes de robustez paramétricos e uma comparação com o controlador linear tradicional. O esquema de máquina síncrona virtual (VSM) é implementado na Microrrede para compartilhamento de potência e melhoria da estabilidade de frequência. Então é proposto o uso de inércia virtual adaptativa, no qual a constante de inércia se torna variável de estado do sistema, projetada para melhorar a estabilidade da frequência e prover suporte inercial. Portanto, o VSM realiza a conexão entre lado CC e CA da Microrrede, onde a energia disponível na rede CC é usada para prestar serviços anciliares no lado CA da Microrrede. Os resultados da simulação mostram a eficácia da inércia adaptativa proposta, sendo realizada uma comparação entre o controle *droop* e outras técnicas de controle convencionais.

Index Terms: Microrredes, Controle não-linear, Estabilidade de sistemas de potência, Regulação de tensão e frequência, Métodos de Lyapunov, Inércia virtual, Serviços ancilares.

CHAPTER 1

General Introduction

1.1. Context

The electrical grid is going through a revolution since the years 2000s. Such revolution is composed first by economic aspects as the liberalization of power markets and the unbundling and privatization of previously state-owned power companies, which brings new dynamics to the energy market. Next, because of environmental and societal concerns, there has been a choice for reducing the use of fossil-based sources, and to some extent even nuclear power. This fundamental change of the power matrix has introduced ever-increasing shares of renewable energy sources (*renewables*). Such changes, if continued in the future, will completely reshape the way power grids operate, in particular because the two previous points (economic and environmental) are rather antagonistic. Also, renewables introduce large variability in the electrical grid, which need a perfect equilibrium at all time on the produced and consumed electric power [1]. The solution to attain stability in such time-varying production and consumption has been the introduction of new elements from Information and Communication Technologies (ICT). Such merge of traditional power grids with ICT is now known as *Smart-Grids* [2–4].

The power system modernization is also related with the constant growth of energy demand and modern loads based on power electronics. Therefore, when modern loads and renewables interfaced by power converter reach high penetration levels, the planning and operation of the system can become a very complex challenge. In this context, Smart-Grids are composed of several elements that use various new computational tools such as Big Data, Machine Learning and Optimization together with ICT to make feasible the interconnection of heterogeneous technologies. So, the fast communication between elements with

information processing build up self-healing philosophy, black-start capacity, smart-metering application, etc [5, 6].

1.1.1. Renewable energy sources

High penetration of Distributed Energy Resources (DER), characterized by small generations close to consumers' centers (connected to Distribution Systems) bring some advantages like power loss reduction, supply cost reduction, transmission relief and more. The biggest part of DER are composed by renewables. Renewables have some characteristics that completely distinguish them from other power sources, like diesel generators that are dispatchable sources. The most prevalent feature is that renewables are not controlled to dispatch energy. Wind, sun, tides, and other natural phenomena are uncorrelated with the needs of consumers, which means intermittent energy production. For this reason, it is not possible to have at all time the production that matches the consumption; this intermittent generation is the largest challenge renewables pose, and must be considered either in the framework of power and of energy. A second characteristic is that most renewables have large dispersion. For this reason, electric production by renewables is often distributed, and then much harder to be integrated. Thus, renewables are mostly integrated into low and medium voltage levels, which is in complete antagonism with the way power systems were designed [7–9].

The diversity of renewables also includes the possibility of integrating non-conventional kinds of energy sources, as for example railways' braking energy recovery systems that regenerates this energy by providing negative torque to the driven wheels of trains, subway, tramways, etc. In that case, the engine's motor act as a generator, injecting power into the grid. Since the generated energy in regenerative braking is free from pollutant emission and waste, it can be considered a renewable energy source [10–12]. In a railway station, the regenerated energy is usually transferred to the third rail in order to let nearby trains utilize it. In case it cannot be used by other trains, it is dissipated on resistors. To improve system efficiency, the energy available can be seized to be stored or used when needed [13].

In transportation context, electric vehicles and trains can be integrated into the power system, which helps to reduce CO_2 emissions, increasing the efficiency in power conversion. But at the same time, electric vehicles considerably increases the demand for power in the distribution system, moreover, regenerative braking of train injects a big amount of power into the system in few seconds, which may bring

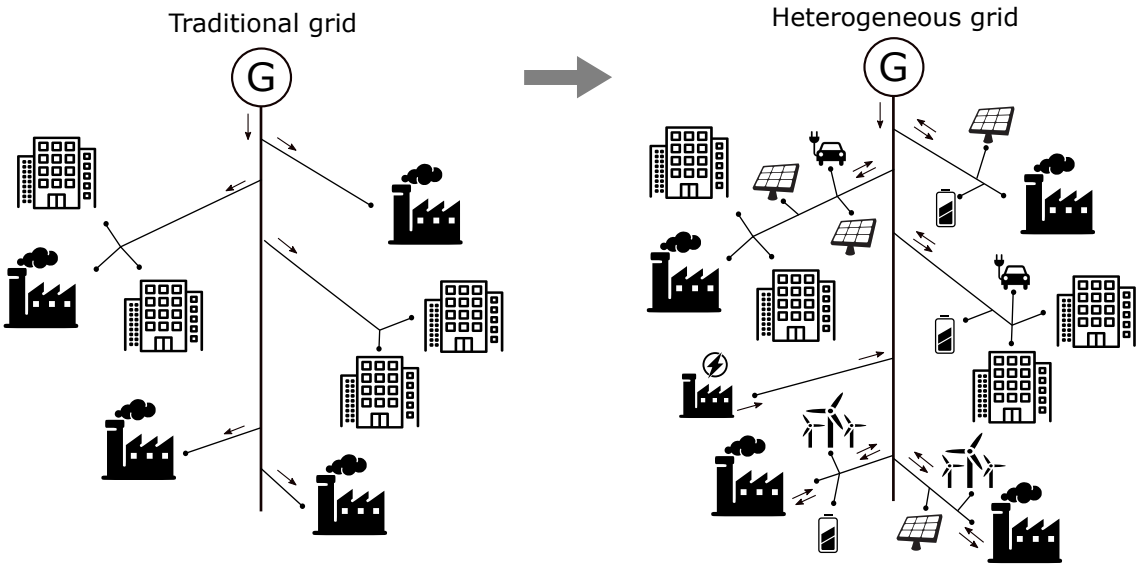

Figure 1.1: The transformation of the distribution grid from a centralized generation to a heterogeneous grid.

instability problems. Therefore, a proper control strategy to integrate it is necessary because of the power bursts [14–16].

Renewables are mostly integrated into electrical grid by power converters, which also present specific features. The switching of their semiconductors, either by IGBT, MOSFET or thyristors generate synchronized waveform to properly inject power to the grid created by a Pulse Width Modulation (PWM) signal. The switching process generates harmonics in the voltage and current signals, which may harm power quality indexes. Therefore, passive filters and multilevel converters have been studied to reduce the impact of harmonics and improve the controllability of the equipment. Power converters are also distinguished by their absence of inertia, since there is no rotating machine in the energy conversion, as a consequence the high penetration of renewables are impacting the system inertia as a whole. Hence, low inertia grids are becoming more common, directly affecting the stability of the system. In this context, isolated Microgrids represent a major challenge, since they may be completely composed of interconnected power converters [17, 18].

Figure 1.1 depicts the power system revolution representing the transition from the traditional network composed of generation units supplying the load in unidirectional way to the future choice of network composed of multiple distributed generations, storage systems and smart devices [19].

1.1.2. Energy storage systems

Energy Storage System (ESS) is one of the solutions to mitigate the impact of renewables, since a number of operation modes to manage ESS are well known and have been largely applied to other applications like transportation and Uninterruptible Power Supply (UPS) [8, 20]. Energy storage techniques can be mechanical, electro-chemical, thermal, etc. The most popular are the hydraulic in pumped storage and stored fuel for thermal power plants. ESS has been widely used to meet the energy generation with energy consumption, such as reservoirs for hydroelectric plants in Brazil, and Pumped Storage Plants (PSP) in France, being a mature technology. Therefore, ESS have the ability to improve many aspects of power systems directly related to power quality and stability. The main benefits of ESS to power systems are summarized in Table 1.1 according with [8].

Table 1.1: Electric grid energy storage services.

Bulk energy services:	**Infrastructure services:**
Energy arbitrage	Update deferral
Supply capacity	Congestion relief
Ancillary services:	**Customer energy management services:**
Regulation	Power quality
Spinning reserves (inertia)	Power reliability
Voltage support	Energy time-shift
Black start	Demand charge management

However, new technologies such as supercapacitors and batteries have limited power and energy capacities. In the same way, concerning efficiency, some technologies have yet to achieve high performance level. In particular when considering high levels of energy storage, since power losses may become considerable high [8]. All things considered, the major challenge for ESS is to find a tradeoff between investment and operational costs, while fulfilling economical constraints [20].

There is a very diverse range of ESS that are distinguished by their storage capacities, technology, or the way they store energy. The different ESS technologies can be seen in Figure 1.2 adapted from [9], exposing the relation between power and energy capacity. Technologies such as batteries have been widely exploited, especially in renewables integration and Microgrids. However, the operational cost of batteries becomes harmful, since the unpredictable power generation, has a significant impact on batteries' life-cycle. On the other hand, supercapacitors are devices capable of handling large variations of power within small time intervals compared to batteries.

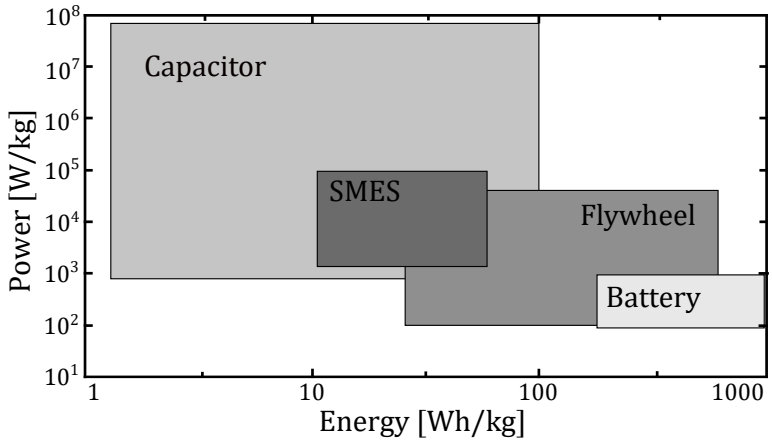

Figure 1.2: Relation between energy density and power density for different ESS.

This is due to its high power density, so they can supply much more power for a sudden demand.

At the same time, supercapacitors can inject/absorb power extremely quickly, which is a great advantage for applications with large spikes in power range. However, applications with large amounts of stored energy turn this equipment economically less viable. For this reason, Hybrid Energy Storage System (HESS) may be applied as optimized solution to store energy, putting together the advantages of each technology [21–24]. Since, each storage technology has a more suitable mean of application, the combined operation of different energy storage technologies (HESS) can greatly improve their application in power systems. In this work it will be considered the application o HESS mainly combining electro-chemical batteries and supercapacitors.

1.2. Microgrids

Among a number of elements, the concept of *Microgrids* has risen as an interesting solution to integrate renewables, loads and ESS as an autonomous system. Microgrids are small portions of the electric grid that can, to some extent, balance itself with the production and consumption of electricity and can stabilize its fundamental states. The United States Department of Energy Microgrids Exchange Group has defined Microgrid as [25]:

"A Microgrid is a group of interconnected loads and distributed energy resources within clearly defined electrical boundaries that acts as a single controllable entity with respect to the grid. A Microgrid can connect and disconnect from the grid to enable it to operate in both grid-connected or island-mode".

When the Microgrid is always connected to the main grid, thus importing and exporting arbitrary amounts of power, the Microgrid is said to be in grid-connected mode. In this case, the Microgrid is kept synchronized to the main grid, and as a consequence, frequency, angle, and inertia phenomena are dealt with by the main grid. Then, the Microgrid only needs to ensure voltage stability and mitigation of power congestion in lines, and optimize some power consumption patterns. This optimization may be regarding auto-consumption, renewables' share, profit, among others, and will be obtained by managing its production, the amount of power imported from the main grid, and possibly the use of storage [26–28].

But when the Microgrid may be disconnected (or at least not be synchronized) from the main grid, the Microgrid is said to be in island mode. In this case, the Microgrid is responsible for keeping stability in all states that compose it, i.e., frequency, angle (mainly inertia problems), voltage, power flow congestion, and profit. This case is far more complicated than the first. Then, if there is at least one large synchronous generator in the Microgrid, a diesel generator for example, that provides the largest share of the consumed power, then the system degenerates to the standard isolated Microgrid one can find in remote locations. But when larger shares of renewables are present in such grids, the problem may become very complex [28–30].

Another important aspect is the significant number of people in remote communities living without access to electricity. These villages may never have grid connection because of economic reasons and remoteness, therefore Microgrid is a great solution for electricity supply. On the other hand, many of isolated communities, such as African, Brazilian, Canadian or island communities, have great potential for solar radiation and wind, emphasizing the use of renewables. Electricity supply can be seen as a contribution to social inclusion and improvement of life's quality where electricity is mainly used for household purposes such as lighting, heating, water management and others to meet local energy demand [31, 32]. In addition, the transition to an electricity based energy usage avoids consuming local carbon-based resources like coal or wood, and helps to improve the conservation of ecosystems and mitigation of CO_2 emissions.

The stand-alone grid application (island mode) requires a proper operation to provide reliable, continuous, sustainable, and good-quality electricity to consumers, which brings several technical challenges for renewables application. The intermittent and non-dispatchable characteristic of renewables cause great impacts related to instability and fluctuations in their energy generation. In this context, the use of ESS coupled with renewables operating to supply a local load properly highlighted

the Microgrid concept, which is a powerful solution to accomplish the targets of stand-alone grid operation, improving reliability, resilience, and availability of the whole system [33–35].

Microgrids may indeed bring an important answer for most of these problems and may represent in the future the new standard for power systems. Nevertheless, it is still a very difficult problem to guarantee reliable operation and attain stability of the system considering the grid requirements, thus much effort is necessary to make such grids a widespread reality.

In Microgrid context, Direct Current (DC) Microgrids are seen as a major advantage, since renewables (Photovoltaic Panel (PV), Wind turbines, fuel cells), electronic loads, electric vehicles, and storage (batteries, supercapacitors) have DC nature. If they are connected through a DC grid, they would need a smaller number of converters, and those converters would be simpler than if they are connected through an Alternating Current (AC) grid. The result would be less expensive materials, and better efficiency (fewer losses). Also, direct current can be more efficient due to its simpler topology; the absence of reactive power and frequency to be controlled; the harmonic distortion is not a problem anymore; and there is no need of synchronization with the network. The consequence is a simpler control structure based on the interaction of currents between the converters, being the DC bus voltage the main control priority, that is, the voltage is a natural indicator of power balance conditions [36–40]. At the same time, the DC Microgrid is a challenge because the structure of the current power grid, power supplies, transformers, cables, and protection are designed for alternating current. For this reason, hybrid AC/DC Microgrid is seen as a compromise between AC and DC to allow better integration between these new devices and the classical electric grid components [41–43]. Figure 1.3 depicts a general DC Microgrid composed of renewables generation, ESS, loads and grid-connection.

Nowadays there exist several examples of small DC Microgrids, as in marine, aviation, automotive, and manufacturing industries. In all these examples, it is extremely important that the Microgrid is controlled in such a way to present reliability and proper operation. To attain this goal, there are many control strategies proposed for Microgrids. The linear technique is the most popular one, due its simplicity and robustness; in addition linear control is well known for both academia and industry. Linear control is based on a linearized model given by the electrical circuit equations of the Microgrid, where the nonlinearities are not considered. As a consequence, this simplified model is only valid in a small region around the operation point where the linearization was made. There are several approaches to

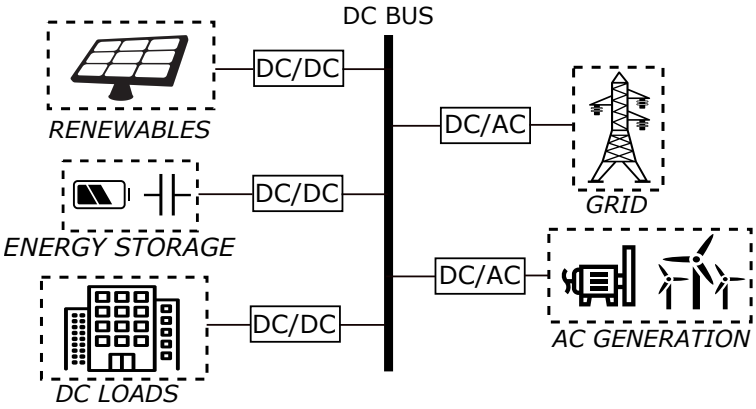

Figure 1.3: A general DC Microgrid scheme.

design linear control, for example, in frequency domain via transfer functions or by state space modeling, where Proportional-Integral-Derivative (PID), state feedback via pole placement and Linear Quadratic Regulator (LQR) optimization are common strategies. The minor loop gain is another example of linear technique that relates source and load impedance to determine stability in the grid and this strategy maintains the system dynamics even when connecting more devices like filters. The impedance-based approach provides a good perspective on dynamics like the well-known state space modeling [35, 44, 45].

Nonlinear control, on the other hand is based on a more detailed model of the system, in the sense that nonlinear dynamics and the whole operation space are considered. Then, the nonlinear theory allows for a more realistic grid modeling, a more effective stability analysis, and a broader range of operation. The utilization of nonlinear control techniques may also improve power flow performances in the Microgrid, since the system is not restricted to a specific operating point. As a consequence, there is the possibility to work in a wider region of operation, considering just the physical limitations of the system as restrictions. A drawback of the use of nonlinear control technique is the increased complexity of analysis and sometimes in the resulting control law, which is sometimes harder to be implemented [36, 37, 46, 47].

1.2.1. Hierarchical structure

To provide proper operation of the system, it is necessary to implement a full control strategy involving different time scales, referring to a hierarchical control structure. The hierarchical control structure spans local, primary, secondary, and tertiary controllers, ranging from milliseconds to hours or a day. Figure 1.4 describes the hierarchical control structure in a Microgrid.

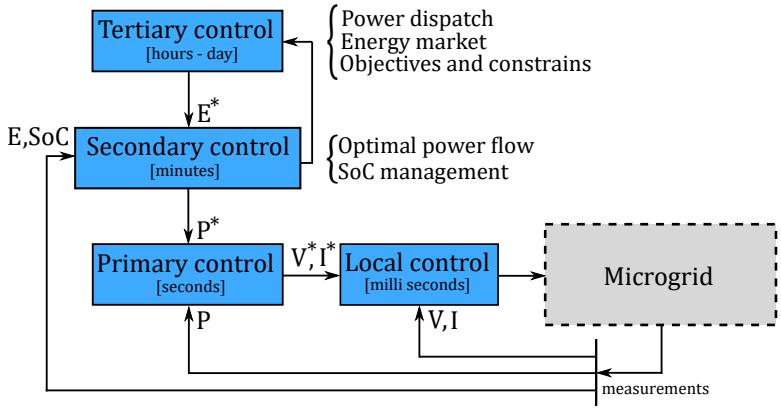

Figure 1.4: The traditional hierarchical control structure for a Microgrid. The local and primary control generate the references for lower level power converters, while the secondary control deals with power flow regulation and the tertiary control covers the energy dispatch and energy market.

The **local controllers** are the mathematical algorithms that assure stability of the lower level variables and counteract disturbances with fast response, good transient and steady-state performances. Hence, local controllers ensure the transient stability of the system in milliseconds to seconds, and currents and voltages references are given by higher level controllers. The local control acts on the power converters of the Microgrids devices usually using their PWM modulation to control the converters' dynamics [48, 49].

The **primary control** operates in a time range of a few seconds; its responsibility is to adapt the grid operation points to a disturbance acting during the time interval the secondary controller needs to calculate new optimal operation set points. For smaller Microgrids, the primary can be integrated into the local controller, in a master–slave approach. In this case, one converter is assumed to keep the grid's stability (master).

The **secondary control** level carries out the power flow regulation of the system taking into account the State of Charge (SoC) of ESS (battery and supercapacitor), then an optimal power flow is generated. The power flow is calculated by sharing the load demand in the system among the renewables generation and the storage elements also taking care of their SoC to allow for proper functioning and save battery lifetime. The secondary control provides a reference of power to the grid assuring power balance in the system; it is also related to power quality requirements and device operating limits where the constraints must be respected [50].

The **tertiary control** deals with the energy market, organizing the energy dispatch schedule according to an economic point of view, taking into account nego-

tiation between consumers and producers. This level also deals with human–machine interaction and social aspects [48, 51].

1.3. Ancillary Services

Historically, power systems were based on synchronous machines rotating in synchronism, sharing power to suppply the load, and providing natural inertia (frequency response) following disturbances or simply changes on operating conditions. This classical scheme is less and less true, because of the large penetration of power electronic devices like power converters and modern loads.

Power converters are inherent to the interconnection of renewable energy sources and storage units as mentioned before, but also by the High-Voltage Direct Current (HVDC) lines that are being built to reinforce current transmission systems. For this reason, inertia is reducing fast, and in some situations, there are grids mostly composed of power converters where the frequency reference is completely lost [52–54]. This situation is a change of paradigm from the classic electric grid, and power systems practitioners are struggling to keep the grid running. A recent example of such situation is the 9 august 2019 black-out in the United Kingdon [55], where the main cause was the reduction of inertia, and its effect in several power converters interconnecting distributed generation.

DER are mostly formed by renewable energy sources, which have a power electronic interface. And so, the power converters do not have an inertial response due to the absence of a rotating mass, as conventional synchronous generators do. Power converters are unable to naturally respond to a load change. Consequently, the frequency response worsens, causing oscillations and operating margins problems. Thus, the integration of renewables has a direct relationship with the reduction of inertia in power systems.

The consequences on frequency response from the inertia reduction is depicted in Figure 1.5 [56]. The integration of renewables in power system induces a higher frequency deviation from a load change. As the level of penetration of renewables increases, the inertia of the system decreases resulting in larger frequency variations. The effect of inertia reduction in frequency response is compared according with the level of renewable participation (20%, 40% and 60%). The Rate of Change of Frequency (RoCoF) indicates how fast the variations of frequency become as the level of renewables penetration increases.

The inherent features that systems mainly composed of power converters are:

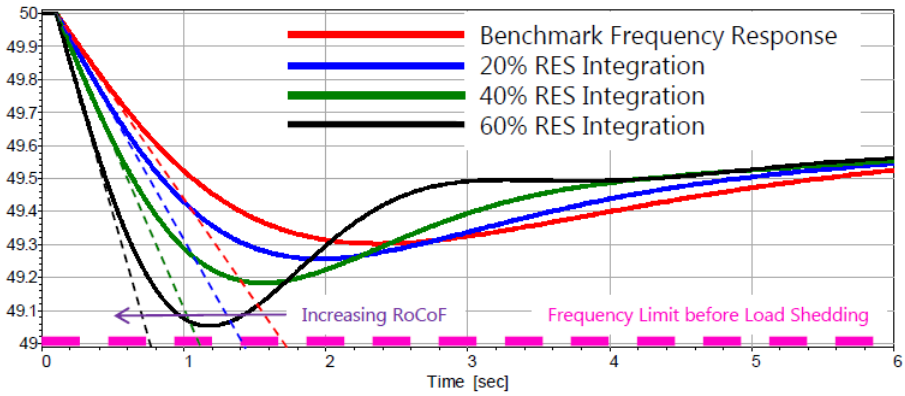

Figure 1.5: The effect of the inertia reduction according to the renewable integration levels in the network.

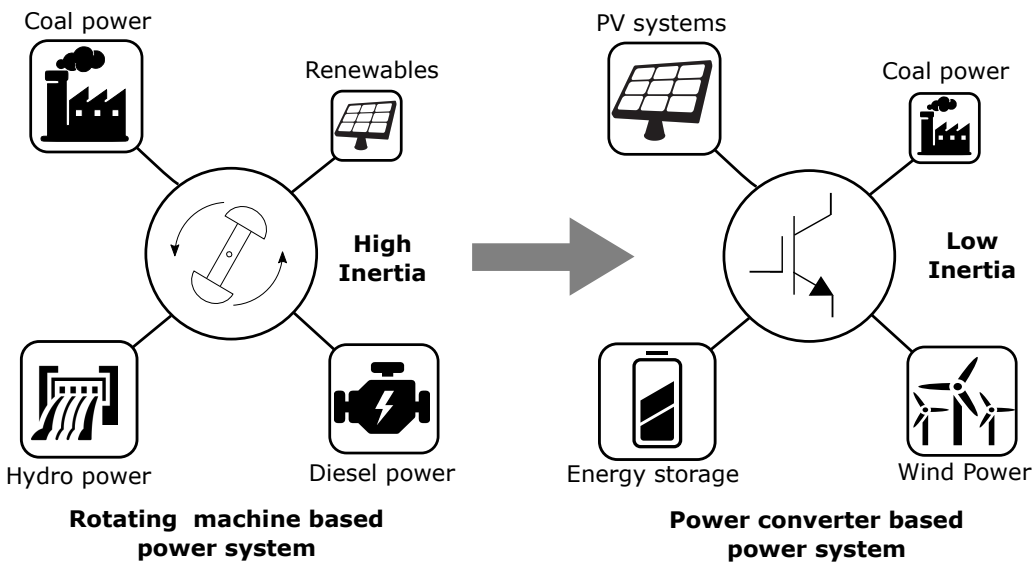

Figure 1.6: Network evolution towards power converters' systems.

1. Fast response;
2. Lack of inertia;
3. Harmonic issues;
4. Interaction between controls;
5. Weak overload capacity.

The converter dominated grid is emerging from a traditional generator dominated grid, therefore the lack of inertia is becoming a main issue of concern. The grid modernization through power electronics advancements is illustrated in Figure 1.6, adapted from [57]. Therefore, energy storage is required to balance generation and consumption in this kind of system, specially for strong variations on load or generation, when compared to the case of rotating mass reserve (inertia)

and damping winding in traditional synchronous machines that buffer the strong oscillations improving the system's stability.

Many studies proposed different control strategies to maintain voltage and frequency stability in weak/isolated grids. Indeed, such low-inertia power converter interfaces tend to make the system sensitive to disturbances. The most relevant strategy is the droop control, where Active Power and Frequency ($P - f$) relation together with Reactive Power and Voltage ($Q - V$) are made to assure stable operation of the system. This control technique has been widely applied enabling flexible operation of the connected distributed resources making possible to share the burden of keeping frequency and voltage stability in the network. Anyway, classic $P-f$ and $Q-V$ droop strategy act only in the steady state regime, and then the lack of effect in transients make droop control unsuitable to improve frequency stability. But we already have some variants of droop control that consider the transient response by inserting a frequency derivative term. Usually, droop control is applied as the primary control in a hierarchical structure, where the secondary control is designed to mitigate frequency and voltage deviation in a slower time scale [58–62].

An interesting possibility for solving these problems, is represented by the concept of synchronverters [63], called VSM[1] in [64–67], or even VISMA in [68]. These are composed of power converters that mimic synchronous machines. In this way, it is much easier to integrate such systems to the power network, providing a framework that practitioners are well acquainted [57, 69, 70]. These synchronverters have raised much interest in recent years. In this approach, it is proposed to mimic the steady state and the transient characteristics of synchronous machines by inserting the swing equation to provide an inertial response improvement.

Many studies have been carried out concerning the application of virtual inertia in power converters, such as integration of distributed generation [70–72], improvements in Microgrids [73, 74] and isolated power systems [75]. In [76], a comparison on the dynamics between virtual inertia and droop control strategy is done, pointing out the similarities and the advantages of each control strategy, as well as the relevance of inertia properties. As the next step, new propositions of virtual inertia emerged, for example, in [67], the parameters of virtual synchronous machines can be controlled, and then, VSM with alternating moment of inertia is developed. The damping effect of the alternating inertia scheme is investigated by transient energy analysis.

[1]Note that VSM is said as the VSC operating as a synchronous machine.

In the following chapters it will be presented new results for these systems, but now acknowledging that if power converters act as synchronous machines, they are not limited to this behaviour, and can provide extended support than physical machines do. In this way, it was studied the contribution that Virtual Synchronous Machines may bring to the overall inertia of a power grid, and how they can provide ancillary services, considering frequency support and synthetic inertia. In particular, this approach can contribute to solve problems brought by renewables in modern power systems, and allow much larger penetration of such intermittent energies.

1.4. Thesis Contribution

This thesis constitutes a step forward of hybrid AC/DC Microgrid control and introduces rigorous stability analysis via Lyapunov techniques considering nonlinear dynamical model of the studied system. In the same context, the behavior of multiple interconnected devices are carried out considering a *System-of-Systems* approach, where different generations, loads and storage systems must properly operate.

The studied Microgrid is composed of renewables, such as PV arrays controlled to extract the maximum available power, and regenerative braking from subways or tramways where the generated energy from braking is harnessed and correctly stored to be used when needed.

A HESS composed of batteries and supercapacitors is applied. The battery is used to realize the power flow in long term, without harming its life cycle, and the supercapacitor is used to regulate the DC bus of the grid assuring the power balance of the system.

Different kinds of loads (AC, DC and Constant Power Load (CPL)) are inserted into the Microgrid to understand the perturbations caused and how the system reacts to these variations.

At last, connection with the main AC grid is done, where the DC side of the grid supports the AC side with different control strategies. When there is a strong main AC grid, the control target is to provide ancillary services by injecting/absorbing active and reactive power for the main grid. When there is a weak grid, or even in an isolated case (no synchronous machine case), the control target is to control frequency and voltage of the AC system, assuring proper operation and system stability. Therefore, the voltage and frequency support highlight the ancillary services provision.

In this last case of the interconnection with the AC weak grid, the is developed a virtual synchronous machine approach, where the swing equation of a traditional synchronous generator is introduced in the AC/DC converter to mimic the inertial behavior of a synchronous machine. Therefore, the control strategy is designed to provide inertial support, improving voltage and frequency stability. A next step is taken using the inertia value as a state variable to improve the frequency support and robustness.

From the resulted Microgrid model, a distributed nonlinear control is developed considering the operation of each device of the system and the stability of the whole grid. Therefore, the proposed nonlinear controller is able to integrate renewables while properly supplying the local loads. The control of the DC bus of the Microgrid, and the regenerative braking system from trains when that is the case, are designed based on control induced singular perturbation and dynamic feedback linearization. The controllers for the Microgrid equipment are designed via feedback linearization and backstepping control techniques while a Lyapunov function considering the whole system is build to guarantee the stability of the system.

Therefore, disturbances to the system such as high energy peaks from trains' braking, intermittent nature of renewables, load variations and nonlinear dynamics are considered in the evaluations of the nonlinear control strategy. The performance of the proposed controller is highlighted by detailed simulations and the comparison of classical linear control strategy is conducted to emphasize the improvements in control response and robustness properties of the nonlinear control in contrast with the linear approach.

The contributions and proposed investigations of the thesis can be summarized as follows:

- Design of a flexible hybrid AC/DC Microgrid capable of integrating a number of distributed generators without affecting system stability.
- Integrating different ESSs into a HESS that can balance the whole grid in transients and steady state (long term stability).
- Study the perturbation caused by different loads connected into the Microgrid and the intermittent behavior of the renewables.
- Design a control strategy to allow regenerative braking from trains, such that the burst of power is properly absorbed by the storage system.
- Modeling the system, and design a distributed nonlinear control strategy to the entire Microgrid according to physical characteristics of their components, such that stability is guaranteed.

- Develop a complete and rigorous stability analysis, such that the stability properties are demonstrated.
- Develop a control strategy via virtual inertia approach, such that the DC side of the grid is able to properly provide ancillary services to the AC grid, considering strong and weak grid.
- Proposition of variable virtual moment of inertia to improve the frequency stability and the inertial support.

1.5. Thesis Outcomes

Journal Articles

1. F. Perez, A. Iovine, G. Damm, L. Galai-Dol, and P. Ribeiro, "Stability analysis of a DC Microgrid for a smart railway station integrating renewable sources," IEEE Transactions on Control Systems Technology, 2019.
2. F. Perez, G. Damm, F. Lamnabhi-Lagarrigue, and P. Ribeiro, "Nonlinear control for isolated DC Microgrid," Revue Africaine de la Recherche en Informatique et Mathematiques Appliquees, vol. 30, 2019.
3. F. Perez, G. Damm, F. Lamnabhi-Lagarrigue, and P. Ribeiro, "Stability Analysis of a Hybrid AC/DC Microgrid based on Nonlinear Control including Adaptive Virtual Inertia for Ancillary Services Provision", IEEE Transactions on Smart Grid, 2020, submitted.

Book Chapters

1. F. Perez and G. Damm, "DC Microgrids," in Microgrid Design and Implementation. Springer, Cham, 2019, pp. 447–475.

Conference Articles

1. F. Perez, A. Iovine, G. Damm, and P. Ribeiro, "DC Microgrid Voltage Stability by Dynamic Feedback Linearization," in 2018 IEEE International Conference on Industrial Technology (ICIT). IEEE, 2018, pp.129–134.
2. F. Perez, A. Iovine, G. Damm, L. Galai-Dol, and P. Ribeiro, "Regenerative Braking Control for Trains in a DC Microgrid Using Dynamic Feedback Linearization Techniques," in IFAC Workshop on Control of Smart Grid and Renewable Energy Systems CSGRES 2019, vol. 52, no. 4,pp. 401–406, 2019.
3. F. Perez, G. Damm, P. Ribeiro, F. Lamnabhi-Lagarrigue and L. Galai-Dol, "A Nonlinear Distributed Control Strategy for a DC Microgrid using Hybrid Energy Storage for Voltage Stability," IEEE Conference on Decision and Control, 2019.

4. F. Perez, G. Damm, F. Lamnabhi-Lagarrigue, P. Ribeiro and R. Monaro, "Adaptive Variable Synthetic Inertia from a Virtual Synchronous Machine Providing Ancillary Services for an AC Microgrid," IFAC world congress, 2020.
5. F. Perez, G. Damm, F. Lamnabhi-Lagarrigue, P. Ribeiro and Guacira C. de Oliveira, "Voltage and Frequency Control of an Isolated Hybrid AC/DC Microgrid using Virtual Synchronous Generator," EPE'20 ECCE Europe Conference, 2020, accepted.

CHAPTER 2

Microgrid Overview

2.1. Introduction

In this chapter, a review in Microgrid operation and control is developed, where the conventional management strategies are presented and real application examples are cited. The standard control structures are discussed to understand the features and behavior of the system, regarding stability aspects. DC and AC Microgrids' design are also presented, considering the different control targets for grid-connected and isolated systems. The chapter highlight the challenges for Microgrid operation to reduce the impact of renewable generation, improve system reliability and provide ancillary services. The goal is to present the state of the art in Microgrids to emphasize its importance in modern power systems.

2.1.1. General review

Microgrids allow better integration of renewable sources, supply of local loads regardless the network, i.e., operation in island mode, through the management of the ESS. Thus, the benefits generated by the use of Microgrids bring greater reliability and resilience to the distribution system with better energy efficiency. More benefits of using Microgrids and the possibilities of operating this system are cited in the following.

Microgrids may interconnect Distributed Energy Resources (DER) and loads with a dedicated control strategy aiming at suitable operation of the system, considering the behavior and limitation of the DER while keeping the system's stability and the required operational margins. In this regard, Microgrids can better integrate renewables, since the control strategy is designed considering the system as a whole, including loads and generations' particular characteristics, which improves

the operation of DER in the Microgrid context. Among the control techniques used in Microgrids, the droop control stands out. This is applied to coordinate the different units of DER and to operate the converters connected in parallel for load sharing in the electrical network. A comparative analysis between the main droop control methods and their variations is presented in [61]. In [77], a droop control scheme for voltage and frequency is proposed, which allows multiple VSC converters to operate in parallel in a Microgrid, sharing active and reactive power. Converters are needed to integrate renewable energy sources such as wind turbines and fuel cells. The droop control scheme has its limitations, generally presenting a slow response in transients with small errors in steady state, however it is simple to implement and allows good sharing of multiple distributed generators.

Power quality is a great issue in Microgrids, since the operation is limited accordingly with the technology and control scheme of the DER integrated into the grid. The power converters used for DER connection have brought solutions that improved the operation of the system, but harmonic problems, and voltage and power fluctuations arrived as a consequence, which brings other power quality problems. The main power quality problems and possible solutions for Microgrid application is summarized in [78], where cooperative control is used to enhance voltage harmonics and unbalances in the grid. Then, Static Synchronous Compensator (STATCOM) is introduced to improve voltage sags and voltage swells, allowing multiple DER operating in parallel with acceptable voltage level. In conclusion, the coordination of power converters in Microgrids are capable of enforcing rated proportional power sharing among the different sources, where wind turbines and PV converters can be used to improve the power quality of the grid.

In view of the complexity of Microgrids, both DC and AC systems have operational challenges, when interconnecting multiple energy sources to properly supply the loads. A comparison between AC and DC Microgrids is provided in [29] considering different equipment technologies based on economical, technical and environmental benefits related to DER units. The feasibility of control and energy management strategies is investigated, where real applications examples of DC and AC Microgrids are given. The paper also presents a study over different configurations of DER in low voltage distribution networks, considering distribution lines and protections schemes for AC and DC Microgrids. The importance of the DC Microgrids is highlighted in the future power system.

AC Microgrids present difficulties of frequency synchronization, voltage control in islanding operation and control of reactive power flow, when compared to DC Microgrids, however DC grids also have problems regarding stability. In [38], the

stability problems of DC Microgrids are addressed together with control strategies typically used in these systems. It is pointed out that the limitations of the proposed control strategies are assessed by the complexity of implementation, operation performance and verification of stability margins. In the exploited approach, the stability of the whole system can be defined by the relationship of the source and load impedances, referred to as the minor loop gain, that has the advantage of directly defining the stability criteria for each individual subsystem. Another approach to solve voltage stability issues in Microgrids is presented in [79], based on passivity-based control. The proposed control design is decentralized and allows the addition and removal of DER units in a "plug n' play" manner.

In [80], an overview of the Microgrid control techniques for different hierarchical levels is provided. An analysis of the main operation modes and control structures is performed, for the converter control level, considering the power supply and support for the network. Also, the importance of the high-level control layer to optimize the network efficiency and performance is highlighted. Therefore, the optimal operation is met based on strategic criteria, such as operating cost and power quality. Depending on the hierarchical control levels, it is possible to split the time scales of the system for different control action and operation modes.

Concerning the challenge of coordinating Microgrid storage systems, a general review of the control strategies for this purpose is provided in [49]. A multi-agent control is proposed as a direction for future research, as it presents the desirable middle ground between the decentralized control structure, which is not able to fully utilize the combined power and energy capacities of the storage system, and the centralized one that raises concerns about the security and communication resources required. This theme is also addressed in [81], where a control scheme based exclusively on local measurements is presented for isolated Microgrids. The focus is to perform frequency restoration and maintain the SoC of the storage elements, without the need of communication, which can impact the reliability of the Microgrid. Thus, it is possible to keep the system frequency within the desired levels using only local controllers.

2.1.2. Supervision and optimal operation

There are many challenges that need to be faced in controlling Microgrids. Unlike conventional networks, Microgrids bring the integration of energy sources in the form of DER, which can cause bidirectional power flow complicating the protection and control schemes of these systems. In addition, instability problems, due to the

interaction of controls and transitions to different operation modes (connected or isolated). The reduced inertia of the Microgrids due to the composition of loads and generators based on power electronics, bring problems in the system's operating margin, reducing the system's robustness in face of disturbances and load changes. There are various factors of uncertainty associated with load demand and especially with renewable energy sources, that have intermittent characteristics. Thus, reliable operation of the system needs to involve load forecasting and weather forecasting models. Another important factor is the Microgrid's electric models, where several assumptions are made, as balanced three-phase systems, inductive lines and constant loads, which deviate traditional models from reality.

To address these challenges, control systems must ensure reliable system operation. Thus, currents and voltages must be properly controlled to reduce oscillations, frequency must be kept within the operating margins in both connected and isolated operation. The power balance must be regulated to maintain the balance between demanded load and generated power, with smooth variations for different operating modes transition and fast fault detection. In addition, economic dispatch with power sharing between generations can reduce operating costs and maintain system reliability. The optimization of operating costs can also include the provision of ancillary services together with optimal management of the power flow for the entire network. Thus, an adequate control strategy guarantees the proper operation for a Microgrid.

The main challenge in the operation of the Microgrids is to maintain a safe operation of the system, balancing generation and demand, where the optimal management of the system can be done through heuristic algorithms or intelligent control. Model Predictive Control (MPC) is also widely applied in Microgrids to assure the optimal operation. MPC solves optimization problems in each sampling time, in order to determine the operational minimum (economic or technical) considering the physical limits and technical restrictions of the grid. Thus, the MPC includes a feedback feature in the optimization process to withstand uncertainties and disturbances, dealing with operational restrictions, such as the limits of storage capacity or the rate of power variation. MPC can also incorporate generation and load demand forecasts, based on the future behavior of the system. It is possible to obtain an optimal operation considering economic and technical criteria, which makes the MPC a very relevant control strategy for Microgrids [82–84].

The Microgrid operation address different energy scenarios, where generation excess/deficit is minimized trough optimization methods composed of cost functions. However, the open-loop feature of optimization systems does not allow to com-

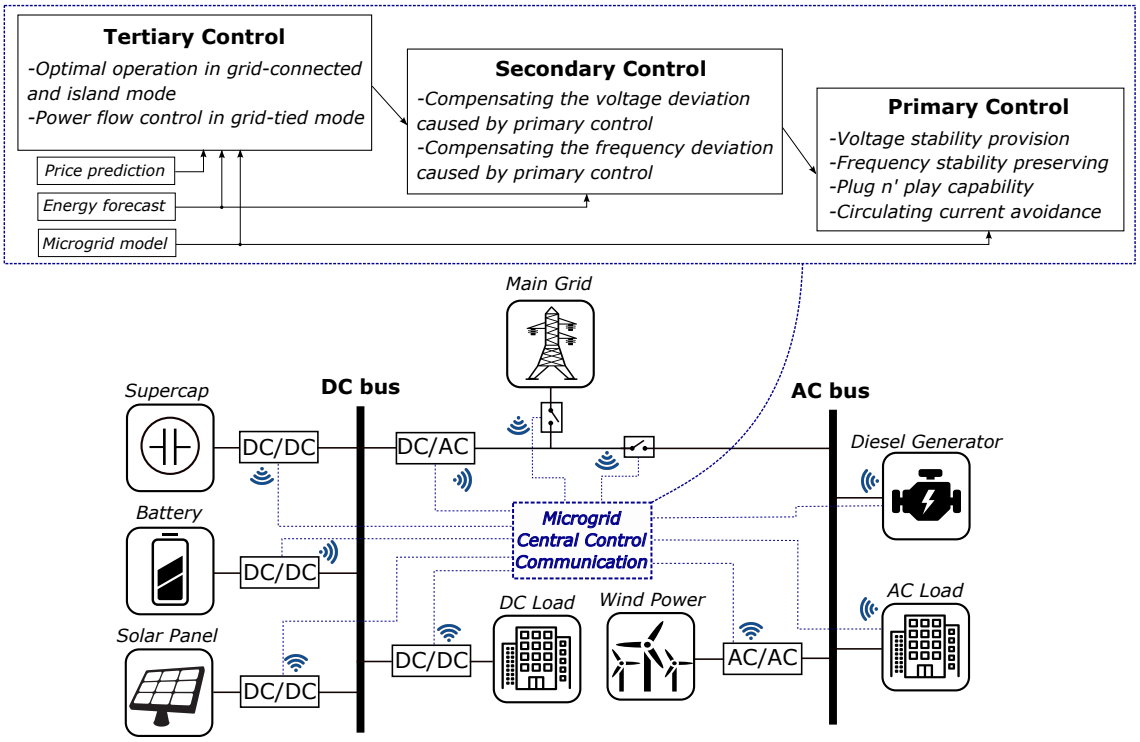

Figure 2.1: A Microgrid composed of central control with hierarchical structure.

pensate uncertainties and disturbances. Therefore, MPC closed-loop feature allows corrective actions using measurements to update the optimization problem, which ensures the optimal operation of the system [82].

The hierarchical control structure of Microgrids perform the separation of the variables according to time scale, therefore, variables with close time response are controlled in the same control level. Hierarchical control are typically composed of three different levels: primary, secondary and tertiary level. Primary control deals with the stability of currents and voltages at the transient level, on a time scale from milliseconds to seconds. The secondary control performs the control of power and energy of the system through optimization techniques in minutes to hours. The tertiary control deals with strategic dispatches, according to an energy market or human factors, in the order of hours or days [85, 86]. A general scheme of a Microgrid is presented in Figure 2.1, where the Microgrid central control contains the hierarchical structure to optimal operation of the entire system.

In [87], a control strategy using MPC is proposed for the optimal power flow among ESS in a Microgrid. The proposed control strategy solves the optimal power flow problem considering line losses, voltage restrictions and current restrictions in converters, as it does not assume that active and reactive power flows are dissociated. Nonlinear variations in efficiency of the batteries are also considered,

which contributes to improve the optimization result. The real time implementation is possible thanks to the reduced computational effort of the strategy.

In [88], a structure of control and supervision is designed for the management of the optimal energy cost in a grid-connected DC Microgrid. The Microgrid is composed of PV generation, ESS and DC loads. The work combines power balance regulation with real time optimization. The control structure of the Microgrid is composed of four layers: human machine interface; the forecast layer, which provides load consumption and PV generation; energy management layer, where the power flow optimization is realized; and operating layer that perform the balance of instantaneous power. The multi-layer structure simplifies the implementation of a complex control scheme, since each layer provides an independent function. Thus, the power balance optimization and control is carried out simultaneously without interfering with each other.

2.1.3. Microgrid examples

In [89], the implementation of a *Smart Village Microgrid* is introduced, which is applied to isolated communities of African villages that are not connected to the main electricity grid. This concept was supported by the programs: *Institute of Electrical and Electronics Engineers (IEEE) Smart Village Program*, *Oxford University Smart Villages* and *NREL's International Sustainable Village Power Program* for township electrification programs for informal settlements. The idea of this kind of Microgrid, is to promote energy justice and quality of life, together with sustainable employment and energy supply, to offer a new paradigm for modeling sustainable development capable of supporting isolated communities. At the same time, Microgrids can help accelerate the development of energy and entrepreneurship. The Smart Village approach provides an understanding of the real barriers to access energy (technological, political and financial barriers) and how to overcome these barriers in remote communities in a practical way to provide access to education, health, drinking water, technologies information and communication, entertainment and sustainable livelihoods.

The Microgrid at Gaidouromantra, in Kythnos, electrifies 12 residences in a small valley located in the middle of the Aegean Sea, is introduced in [90]. The system is built via an aerial distribution network and parallel communication cables. This valley is located 4 km from the nearest medium voltage network and, due to access difficulties, the island's isolated operation was chosen. The network is powered by three converters connected in parallel, operating together in a master-

slave configuration, allowing the use of more than one converter, only when power is required. Each battery system has a maximum capacity of 3.6 kW and operate in droop control mode. This mode of operation distributes the duty to stabilize voltage and frequency (active and reactive power control) in the network. The control also allows limiting the PV converters if the storage system is totally charged, and even perform load shedding at critical moments (low generation and empty storage system).

The system consists of a 10 kWp photovoltaic module installed in the roof of the houses, divided into smaller subsystems, a battery bank with a nominal capacity of 53 kWh, and a diesel generator set with 5 kVA nominal power. A second PV system with 2 kWp is connected to a 32 kWh battery bank to provide power for the monitoring and communication system.

The objective of this Microgrid was to test centralized and decentralized control strategies in island mode and to test different communication configuration. Wind turbine integration is proposed as future investments to reduce the use of the diesel generator and diversifying energy resources. Also is proposed, new monitoring system to allow remote connection via cell phone, check the system's operating status and transfer data.

In [91], a DC Microgrid is integrated into a train station, controlled by a low level distributed nonlinear controller. A number of elements compose the Microgrid: a PV plant, a train line for power injection through regenerative braking, a battery system, a supercapacitor and a local load. The aim of the paper is to ensure voltage stability in the DC network and correctly supply the load while both the PV system and the braking energy recovery system inject as much energy into the grid as possible. As the braking energy recovery system introduces high current in a short period of time, battery life could be reduced quickly. Therefore, the supercapacitor is the most suitable storage element to absorb the large peaks of power injection in the network, since its lifespan is not affected by this kind of operation. The energy from the battery provides the stability in long term, considering the system power flow and the SoC of the storage elements. The supercapacitor duty is to control the voltage on the DC bus to meet the power imbalance in the whole system, assuring voltage stability. In this way, the paper presents an interesting application of HESS, composed of battery and supercapacitor, for voltage stabilization in a DC Microgrid.

An isolated Microgrid project in Bella Coola, Canada, is presented in [92]. The project aims to reduce the use of diesel generators improving reliance on cost and decrease emission of pollution. The idea is to replace the generators with clean renewable energy. The paper describes the technical challenges with emphasis on the

control and monitoring part, highlighting the lessons learned that can be inspiring for future projects.

The Microgrid is composed by 8 diesel generators from 300 kVA to 2500 kVA, where the total capacity is about 7200 kVA. Also, two hydro plants with power rate of 720 kVA and 1400 kVA are installed. The peak load values are 4.3 MW during the winter and 2.3 MW during summer season. The diesel generator duty is to regulate the frequency and the hydro plants complement the load demand supply, according to the available power. However, during the summer due to the significant contribution of hydro units, the larger hydro turbine is operated in isochronous mode. Therefore, the diesel consumption is reduced, but since the hydro turbine has slower dynamics response, the diesel is occasionally used to maintain the desired frequency control.

To improve the system operation, a fuel cell of 100 kW, composed of electrolyzer, compressor and hydrogen storage cylinder is proposed as ESS. The fuel cell can balance power mismatch between power generation and load demand in a proper way, improving the system efficiency. The use of the diesel generator is reduced to frequency regulation purposes. The monitoring system was proven to be an efficient tool for system operation, meeting the project expectations, which provides a good example of Microgrid operation.

There are many papers in literature that identify the technical challenges of Microgrids in order to maintain power quality. A transition from the connected mode to the island mode and vice-versa must be accurate, as well as control strategy and protection schemes. The main regulatory barriers of Microgrids are related to grid-connection, bidirectional power flow restrictions and energy commercialization. Although many generation and storage technologies incorporated to Microgrids have economic government incentives, renewable generation, batteries and other storage technologies still present relatively high costs, which is a great challenge for practical implementation of Microgrids. Thus, incentives and financial support from research developers are still the biggest investors in this technology considered innovative.

In [93], is pointed out the main necessary characteristics for a Microgrid to operate within techno-commercial trends. These success factors can be described as:

- Stable, reliable and economically viable energy sources, such as combined heat and power, hydro power, wind generation, diesel generators, among others, must be part of the Microgrid to provide stable electricity during outage periods;

- Optimize the equipment size of the Microgrid to meet energy demands and maintain power quality more efficiently when the Microgrid operates in island mode;
- Backup equipment, especially energy storage, to ensure the power supply during peak demand and facilitate the transition between grid-connected and island operation;
- Effective power quality and Energy Management System (EMS) communicate with distributed generators and the main grid, therefore the consumption is optimized and power quality is attained within grid requirements;
- Supportive regulatory and market framework, such that the energy commercialization between consumers is promoted, facilitates trading with the main network and between constituents, therefore an energy market is developed;
- Stakeholder involvement, building a cooperative relationship between the energy provider and the consumer is especially important in isolated Microgrids to preserve equipment and its maintenance;
- Training of Microgrid operators, as well as an easy-to-use interface to facilitate maintenance during unforeseen events, such as failures and natural disasters.

2.2. Classification and Stability

The Microgrid configuration goes from low voltage to medium voltage, normally the voltage values are between $220V$ to $69kV$. Their dimensions can be as varied as possible from a few units of kilowatts, supplying few consumers, even large and complex interconnected systems with dozens of Megawatts. The ability of Microgrid to operate in island mode, with seamless transition towards grid-connection and the capacity to provide a black start, improve the resiliency and the reliability of distribution systems against blackouts [94].

The required control scheme to operate a Microgrid can be centralized, decentralized and distributed. In centralized control, the measurements and grid information is allocated in a Central Command trough a communication infrastructure. In decentralized control, the communication remains locally, but the operation of the whole system is assured. Decentralized control uses local metering to estimate the neighbor variables, which has a considerably lower installation cost, due to the absence of communication cables, but its implementation complexity is much larger than the centralized control.

The distributed scheme exchange information with neighbors to provide local actions. Distributed control allows independent operation of each device in the

Table 2.1: Categories of Microgrid control from communication perspective.

Category	Definition	Technical features
Centralized control	Data acquisition from distributed units, central aggregators collect and store information, processed and feedback commands are send via digital communication links	Reliability is degraded, high computational effort, optimal decision assured, plug n' play is difficult
Distributed control	Digital communication link are implemented among different generation units, coordinated control strategies have local action	Reliability is maintained, less communication effort, optimal decision is possible, plug 'n play is possible
Decentralized control	Digital communication link are not implemented in this case, The local controllers do not receive information from higher control layers	Reliability is maintained, least computational effort, not guaranteed optimal decision, easy to plug n' play

system assuring greater flexibility and improving reliability, compared to the centralized strategy where a communication fail can bring down the whole system [36, 95]. Indeed, the advantages of the distributed control for Microgrids is because the control laws are developed for each converter connected to the grid, in which coordinated strategies provides the operation of the whole system [27, 51]. Table 2.1 introduces the aspects of centralized and distributed control from the communication point of view for Microgrids.

Typically, the Microgrid contains a communication structure and metering devices to provide information from primary control layer (local control) to higher control layers, such as the secondary and tertiary control layer. The control layers are organized by the hierarchical control structure of the Microgrid[1]. The hierarchical control ensure operational stability, optimality and reliability.

According to [96,97], to maintain the proper operation of a Microgrid, the control functions must include:

1. Regulate voltages, currents, angles and frequency inside the desired margins;
2. Maintain the balance between power supply and load demand;
3. Realize economic dispatch and demand side management;
4. Acceptable transition between different operational modes.

The stability properties of a Microgrid relies on primary control, which pertains faster control actions, oriented to frequency and voltage control, island transition and power sharing. When dealing with grid-forming synchronous machines, the power and frequency control is done by governors and machine inertia, the

[1]The hierarchical control structure was detailed in Figure 1.4 from Chapter 1

exciters are used to control voltage and reactive power. Alternatively, the control strategy is distinguished for grid-forming converters, which have much faster control response and are associated with Phase Locked Loop (PLL) to provide frequency measurement and grid synchronism. Therefore, grid-forming converters are more susceptible to perturbations and black-outs, which bring voltage and frequency deviations due the fast control action of these converters. This issue is the subject of research for the development of new control strategies, such that grid-forming converters are more resilient for operating Microgrids.

Considering the stability problem of Microgrids, the dynamics of this system is completely different from traditional power system. The Microgrid parameters have lower impedance with reduced short-circuit capacity, and therefore, the relation among voltage, angle and power differs from conventional power system, with faster dynamics, and higher uncertainty from the load demand and renewable sources. The variable feature of the local power demand and the intermittent nature of renewables is critical to balance power in these grids. Also, the bidirectional power flow caused by DER and prosumers is very common, resulting in protection problems. Power converter-interfaced systems pose challenges to stability, since the system is more sensitive to perturbations, and may lead to shut down an entire system. The imbalance between phases can also be cited as a common characteristic of Microgrids, since the distribution of loads is more difficult because they are heterogeneous.

Therefore, the most relevant feature of the Microgrids when compared to traditional power systems can be summarized below [98]:

- Reduced system size;
- High integration of renewables;
- Uncertainties and perturbations are more evident;
- Lower X/R relation of the lines;
- Reduced short-circuit capacity;
- Power converter-interfaced.

The loads have influence over power stability, therefore, load shedding operation is possible to be realized, improving the stable operation of the system. In the Microgrid case, the loads can participate actively to perform the stability of the system, where the operation follows a schedule, turning off during peak periods. It is also possible to develop load disconnection criteria, prioritizing more important loads. These control strategies concerning to load shedding and disconnection criteria are inserted within secondary control scheme.

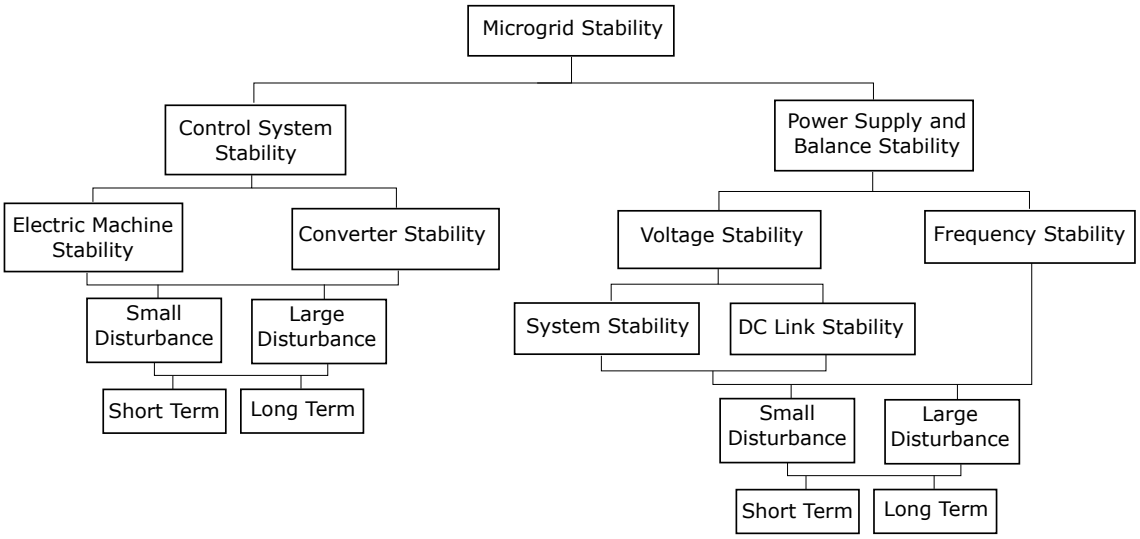

Figure 2.2: The classification of stability in Microgrids.

Considering the above features of Microgrids and its distinctions with the conventional power system, a classification of Microgrid stability is developed in [98]. The scheme of this classification is presented in Figure 2.2 as proposed in [98]. The classification is originally divided into Power Supply and Balance Stability, and Control System Stability. The first refers to the system's ability to maintain power balance and maintain the network within the desired operating requirements. This part deals with generation loss, power sharing between several generating units, and load tripping.

Subsequently, Power Supply and Balance Stability is divided into Voltage stability and Frequency Stability. Frequency Stability in the sense of Microgrids is a concern for isolated systems, which is greatly affected by low inertia and will be detailed in Chapter 6. Voltage Stability is subdivided to also consider DC buses of Microgrids.

In voltage stability, the control is done locally, because the magnitude of voltage varies at different points in the network, therefore, it is more difficult to carry out the sharing of reactive power more adequately. The line impedance is reduced, being more resistive, compromises the relationship between reactive power and voltage magnitude, where the active power also interfere in the voltage of the system. Thus, voltage regulation can become quite complex, a solution widely used for Microgrids is the application of virtual impedance to improve voltage control. The relationship between the voltage and reactive power consumption are determined by the sensitivity to the load voltage, which is not linear in general. Finally, the voltage on the capacitors on the DC side of power converters, maintained by DC/DC converters that interface generators and the grid, also need to be properly controlled.

Table 2.2: Main issues in Control System Stability of Microgrids.

Category	**Control System Stability**	
Subcategory	Electric Machine Stability	Converter Stability
Main reasons	Poor controller tuning	Poor controller tuning, PLL bandwidth, synchronization failure, harmonic instability
Effects	Undamped oscillations, aperiodic voltage and/or frequency deviations	Undamped oscillations, low steady-state voltages, high-frequency oscillations

Variations in the DC bus voltage of the converters can cause power fluctuations and unwanted ripples to the system [99].

Control System Stability is studied to guarantee the proper functioning of the control scheme, related to harmonics compensation, adjustment of the controllers, considering output filters (L or LCL filters) and PLL adjustments. This is subdivided in Electric Machine Stability and Converter Stability. The first one is similar to the traditional power system stability issues, concerning synchronization, damping oscillations and torque control [100]. The particularity in Microgrids is associated with poor adjustments of exciters and governors, which need specific tuning for island operation. The second one is the Converter stability, where the inner voltage and current control loops are the main concern. The tuning of the inner control loops are a challenge in real applications and can affect the behavior of the whole system, which may cause blackouts and have influence in protection schemes. Also, the PLL may introduce negative admittance, that directly affect system stability. In this case, low-bandwidth PLL can mitigate this problem according to [101]. Lastly, the output filter of the converters, when a Microgrid is composed mostly by converters units can cause resonance problems, therefore the control interactions makes this problem even more serious. Tuning the controllers to reduce this problem is often highly complex.

Considering the mentioned instability issues, the knowledge of these issues allows to identify the main causes and difficulties in the operation of Microgrids related to the system's stability. Table 2.2 summarizes the main stability issues related to Control System Stability and Table 2.3 summarizes the issues related to Power Supply and Balance Stability according to a study carried out in [98].

While the stability analysis of conventional power system are well established with standard models of synchronous generators, loads and known perturbations, in Microgrids, the stability study is made individually for each case, where a general

Table 2.3: Main issues in Power Supply and Balance Stability of Microgrids.

Category	**Power Supply and Balance Stability**	
Subcategory	Voltage Stability	Frequency Stability
Main reasons	Distributed generation limits, reactive power supply unbalance, poor reactive power sharing, load voltage sensitive, DC bus voltage (capacitor)	Distributed generation limits, active power supply unbalance, poor active power sharing
Effects	Low steady-state voltages, large power swings, DC bus voltage ripples	RoCoF increase, low steady-state frequency, large power and frequency swings

stability analysis is hard to be achieved. This is due to the great variability of components and the wide power range of Microgrids, in which different technologies and control schemes are applied. The dynamic behavior of Microgrids are mostly investigated via small-signal stability analysis, where too slow and too fast dynamics are neglected.

In these studies, linear state-space model is obtained, where eigenvalue analysis is performed. Therefore, linear controllers are applied to result in closed-loop control system. The small-signal model of each subsystem of the Microgrid is developed, and then the global model set up is inserted in different operating modes to indicate the damping of the oscillatory terms and the effect of the perturbations over the system stability margin [97]. The model of the Microgrid components are detailed in Chapter 3.

The simplified models, such as transfer functions, can be employed for steady state analysis and power/frequency control of Microgrids. A first order transfer function is achieved to present the behavior of the system. Basically, to attain stable operation, the power generation meets the power demand, minimizing the power imbalance (ΔP), which is given by:

$$\Delta P = \Delta P_L - \Delta P_g \tag{2.1}$$

where the ΔP_L is the deviation on power load demand and ΔP_g is the deviation on the generated power. Therefore, the frequency deviation of a simplified Microgrid model can be written as:

$$G_{grid}(s) = \frac{\Delta f}{\Delta P} = \frac{1}{K_{grid}(1 + sT_{grid})} \tag{2.2}$$

where K_{grid} is the Microgrid frequency constant and T_{grid} is the Microgrid time constant associated to the time delay between power and frequency deviations.

Thus, an association with the system inertia (M) and damping constant (D) from conventional power systems can be done. In this case, ΔP_g and ΔP_L are disturbance signals [102].

$$G_{grid}(s) = \frac{1}{D + sM} \tag{2.3}$$

The simplified dynamic model of the Microgrid components together with the obtained Microgrid model can be combined to compose a complete model of the system. The linearized state-space representation model is useful for linear control applications. But, the state-space representation may also include more dynamic details of the system, like converters' output filters (L, LC, or LCL filter). The dynamics of filters, transformers and other relevant disturbances can be included in the Microgrid model [103].

Also, the nonlinearities of the converter's model, such as the control input multiplied by a state variable, typical in DC/DC converters and VSC converters create a more detailed nonlinear state space model. This enables to develop a more specific control strategy, which results in a more rigorous stability analysis considering relevant details of the whole system, when compared with linear analysis, such as Nyquist diagram.

Indeed, due to the fact that they are well known among practitioners because of their simplicity, usually linear control techniques based on Proportional Integral (PI) strategies are used: with the drawbacks that they do not rely on the model and do not provide a rigorous stability analysis [27]. Unfortunately, linear control is limited to a linearized model, which is restricted to only one operating point. When dealing with strong perturbations, as the impact of regenerative energy in a Microgrid, linear techniques may not be enough to solve the question of general stability in a power system [42, 95, 104]. Thus, a nonlinear control approach is more suitable to this purpose, due to the nonlinear nature of the electrical models [91, 105, 106].

2.3. DC Microgrids

Direct Current (DC) Microgrids are attracting interest thanks to their ability to easily integrate modern loads, renewable sources and energy storage [44, 107]. They also acknowledge the fact that most renewable energy sources and storage systems use DC energy (as PV, batteries and even electric vehicles for example), and allow the reduction of the number of power converters in the grid with simpler topology. By doing this, they increase energy efficiency, and allow faster control of the grid [33, 38, 95, 108–110].

DC Microgrids are generally fully composed of DC/DC or AC/DC converters to adequate the voltage level of the system. Commonly, a DC bus operates as the main interconnection link, where power flow control is performed. The devices of the Microgrid are integrated in the DC link to share power, where distributed generators inject the produced power, the load demand is supplied and the storage elements can absorb the power mismatch. The main target here is to control the DC bus voltage to ensure proper operation of the system, since fluctuations, ripples and deviation in the voltage amplitude may cause a collapse, harming the overall operation of the system. Also, DC/DC converters are used to interconnect buses with different voltage levels, so the devices are inserted according to their voltage level. Therefore, sensitive loads can be properly supplied through a specific bus with multiple DC links configuration [27, 41, 42, 111].

On the other hand, the connection of a large number of power converters may lead to stability problems, since the converters can act as a Constant Power Load (CPL), which introduces negative impedance into the system. The effect of the negative impedance reduces significantly the stability margins and the operating region of the entire system. Therefore, standard control techniques, as droop controllers and linear PI controllers, are very limited to attain stability in this case, and different solutions must be achieved to improve the operation of this type of system. The nonlinear control can be introduced as a powerful tool to develop improved controllers, that are robust enough to keep safe operation in a wide operating region. Nonlinear control technique can easily suppress the negative impedance term and insert a stabilizing dynamic through feedback process, when the variables of the system are known [43, 51, 111].

The most relevant feature of DC Microgrids are described as follows [103, 112]:

1. The reduced number of converters between sources and loads improve efficiency and decrease losses.
2. A number of system variables are eliminated, such as frequency, reactive power, power factor and synchronization.
3. The system is more robust against voltage sags and blackouts, since they have fault ride trough capability from voltage control of the power converter and the energy stored in the DC bus capacitor.
4. DC distribution is not the standard shape and need to be built in parallel to the conventional AC distribution system.
5. The system protection is harmed, since zero cross detection is non-existent.

6. The power electronic loads and DC motors are easily integrated in DC systems, but there are a number of loads that must be adapted for DC power supply.
7. The absence of transformers reduces losses and inrush currents.
8. Voltage stability is directly affected by power flow control.

Many studies have been conducted regarding the control of DC Microgrids, a few papers are highlighted next. For example, a complete nonlinear model of a DC distribution system driven by PI cascaded droop-based controllers including a damping factor is developed in [113], where a valid nonlinear stability analysis is conducted using Lyapunov techniques. Also, small signal stability studies are introduced as in [114], where different DC loads and a supercapacitor compose the DC networks of aircrafts. Then, a large-signal-stabilizing study is proposed, to ensure global stability by generating proper stabilizing power references for the whole system. In [115], a simplified model of a small DC Microgrid under droop control is addressed to reduce the complexity of the nonlinear stability analysis, which is based on the bifurcation theory, and a relation among grid parameters is provided. Several strategies for stability analysis and stabilization techniques for DC Microgrids are presented in [95] and in [42].

In [37], a nonlinear distributed local control is proposed to interconnect a number of elements in a DC Microgrid. The Microgrid is composed of different time scale's storage elements, like batteries and supercapacitors that are used to improve the system operation. A stability analysis of the proposed control strategy is conducted considering the system as a whole and its physical limitations. The proposed scheme can easily be scalable to a much larger number of elements and a comparison with standard linear controllers is also carried out. In this way, the control performance of the system is presented towards interconnected disturbances from loads and PV variations. The robustness of the proposed control is highlighted when compared with linear control. Subsequently, a power management controller to ensure power balance and grid stability of the DC Microgrid is designed in [116]. The secondary control scheme, based on MPC, is developed to optimize the operation of the DC Microgrid in long term, considering weather forecasts and load demand profile. In this case, the power balance and the DC bus voltage regulation are considered as constraints.

Therefore, in [36], the connection with the main AC grid is carried out considering the stability of the Microgrid DC bus, still applying nonlinear control techniques. Afterwards, in [117], a more favorable power converter configuration is proposed to improve the electrical scheme of the DC Microgrid. The dynamical feedback

controller is designed to reduce the complexity of the stability analysis and simplify previous controller design keeping the stability properties. And finally, a nonlinear control scheme to integrate regenerative braking from a train line is proposed in [118]. In this case, the DC bus stability is also taken into account, where the power surges from braking periods are considered as disturbances. The proposed controller must be able to properly operate regarding various disturbances in the network.

Ancillary services provision using DC Microgrid is carried out in [119,120], where the available power on the DC side of the Microgrid is used to supply the AC side of the grid appropriately, ensuring voltage limits within grid requirements. Therefore, the power quality of the main grid is improved.

Results are also obtained in [121], where design and control of a DC Microgrid integrated in a railway station is introduced. In this case, a HESS is used to take the available energy from regenerative braking and reusing it to meet local energy demand. In [122], a signal decomposition block, used to filter low and high frequency, is applied in the nonlinear control scheme of hybrid storage system that perform the voltage control of a DC Microgrid. Here, the fast changing components required to regulate the DC bus of the grid is handled by the supercapacitor while the battery provides the slow varying components to perform power flow balance in long term. This approach is verified by experimentation tests.

Relating the different applications of power electronics in power systems, HVDC transmission, Multi-Terminal DC system (MTDC) and Modular Multilevel Converter (MMC) [123–126] results can be adapted for DC Microgrids application, because of the following reasons: they have similar power converter configuration, differentiated only by their size and power value; the electrical model and dynamics of the system are similar; the perturbations' properties can be easily compared to each other; the control schemes are compatible, besides the gain tuning.

2.3.1. Droop control strategies

Droop control strategy traditionally applied in AC Microgrids is also widely applied in DC Microgrids for power sharing purposes. This simple strategy is based on the linearized behavior of the system power flow around a operation point. The output power or output current can be used as the droop feedback. In the Power-based droop, the DC bus voltage reference is given by the power variation in the grid according to the droop coefficient [38,61,115,127].

$$V_{DC,ref} = V_{DC}^{*} - m_p P_{out} \tag{2.4}$$

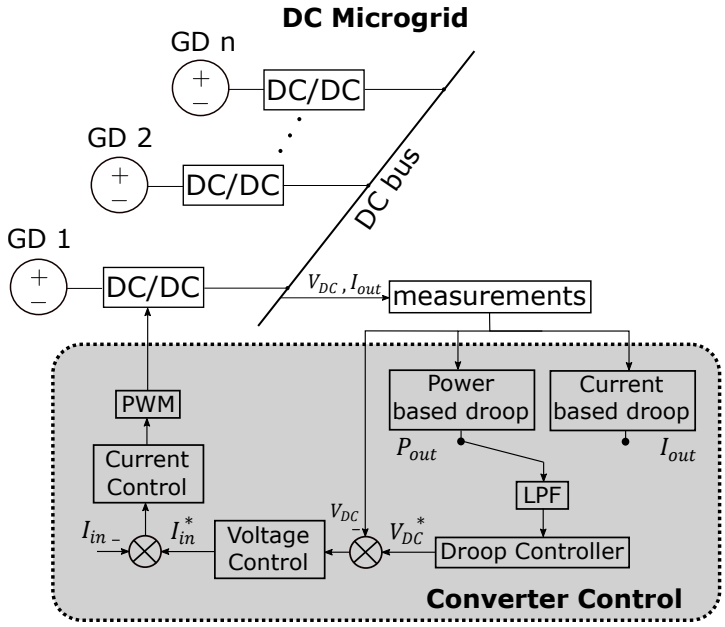

Figure 2.3: Conventional droop control scheme for multiple generations units in a DC Microgrid.

where $V_{dc,ref}$ is the voltage reference value for the given operation condition, V_{DC}^* is the rated DC voltage value. m_p is the droop coefficient and P_{out} is the power output.

In the Current-based droop, the DC bus voltage is the control output, given by the droop coefficient and the current in the converter.

$$V_{DC,ref} = V_{DC}^* - m_i I_{out} \tag{2.5}$$

here, $V_{dc,ref}$ is given by the droop relation according to the current output I_{out}. m_i is the droop coefficient, which can be interpreted as a virtual internal resistance. A general control scheme of the conventional droop control is introduced in Figure 2.3 according with [38].

The droop strategy is associated as an adaptive voltage positioning and the droop coefficients have a direct effect over system stability and power sharing accuracy. Higher droop coefficients may bring better sharing accuracy and damped response, but a commitment must be made not to cause major voltage deviations. Besides that, the droop coefficient can change the power sharing of the generation units. Detailed schemes of the conventional droop control will be developed in Chapter 5.

An extension of conventional droop control is to introduce adaptive feature for droop control, where the droop coefficients become time varying ($m_p(t)$ and $m_i(t)$), and can change according to a specific strategy. The adaptive calculation of droop control can consider the SoC of the energy storage elements or other strong perturbations related to power injection and load demand. With the dynamic

adjustment of the coefficients, the operation of the system and power sharing is improved. This approach also reduces the effects of the line impedance and also reduce line losses, but the control parameterization is too complex [61].

In this sense, it may be proposed a quadratic droop control that can bring benefits since the relationship between power and voltage is nonlinear ($P = V^2/R$). Therefore, the quadratic droop proposition has a physical motivation [128]. The quadratic droop can be written as follows [61]:

$$V_{DC,ref}^2 = V_{DC}^* V_{DC,ref} - m_p P_{out} \tag{2.6}$$

Another well known approach is the virtual resistance-based droop control [61, 129], where a fast control loop that emulates the line resistance of the grid can be inserted as follows:

$$V_{DC,ref} = V_{DC}^* - R_v I_{out} \tag{2.7}$$

where R_v is the virtual resistance considering the grid parameters and the operation margin of the control structure.

The virtual resistance can be chosen via summation approach, when a number of converters is connected to the DC bus. Therefore, the line resistance (R_l) is used to calculate the needed coefficients. Therefore, considering two generation units as an example, the virtual droop strategy for multiple generators is written as follows:

$$V_{droop} = (R_{v1} + R_{l1})I_{l1} = (R_{v2} + R_{l2})I_{l2} \tag{2.8}$$

In this approach, the first virtual resistance is set to zero and the second is set to emulate the desired equivalent impedance. So, if $R_{l1} > R_{l2}$, the virtual resistances can be allocated as: $R_{v1} = 0$ and $R_{v2} = R_{l1} - R_{l2}$ [61].

In [112], a comparison of the relevant control techniques in DC Microgrid is introduced, and is presented here in Table 2.4. The table highlights the mains advantages and disadvantages of the mentioned control techniques.

2.4. AC Microgrids

AC Microgrids are widely employed since conventional distribution feeders, loads, equipment and protections schemes are standardized on AC power, therefore, energy conversion is not required. AC Microgrids incorporates a number of variables, such as frequency, reactive power and angle synchronism, which makes AC grid more complex than DC grids with more control loops. On the other hand, the

Table 2.4: Control techniques feature in DC Microgrids.

Control Scheme	Advantages	Disadvantages
Conventional droop	Easy implementation	Poor voltage regulation; Poor power sharing accuracy
Virtual resistance droop	Unaffected by line resistance	Poor voltage regulation
Adaptive droop	Minimizes circulating current, Improve power sharing	The grid parameters (resistances) must be known
Intelligent techniques (fuzzy logic)	The better adjustment of virtual resistance reduces voltage deviation, proper load sharing	Time consuming process, higher computational effort
Digital average current sharing	Accurate voltage regulation and load sharing	Signal transmission delays
Distributed cooperative control	Robust, extensive and flexible	Signal transmission delays, Security issues in communication

standard control techniques in power systems can be adapted for AC Microgrids, as well as the relation between active power with frequency and reactive power with voltage, regarding the grid size. The main AC bus of the Microgrid is typically the PCC, where the distributed generators, ESS, loads and the main grid connection is done [29, 39, 93, 94].

Synchronous generators, such as diesel, hydro power and thermal power can be directly connected to the AC bus with no need of power converter interface, and the voltage level adjustment is easily done trough transformers. But the natural DC devices, such as PV panels, batteries, fuel cells and electronic loads require a DC/AC converter to be integrated in the AC Microgrid bus, where a decoupling between the AC and DC side can be advantageous. DC/AC converters can also bring harmonic distortion and ripples to AC grid, where the use of passive filters is required to mitigate these problems [62, 77, 80, 130].

Grid-connected operation mode for AC Microgrid requires simple control strategy to inject active and reactive power to the main grid and a PLL structure is used to guarantee synchronism with the main network. In this case, the frequency and voltage output of the Microgrid converters are governed by the main network, which can be represented most of the time as an infinite bus. However, in the absence of the network, the Microgrid operates in island mode. The operation of power converters in grid forming mode perform the control of frequency and voltage of the system, which is challenging for traditional control structures. As mentioned before, the outer voltage control loop cascaded with inner control current loop in power converters have complex tuning and suffer interference from the external parameters of the network, output converter filters and PLL. Therefore,

Table 2.5: Different application of power converters for AC Microgrids.

Grid-forming	Grid-feeding	Grid-supporting
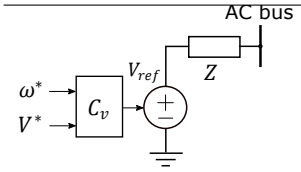	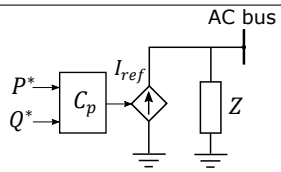	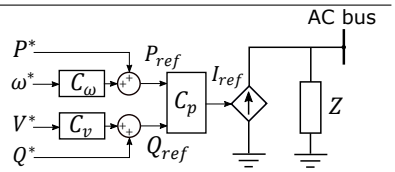
Control inputs are voltage V^* and frequency ω^* to assure grid stability	References of P^* and Q^* power are given, PLL is needed for synchronization	Participation in the regulation of frequency ω^* and voltage V^*, by P^* and Q^* control

robust control techniques are required to maintain suitable operation, regarding the complexity of Microgrid operation [38, 60, 62, 62, 77, 131].

The classification of VSC converters is proposed in [132], based on their different application, such as grid-forming, grid-feeding and grid-supporting. The grid-forming converters are modelled as an ideal AC voltage source with low output impedance, where the amplitude voltage and frequency are controlled to maintain the stable operation of the system. In this case, grid-forming converters need a accurate synchronization to realize power sharing among other generators connected in parallel. Grid-feeding converters are modelled as a current source, typically connected to the grid with high impedance, they are designed to deliver power to the grid, where active and reactive power are controlled for this purpose. In this case, the synchronization with the grid is needed, where stand alone operation is not possible. Last, the grid-supporting converters are modelled as controlled current sources in parallel with a shunt impedance. They are also modelled as voltage source. In this case, the currents and voltages of the converters are controlled to improve frequency and voltage levels of the connected grid. Extra ancillary services for grid-supporting may be implemented locally, such as inertia emulation, damping power oscillation and unbalanced compensation. A general scheme of the three applications of power converters for AC Microgrids is presented in Table 2.5 according to [132].

Synchronization is needed for grid-connected applications and in isolated operation with multiple power converter units for power sharing. A precise synchronization algorithm to estimate the grid parameters is required, such that perform a suitable operation supporting connections/disconnection with the main grid. The system must ensure proper behavior under distorted and unbalanced voltage conditions. The PLL may apply the value of the rated frequency, which is included as a feedforward to improve the phase estimation, given by the integral of frequency. A smooth transition between grid-connected and island operation mode

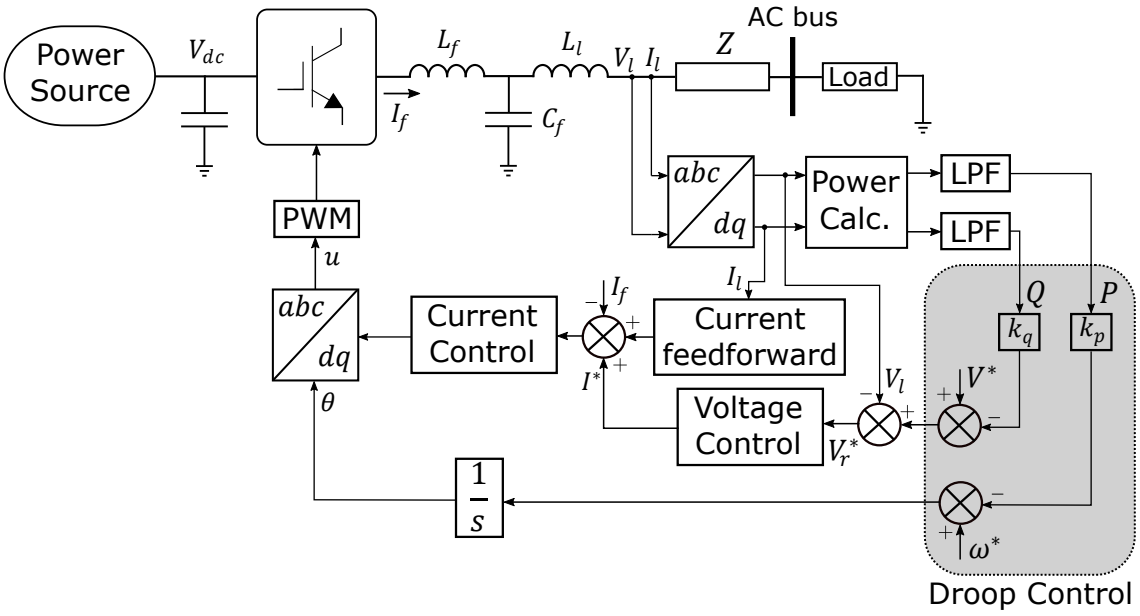

Figure 2.4: Local control loop in a Microgrid using VSC converter.

must be considered to establish stable voltage in the Microgrid. In island mode, the PLL can work as an oscillator with fixed frequency, and can be used for frequency measurement purposes. In the re-connection with the main grid, the PLL slowly varies the phase angle to achieve the grid synchronization [132, 133].

A typical local controller for an AC Microgrid operated by a VSC is introduced in Figure 2.4 adapted from [103], where a distributed generator operates as voltage-controlled system. The voltage references are given by a conventional droop controller where k_p and k_q are the droop coefficients, and nested frequency and voltage control loops are presented. A transfer function is used to feed the current term through a feedforward compensation to improve closed-loop performance. A Low Pass Filter (LPF) is used to provide active and reactive power measurements. PI controllers are implemented in the inner loop current and voltage control to assure proper operation and eliminate the steady state error, where they work in a given operation point. The reference frames are transformed from natural *abc* frame to synchronous reference frame *dq*, which is associated with DC variables, allowing implementation of linear controllers, such as PI controllers, to operate using constant references of currents and voltages [103].

Secondary control has the task of providing references for the inner control loops of the primary control. They improve the parallel operation of the generation units and remove steady-state errors from lower control layers. In this way, the frequency and voltage references are calculated by the secondary control, such that, the power sharing and the load supply are accurate [134]. A secondary control loop can be

implemented via linear techniques, such that, the frequency deviation is eliminated. Therefore, a proportional plus integral term (α_ω) is introduced to improve the convergence speed of frequency and eliminate the steady state error. The control can be developed as follows:

$$\alpha_\omega = K_p^\omega(\omega^* - \omega_g) + K_i^\omega \int (\omega^* - \omega_g)dt \tag{2.9}$$

where ω_g is the grid frequency and ω^* is the reference of frequency. K_p^ω and K_i^ω are the proportional and integral gains of a PI controller and can be allocated according to grid requirements. Therefore, frequency RoCoF and frequency deviation are limited [81, 135].

The secondary control term introduced in (2.9), is inserted in the frequency droop equation as follows, assuring the elimination of deviations in steady state and improving frequency RoCoF:

$$\omega_r = \omega^* - m_p(P_m - P^*) + \alpha_\omega \tag{2.10}$$

where ω_r is the frequency reference from droop scheme, m_p is the droop coefficient, P_m is the measured active power and P^* is the active power reference.

The same consideration of the secondary control can be adopted for voltage regulation, where an integral term given by α_v can be inserted in the voltage droop. Therefore, the voltage droop control considering α_v from secondary control layer can be written as:

$$V_r = V^* - m_q(Q_m - Q^*) + \alpha_v \tag{2.11}$$

where V_r is the voltage reference resulted from droop scheme, V^* is the rated voltage reference. Q_m is the measured reactive power, Q^* is the reactive power reference and α_v is given by:

$$\alpha_v = K_p^v(V^* - V_r) + K_i^\omega \int (V^* - V_r)dt \tag{2.12}$$

The gains K_p^v and K_i^v are calculated according to the desired convergence speed of the secondary control layer [135].

The droop control strategy essentially depends on the impedance of the Microgrid and the X/R ratio. In many cases, the impedance of the system varies according to the connection/disconnection of loads and generators, or when the operation mode is changed from grid-connected to island mode, which harm grid impedance estimation. Therefore, the virtual impedance approach can be applied, introducing a large inductor between the power converter and the AC bus to assure

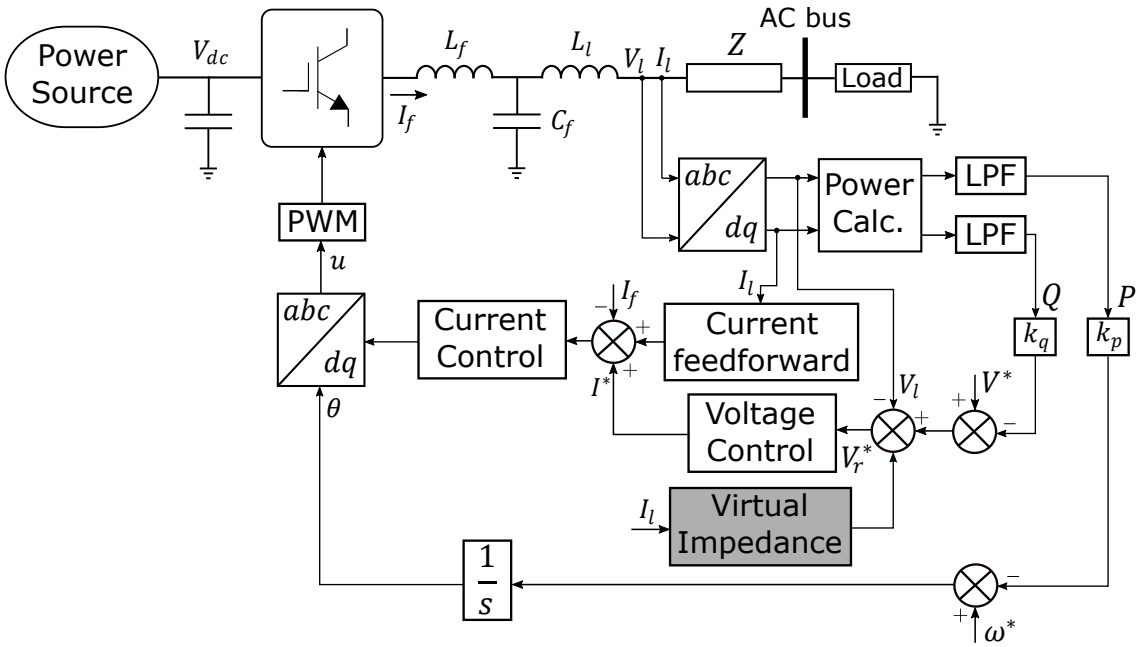

Figure 2.5: Power converter control of a Microgrid applying virtual output impedance loop.

the X/R relation ($X >> R$) of conventional power systems, and then the active power-frequency ($P-f$) and reactive power-voltage ($Q-V$) relation is maintained. The virtual impedance improve power sharing, and limit over current during grid disturbances [103,129]. The virtual impedance is inserted in the reference of voltage of the grid (V_r^*) as a voltage drop. The voltage reference of the virtual impedance approach can be expressed as follows:

$$V_r^* = V_{ref} - Z_v I_g \tag{2.13}$$

where V_{ref} is the voltage reference from the droop control equation, Z_v is the virtual impedance selected according to the nominal power of the converter and I_g is the current output in the grid, which generates a voltage drop in the voltage reference V_r^* [103]. The Microgrid with virtual output impedance loop is introduced in Figure 2.5 adapted from [103], where V_r^* is provided as the reference to the inner voltage control loop.

In [136], a cooperative control for frequency and voltage regulation is proposed for an autonomous Microgrid composed of multiple distributed generators, considering delays and noises in fading channels. Then, based on the droop control equations in (2.10) and (2.11) and removing the integral terms, a dynamical model of the system can be obtained by feedback linearization. Therefore, the frequency and voltage dynamics in this case, can be written as follows.

$$\dot{\omega}_r = \dot{\omega}^* - m_p \dot{P}_m = u_\omega \tag{2.14}$$

$$\dot{V}_r = \dot{V}^* - m_q \dot{Q}_m = u_v \tag{2.15}$$

where u_ω and u_v are auxiliary control inputs. Therefore, (2.14) and (2.15) represent the system dynamics to calculate the control inputs ω^* and V^*. The voltage and frequency restoration of the Microgrid including N distributed generators is introduced by a tracking synchronization problem:

$$\dot{\omega}_{r,i} = u_{\omega i}, i = 1, 2, ..., N \tag{2.16}$$

$$\dot{V}_{r,i} = u_{vi}, i = 1, 2, ..., N \tag{2.17}$$

Therefore, the voltage and frequency can be robustly restored to their reference values with accurate power sharing achieved.

A survey in control techniques of AC Microgrids is carried out in [112] and in [97]. A number of different control approaches are reviewed, such as, PI control, droop control, adaptive droop, angle droop, virtual impedance, adaptive control, optimal control, heuristic algorithms, virtual inertia, MPC, etc. The advantages and drawbacks each control scheme is highlighted and the main applications' scenario proposed. Classical PI control is the most exploited technique, while detailed research on modern control techniques implementation is open [97]. Most of the approached methods are based on small-signal dynamic model or linearized models, where relevant nonlinear dynamics are neglected. Only a few control approaches include the faster dynamics of the converters and other nonlinearities of these systems. Some examples of nonlinear controllers are presented next.

In [137], a nonlinear control scheme for parallel multiple generators in island operation mode is proposed. Due to poor power sharing performance of conventional droop schemes, the design of a nonlinear output feedback linearized droop control is developed, where simulation results highlight the performance of control under load changes. In [138], a robust nonlinear controller is designed in order to maintain active and reactive power balance in islanded Microgrids, where only local and neighbor measurements are required. The proposed controller is developed by partial feedback linearization and robust properties are achieved including uncertainties in the distributed generators and ESS. Simulation results indicates a superior control performance when compared with LQR approach.

The paper in [139] presents a large-signal based control designed for power converters to suitable operate in grid-connected and island mode operation without need to reconfigure the system in transitions periods and without islanding detection. The control structure is made by emulating inertia and damping functions and then an adaptive backstepping technique is applied to guarantee large angle stability and robustness against unmodeled dynamics. The flexible control scheme ensure high performance of the Microgrid during harsh transients, such as islanding

transition. Simulation results show the effectiveness of the proposed nonlinear controller.

A cooperative control for AC Microgrids composed of power converters is addressed in [140], where a distributed feedforward approach based on multi-agents systems is applied in a distributed way. It is only requested local state measurement and reference signal from neighbors. Therefore, the nonlinear and heterogeneous dynamics of power converters are handled by input-output feedback linearization, assuring proper control response. The control gains tuning does not rely on the whole Microgrid dynamics. In [141], a nonlinear stability analysis of AC Microgrids with Constant Power Loads (CPL) is carried out. The complete system considers the AC Microgrid dynamics together with the CPL dynamics, then a set of nonlinear state space equations is resulted. The Lyapunov and Popov's theorems are utilized to analyze the stability conditions of the AC Microgrid. When the power injection/absorption in the CPL satisfies the proposal criteria, the AC Microgrid is absolutely stable.

2.5. Conclusions

In this chapter a literature review in Microgrids structure and control was developed. It has addressed the main technologies of distributed level's generators, renewables and ESS related to Microgrids. Standard control techniques were cited comparing the advantages and the limitations in their application to Microgrid operation and stability. Operation and control of Microgrids is a topic of great interest in academic research and industry due to the development of technologies for Smart-Grids. The design of control strategies is a big challenge considering stability margins, network requirements and power electronics.

CHAPTER 3

The Microgrid Components

3.1. Introduction

In this chapter, the proposed Microgrid components are defined and detailed, where the mathematical model of the devices are introduced. The Microgrid is composed by a number of elements: two different types of renewable energy sources (regenerative braking energy recovery from the trains and photovoltaic panels), two kinds of storages acting at different time-scale (a battery and a supercapacitor), a DC load representing an aggregation of all loads in the Microgrid, and the connection with the main AC grid.

The thesis proposes the development of local distributed control structure for a hybrid AC/DC composed of a several components. A Microgrid for a Smart Railway Station equipped with renewables, as Photovoltaic Panels (PV) and regenerative system, storage devices and loads is proposed, which is able to connect or disconnect to the AC main grid, and the low-level control laws needed to let the Microgrid correctly operate are introduced, together with a complete stability analysis. In the considered framework, a device dedicated to train braking energy recovery is added together with the conventional PV source: the targets are to merge regenerate energy from the trains (that can be very significant) to the one produced by photovoltaic and to keep a desired voltage level for the DC bus. The combination of the two renewable sources stresses the system with respect to any kind of perturbation can take place. As appropriate hypothesis of power availability for the DC Microgrid are taken into account, the AC network does not contribute to the DC Microgrid stability: it is seen as a controllable load to be fed selecting the needed amount of active and reactive power.

Stability of the Microgrid is ensured by different time scale storage devices utilization (batteries and supercapacitors), in order to obtain a flexible and reliable

system in response to the intermittent nature of the renewables: the batteries have the duty to provide energy when it is missing from the renewable sources, while the supercapacitors act to compensate the power transient variations in power production or consumption [36,37,142]. In the following, the Microgrid components are introduced, and then the complete configuration of the system is assembled.

3.2. Microgrid Components

3.2.1. Photovoltaic panels

A photovoltaic panel (PV) converts solar energy into electricity trough the photoelectric effect. The energy is produced when a solar radiation hits a photovoltaic cell, and then produces an electric current. A group of cell compose a photovoltaic module and the set of solar modules produces the PV array. Photovoltaic systems have been one of the most applied kind of renewable energy worldwide, because of their ease of installation and adaptation to facades and buildings. Also because of their wide range of power, from few Watts installed in homes and industries to Mega Watts, installed in solar power plants [143].

The growth in the number of PV modules installed is mainly due to the drastic reduction in the cost of PV modules over the years, costs fell about 20% with every doubling of cumulative capacity since the 1970s. The improvements in the efficiency of the panels contributed with 23% of the price reduction. The development of private research and economies of scale also plays an important role in this cost reduction [144]. For example, in [145] the price of polysilicon in U.S. dollars per Watt was 1.55$\$/W$ in 2010, and a benchmark estimated cost for 2020 is 0.28$\$/W$, which represents a great price reduction compared with other renewable technologies. But, the efficiency of energy conversion depends on the different technologies (crystalline Silicon, amorphous silicon, organic cell, Thin-Film), being still a limitation for PV technologies. So, there are still many studies being carried out to improve these technologies [143,146].

In Microgrids applications, there are many examples in stand alone application, especially in rural areas with hard access to the main grid and grid-connected applications in distribution systems of urban centers. In DC applications, the PV terminals can be directly connected to their loads, without any type of electronic converter. Thus, this application has a very limited operation, and cannot adequately meet the load demand. But when a DC/DC converter is used, it is possible to improve the load supply by controlling its voltage and current. For AC applications,

an AC/DC converter is necessary, usually a Voltage Source Converter (VSC), where a large number of control possibilities can be chosen. In the case where power electronics are used, a Maximum Power Point Tracking (MPPT) algorithm can be inserted to provide a more flexible coupling between systems and to optimize energy production in the PV system.

The electrical circuit of a photovoltaic panel is modeled as a DC current source (I_{pv}) generated by solar irradiance, representing the diode characteristic. The losses by the reverse leakage current of the diode is represented by a parallel resistance (R_p) and the voltage drop is represented by a series resistance (R_s) [147]. The equivalent PV circuit is depicted in Figure 3.1 [148].

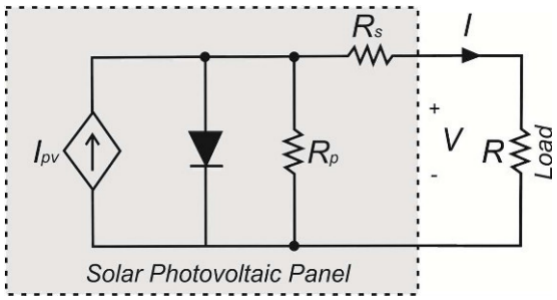

Figure 3.1: Simplified model of photovoltaic panel.

The output current of a PV array can be written as follows:

$$I = I_{pv} - I_D - I_{R_p} \tag{3.1}$$

where I_D is the current of the diode and I_{R_p} is the current of the parallel resistance. The currents I_{pv}, I_D and I_{R_p} are detailed next:

$$I_{pv} = (I_{pv,nom} + K_G \Delta T)\frac{G}{G_{nom}} \tag{3.2}$$

$$I_D = I_0 \left[exp\left(\frac{qV}{akT} \right) \right] \tag{3.3}$$

$$I_{R_p} = \frac{1}{R_p}(V + R_s I) \tag{3.4}$$

$I_{pv,nom}$ is the nominal photoelectric current in the nominal irradiance G_{nom}, K_G is the constant that relates irradiance G with temperature T, with ΔT being the variation of temperature in the PV. I_0 is the reverse diode saturation current, q is the elementary electron charge, a is the diode ideality constant, k is the Boltzmann constant, and V is the output voltage on the PV.

From the electrical model, the characteristic curve of the PV can be generated, where the graphic of current versus voltage and power versus voltage is plotted in

Figure 3.2 [148]. The characteristic curve shows the Maximum Power Point (MPP) of the PV for each irradiance level, where different curves are generated according to the irradiance level. The curves are distinguished in short-circuit current (I_{sc}), which is the current value when terminal voltage in the panel is zero, and in open circuit voltage (V_{oc}) given by the voltage value when the current in the panel is zero.

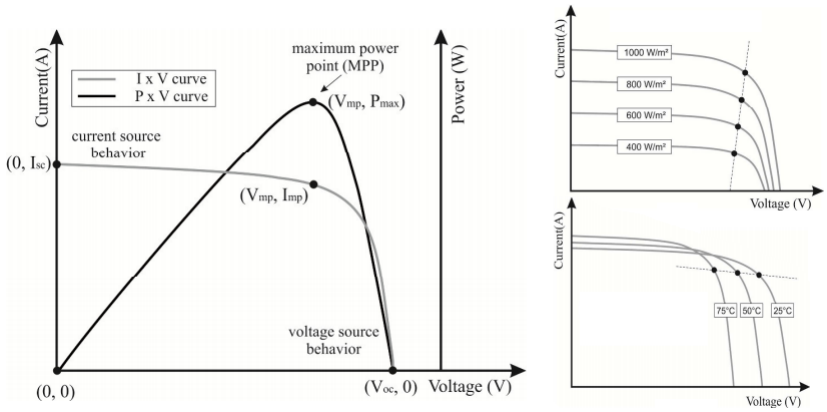

Figure 3.2: Characteristic curve of PV, and curves for different irradiance and temperature values.

3.2.1.1. Maximum power point tracking

The MPP of a PV is the optimal operating point to extract the highest available power from sun. MPP varies according to solar irradiation and temperature. So, to maintain the PV system in the MPP, a dedicate algorithm is necessary to handle with the variations temperature and solar irradiation during the day. The variations on the power generated in the panel is also related with partial shading which affects the operational point of the system. The MPPT provides a current or voltage reference that is sent to the controller, where a power converter is able to maintain the PV in proper operation [149]. Figure 3.3 introduces the MPPT scheme applied to the converter of the PV system. In this case, the voltage and the current in the PV terminal are measured and the calculated reference is sent to the controller.

The Perturbation and Observation (P&O) method is the most simple and well known algorithm. P&O has reasonable performance for tracking, and accompanied by its simplicity allows a low cost application. The method consists of producing disturbances in the current and voltage of the panel, and observing the power. If the power increases, the disturbance continues in the same direction as the previous disturbance, if the power decreases, the disturbance occurs in the opposite direction to the previous direction [150, 151].

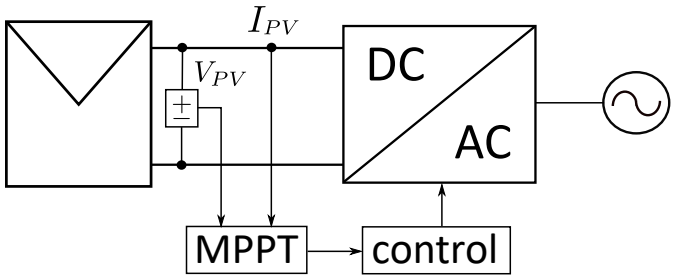

Figure 3.3: Control scheme of the MPPT algorithm.

Many other methods are derived from P&O algorithm. For example, the incremental conductance algorithm, which has good tracking performance with simple implementation and fast responses over irradiation changes. The incremental conductance algorithm is based on the power curve of the panel, in which the power derivative is calculated. When the power derivative is zero, the PV is at the MPP and when the derivative is different of zero, a voltage step is given to find a new operating point. Incremental conductance algorithm can reduce steady state errors and is more robust to perturbation than other methods [147]. Figure 3.4 depicts the scheme of the incremental conductance algorithm.

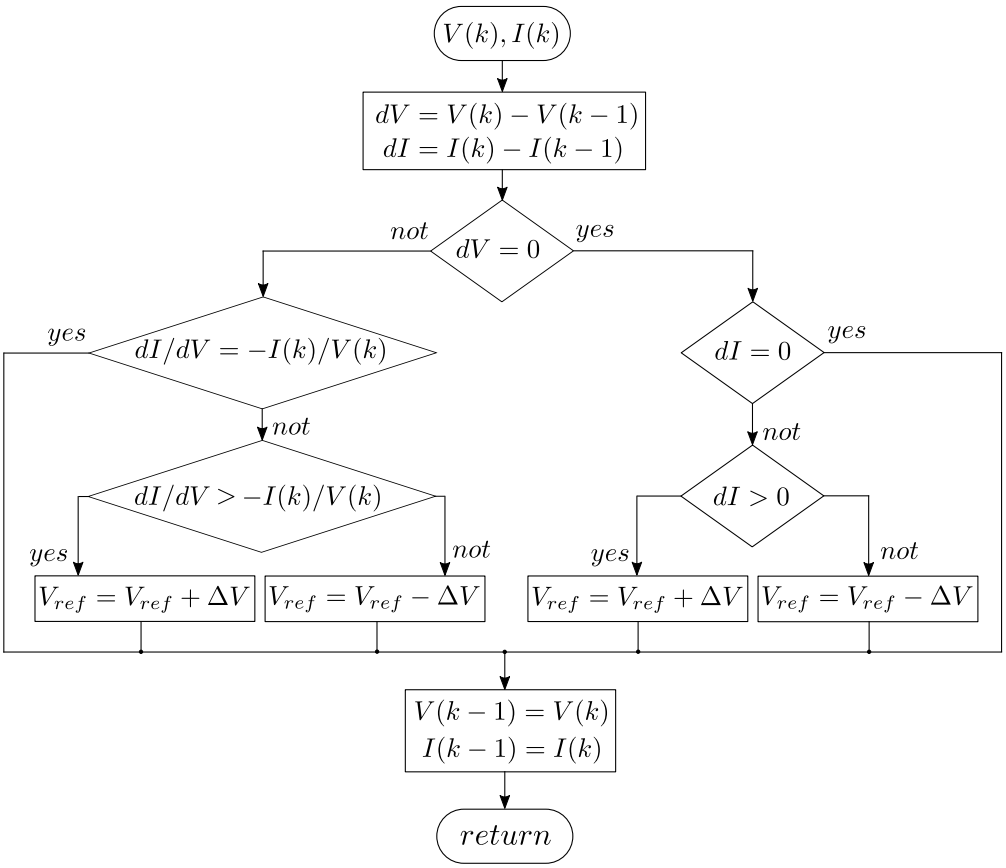

Figure 3.4: Incremental conductance scheme.

According to the flow chart described in Figure 3.4, the voltage step (ΔV) can be changed to control the tracking speed of the algorithm. Therefore, when the system is far from the MPP, ΔV value is increased, and to improve the tracking accuracy, the voltage increment is decreased with the operational point around MPP.

3.2.1.2. Photovoltaic structure

The PV panels are arranged to be composed in array structures, by the association of series and parallel modules. These groups are called photovoltaic string and they are accompanied by crossover diodes to improve their performance in chain arrangements and blocking diode to prevent the circulation of reverse current in the system. The strings are organized in series and parallel form according to the desired level of terminal voltage and current of the system. Therefore, the PV system can be arranged to be directly connected to the power converter and the converter topology can be determined [152]. A PV arrangement scheme is depicted in Figure 3.5 to exemplify the series and parallel modules connection.

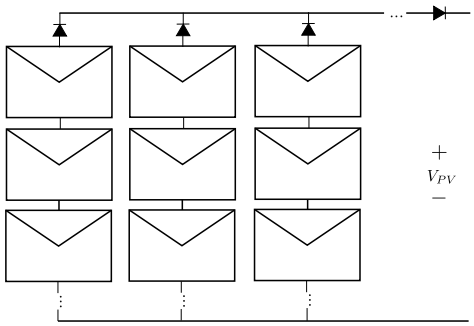

Figure 3.5: Parallel and series arrangement of PV arrays.

To increase the terminal voltage (V_{pv}) of the PV system, the number of series connection in the string is also increased, and the current level is determined by the number of parallel string connections, where each column of series panel is called as one string.

The power converters are the main devices to connect PV systems into an electrical grid and there are a number of possibilities to connect PV through different converters. Basically, the converters can be single-phase, or three-phase according to the power level or desired application. Also, the converters can be structured according to the number of conversion stages and series or parallel configuration [152]. Table 3.1 summarises the most common PV application in grid-connected systems.

Table 3.1: Different topologies of grid-connected photovoltaic systems.

Topology	Figure	Characteristics
One stage converter	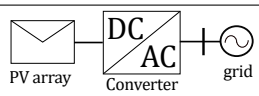	-simple installation; -reduced number of components; -poor isolation between panels and grid. -simple modulation process.
Two stage converter	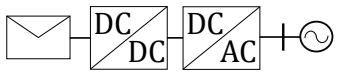	-decoupling between panels and grid; -wide voltage operation range on PV; -better isolation properties. -simple modulation process.
Multi converter individual AC/DC	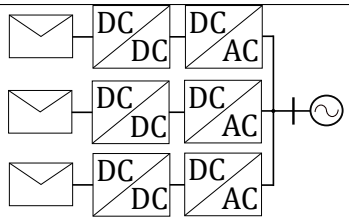	-better reliability in case of failure; -higher efficiency of conversion; -partial shading impact reduced; -better individual operation of the array; -simple modulation process.
Multi converter shared AC/DC	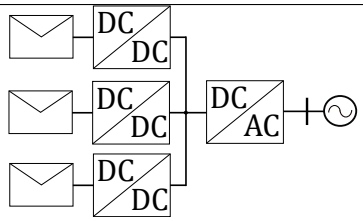	-reduced number of converters; -complex modulation process; -economic advantage compared with individual AC/DC converter; -multi-terminal DC link.

The PV is the main generation in the proposed Microgrid of this thesis, and it is obviously scaled according to the Microgrid's load. The incremental conductance algorithm is applied to track the reference for the PV array in the maximum power point. The MPPT algorithm is chosen to be used as the reference to PV's control strategy optimizing the power generation in the Microgrid. Then, the voltage step is calculated according to the desired convergence speed of the MPPT. The PV array model is composed of 15 modules in series (string), which results in total open circuit voltage of $V_{oc} = 331.5\ V$ and 100 strings in parallel, with total short circuit current of $I_{sc} = 289\ A$. The system is composed of Kyocera SM48-KSM model, which generates 72 kW in nominal conditions (1000 W/m^2 irradiation and 25°C temperature).

The characteristic curve of the PV subsystem (complete array) is presented in Figure 3.6, where the influence of irradiation and temperature variation is shown. The open circuit (V_{oc}) voltage is directly affected by the temperature changes, while the short circuit current (I_{sc}) is affected by irradiation profile.

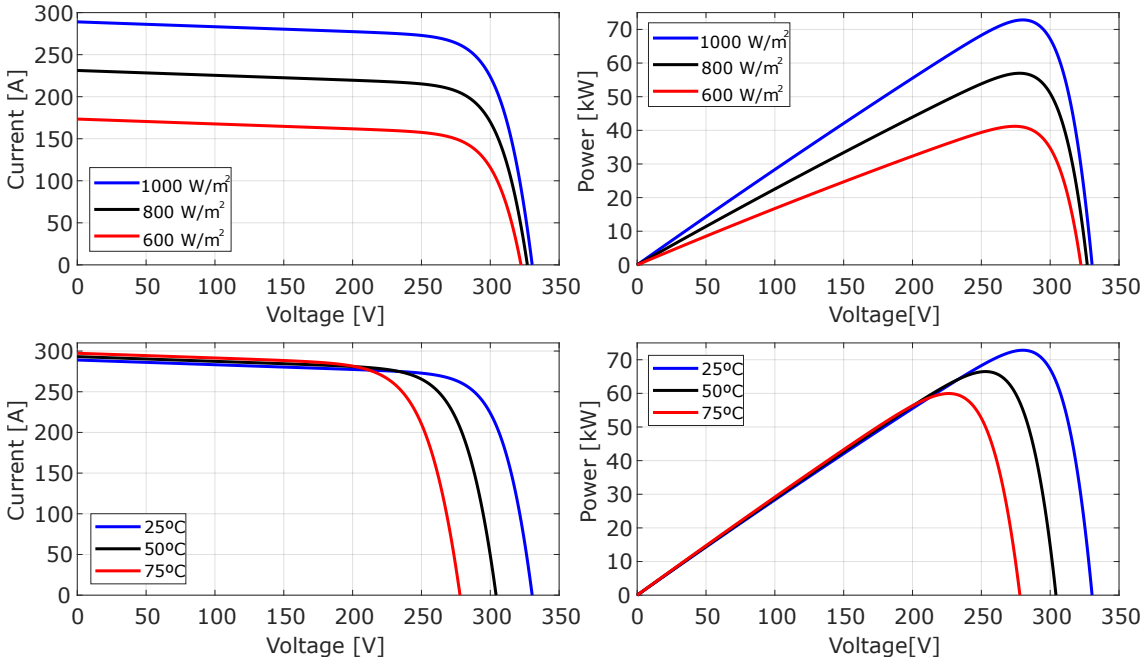

Figure 3.6: Characteristic curve of the entire PV system considering different irradiation and temperature levels.

3.2.2. Energy storage systems

Energy Storage Systems (ESS) in the Microgrid context are elements that enable strategic management of the generated energy, in order to optimize the power flow. ESS provides mitigation of the impact of renewable energy sources' intermittency, and increase the reliability of the system in the event of a power supply failure. Smart Grid application of ESS can be seen as a management tool on the demand side, power flow control, load displacement, etc. The main advantages of ESS is to improve stability, power quality and reliability of supply in power systems through different operation modes [9]. They have the ability to quickly vary power, because of the power converter characteristics without impacting the system power flow, when compared with typical synchronous generators.

In the design of ESS, important aspects must be taken into account, such as the life cycle of the equipment, storage capacity, physical space, technology cost, loading and unloading power, energy conversion technology, among others. Typically, they are classified according to the way they store energy. In [20], the ESS technologies are categorized in Table 3.2 according to the form of energy storage.

Solid-state storages includes electrochemical solutions, advanced chemical cells and supercapacitors. Flow batteries store energy directly in the electrolytic solution for a longer life and fast response. Flywheels are mechanical devices that store energy in a rotational mechanism with the ability to deliver high values of

Table 3.2: Energy storage systems classification according to the form of store energy.

<table>
<tr><th>Mechanical</th><th>Electrochemical</th><th>Chemical</th><th>Thermal</th></tr>
<tr><td>Pumped Hydro Storage (PHS)</td><td>Solid-state batteries</td><td>Hydrogen Storage</td><td rowspan="2">Sensible Heat Storage</td></tr>
<tr><td rowspan="2">Compressed Air Storage (CAES)</td><td>Superconducting Magnetic Energy Storage (SMES)</td><td rowspan="2">Fuel Cells</td></tr>
<tr><td>Flow batteries</td><td rowspan="2">Latent Heat Storage</td></tr>
<tr><td>Flywheel</td><td>SuperCapacitors</td><td>Biofuels</td></tr>
</table>

instantaneous power. Compressed air storage uses underground spaces with hermetic characteristics to compress air for bulk energy reserve. Thermal storage captures heat to meet energy needs of the load demand. And Pumped Hydro Storage (PHS) are large energy reservoirs through water deposits according to gravitational potential. The focus here are the solid-state storage that includes chemical batteries, especially, Lithium-ion batteries and supercapacitors [153].

To exemplify the wide application of ESS in power systems, the description of the main ESS application is done, according to [8]. Thus, the application of ESS can bring improvements for power quality, minimizing voltage and frequency variations, providing support to the network and improving system reliability and resilience. ESS applications are described next:

1. Ancillary services:
    - Voltage and frequency regulation: minimizes the fluctuation impacts from generation, which can be caused by the imbalance between demand and generation or insertion of renewables, through active and reactive power injection. Brings improvements in network stability.
    - Spinning reserve: ability to respond to compensate a generation or transmission contingency and maintain the system for as long as it is determined.
    - Support voltage: maintains the voltage within the network operating limit requirements, mostly related to reactive power management for power balance.
    - Black start: ability to restore the network in cases of contingencies, where storage provides the power needed to restore the system.
2. Bulk storage:
    - Arbitrage: during low cost energy period, the storage system absorbs energy from the grid for later sale or use during expensive energy cost.

It can also be used to store energy with surplus of renewable energy sources.

- Supply capacity: characterized by annual operating hours, frequency of operation and duration of operation for each use. For example, if price is per hour, storage brings flexibility in supplementary hours. Supply capacity can be used to peak shaving.

3. Infrastructure service (transmission and distribution):
   - Update deferral: delay for improvements expenses, an example is the installation of storage systems close to the consumers relieving the transmission, and providing capacity of supply without the need to invest in transmission equipment.
   - Line decongestion: with the natural growth of peak demand, the line may lose the ability to deliver all the power demanded by the load, so the storage systems are allocated to supply those peaks.
4. Energy management:
   - Power quality: short-duration voltage variations, primary frequency regulation, power factor control, harmonic reduction, and uninterrupted service (UPS, for example).
   - Reliability: greater guarantee of the energy supply, even in the face of disturbances and contingencies of the network.

Within the applications mentioned above, the supercapacitors and batteries have great potential for ancillary services, voltage and frequency regulation, and mainly in applications for improving power quality, which require a fast response or great amount of energy from the storage system.

3.2.2.1. Batteries

Batteries store energy electrochemically and are the most cost-effective technology available, been widely applied in power systems, especially combined with renewables and in Microgrids [154]. They have modular feature, that allows its application in a wide range of power from few Watts to Megawatts, by combining series and parallel modules to reach the desired electrical characteristic. Key factors for batteries application are mentioned:

1. High energy density
2. High energy capability
3. Round trip efficiency
4. Cycling capability

5. Viable initial cost

The impact of deep cycle in batteries is a current concern, since the operation mode can drastically affects the life cycle of a battery system. Researches to model the aging factor in batteries are also emphasized because they bring many impacts to the system operation in long term. Different batteries technologies have been developed to improve their operation in deep charge/discharge operation modes and reduces the aging factors, but the main results are given by the strategies on the operation mode and optimization techniques [154–156].

Lead–acid batteries are the most mature with lower cost options for most large applications requirements, considering all the battery technologies available. They are considered a save technology, with relatively low maintenance (usually periodic water maintenance), have high conversion efficiency (around 80% to 90%) and self discharge rate is also low. However, the poor performance at low and high temperatures combined with short lifetime due to frequent deep charge/discharge operation and relatively low power density handicap the use of this technology for particular applications like isolated Microgrids [153, 157].

Lithium-ion batteries on the other hand, have grown as prominent technology with longer life cycle, since the deep charge operation and aging factors doesn't have much impact in this technology. Lithium-ion batteries also have a higher energy and power density, with higher conversion efficiency (around 95%) compared with other technologies. Other features are the lower self discharge and maintenance, and absence of memory effect. For these reasons, Lithium-ion technologies are being widely applied in Microgrid context [153]. The main concern in Lithium-ion applications is the sensitivity to temperature variations, with the risk of explosion. Thus, it is necessary to use a dedicated unit for temperature control.

3.2.2.2. Batteries model

The studies of models of batteries depends on the approach and the desired physical characteristics to be obtained. If the studies consider temperature and aging effects or even the chemical process inside of the battery, the parameters required are very specific. In the thesis, the focus is on the electrical behavior of the battery, therefore the electrical model is fundamental.

A simple way to model a battery is to use an internal ideal voltage source with a series resistance to compose the terminal voltage represented by V_{bat}. This is the most common battery model, that besides its simplicity, it provides a reasonable performance for electrical studies. The electrical model of the battery is depicted in

Figure 3.7. The battery voltage equation can described as follows, according to the equivalent model.

$$V_{bat} = V_{int} - R_{int} I_{bat} \tag{3.5}$$

In this case, the battery is seen as a variable voltage source where V_{int} is the ideal open-circuit voltage and R_{int} is the equivalent internal resistance where the output voltage V_{bat} varies according to the injected/absorbed current in the terminals of the battery. Ideal open-circuit voltage is obtained by open-circuit measurement and the internal resistance is measured in fully charged condition by inserting a load in the battery terminal while measuring both terminal voltage and current.

The internal resistance represents the charge/discharge losses associated with electrolyte resistance, plate resistance and fluid resistance. Also, it can represent self-discharge phenomena. However, this model is limited and does not consider the variations in the internal resistance caused by temperature, SoC and electrolytic concentration.

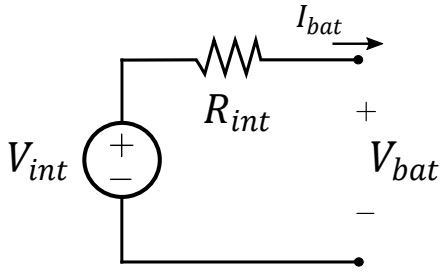

Figure 3.7: Battery electrical model based on internal resistance.

The battery model from Matlab/Simulink follows the same idea of the simple model presented in Figure 3.7. But a variable voltage source V_{int} is proposed based on the equations developed in [158]. Also, temperature and aging effects can be considered in Simulink's model following the propositions in [159] and [155]. The limitations of this model are:

- The internal resistance is assumed constant during charge/discharge cycles and is not affected by current variations;
- The parameters derived from discharge model are considered the same for charge model;
- The battery capacity is not changed by the level of current in the battery operation;
- The self-discharge is not considered.

The SoC is calculated according to the nominal capacity of the battery (Q) and the measured current in the battery terminals ($I_{bat}(t)$). The SoC equation is written

as follows:

$$SoC = 100\left[1 - \frac{1}{Q}\int_0^t I_{bat}(t)dt\right] \tag{3.6}$$

where SoC is given in percentage and the limits are between 0 and 100%.

3.2.2.3. Supercapacitors

Capacitors store energy trough electrostatic field, by accumulating opposite charges in parallel plates. The energy stored in the supercapacitor is proportional to the voltage square value as expressed in (3.7):

$$E_{cap} = \frac{CV_{cap}^2}{2} \tag{3.7}$$

where E_{cap} is the potential energy in the supercapacitor, C is the capacitance of the supercapacitor, and V_{cap} is the voltage on the capacitor terminals.

Therefore, the capacitance value and the voltage level are key to improve the energy storage capacity of a supercapacitor. This can be done by increasing the area of the plates, or decreasing the distance between the plates, maintaining the dielectric feature to satisfy maximum voltage limits, since the capacitance is given by:

$$C = \frac{\varepsilon A}{d} \tag{3.8}$$

where ε is the dielectric constant, A is the area of the plates and d is the distance between the plates.

The supercapacitors offer a higher surface area by using thin layers of electrolyte as a dielectric between them. The double layers capacitors used carbon electrodes with a separator between the electrolyte. The energy capacity is improved due to large increase of surface area in the electrolyte.

The supercapacitors are still in development with few applications in power systems, since they have high cost and limited energy density and large-scale energy applications. They are mostly used in DC power applications and for high peak power, low energy situations, because of the high power density of this technology. So, supercapacitors have a great potential in Microgrid systems, since they have a wide operation region, which can be completely discharged (unlike batteries) and operate effectively in several environments without damage (hot, cold and moist) [9, 20].

Supercapacitors in power applications are made by modules, where series and parallel capacitors are combined to compose a supercapacitor module. The voltage

of the supercapacitor system is calculated by:

$$V_{cap} = \frac{1}{C_{tot}} \int_0^t I_{cap}(t)dt + R_{tot} I_{cap}(t) \tag{3.9}$$

where C_{tot} and R_{tot} are the equivalent capacitance and resistance of the combined series/parallel configuration of the supercapacitors cells. The product $R_{tot}C_{tot}$ is the time response on the module. In this case, the effective series resistance has significant impact on the charge/discharge efficiency and in the time response of the supercapacitor.

The main characteristics of supercapacitors are: high charge/ discharge rates; low degradation over several hundred thousand cycles; good reversibility; less weight than the others (higher specific energy); low toxicity in the materials used for manufacturing and high cycle efficiency, approximately 95%. However, the main problem presented is the lower energy density compared with other technologies.

The supercapacitor model on Matlab/Simulink is a double layer capacitor, which is represented by a variable voltage source and an internal fixed resistance. The proposed voltage equation is given in [160], where the self-discharge process is also considered. In this model, the input is the measured current in the supercapacitor I_{cap} and the output is the measured voltage V_{cap}. The SoC of the supercapacitor is written as follows:

$$SoC = \frac{100}{Q_T} \left[Q_i - \int_0^t I_{cap}(t)dt \right] \tag{3.10}$$

where Q_T is the supecapacitor's capacity and Q_i is the initial capacity condition. SoC of the supercapacitor is given in percentage with 0 to 100% range.

The assumption made in the Simulink model are:

- Internal resistance is constant during charge and discharge operation;
- The temperature effect is not considered in the electrolyte;
- The aging effect and cell balancing are not modeled;
- Charge redistribution is the same for all values of voltage;
- The current is assumed to be continuous.

3.2.2.4. Hybrid energy storage systems

Hybrid Energy Storage Systems (HESS) are composed of two or more storage technologies aiming to optimally exploit the benefits of different ESS elements. Several management solutions of HESS have been proposed in the literature through computational modeling and simulations, demonstrating their potential

and technical feasibility mainly related to Microgrids and isolated systems [161,162]. These hybrid systems exploit the advantages of each type of storage combined to compensate for the weaknesses of each one individually. The most common HESS use the complement between the battery, which has the most predominant characteristic of energy density, and the supercapacitor, where high power density predominates. The supercapacitors when used with batteries demonstrates as advantages: high durability (over 10,000 cycles); lower environmental impact, since they do not contain harmful electrolytes; relieving peak loads and discharges in the batteries, promoting prolonged ESS lifetime [163,164].

Supercapacitors are devices capable of handling large variations of power compared to batteries. This is due to its high power density, so it can supply much more power for a sudden demand. At the same time, supercapacitors can inject/absorb power extremely quickly, which is a great advantage for applications with large spikes in power range. However, applications with large amounts of stored energy turn this equipment unfeasible, bringing the batteries in evidence for this kind of application. Therefore, each storage technology has a more suitable means of application. The application of batteries for large-scale energy storage and the application of supercapacitors in the power peaks are highlighted in [161]. The maximum instantaneous power that a supercapacitor can deliver is written as follows:

$$P_{cap,max} = \frac{V_{cap}^2}{4R_{tot}} \tag{3.11}$$

where the power delivered depends on the voltage level in the supercapacitor (V_{cap}) and the internal supercapacitor resistance R_{tot}.

When combined with the use of batteries and supercapacitors, the operation field of HESS becomes even more powerful, seen as the management unit of electrical systems in Microgrids. Then, the hybrid storage becomes responsible for transient stability of the system, and also guarantees the long-term energy supply reducing damage or degradation of the storage [165–167]. Batteries and supercapacitors have been one of the most popular combinations to compose HESS structures. In this sense, HESS can be categorised based on the number of ESS elements and converter configuration connected to the system. In [162] the classification of battery-supercapacitor HESS topologies is provided, and is depicted in Figure 3.8.

HESS can be configured in passive, active or parallel and series connections. The passive configuration is the most simple one, where the supercapacitor and the battery are directly connected to the DC bus as depicted in Figure 3.8-(a). In this case, the system works according to the devices' time constants to provide power

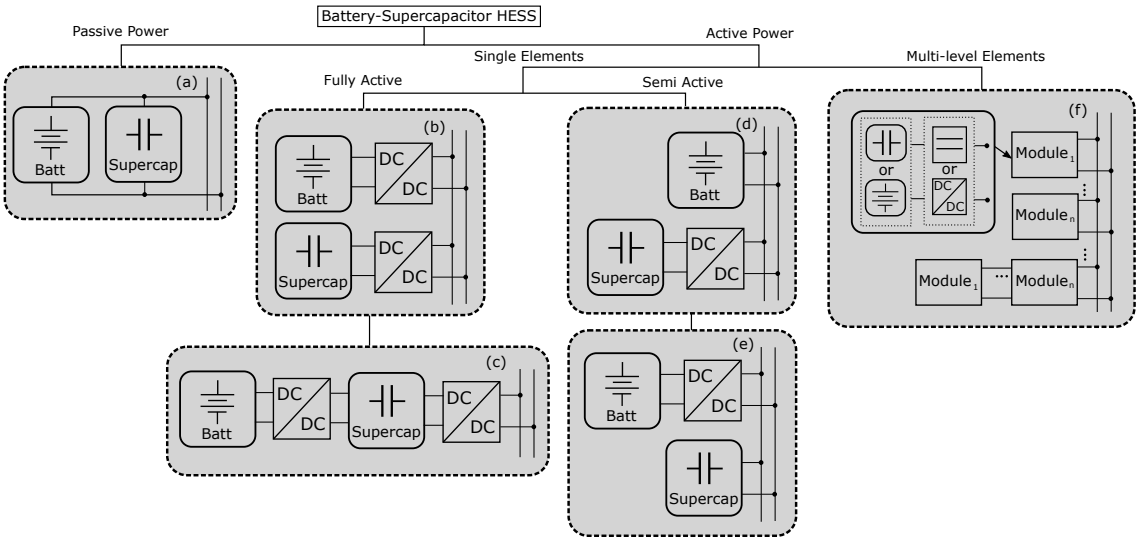

Figure 3.8: Different HESS configurations among passive, active, cascaded and multi-level applications.

sharing in the DC bus. The capacity of the battery and the supercapacitor cannot be fully used because the range of voltage in a DC bus is not flexible to prevent voltage fluctuations.

A example of passive HESS operation is depicted in Figure 3.9, where the power sharing between the supercapacitor and the battery under a period pulsed load is presented. In this example, the supercapacitor has much faster response to immediately provide the total amount of the power demand, then the power of the battery slowly increases to reach the power demand while the supercapacitor reduces its contribution. Finally, in steady state, the battery supply the load demand and the supercapacitor contributes only during the transients. The idea in the thesis is to use the supercapacitor feature to regulate the DC bus of the grid, therefore the high frequency variations will be handled by the supercapacitor, and the battery will be controlled by the a secondary controller to regulate the power flow in long term [161].

The active configuration uses a bidirectional DC/DC converter to control the power flow in the ESS, which results in a more flexible operation of system. The active configuration of HESS can be done in parallel (Figure 3.8-(b)), or cascaded (Figure 3.8-(c)). In fully active HESS application, the ESS elements are independents and can perform individual control targets allowing different control approaches at the same time, which results in much better system operation. Usually, the faster storage elements (supercapacitors) are used to act in transients and fast perturbations and slower but higher energy density elements (batteries) are used in power flow regulation in long term. Therefore, active configuration has the best

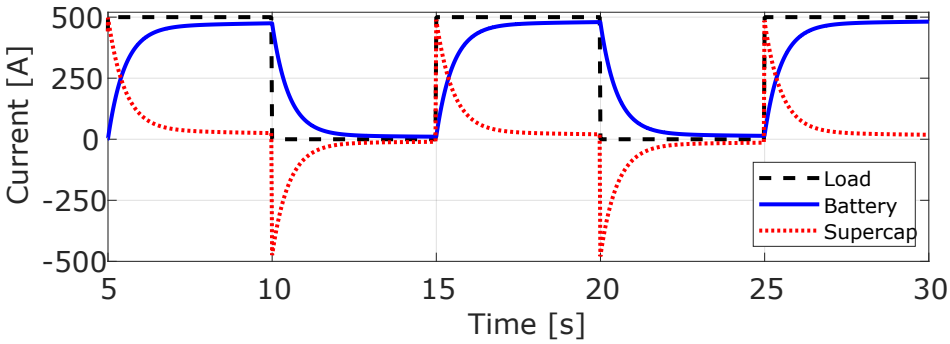

Figure 3.9: Power sharing of passive HESS where supercapacitor and battery time constant is highlighted.

technical solution, but can be considered as a expensive and complex solution. The cascaded configuration can be used for devices with different voltage rate operation, according to the construction of the element, but this configuration also increases the controller complexity.

Semi-active HESS topologies are explored as a good compromise between active and passive configurations (Figure 3.8-(d)-(e)). For (d) configuration, the flexible operation of supercapacitor is assured, improving volumetric efficiency. The supercapacitor is controlled to absorb the high frequency fluctuations in the DC bus, while the battery passively maintains the voltage variation inside the limits, since the battery presents stable electrical characteristics [161, 162]. In (e) configuration, the system is required to have a wider DC bus voltage range because of supercapacitor characteristics, which can be an issue for many applications.

In Figure 3.8-(f) is presented a multi-level HESS configuration, where the combination of passive and active elements are configured to create a unique power system management. A example of multi-level configuration is presented in [163], where a more adaptable and sophisticated system can be obtained for complex energy applications.

A common control strategy of parallel active HESS is to design Low-Pass Filter (LPF) and Moving Average Smoothing Method (MASM) to decompose the frequency in low and high component. Thus, the supercapacitor is allocated to have fast response, dealing with high frequency perturbations, and the battery is allocated to deal with long term supply to mitigate the high frequency operations impacts. The bandwidth and the cut-off frequency of the LPF is chosen to smooth the battery current, while the supercapacitor is demanded according to its capacity (or the DC/DC converter capacity), then a trade-off between supercapacitor and battery operation is necessary to assure proper operation of the HESS.

The decomposition approach is developed in [168] where the supercapacitor respond to fast power variations and the battery respond to slower variations. According to the power reserve of the proposed Microgrid, the voltage variation (dV/dt) is decomposed in two components, a slower one to provide battery reference and a faster component to the supercapacitor.

3.2.2.5. HESS structure

The Hybrid Energy Storage System (HESS) in the Microgrid is composed by a battery and a supercapacitor, with fully active configuration, which means that there is an exclusive DC/DC converter for each technology. The configuration optimize the system operation allowing a different control target for each technology. Therefore, the energy stored in supercapacitor can be better used, and the battery is used actively according to the control strategy in long term.

A proper sizing is mandatory for the battery to be able to inject or absorb the needed amount of power. A piecewise constant power supply is demanded for maximizing its lifetime. In this case, a Lithium-ion battery is designed for the proposed function according to the Microgrid size. The battery is designed as the proposed model from Simulink, where the input is the measured current (I_{bat}) and the output is voltage V_{bat}. The chosen battery has 380 V of nominal voltage, current capacity of 1000 Ah and nominal discharge current of 434.78 A, resulting in 380 kWh of energy capacity and 165 kW of nominal power.

Figure 3.10 depicts the discharge curve of the Lithium-ion battery with different current rate. The discharge curve presents the nominal area where the battery operates. The limits of the nominal area are given by the nominal value of battery voltage (380 V), which is the lower voltage limits, and the exponential zone is the upper voltage limit when the battery is fully charged. The discharge curve is given by the complete discharge of the battery with nominal current (434.78 A).

The considered supercapacitor is composed of 4 parallel and 18 series cells with 8.9 $m\Omega$ of equivalent DC series resistance, resulting in 50 F of total capacitance, 420 V of nominal voltage and has 1.225 kWh of nominal energy capacity. The number of layers is 1, with 1^{-9} m of molecular radius and 6.02^{-10} F/m permittivity of electrolyte material. The size of the supercapacitor is calculated according to the peak power variations of the Microgrid, which in this thesis was in the case when addressing regenerative train braking. Therefore, the supercapacitor must be able to absorb about 0.5 MW in few seconds.

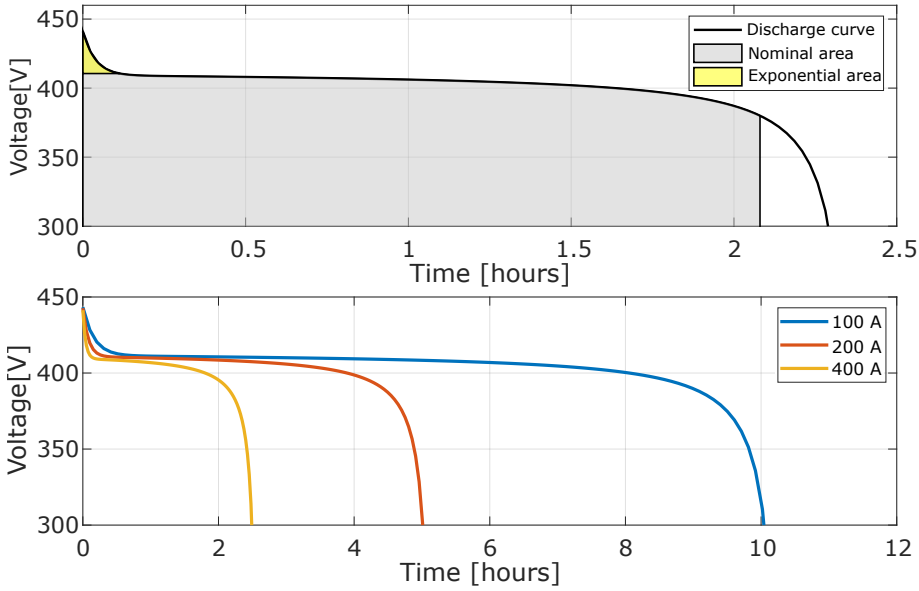

Figure 3.10: Discharge curve of the Lithium-ion battery from Simulink model.

The charge curve of the supercapacitor is depicted in Figure 3.11 for different constant charge current levels. The curve shows the voltage variation in the supercapacitor and the charge duration for a given constant current level.

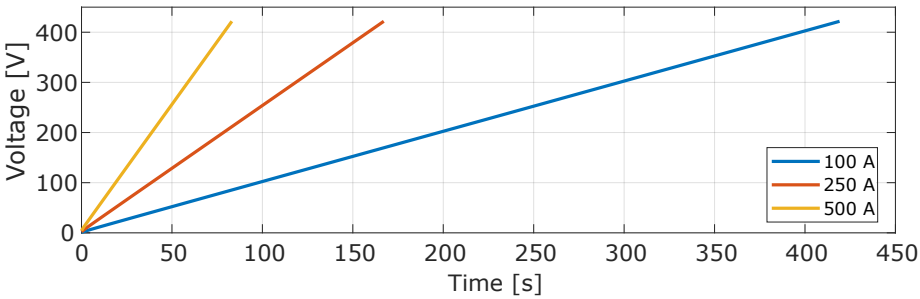

Figure 3.11: Supercapacitor charge characteristic.

3.2.3. Braking energy recovery system

Microgrids are considered innovative solutions to be used also in transportation systems to integrate the advantages of energy storage utilization [13–15, 169–171]. Indeed, they can help to reach the target of increasing energy saving [172] and the capability to compensate strong perturbations [173]. In urban railways, the power consumption is very high, therefore the optimization of energy consumption in this field means a great contribution for energy efficiency, specially when dealing with braking energy recovery. The trains' braking energy recovery system represents a new possibility of integrating a different kind of energy resource, in which since the

energy produced is free of any kind of pollution, regenerative energy braking from trains can be seen as a alternative energy source [10–12].

A train line can recover energy through regenerative braking when the train motor occasionally becomes a generator by producing a counter-torque in the electrical motor, where negative torque is provided to the driven wheels [11]. The braking energy recovery system is a renewable energy source, and the perturbation it introduces is different with respect to the usually considered ones. Indeed, it introduces a high level of current in a short time period [14–16] in a predictable way. However, this intermittent high power peak can cause instability in a Microgrid context; to avoid it, the supercapacitor has the duty to absorb the transient peak of energy [173–176]. As a consequence, the battery is less stressed.

In a railway station, the regenerated energy is usually transferred to the third rail in order to let nearby trains utilize it. In case it cannot be used by other trains, it is dissipated on resistors. The purpose of this part of the thesis is to introduce a model and related control methods for a Smart Railway Station able to store the regenerated energy in a battery, common to other renewable energy sources, allowing the station to become a market participant and sell the energy (maybe providing also ancillary services through a connection to the main AC grid) or simply to have the energy available if needed [13].

Figure 3.12 introduces the power consumed during the acceleration process and the absorbed power during the braking energy recovery process compared with the speed of an urban train [170].

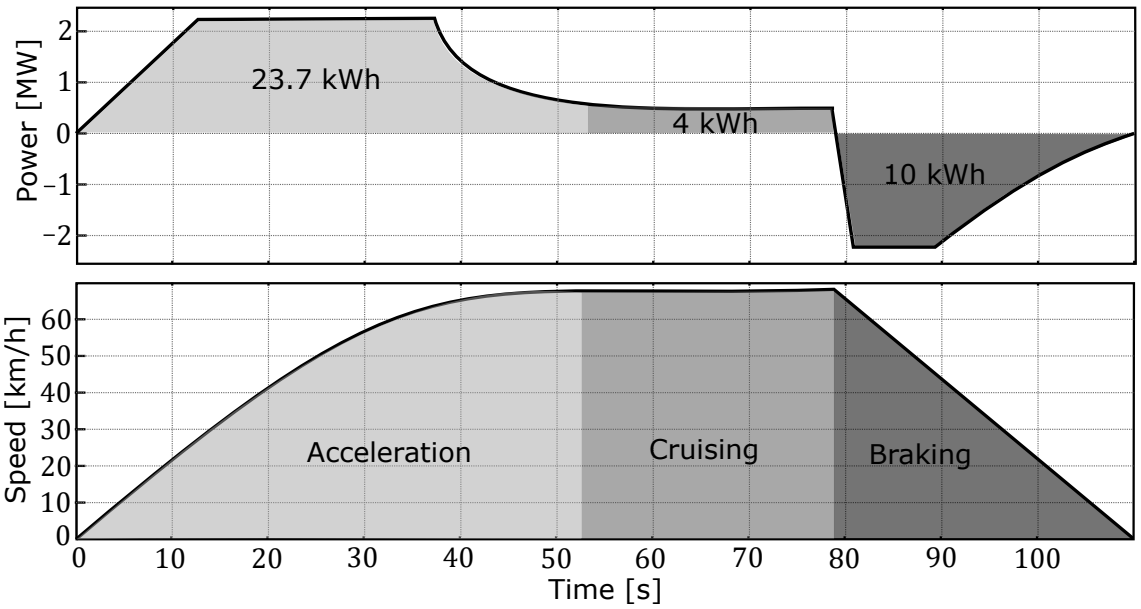

Figure 3.12: The power and speed variation of a urban train between two stations.

The train departs from the station and starts the acceleration process until it reaches cruising speed, where the power consumed grows in the form of a ramp until it reaches its nominal power value. Then, the power consumption decreases, as the train has already reached its rated speed, so only the losses (friction) need to be overcome to maintain the speed of the train. Finally, when the train approaches the next station, braking begins, where energy is then recovered until the train reaches zero speed. Usually, the braking recovery period is combined with the departs of other train to reduce the impacts caused by the spikes of power in the acceleration and braking process. In this combined operation, there are still some problems that may be minimized using ESS.

In this example, the energy recovered during braking is about 42% of the required energy to accelerate the train and 36% of the total energy consumed, which means that the regenerative braking can save a considerable amount of energy in this operation. When the losses are considered, the total restored energy is not the same as the energy produced during the braking recovery period. The rheostatic losses are the most important of braking recovery process, since they are related to the receptivity of the system due to regenerated energy excess [177]. A losses diagram of a DC railway system is presented in Figure 3.13 from [177].

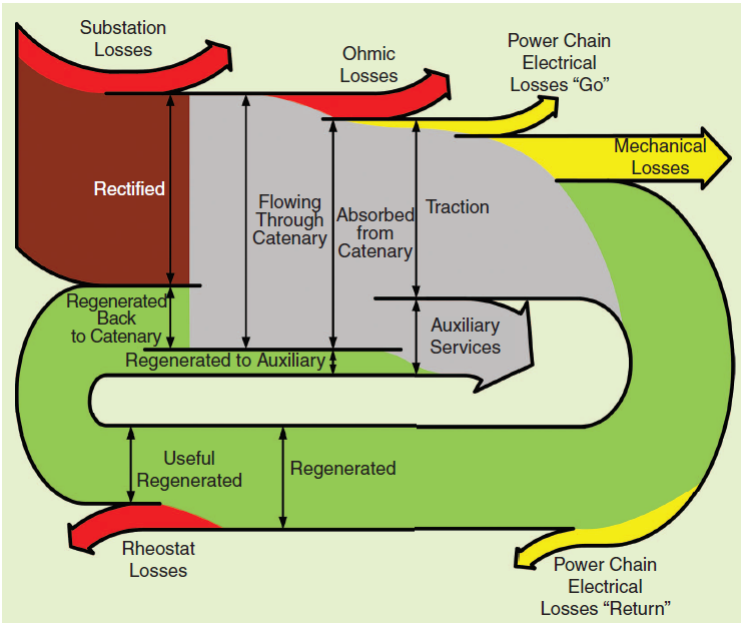

Figure 3.13: Sankey diagram for DC railway station extracted from.

Trains are mostly supplied by DC systems, where a non-controlled rectifier is connected between the catenary bus of the train and the grid. Therefore, there are two possibilities for regenerative braking systems. The first consists in connecting AC/DC converter in parallel with the existing substation to absorb the energy from

train braking. The second possibility, is to install a DC/DC converter that connects the train bus and the ESS to absorb the regenerated power. Figure 3.14 presents the two kinds of energy braking recovery introduced here.

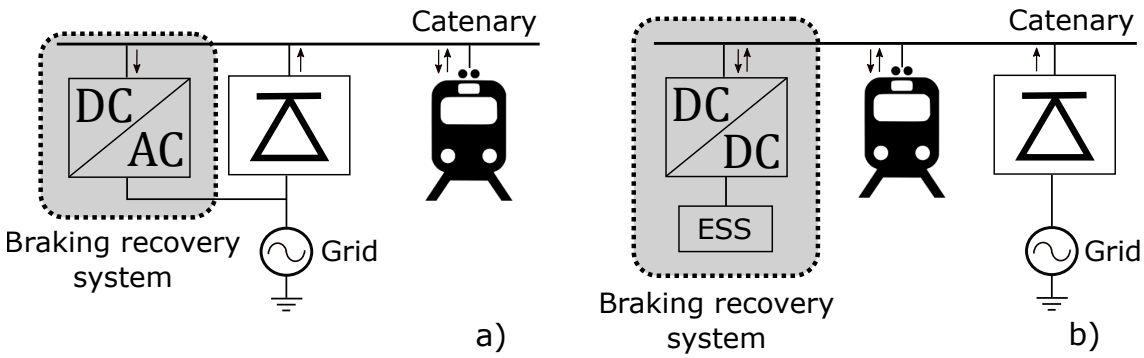

Figure 3.14: a) Traditional braking energy recovery. b) Braking energy recovery with energy storage system.

In the traditional braking energy recovery, the energy absorbed by the AC/DC converter is inserted in the main grid, which is seen as a strong perturbation and may cause many impacts in the network as power and voltage fluctuations. In the case of weak grids, the impacts are stronger and they may cause instabilities issues. Therefore, a good solution is to use the energy storage system to absorb the braking energy from the train, because the main grid is not impacted by this operation [13,171]. As consequence, the energy storage must be able to deal with this high peak of power in few seconds[1]. So, a supercapacitor fulfill this target because for batteries, the impact on their life cycle would be prohibitive. As seen earlier, a combination of the two technologies will optimize the use of ESS.

A step further is to insert the braking energy recovery system in a Microgrid, where energy management can be better provided and stronger DC bus stabilization is assured. Hence in this thesis, the braking energy is inserted in the Microgrid such as to perform the braking energy properly, without instability problems. Several results on EMS for optimal management of the regenerative energy can be cited [171, 178–180], but only few results focus on the physical systems' interconnection and on the overall stability analysis [13, 174, 181]. The target here is to propose a regenerative braking control strategy regarding the system stability.

In this thesis, the investigated railway station has nominal train line's DC voltage $V_T = 750\ V$, which models the train DC bus. When the regenerative braking takes place, the voltage of the train line increases to reach values around 900 V. A buck

[1]The time duration of braking energy recovery from trains are about 40 seconds, according with RATP company from Paris's metro.

converter is exclusively dedicated to the energy recovery, connecting the train line to the DC Microgrid. The train load (energy demanded to accelerate and drive the train) is fed by one or more converters and they are independent: train's load is not included in the regenerative braking system. This system recovers the braking energy instead of wasting it, and also helps the train's grid to keep its voltage inside desired operational margins. The converter's target is to keep rail voltage to its constant value, resulting in a power injection of approximately $0.5 - 1.0\ MW$ in a few seconds when the regenerative energy is recovered.

To include the train as a load on the Microgrid, such that the train is completely independent of the main grid, a considerable increase in the power rating of the Microgrid would be necessary. This would require a power generation in *Megawatts*, which may not be feasible for photovoltaic generation systems. A possible solution would be the use of hydro power or wind generators to meet the power demand from a train station.

3.2.4. Local loads

The DC load of the Microgrid is considered a combination of the load demand in the DC side of the grid and is composed of lights, heating systems, ventilation, escalators, electrical vehicles and more. Most of them are connected through a power converter, which are CPL, while others may be directly connected to the grid, and may be represented by a resistance. Therefore, the DC load is a time-varying variable, represented as a current source, where the voltage must be controlled. In this case, the usual voltage level in DC systems in France is $500\ V$.

The local AC load is supplied with $400V$ root mean square (rms) voltage and $50Hz$ of nominal frequency, where piecewise constant variations are done to emulate load changes during the simulation period. The loads are designed as constant impedance, where the load impedance is determined from the nominal voltage, than effective power varies proportionally to the square of the measured voltage; constant current, where the power also varies according to the voltage level; and constant PQ, where the demanded power is kept constant independent of the voltage variations in the network. This is implemented to diversify the types of loads included in the AC bus of the Microgrid. They may represent a number of different linear loads in the AC side of the grid.

3.2.5. Grid-connection

The connection with the main grid is done through a three-phase AC bus of 400 V rms and $\omega_r = 50\ Hz$ of fundamental frequency. The equivalent impedance of the grid is $L_l = 250\ mH$ and $R_l = 2\ m\Omega$, and the short-circuit power is $P_{sc} = 50\ MVA$. The main grid is represented by an infinite bus, in which the voltage and frequency stability is assured. In other words, the Microgrid only inject/absorb active and reactive power to the main grid without voltage and frequency support.

The DC side of the Microgrid is connected with AC bus trough a VSC converter. The AC bus represents a weak grid, where the AC loads and a diesel generator is integrated. The details of the weak grid will be presented in Chapter 5. In the case of a weak grid, the frequency and voltage stability must be assured by the Microgrid control strategy, allowing the operation in island mode.

3.3. Proposed Microgrid Design

This thesis proposes the design of a hybrid AC/DC Microgrid composed by a number of devices with the possibility of either grid-connection or island mode.

A HESS composed of a supercapacitor and a Lithium-ion battery is connected to the DC bus as the energy storage of the system. A PV array is integrated as the main generation of the system, where the PV is sized according to the load demand. A train braking recovery system is inserted in the system by connecting the train terminal to inject power in the DC bus of the Microgrid. The train supply is realized by the main grid, only the energy recovery from braking is injected into the Microgrid system. A variable DC load is connected to the DC bus of the Microgrid, where DC load must be properly supplied meeting network requirements. The DC load represents the load demand in the DC side of the grid. Therefore, heating, motors and electrical vehicles are included here, containing the non-linearities of this kind of loads.

The DC bus of the Microgrid integrated all DC devices of the system, including the connection with the main grid and the AC side of the Microgrid. The DC bus is used to balance the power flow in the whole system and even provide support to the AC side. The main grid is seen as an infinite bus (strong grid) able to assure voltage and frequency stability, where only active and reactive power injection is controlled. The AC side of the Microgrid is composed by a diesel generator with an Automatic Voltage Regulator (AVR) and a governor to maintain the AC Microgrid operation. This side of the grid is seen as a weak grid, where voltage and frequency support

is needed. A variable AC load is connected to the AC bus of the Microgrid, where proper supply must be assured. The AC load is modelled as piecewise-constant active and reactive power demands.

The Microgrid size must be designed in order to always supply the load requested power. Here, the DC side of the Microgrid is sized to be able to supply the whole system power demand. The PV array power (P_{PV}) is sized according to the energy consumption of the load (AC and DC) during the full day as written in (3.12) where P_L is the total power load demand, therefore the energy produced by the PV meet the energy demand.

$$\int_0^{day} P_{PV} dt \geq \int_0^{day} P_L dt \tag{3.12}$$

To make the Microgrid independent of weather conditions, the battery should be able of supply power to the load (in a worst case scenario) during an arbitrary period of time (T_1), given according to the desired reliability of the grid as expressed in (3.13).

$$\int_0^{T_1} P_B dt \geq \int_0^{T_1} P_L dt \tag{3.13}$$

where T_1 is the considered time interval for battery reliability, considering the environmental and climatic characteristics of the installation region, in addition to the type of load to be applied to the microgrid.

Finally, the supercapacitor must provide power to the Microgrid during a specific time interval (T_2) as given in (3.14), dealing with the strongest power peak variation in the grid. Here, the power variations are a task of the supercapacitor, which needs to maintain the power balance in the order of seconds.

$$\int_0^{T_2} P_S dt \geq \int_0^{T_2} (\Delta P_{PV} + \Delta P_L - \Delta P_B - \Delta P_T) dt \tag{3.14}$$

T_2 is the time step duration for the supercapacitor considering the transient variations in the grid. ΔP_{PV} and ΔP_L are the worst case power variations the PV and the load (AC and DC) can produce, ΔP_B the allowed battery's power variation, and ΔP_T is the power variation produced by the train during the regenerative braking period [37, 182, 183].

It is important to highlight that the Microgrid is composed of two main buses (see Fig. 3.15): first the DC bus interconnecting the DC elements, where the voltage in DC bus is controlled to allow the correct operation of the equipment connected to this link and to regulate the power flow in the system; second the AC bus that

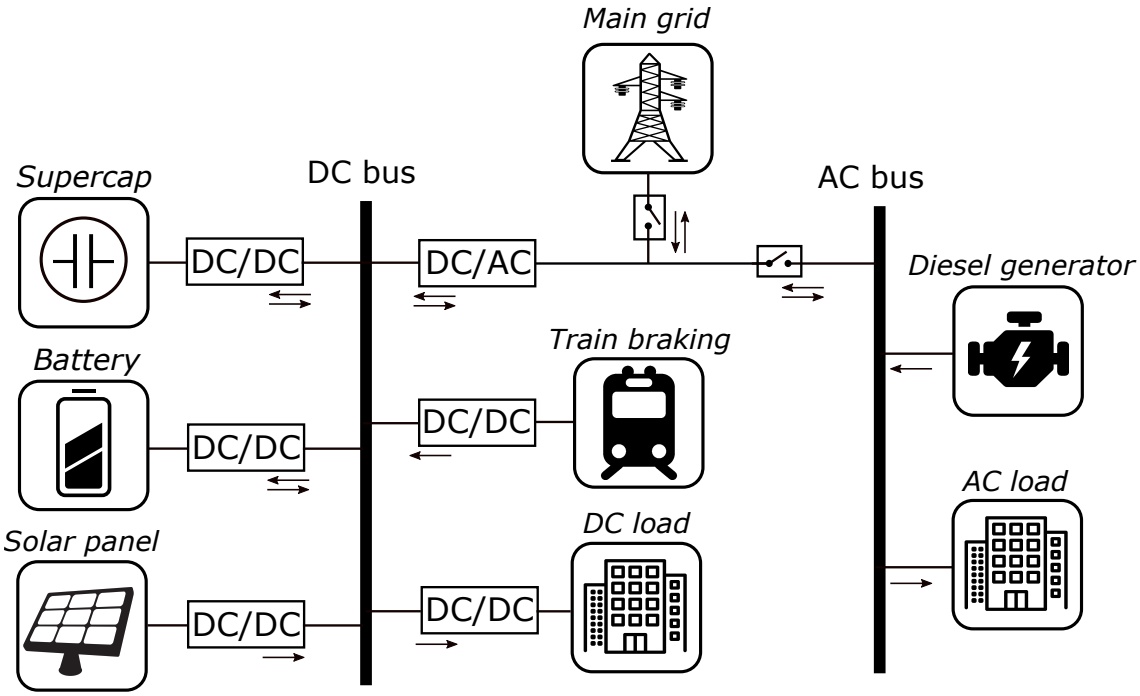

Figure 3.15: The general AC/DC hybrid Microgrid scheme.

interconnects the devices on the AC side of the grid with same voltage level and it is also controlled to attain stability of the AC grid. The AC bus is connected to the DC one by an AC/DC converter, which can perform ancillary services to the AC side of the grid. The main grid is considered a medium voltage transmission line, connected to the same point of coupling of the AC/DC Microgrid, where a transformer is applied to connect systems with same voltage level.

To analyze the operation of the proposed Microgrid, it may be disconnected from the main grid, then operating in island mode. Therefore, this critical operation of the system and the stability analysis of the system can be proved. Also, different operation profiles for the devices are performed to study the operation region of the system. The hierarchical control structured in different levels are assumed here, where the secondary and tertiary control are not detailed, since the focus is on the development of a distributed local nonlinear control. The references of the secondary controller are given to the local level in order to test the proposed controller. A comparison with linear standard control will be realized to analyze the control performance.

The general scheme of the proposed AC/DC hybrid Microgrid is depicted in Figure 3.15, where the DC and the AC side of the grid are highlighted.

3.3.1. Power converters configuration

A voltage level study is necessary to implement the proposed Microgrid. The DC bus voltage level must be compatible with the other devices in the grid. In the same way, the AC devices must be consistent with the voltage level in the AC bus. First, it is analyzed the voltage level of the Microgrid equipment and the grid requirements to determine the power converters configuration and the voltage levels.

The DC devices of the Microgrid are mostly modular, which means that the equipment can be rearranged to obtain the desired configuration. But, that configuration and the modular arrange can impact the costs of the system. The ESS is a clear example of modular devices, where smaller parts are integrated to each other to compose the desired configuration. The supercapacitor and the Lithium-ion battery can be structured to have the desired level of voltages by inserting series and parallel modules. The PV array also can be arranged according to the desired level of voltage and current changing the number of series and parallel modules connection. Therefore, the critical criterion to determine the voltages in the buses are the grid requirements.

The proposed Microgrid was designed to be part of a Smart Train Station in Paris, France, being part of a RATP train station. Therefore, the grid arrangements are based on french grid's standard. The AC voltage level in industrial distribution system is $V_{l,rms} = 400\ V$ phase-to-phase, which means that the AC bus of the Microgrid is set to have rms voltage $V_{AC,bus} = 400\ V$ three-phase with nominal frequency of $f_g = 50\ Hz$. Therefore, the AC load and diesel generator in the Microgrid have the same voltage as the AC bus voltage because of grid standard.

To connect the AC side of the grid with the DC side, a three level VSC converter is applied, where the AC voltage is well defined. Then, to allow current inversion DC to AC the following relation must be guaranteed [184]:

$$V_{dc} \geq \sqrt{2} V_{l,rms} \tag{3.15}$$

where V_{dc} is the DC bus voltage.

According to this relation, the minimum voltage for the DC bus is $V_{dc,min} = 565.68\ V$. Considering that the DC bus voltage may have $\pm 10\%$ maximum variation according to grid general standard, $V_{dc,min}$ is the smaller value of the DC bus already considering the maximum allowed variation. To keep stable operation, even considering strong perturbations and the maximum allowed voltage variation, the DC bus voltage can be determined considering a 10% addition to the minimum DC

voltage value to give margin for adjustments during transients.

$$V_{dc} \geq 1.1 V_{dc,min} = 622.25\ V \tag{3.16}$$

Once defined the minimum value of the DC bus voltage, the cost aspect is taken into account. From the economic point of view, higher is the DC bus voltage, more expensive is the converter. Because of technological reasons, the semiconductors (IGBT, MOSFET, Thyristor, etc) are more expensive for higher voltage levels. Also, the remaining equipment have this same feature, becoming more expensive for higher voltages, since the insulation materials and protections need to be designed according to the voltage level. The DC bus voltage is designed to have the lower voltage value according to these reasons. Therefore, the nominal value of DC bus voltage is $V_{dc} = 630\ V$, making a good compromise between technical and economic reasons.

In a previous work [37], the supercapacitor voltage was adopted to have a higher voltage than the DC bus voltage, where a bidirectional buck converter was applied. This is because a simpler control law can be developed, avoiding a non-minimal phase problem according to the chosen control target. But this scheme also presents drawbacks, mainly the fact that the supercapacitor must work in a even higher voltage, what makes it more expensive and difficult to build. For this reason, in this thesis the voltage level of the supercapacitor is considered also from the economical point of view and from the technological construction difficulty of such devices. Indeed, the lower the voltage, the easier is the construction and lower the cost of the device. Then, in this case, a bidirectional boost converter for the supercapacitor subsystem is chosen as a more reasonable solution. The rated voltage for the supercapacitor subsystem is $V_{cap} = 420\ V$, which maintains a good relation ($V_{dc}/V_{cap} = 1.5$) compared with the DC bus level, assuring proper operation of the boost converters.

As the supercapacitor injects energy in the system, its voltage V_{cap} drops proportionally till reaching the converter's limitation. Usually, considering technical bounds in practical industry applications, a good relation between output (V_{out}) and input (V_{in}) voltage for a boost converter is given by:

$$\frac{V_{out}}{V_{in}} < 4 \tag{3.17}$$

Gain limitation of boost converter due to the losses, mostly because of the inductor resistance. Therefore, the minimum value of supercapacitor's voltage that assures suitable converter's operation is given by: $V_{cap,min} = V_{dc}/4$. As a consequence,

the minimal energy stored in the supercapacitor is:

$$E_{cap,min} = E_{cap}\left(\frac{V_{dc}}{4V_{cap}}\right)^2 \tag{3.18}$$

which means that $14,06\%$ of the energy stored in the supercapacitor is not usable because of the conversion limits of the boost converter.

The Lithium-ion battery system is structured to have nominal voltage of $V_{bat} = 380\ V$, where a bidirectional boost converter is chosen to connect this system into the DC bus. In the battery case, the voltage variation between complete charge and discharge is not high enough to harm the converter operation and the voltage level of the battery assures proper operation of the boost converter.

In the PV system, the maximum possible voltage is the open circuit voltage $V_{oc,pv}$ of the PV array, which is given by the open circuit voltage of each module multiplied by the number of series modules configuration. The result is $V_{oc,pv} = 285\ V$ with a boost converter applied to the panel. In this case, the PV also doesn't have significant voltage variation to harm the system operation.

The transmission line connected to the Microgrid have nominal voltage of $34\ kV$, where a step down transformer is applied to reduce the line voltage to the AC bus' voltage level, while the diesel generator and the AC load are directed connected to the AC bus, since they have same nominal voltage as the AC bus $V_{l,rms} = 400\ V$.

For the remaining devices of the Microgrid, as the DC load and the braking energy recovery system, have their voltage defined previously by their manufacturers. The DC load is set to $500\ V$, which is a common value for the DC system of the Smart train Station in France (RATP Transports Parisiens). So a buck converter is used, since the current is flowing from the DC bus to the load. The nominal Train voltage is $V_T = 750\ V$, which is predefined by the railway. A buck converter is chosen for the braking energy recovery, since the DC bus voltage is smaller than the rail's voltage. During the regenerative braking, the voltage in the train increases up to $900\ V$, that despite being a considerably high value, does not hinder the conversion process of the buck converter. Table 3.3 summarizes the voltage level of the Microgrid and the chosen power converters.

3.3.2. Sizing of DC/DC converters

According to [184], the minimum inductance (L) to guarantee the desired current ripple value (ΔI_L) for the boost converter is given by:

$$L = \frac{V_{in}D}{\Delta I_L f_s} \tag{3.19}$$

Table 3.3: Power converters configuration in the Microgrid.

Device	Voltage level	Converter configuration	Nominal power
DC bus	630 V	-	-
Supercapacitor	420 V	Bidirectional boost	230 kW
Battery	380 V	Bidirectional boost	760kW
PV array	285 V	Boost converter	180kW
DC load	500 V	Buck converter	100kW
Train braking	750 V	Buck converter	0.8MW
AC bus	400 V	VSC converter	1 MVA
AC load	400 V	-	2MVA
Diesel generator	400 V	-	2 MVA

where D is the steady state value of the duty cycle on the converter in nominal conditions and f_s is the switching frequency. In bidirectional converters, the power switches are controlled complementarily, i.e., D is applied for first switch and $\bar{D}$ for the other switch. The bidirectional converters always operate in current continuous conduction mode, allowing the circulation of current in both directions.

The output capacitor of the boost converter is sized according to the voltage ripple (ΔV_{out}). This ripple is the result of the current variation in diode over capacitor causing a load change, which is defined by $\Delta Q_c = C\Delta V_{out}$, where C is the output capacitance. Therefore, the capacitance that assures the voltage to be inside of the ripple limits is given by [185]:

$$C = \frac{I_{out} D}{\Delta V_{out} f_s} \tag{3.20}$$

where I_{out} is the steady state output current on the converter in nominal operation conditions.

To improve life-time of the connected devices of the Microgrid, an input capacitor is inserted, acting as a capacitive filter to reduce high frequency oscillations from the power electronic's point of view, and at the same time introducing one more state variable to the system from the control's point of view. The input capacitance value (C_{in}) is obtained numerically, integrating its value till reaching the desired ripple level for the voltage input V_{in} [186]. The design of the buck converter is developed following same idea.

3.4. Conclusions

In this chapter, the components of the proposed Microgrid is introduced, where the equipment model are detailed. Hybrid Energy Storage System (ESS)

was adopted because its advantages compared to other technologies. Regenerative braking from trains was introduced, describing the way energy is recovered from trains' braking and how to be integrated to smart train stations. The AC/DC hybrid Microgrid proposal is introduced here presenting the approach for modeling and control of this Microgrid, and its form of operation.

CHAPTER 4

Control Strategy

4.1. Introduction

In this chapter, the nonlinear model of the proposed Microgrid is developed as a realistic average model where the dynamics of the system are expressed by nonlinear differential equations. A nonlinear distributed control strategy is developed based on the Microgrid model, assuring the stability of the DC bus to guarantee the proper operation of each component of the Microgrid. In addition to standard renewables, a regenerative train braking system is considered in the Microgrid. The ESS are separated according to their time-scale operation, where a faster one (supercapacitor) controls voltage variations on the DC bus, and a slower one (battery) provides the power flow balance. The proposed nonlinear controller is analysed in a rigorous way through Lyapunov theory. The operation of the grid is then analyzed by detailed simulations where the behavior of the interconnected devices are investigated as a whole system. The comparison with classical linear controllers is carried out in simulations to highlight the better performance of the nonlinear approach.

A System of Systems approach like the one introduced in [104] is utilized to develop the controllers for letting each converter carry out its task at local level and for performing whole system stability, similarly to [37,91,187]. Here the topology of some key converters has been reconsidered: since low voltage and high energy density is desired for the fast storage device, due to usual standard and economical reasons, a bidirectional boost converter (presenting non-minimum phase characteristics in the control target variables) is connected to the storage in charge of controlling the DC bus [113]. Also, according to the application, reconsiderations on the DC voltage bus value brought to the necessity of the utilization of buck converters for the loads and the regenerative system. The emerging model results to be more complex to

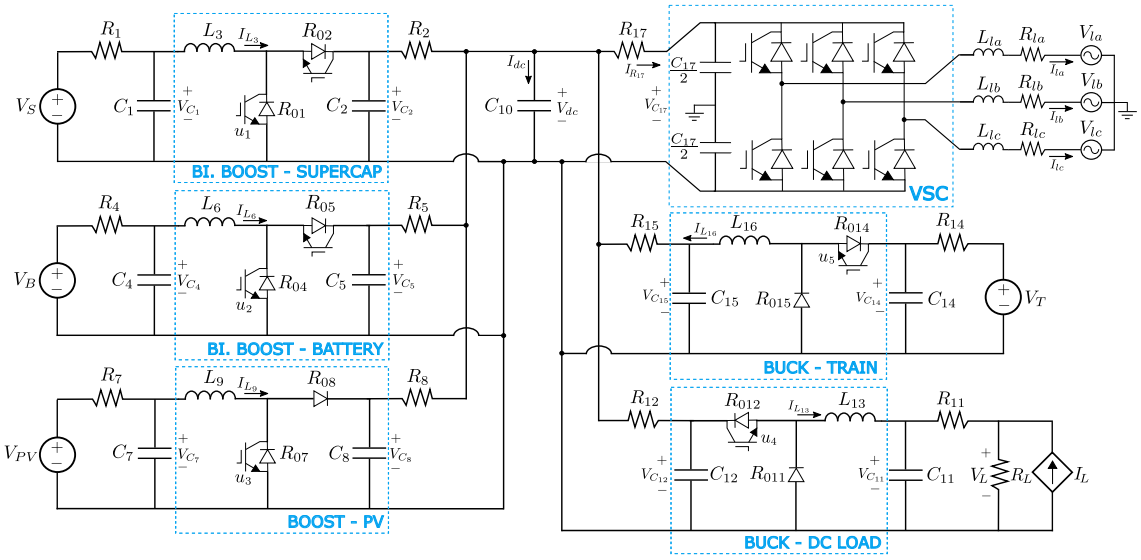

Figure 4.1: The considered Microgrid framework.

control with respect to the one in [91], and with the necessity to use together several control tools as feedback linearization [188], dynamic feedback linearization [189] and Input-to-Stable Stability (ISS) [190–192] to prove stability of the system as a whole. Furthermore, with respect to the stability analysis in [37], the property of Input to State Stability (ISS)-like Lyapunov function applied here produces less complexity to implement control laws. The proposed distributed nonlinear control technique is shown to ensure better performances of the interconnected nonlinear system with respect to linear control techniques, impacting positively the power quality and allowing for the possibility to perform a system's operating region analysis [42].

4.1.1. Model introduction

The considered DC Microgrid is depicted in Figure 4.1: it is composed by two different types of renewable energy sources (braking energy recovery from the trains and photovoltaic panels), two kinds of storage acting at different time-scales (a battery and a supercapacitor), a DC load and the connection with the main AC grid. The target is to assure voltage stability in the DC grid and correctly feed power to the load while absorbing power from the SoC array and the braking energy recovery system. To each component of the Microgrid (array, energy recovery system, battery, supercapacitor, load) a DC/DC converter is used, and a DC/AC one for the AC grid connection. By applying Kirchhoff law in the Microgrid circuit in Figure 4.1, the dynamical equations for the state space modelling of the whole system are obtained, where development of each equipment model is detailed in the next sections.

Another important target to be accomplished is to save the battery lifetime. Since the regenerative system introduces a very high peak current in a very short time period, the battery would be stressed if it is in charge of absorbing it and its lifetime would be significantly reduced. The supercapacitor is chosen to absorb this amount of power; indeed, thanks to its different characteristics, its lifetime will not be affected as the battery's. Power coming from the battery will then be modified according to the new level of energy in the supercapacitor, and according to a desired charge/discharge rate [28, 193].

The braking energy recovery is made by a reverse torque generated in the train drive when the train brakes. So, when the train brakes, the energy produced is injected into the system by a dedicated DC/DC converter, where the storage system manage the generated energy.

Finally, this DC grid is used to provide ancillary services of active and reactive power to an AC grid. In the first case, a strong grid (infinite bus) is modeled, therefore there is a reference of active and reactive power to be provided, such as to procure ancillary services to that grid. Voltage and frequency control will be introduced in next chapter when it will be considered a weak grid. Two assumptions are made in this first step: a higher level controller is supposed to provide references[1] to be accomplished by the local controllers [27, 116]; the second one is about a proper sizing of PV array, battery and supercapacitor in order to have feasible power balance with respect to the sizing of the load and of the power coming from the braking recovery system.

4.2. Supercapacitor Subsystem

The supercapacitor is an energy storage device which is used to improve power quality, due to its capability to provide fast response to grid oscillations. It has high power density and an increased life-cycle while having a considerably low energy density. The combination of such device with a slower one (like batteries) allows to ensure proper control and management strategies of the power flow, dealing with the multiple time-scale characteristic of DC Microgrids [43]. Indeed, combining the battery characteristics with the supercapacitor ones, it is possible to have the supercapacitor acting to counteract grid's transient variations, while the battery deals with the power flow [175].

[1] The references are computed by a secondary control that considers the optimization of the grid, aiming at physical characteristics as reducing losses, or aiming economical aspects as cost reduction.

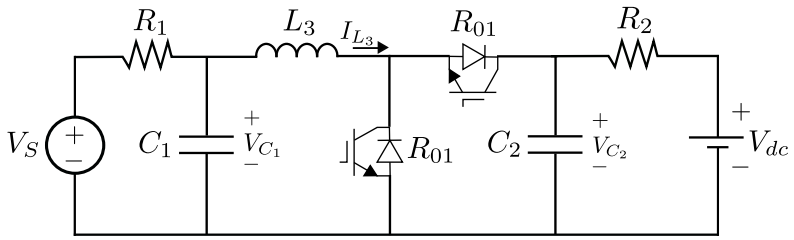

Figure 4.2: The bidirectional boost converter of the supercapacitor subsystem.

4.2.1. Supercapacitor model

A bidirectional-boost converter connects the supercapacitor to the DC link. The boost configuration of the supercapacitor is depicted in Figure 4.2.

Using Kirchhoff's circuit law, average state-space model is introduced as follows:

$$\dot{V}_{C_1} = \frac{1}{R_1 C_1} V_S - \frac{1}{R_1 C_1} V_{C_1} - \frac{1}{C_1} I_{L_3} \tag{4.1}$$

$$\dot{V}_{C_2} = \frac{1}{R_2 C_2} V_{dc} - \frac{1}{R_2 C_2} V_{C_2} + \frac{1}{C_2} I_{L_3}(1 - u_1) \tag{4.2}$$

$$\dot{I}_{L_3} = \frac{1}{L_3} V_{C_1} - \frac{1}{L_3} V_{C_2}(1 - u_1) - \frac{R_{01}}{L_3} I_{L_3} \tag{4.3}$$

where V_S is the supercapacitor's voltage, V_{C_1} is the voltage of capacitor C_1, V_{C_2} is the voltage on capacitor C_2 and I_{L_3} is the current on inductor L_3. R_1 and R_2 are the resistances representing the cable losses, while R_{01} and R_{02} represent the semiconductor losses, where $R_{01} = R_{02}$ when dealing with bidirectional converters. The inductor losses may be inserted as a series resistance with the converter inductor, or it can be merged with the semiconductor losses in R_{01} and R_{02}. u_1 is the duty cycle of the converter, where $u_1 \in [0, 1]$ for the average model. V_{dc} is the voltage on the DC bus (its dynamics will be detailed later on).

The supercapacitor target is to regulate the voltage on the DC bus (V_{dc}) to assure power balance in transients. Therefore the voltage V_{C_2} is controlled such that, DC bus voltage V_{dc} is driven to V_{dc}^*. In this formulation, V_{C_1}, V_{C_2} and I_{L_3} are the state variables, u_1 is the control input and voltages V_S is seen as a disturbance.

4.2.2. Non-minimum phase problem

Then, taking u_1 as the control input and V_{C_2} as the control output in (4.2), one can calculate a control law to steer $V_{C_2} \to V_{C_2}^e$.

$$u_1 = \frac{1}{I_{L_3}} \left[I_{L_3} - C_2 v_2 + \frac{1}{R_2}(V_{dc} - V_{C_2}) \right] \tag{4.4}$$

where v_2 is an additional control input to give the desired dynamics to V_{C_2} as follows:

$$v_2 = -K_2(V_{C_2} - V_{C_2}^e) - K_2^\alpha \alpha_2 \tag{4.5}$$

$$\dot{\alpha}_2 = V_{C_2} - V_{C_2}^e \tag{4.6}$$

The closed-loop for the supercapacitor's system using this control is presented as:

$$\begin{cases} \dot{V}_{C_2} = -K_2(V_{C_2} - V_{C_2}^e) - K_2^\alpha \alpha_2 \\ \dot{\alpha}_2 = V_{C_2} - V_{C_2}^e \\ \dot{V}_{C_1} = \frac{1}{R_1 C_1} V_S - \frac{1}{R_1 C_1} V_{C_1} - \frac{1}{C_1} I_{L_3} \\ \dot{I}_{L_3} = \frac{1}{L_3} V_{C_1} + \frac{V_{C_2}^e}{R_2 L_3 I_{L_3}} (V_{dc} - V_{C_2}^e) - \frac{R_{01}}{L_3} I_{L_3} \end{cases} \tag{4.7}$$

One may remark a problem because current I_{L_3} can cross zero, assuming positive values when the supercapacitor is discharging and negative values when the supercapacitor is charging, which generates a singularity in the calculation of the control input. This already illustrates a non-minimum phase phenomena that will be explicit in the following. Choosing V_{C_2} as the considered output (or α_2 if this one is used), V_{C_1} and I_{L_3} compose the non-controlled dynamics, i.e., zero dynamics of this system, that are expressed as follows:

$$\dot{V}_{C_1} = \frac{1}{R_1 C_1} V_S - \frac{1}{R_1 C_1} V_{C_1} - \frac{1}{C_1} I_{L_3} \tag{4.8}$$

$$\dot{I}_{L_3} = \frac{1}{L_3} V_{C_1} + \frac{V_{C_2}^e}{R_2 L_3 I_{L_3}} (V_{dc} - V_{C_2}^e) - \frac{R_{01}}{L_3} I_{L_3} \tag{4.9}$$

Based on (4.8) and (4.9), the equilibrium points are calculated as:

$$V_{C_1}^e = V_S - R_1 I_{L_3}^e \tag{4.10}$$

$$I_{L_3}^e = \frac{V_{C_1}^e}{2R_{01}} \pm \frac{1}{2R_{01}} \sqrt{{V_{C_1}^e}^2 + 4\frac{R_{01}}{R_2} V_{C_2}^e (V_{dc} - V_{C_2}^e)} \tag{4.11}$$

which is well defined for $R_{01} \leq R_2/4$.

The local stability analysis of the zero dynamics is given by the Jacobian matrix as follows:

$$\mathcal{J}_0 = \begin{bmatrix} -\frac{1}{R_1 C_1} & -\frac{1}{C_1} \\ \frac{1}{L_3} & -\frac{1}{R_2 L_3} \frac{V_{C_2}^e}{{I_{L_3}^e}^2} (V_{dc} - V_{C_2}^e) - \frac{R_{01}}{L_3} \end{bmatrix} = \begin{bmatrix} a_0 & b_0 \\ c_0 & d_0 \end{bmatrix}$$

and its eigenvalues are calculated as:

$$\lambda_{1,2} = \frac{a_0 + d_0}{2} \pm \frac{1}{2} \sqrt{(a_0 + d_0)^2 - 4(a_0 d_0 - b_0 c_0)} \tag{4.12}$$

Therefore, the region of stability can be defined by the inequalities $a_0 + d_0 < 0$ and $a_0 d_0 < 0$, since $b_0 c_0$ is always negative. The region of stability is given by the intersection of the above inequalities and can be written as:

$$-\frac{1}{R_2 L_3}\frac{V_{C_2}^e}{{I_{L_3}^e}^2}(V_{dc} - V_{C_2}^e) - \frac{R_{01}}{L_3} < 0 \tag{4.13}$$

and then:

$$V_{C_2}\frac{(V_{C_2} - V_{dc})}{R_2} \quad < \quad R_{01}{I_{L_3}}^2 \tag{4.14}$$

When $I_{L_3} < 0$ (i.e. $V_{dc} > V_{C_2}$) the inequality is valid, but when $I_{L_3} > 0$ (i.e. $V_{dc} < V_{C_2}$) the zero dynamics are unstable, i.e., there is a non-minimum phase characteristic for this choice of control output [188, 194].

In the following, it is considered I_{L_3} as the output of the subsystem (4.1)-(4.3) (relative degree equal to 1), and V_{C_1} and V_{C_2} the zero dynamics. The control target will be to properly let the voltage V_{C_2} track a desired trajectory, which is $V_{C_2}^e$, in order to accomplish the aforementioned duty of ensuring voltage stability. The choice of controlling directly the current is done according to a common practice in power systems community and the physics of the device. Indeed, to directly control the voltage would bring several difficulties that come from the characteristics of the system. These difficulties can be dealt with by creating a multi-time scale behavior on the system by the control scheme, since the current dynamics can be designed to be faster than the voltage one [117, 125, 188, 195]. As showed, to directly control the voltage would result in an oscillating behavior, because of the non-minimum phase characteristics of the subsystem. Then, the dynamic feedback linearization technique will be used (see [189, 196]), as in [117].

4.2.3. Control induced time-scale separation

A common practice in power converter applications is to use the so called vector control, an inner current loop with faster dynamics and a second slower one for output capacitor voltage. It is empirically assumed that the outer voltage loop control can be designed independently from the inner current loop. But, mathematical explanation and validity of such hypothesis is seldom made. This subsection provides a formal analysis for control induced time-scale separation, where the control scheme is able to artificially induces two different closed-loop subsystems. The time-scale separation is studied by means of singular perturbation theory, in which the controller makes the full system to be split into a boundary layer and a reduced model [195, 197], providing a mathematical proof for this common practice of time-scale separation from power system community [198].

Based on singular perturbation theory, lower-order subsystems in different time scales can be obtained to approximate the behavior of the original system. In this case two subsystems, i.e. the driving and the driven subsystems. The driving subsystem composes the fundamental control module (u) and the driven subsystem constitutes the outer control module. In the present case, different from the traditional results on power system's applications, the time-scale separation is induced by the control input, which means that the system has no natural multi time scales, but the controller creates it. Therefore, the target here is to propose a control induced time scale separation for a DC/DC converter, such that a faster (inner) current control loop and a slower (outer) voltage control loop is created comparable with standard power converter's control application [199].

The system (4.1)-(4.3) consists of two interconnected subsystems[2], i.e., the current I_{L_3} is from subsystem 1 and the voltage V_{C_2} is from subsystem 2. Therefore, one can develop a control such that the voltage V_{C_2} is designed to have slower dynamics than the current I_{L_3}, resulting in a explicit time-scale separation, where the singular perturbation condition is created. With this consideration the control design can be developed separately for each subsystem. As V_{C_1} is just a stable first order filter of I_{L_3}, it is left out of the main analysis.

Defining $x = V_{C_2}$ and $z = I_{L_3}$, the subsystems can be generically written as:

$$\dot{x} = f_x(x, z) + g_x(z)u \tag{4.15}$$

$$\dot{z} = f_z(x, z) + g_z(x)u \tag{4.16}$$

This system is a second order one with one control input: therefore, the uncontrolled dynamic should be brought to the equilibrium point by the controlled one. The idea is to develop a control law where u tracks a reference trajectory x^*, yet to be defined. In this case, $V^*_{C_2}$ is designed aiming to obtain the DC bus stabilization developed in Section 4.8, but $I^e_{L_3}$ is yet not available. Therefore, it is a crucial step to determine $I^e_{L_3}$, which is the desired trajectory of I_{L_3}.

Suppose that there is a control law $u = h(x, z)$ for the current subsystem, such that z in (4.16) converges to an equilibrium point z^* as follows:

$$\dot{z} = -a(z - z^*) + r(z, z^*) \tag{4.17}$$

where a is a positive real number such that $a = 1/\epsilon, \quad \epsilon \in \mathbb{R}^*_+$, and the nonlinear function r is chosen such that:

$$\frac{||r(z, z^*)||}{||z - z^*||} \longrightarrow 0 \; as \; ||z - z^*|| \longrightarrow 0 \tag{4.18}$$

[2]The same analogy will be made for train subsystem in (4.100)-(4.102).

Assuming that for any $\gamma > 0$, there is a region $\mathbf{B}_r$ which implies in the following inequality:

$$||r(z, z^*)|| \leq \gamma||(z - z^*)|| \tag{4.19}$$

$\forall(z - z^*) \in \mathbf{B}_r$.

The nonlinear part is dominated by the linear part in a small neighborhood of the equilibrium point. Consequently, one can impose faster dynamics on the current subsystem by designing dynamics given by constant a much faster than the voltage subsystem. Then, the control input can be written as:

$$h(x, z) = \frac{1}{g_z}[-a(z - z^*) + r(z, z^*) - f_z] \tag{4.20}$$

where g_z must be non-singular.

The closed loop system then becomes:

$$\dot{x} = f_x(x, z) + \frac{g_x}{g_z}[-a(z - z^*) + r(z, z^*) - f_z] \tag{4.21}$$

$$\epsilon\dot{z} = -(z - z^*) + \epsilon r(z, z^*) \tag{4.22}$$

which is in the standard singular perturbation form. Following the standard procedure from singular perturbation [188], one may take the current subsystem z already in its final manifold, z^* driven by (4.20). Hence, the control input can be written as:

$$u' = h(x, z^*) = -g_z^{-1}(x, z^*)f_z(x, z^*) \tag{4.23}$$

Therefore, substituting $z = z^*$ and $u = u'$, one may obtain the reduced boundary layer model:

$$\dot{x} = f_x(x, z^*) - g_x(x, z^*)g_z^{-1}(x, z^*)f_z(x, z^*) \tag{4.24}$$

The control target at this point is to make x steer x^* exponentially, so in (4.24) it is used z^* as a virtual control for this boundary layer x dynamic. It is then supposed that there exists a control law $z^* = h_2(x)$ where x can be exponentially stabilized at x^*, in the form:

$$\dot{x} = -b(x - x^*) + r_2(z, z^*) \tag{4.25}$$

where b is a design positive number, such that $b << a$ and r_2 is the nonlinear part as proceeded in (4.18):

$$\frac{||r_2(z, z^*)||}{||z - z^*||} \longrightarrow 0 \; as \; ||z - z^*|| \longrightarrow 0 \tag{4.26}$$

or in another words:

$$||r_2(x, x^*)|| \quad \leq \gamma_2 ||z - z^*||$$

Now it is possible, by singular perturbation analysis, to assure that there exists $\epsilon^* > 0$ such that for all $\epsilon < \epsilon^*$, the origin of the full system is exponentially stable.

Furthermore, the new closed loop system taking the boundary layer model becomes:

$$\begin{aligned} \dot{x} &= -b(x - x^*) + r_2(z, z^*) \\ \dot{z} &= -a(z - z^*) + r(z, z^*) \end{aligned} \tag{4.27}$$

We may now estimate the region of convergence of this system by stating a Lyapunov function:

$$V_{sp} = \frac{1}{2}(x - x^*)^2 + \frac{1}{2}(z - z^*)^2$$

which derivative is:

$$\begin{aligned} \dot{V}_{sp} &= -b(x - x^*)^2 + r_2(x - x^*)(z - z^*) - a(z - z^*)^2 + r(z - z^*)^2 \\ &\leq -b||x - x^*||^2 + \gamma_2 ||x - x^*|| ||z - z^*|| - a||z - z^*||^2 + \gamma ||z - z^*||^2 \end{aligned}$$

Applying Young's inequality for the product

$$||\tilde{x}|| \; ||\tilde{y}|| \leq \frac{1}{2m}||\tilde{x}||^2 + \frac{m}{2}||\tilde{z}||^2 \tag{4.28}$$

where m is positive, the derivative of V_{sp} satisfies

$$\begin{aligned} \dot{V}_{sp} &\leq -b||x - x^*||^2 + \frac{\gamma_2}{2m}||x - x^*||^2 + \frac{m\gamma_2}{2}||z - z^*||^2 - a||z - z^*||^2 + \gamma ||z - z^*||^2 \\ &\leq -(b - \frac{\gamma_2}{2m})||x - x^*||^2 - (a - \gamma - \frac{m\gamma_2}{2})||z - z^*||^2 \end{aligned}$$

assuring exponential stability for the whole system. This Lyapunov function can now be used for establishing the conditions on a and b gains that fulfill this result.

Remark 1. *The singular perturbation analysis is the result of an explicit time-scale separation of two interconnected subsystems where a simpler control approach can be developed.*

Remark 2. *The convergence speed of x and z are dominated by b and a respectively, in which by singular perturbation techniques, one can prove that if the convergence speed of z is designed to be much faster, the error of the reduced model x becomes small. In the following this approach will be used to design the controllers for the converters that present non-minimum phase characteristics.*

4.2.4. Supercapacitor control application

According to its multi-time scale characteristics, the system introduced in (4.1)-(4.3) consists of two interconnected sub-systems; i.e., subsystem 1 is composed only by the current I_{L_3}, while the other one represents the three voltages V_{C_1}, V_{C_2} and V_{dc}. To correctly address the desired actions, three steps need to be envisaged for performing the control algorithm:

1. To introduce a stabilizing controller for the subsystem 1, representing the current I_{L_3}. Indeed, this subsystem is controllable and is designed to have faster dynamics than the second one. The first target will be to steer the controllable faster dynamics I_{L_3} to bringing it to a desired manifold $I_{L_3} \rightarrow I^e_{L_3}$, where $I^e_{L_3}$ is yet to be designed. To develop the controller for the fast dynamics separately from the slow dynamics some mild conditions concerning singular perturbation are used and verified (see [188]).
2. To define the operating region where the controller introduced in step 1, is able to work with respect to the reference $I^e_{L_3}$. This operation region clearly depends on the state of the system and on the tuning values.
3. To calculate the reference $I^e_{L_3}$ for the current dynamics, according to the desired equilibrium point for voltage V_{C_2}, i.e. $V^e_{C_2}$. This reference is obtained by considerations about singular perturbation analysis. Thus, $I^e_{L_3}$ will be deduced from the desired equilibrium point of the output capacitor voltage $V^e_{C_2}$.

With this methodology, it is possible to avoid the problems related to the non-minimum phase characteristics of the system that is due to the structure of the boost converter. The target will be to steer V_{C_2} to a desired $V^e_{C_2}$, providing DC bus voltage regulation.

The first step is to control the current I_{L_3} in the supercapacitor's converter, tracking its reference $I^e_{L_3}$, which is now supposed to be know, as well as its evolution over the time. From singular perturbation analysis [125], one can consider the states V_{dc}, V_{C_1} and V_{C_2}, as constant in this part and then just study the subsystem describing the current. According to the control objective, the output is defined

as $y_1 = I_{L_3}$. The system is a single-input single-output one:

$$\begin{cases} \dot{I}_{L_3} = f_1(V_{C_1}, V_{C_2}, I_{L_3}) + g_1 u_1 \\ y_1 = I_{L_3} \end{cases} \tag{4.29}$$

where f_1 and g_1 are defined in (4.1)-(4.3), and where the Lie derivative of the output with respect to g_1 is calculated as:

$$\mathcal{L}_{g_1}(I_{L_3}) = \frac{V_{C_2}}{L_3} \tag{4.30}$$

Since V_{C_2} is always positive by technological reasons, Lie derivative in (4.30) is non-singular and therefore a nonlinear feedback linearizing control for the control input u_1 can be written as:

$$u_1 = L_{g_1}(I_{L_3})^{-1}\left[v_3 - \frac{1}{L_3}\left(V_{C_1} - V_{C_2} - R_{01} I_{L_3}\right)\right] \tag{4.31}$$

$$u_1 = 1 + \frac{1}{V_{C_2}}\left[L_3 v_3 - V_{C_1} + R_{01} I_{L_3}\right] \tag{4.32}$$

where v_3 is the additional input to be designed. It must to be noticed that V_{C_1} and V_{C_2} are considered constant because of the time-scale separation, where the voltages are allocated to have much slower dynamics.

The additional input v_3 is designed following linear theory in order to place poles and to bring the output I_{L_3} to its desired trajectory $I^e_{L_3}$:

$$v_3 = -K_3(I_{L_3} - I^e_{L_3}) - K^\alpha_3 \alpha_3 \tag{4.33}$$

$$\dot{\alpha}_3 = I_{L_3} - I^e_{L_3} \tag{4.34}$$

where K_3 and K^α_3 are positive constants, chosen in a way such that the multi-time scale nature of the dynamics of I_{L_3} with respect to the voltages is preserved, or even enlarged. By substituting (4.32), (4.33) and (4.34) in (4.29), the resulting dynamics is linear and stable, where α_3 is the auxiliary variable that can be interpreted as an auxiliary integral term. $I^e_{L_3}$ is the desired current that has to be designed.

4.2.5. Zero dynamics analysis

The states V_{C_1} and V_{C_2} are the zero dynamics of the whole system with respect to output I_{L_3}.

$$\dot{V}_{C_1} = \frac{1}{R_1 C_1}(V_S - V_{C_1}) - \frac{1}{C_1} I^e_{L_3} \tag{4.35}$$

$$\dot{V}_{C_2} = \frac{1}{R_2 C_2}(V_{dc} - V_{C_2} + \frac{1}{C_2}\frac{I^e_{L_3}}{V_{C_2}}(V_{C_1} - R_{01} I^e_{L_3}) \tag{4.36}$$

A stability study is presented for this two variables. Based on (4.1) and (4.2), the calculated equilibrium points for V_{C_1} and V_{C_2} are:

$$V_{C_1}^e = V_S - R_1 I_{L_3}^e \tag{4.37}$$

$$V_{C_2}^e = \frac{V_{dc}}{2} \pm \frac{1}{2}\sqrt{V_{dc}^2 + 4R_2 I_{L_3}^e (V_{C_1} - R_{01} I_{L_3}^e)} \tag{4.38}$$

As stated in (4.37), the variable V_{C_1} has just one equilibrium point while V_{C_2} has two equilibrium points (see (4.38)); the linearization technique will be used for local stability analysis in these equilibrium points. The resulting Jacobian linearization matrix $\mathcal{J}_A$ is:

$$\mathcal{J}_A = \begin{bmatrix} -\frac{1}{R_1 C_1} & 0 \\ \frac{1}{R_2 C_2} & -\frac{1}{R_2 C_2} - \frac{I_{L_3}^e (V_{C_1}^e - R_{01} I_{L_3}^e)}{C_2 {V_{C_2}^e}^2} \end{bmatrix}$$

and its eigenvalues can be written as:

$$\lambda_{1,2} = -\frac{a_1}{2} \pm \frac{1}{2}\sqrt{a_1^2 - 4b_1} \tag{4.39}$$

where:

$$a_1 = \frac{1}{R_1 C_1} + \frac{1}{R_2 C_2} + \frac{I_{L_3}^e}{C_2 {V_{C_2}^e}^2}(V_{C_1} - R_{01} I_{L_3}^e) \tag{4.40}$$

$$b_1 = \frac{1}{R_1 C_1}\left[\frac{1}{R_2 C_2} + \frac{I_{L_3}^e}{C_2 {V_{C_2}^e}^2}(V_{C_1} - R_{01} I_{L_3}^e)\right] \tag{4.41}$$

A stability region can then be established with respect to the values of a_1 and b_1; in the following, a dedicated analysis is introduced according to their signs:

1) For $a_1 > 0$ and $b_1 > 0$: the eigenvalues are such that $Re[\lambda_{1,2} < 0]$, and consequently the equilibrium points of the zero dynamics are stable. By considerations on the above inequalities, one can find out a region related to the value of $I_{L_3}^e$. The first region is given by $a_1 > 0$:

$$\frac{V_{C_1}}{2R_{01}} - \frac{1}{2R_{01}}\sqrt{\Delta_1} < I_{L_3}^e < \frac{V_{C_1}}{2R_{01}} + \frac{1}{2R_{01}}\sqrt{\Delta_1} \tag{4.42}$$

where:

$$\Delta_1 = {V_{C_1}}^2 + 4R_{01} C_2 {V_{C_2}^e}^2 \left[\frac{1}{R_1 C_1} + \frac{1}{R_2 C_2}\right]$$

The second region is given considering $b_1 > 0$, and it can be expressed as:

$$\frac{V_{C_1}}{2R_{01}} - \frac{1}{2R_{01}}\sqrt{\Delta_2} < I_{L_3}^e < \frac{V_{C_1}}{2R_{01}} + \frac{1}{2R_{01}}\sqrt{\Delta_2} \tag{4.43}$$

with:

$$\Delta_2 = {V_{C_1}}^2 + \frac{4R_{01}}{R_2}{V_{C_2}^e}^2$$

Since (4.43) is in (4.42), the intersection of (4.42) and (4.43) is given by (4.43), which is the region of stability for $I_{L_3}^e$.

2) For $a_1 \geq 0$ and $b_1 \leq 0$: at least one eigenvalue has a positive real part $Re[\lambda_{1,2} \geq 0]$, then the system is not stable.

3) For $a_1 \leq 0$: there is at least one eigenvalue with positive real part $Re[\lambda_{1,2} \geq 0]$ where the zero dynamics are not stable.

The introduced analysis describes the operating regions where the control of $I_{L_3} \rightarrow I_{L_3}^e$ is stable, both for the charge and the discharge of the supercapacitor, and implicitly provides some bounds for the reference $I_{L_3}^e$. In fact, it is necessary to realize that they reflect the physical limitations of the converter. So, the two zero dynamics are stable according to the aforementioned operating regions. In the following, a reasonable assumption is made to not violate the bounds and then to operate in the region of stability for the interconnected system.

4.2.6. Reference calculation

Now, the crucial step is to correctly compute the reference value $I_{L_3}^e$ used as a control input such that $V_{C_2} \rightarrow V_{C_2}^e$. It is necessary to design a slowly varying $I_{L_3}^e$, in order to respect the singular perturbation condition of being much slower than the imposed dynamic of I_{L_3}. The induced time scale separation and its singular perturbation analysis boils down to formalize cascaded control loops, given by a faster inner current loop and a slower voltage loop, broadly applied in power converter controllers, usually composed of well known linear controllers such as PI.

From singular perturbation analysis, we can consider that I_{L_3} has already reached $I_{L_3}^e$ on V_{C_2} dynamics because of time-scale separation (I_{L_3} is considered much faster than V_{C_2} depending on the choice of a sufficient large K_3 and K_3^α in (4.33)). Therefore, we may replace V_{C_2} dynamics as follows [189, 196, 200, 201].

$$\dot{V}_{C_2} = \frac{1}{R_2C_2}V_{dc} - \frac{1}{R_2C_2}V_{C_2} + \frac{1}{C_2}I_{L_3}^e(1 - u_1^*) \tag{4.44}$$

where:

$$u_1^* = 1 - \frac{1}{V_{C_2}}[V_{C_1} - R_{01}I_{L_3}^e]$$

Therefore, the result is a boundary layer model of V_{C_2} dynamics, which can be written as:

$$\dot{V}_{C_2} = \frac{1}{R_2 C_2} V_{dc} - \frac{1}{R_2 C_2} V_{C_2} + \frac{I^e_{L_3}}{C_2 V_{C_2}} [V_{C_1} - R_{01} I^e_{L_3}] \tag{4.45}$$

From this reduced model for V_{C_2}, a good choice for the new control input is $v_d = \dot{I}^e_{L_3}$, such as obtain a dynamical feedback controller. The reason for this choice is that if we chose $I^e_{L_3}$ as the control input, it would result in non-minimum phase problems again, since ${I^e_{L_3}}^2$ explicitly appears in (4.45). With $\dot{I}^e_{L_3}$ as the new control input, one has a full-state transformation with no zero dynamics, which yields a higher order system. Besides that, one can easily find the control reference $I^e_{L_3}$ by integrating the new control input $I^e_{L_3} = \int v_d dt$. The dynamical feedback control results to be a proper solution to deal with the non-minimal phase problem of power converters, allowing suitable calculation of reference current $I^e_{L_3}$ with full state transformation.

Applying input/output feedback linearization theory and defining V_{C_2} as the control output, the relative degree is 2. Consequently, one may find v_d in the second time-derivative of the simplified V_{C_2} dynamics. The following Lie derivatives can be deduced as:

$$\dot{V}_{C_2} = \mathcal{L}^1_{f_2}(V_{C_2}) \tag{4.46}$$

$$\begin{aligned} \ddot{V}_{C_2} &= \frac{\dot{V}_{dc}}{R_2 C_2} - \dot{V}_{C_2}\left[\frac{1}{R_2 C_2} + \frac{V_{C_1} I^e_{L_3} - R_{01} {I^e_{L_3}}^2}{C_2 {V_{C_2}}^2}\right] + \\ &+ \frac{1}{C_2 V_{C_2}} I^e_{L_3} \dot{V}_{C_1} + \frac{1}{C_2 V_{C_2}} (V_{C_1} - 2R_{01} I^e_{L_3}) \dot{I}^e_{L_3} \end{aligned} \tag{4.47}$$

Therefore, one have found the control input v_d as follows:

$$\ddot{V}_{C_2} = \mathcal{L}^2_{f_2}(V_{C_2}) + \mathcal{L}_{g_2}\mathcal{L}^1_{f_2}(V_{C_2}) v_d \tag{4.48}$$

By introducing a synthetic input θ_d to steer $V_{C_2} \to V^e_{C_2}$, the input v_d can be designed as:

$$v_d = \frac{1}{\mathcal{L}_{g_2}\mathcal{L}^1_{f_2}(V_{C_2})} [\theta_d - \mathcal{L}^2_{f_2}(V_{C_2})] \tag{4.49}$$

The synthetic input is chosen using linear techniques as pole placement to set new desired dynamics for V_{C_2}.

$$\theta_d = -K_2(\dot{V}_{C_2} - \dot{V}^e_{C_2}) + K^\alpha_2 (V_{C_2} - V^e_{C_2}) \tag{4.50}$$

where K_2 and K_2^α are positive gains calculated by linear techniques.

By substituting (4.49) and (4.50) in (4.45) and (4.48), the resulted closed-loop is a linear second-order system.

$$\begin{bmatrix} \dot{V}_{C_2} \\ \ddot{V}_{C_2} \end{bmatrix} = \begin{bmatrix} 0 & 1 \\ -K_2^\alpha & -K_2 \end{bmatrix} \begin{bmatrix} V_{C_2} - V_{C_2}^e \\ \dot{V}_{C_2} - \dot{V}_{C_2}^e \end{bmatrix} \tag{4.51}$$

where it is defined the speed of convergence for V_{C_2} using K_2 and K_2^α by pole placement to get slower voltage dynamics for the simplified model.

Theorem 1. *System (4.1)-(4.3) is asymptotically stable at the desired equilibrium point under utilization of the control law (4.32) and of a reference trajectory for the current given by (4.49) in (4.45). The gains K_2, K_2^α, K_3 and K_3^α in (4.51) and (4.33) have to be suitably chosen to define the proper control action.*

The overall strategy may be seen as composed in two parts: at first, the compensation of the nonlinearities takes places to enlarge the operating region, and then the steering of the resulting system to its equilibrium point by pole placement procedure, with the advantage to easily be able to chose the gains.

Remark 3. *One of the tasks is to design a slowly varying $I_{L_3}^e$ whose derivative has negligible effects on the current subsystem.*

Remark 4. *The use of singular perturbation to obtain the simplified model is valid inside an operating region that is given by the time-scale ratio from the two subsystems. As a consequence, the desired imposed dynamics should be chosen such as to obtain a suitable operation region for the DC Microgrid.*

Remark 5. *In the proposed control law, the dynamical feedback linearization approach is chosen since one gets full state transformation achieving a linear second-order system.*

4.3. Battery Subsystem

The battery is a storage device which is usually used as energy reservoir. Here, an ion-lithium battery bank is considered. Compared to other battery technologies, this kind of battery has a higher energy density, longer life cycle and absence of memory effect [8,107]. Battery storage systems can be used for many purposes, such as power quality improvements, power supply and even ancillary services provision. A proper sizing is mandatory for the battery to be able to inject or absorb the needed amount of power. In this work the battery is applied for power flow balance in long term, since the energy dispatch is given by the secondary control.

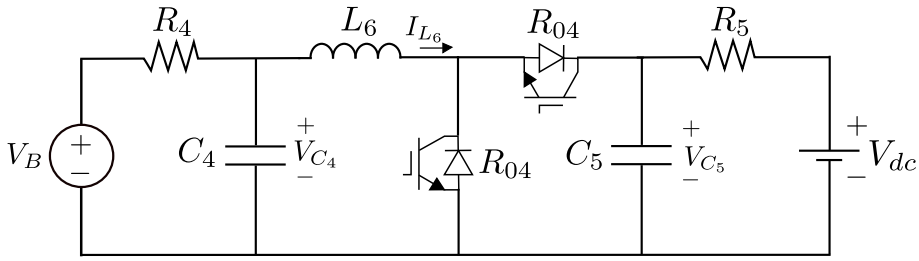

Figure 4.3: The bidirectional boost converter of the battery subsystem.

4.3.1. Battery model

A bidirectional-boost converter is also used to integrate the battery in the Microgrid as depicted in Figure 4.3. The average state-space model of the battery converter is introduced in (4.52)-(4.54), where the equations are similar to the supercapacitor subsystem in (4.1)-(4.3) because the same power converter is applied here.

$$\dot{V}_{C_4} = \frac{1}{R_4 C_4} V_B - \frac{1}{R_4 C_4} V_{C_4} - \frac{1}{C_4} I_{L_6} \tag{4.52}$$

$$\dot{V}_{C_5} = \frac{1}{R_5 C_5} V_{dc} - \frac{1}{R_5 C_5} V_{C_5} + \frac{1}{C_5} I_{L_6}(1 - u_2) \tag{4.53}$$

$$\dot{I}_{L_6} = \frac{1}{L_6} V_{C_4} - \frac{1}{L_6} V_{C_5}(1 - u_2) - \frac{R_{04}}{L_6} I_{L_6} \tag{4.54}$$

where V_B is the battery's voltage, V_{C_4} and V_{C_5} are the voltages on capacitors C_4 and C_5, respectively, and I_{L_6} is the current on the inductor L_6. R_4 and R_5 are the resistances representing the cable losses, while R_{04} and R_{05} represent the semiconductor losses plus the inductor losses, where $R_{04} = R_{05}$. u_2 is the duty cycle of the converter. Here, V_{C_4}, V_{C_5} and I_{L_6} are the state variables of the system, u_2 is the input control and V_B and V_{dc} are seen as perturbations.

The battery's duty is to provide long term stability, by balancing the energy of the whole grid. Consequently, the battery subsystem supply the power imbalance among the Microgrid's equipments, according to the power variation for each device of the Microgrid (PV, DC loads, AC grid, etc). Considering the proposed Microgrid structure, a power balance equation can be written, such that, the power reference on the battery is obtained:

$$P_B + P_{PV} + P_T + P_{DC} + P_{AC} = 0 \tag{4.55}$$

where P_B is the power supplied by the battery, P_{PV} is the generated power in the PV array, P_T is the regenerative braking power generated from train, P_{DC} is the power consumption on the DC load, P_{AC} is the demanded power by the AC grid.

Hence, the battery power reference is calculated as follows:

$$P_B^* = -P_{PV} - P_T - P_{DC} - P_{AC} \tag{4.56}$$

P_B^* is the desired amount of power to balance the energy in the Microgrid.

The battery reference is given by a secondary control, that consider the energy balance in the Microgrid, but also take into account the SoC level of the supercapacitor to maintain this device properly working. In this case, battery behave with piecewise constant variations according to second level control sampling rate to save its lifetime. This can be a complex target for secondary control, and therefore the supercapacitor can assume the target to respond in fast variation not considered for the battery.

4.3.2. Feedback linearization

Current I_{L_6} is the chosen control output for the battery's subsystem. According to the control objective, let us define the considered output as $y_2 = I_{L_6}$. It is considered that the system has one output and one input, and thus the system is shown in (4.57).

$$\begin{cases} \dot{I}_{L_6} = f_2(V_{C_4}, V_{C_5}, I_{L_6}) + g_2 u_2 \\ y_2 = I_{L_6} \end{cases} \tag{4.57}$$

The Lie derivative of the output with respect to g_2 is:

$$\mathcal{L}_{g_2}(I_{L_6}) = -\frac{V_{C_5}}{L_6}$$

Lie derivative is non-singular since V_{C_5} is always positive by technological reasons, and therefore a nonlinear feedback linearizing control input can be written as:

$$u_2 \;=\; \mathcal{L}_{g_2}(I_{L_6})^{-1}\left[v_6 - \frac{1}{L_6}\left(V_{C_4} - V_{C_5} - R_{04} I_{L_6}\right)\right] \tag{4.58}$$

Therefore:

$$u_2 = 1 + \frac{1}{V_{C_5}}\left[L_6 v_6 - V_{C_4} + R_{04} I_{L_6}\right] \tag{4.59}$$

where v_6 is the additional input defined by linear techniques, such that $I_{L_6} \to I_{L_6}^*$.

Since $I_{L_6}^*$ is the desired trajectory for I_{L_6}, it is possible to design the additional input v_6 in a linear manner with respect to the output I_{L_6} and hence a linear stable

subspace is generated.

$$v_6 = -K_6(I_{L_6} - I^*_{L_6}) - K_6^{\alpha}\alpha_6$$
$$\dot{\alpha_6} = I_{L_6} - I^*_{L_6}$$

where K_6 and K_6^{α} are positive constants, that may be chosen by poles allocation.

4.3.3. Zero dynamics analysis

The same procedure made in subsection 4.2.5 is developed here. The states V_{C_4} and V_{C_5} are the zero dynamics in the battery subsystem.

$$\dot{V}_{C_4} = \frac{1}{R_4C_4}(V_B - V_{C_4}) - \frac{1}{C_4}I^*_{L_6} \tag{4.60}$$
$$\dot{V}_{C_5} = \frac{1}{R_5C_5}(V_{dc} - V_{C_5}) + \frac{1}{C_5}\frac{I^*_{L6}}{V_{C_5}}(V^e_{C_4} - R_{04}I^*_{L_6}) \tag{4.61}$$

The calculated equilibrium points are given by:

$$V^e_{C_4} = V_B - R_4I^*_{L_6}$$

$$V^e_{C_5} = \frac{V_{dc}}{2} \pm \frac{1}{2}\sqrt{V^2_{dc} + 4R_5I^*_{L_6}(V^e_{C_4} - R_{04}I^*_{L_6})}$$

To analyze the zero dynamics local stability, the Jacobian linearization matrix $\mathcal{J}_B$ is presented bellow:

$$\mathcal{J}_B = \begin{bmatrix} -\frac{1}{R_4C_4} & 0 \\ \frac{1}{C_5}\frac{I^*_{L_6}}{V^e_{C_5}} & -\frac{1}{R_5C_5} - \frac{I^*_{L_6}(V^e_{C_4} - R_{04}I^*_{L_6})}{C_5{V^e_{C_5}}^2} \end{bmatrix}$$

The eigenvalues of λ can be written as:

$$\lambda_{1,2} = -\frac{a_2}{2} \pm \frac{1}{2}\sqrt{a_2^2 - 4b_2}$$

where:

$$a_2 = \frac{1}{R_4C_4} + \frac{1}{R_5C_5} + \frac{I^*_{L_6}}{C_5{V^e_{C_5}}^2}(V_{C_4} - R_{04}I^*_{L_6}) \tag{4.62}$$

$$b_2 = \frac{1}{R_4C_4}\left[\frac{1}{R_5C_5} + \frac{I^*_{L_6}}{C_5{V^e_{C_5}}^2}(V_{C_4} - R_{04}I^*_{L_6})\right] \tag{4.63}$$

Stability of the equilibrium points will depend on the sign of a_2 and b_2, then the following stability analysis is made.

1. For $a_2 > 0$ and $b_2 > 0$: the eigenvalues are $Re[\lambda_{1,2} < 0]$; consequently the equilibrium points of the zero dynamics are stable. Working on the above inequalities, we find out a region related to $I^*_{L_6}$. The first region is given by $a_2 > 0$:

$$\frac{V_{C_4} - \sqrt{\Delta_3}}{2R_{04}} < I^*_{L_6} < \frac{V_{C_4} + \sqrt{\Delta_3}}{2R_{04}} \tag{4.64}$$

   where:

$$\Delta_3 = {V_{C_4}}^2 + 4R_{04}C_5{V^e_{C_5}}^2\left[\frac{1}{R_4C_4} + \frac{1}{R_5C_5}\right]$$

   The second region given by $b_2 > 0$ can be expressed as:

$$\frac{V_{C_4} - \sqrt{\Delta_4}}{2R_{04}} < I^*_{L_6} < \frac{V_{C_4} + \sqrt{\Delta_4}}{2R_{04}} \tag{4.65}$$

   with:

$$\Delta_4 = {V_{C_4}}^2 + \frac{4R_{04}}{R_5}{V^e_{C_5}}^2$$

   The intersection of (4.64) and (4.65) is actually given by (4.65), which is the region of stability for $I^*_{L_6}$.
2. For $a_2 \geq 0$ and $b_2 \leq 0$: at least one eigenvalue will have a positive real part $Re[\lambda_{1,2} \geq 0]$, then the system is not stable.
3. For $a_2 \leq 0$: there is also at least one eigenvalue with positive real part $Re[\lambda_{1,2} \geq 0]$ where the zero dynamics are not stable.

The control of $I_{L_6} \rightarrow I^*_{L_6}$ is stable to charge and discharge the battery as long as the reference $I^*_{L_6}$ is designed respecting condition (4.65).

4.4. PV Array Subsystem

The PV subsystem is a renewable energy source with non-dispatchable feature. Therefore, the target here is to provide the maximum power to the system according to power generated. The PV is the main generation in the considered Microgrid, and it is obviously scaled according to the Microgrid's load. The incremental conductance algorithm is applied to track the reference for the PV array in the maximum power point. This method is one of the classical MPPT algorithms, and is characterized by fast response and simple design [150, 151]. The MPPT algorithm is chosen to be used as the reference to PV's control strategy optimizing the power generation in the Microgrid.

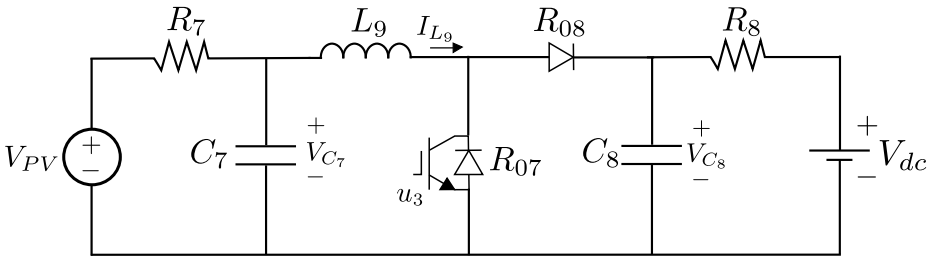

Figure 4.4: The boost converter of the PV array subsystem.

4.4.1. PV array model

Figure 4.4 depicts the converter configuration o the PV subsystem.

A boost converter connects the PV to the DC bus. The state-space model of the PV converter is presented in equations (4.66)-(4.68):

$$\dot{V}_{C_7} = \frac{1}{R_7 C_7} V_{PV} - \frac{1}{R_7 C_7} V_{C_7} - \frac{1}{C_7} I_{L_9} \tag{4.66}$$

$$\dot{V}_{C_8} = \frac{1}{R_8 C_8} V_{dc} - \frac{1}{R_8 C_8} V_{C_8} + \frac{1}{C_8} I_{L_9}(1 - u_3) \tag{4.67}$$

$$\dot{I}_{L_9} = \frac{1}{L_9} V_{C_7} - \frac{1}{L_9} V_{C_8}(1 - u_3) - \frac{R_{08}}{L_9} I_{L_9} + \frac{1}{L_9}(R_{08} - R_{07}) I_{L_9} u_3 \tag{4.68}$$

where, V_{PV} is the panel's voltage, V_{C_7} is the voltage on capacitor C_7, V_{C_8} is the voltage on capacitor C_8, while I_{L_9} is the current on the inductor L_9. R_7 and R_8 are the resistances representing the cable losses, and R_{07} and R_{08} are the semiconductor losses plus the inductor losses. u_3 is the duty cycle of the converter.

4.4.2. Feedback linearization

The secondary control contains a MPPT algorithm to track the maximum power point for different weather conditions. The higher level controller provides the current reference $I^*_{L_9}$, then according to the control objective, let us define the control output as $y_3 = I_{L_9}$. It is considered that the system has one output and one input, thus a square system is shown in (4.69).

$$\begin{cases} \dot{I}_{L_9} = f_3(V_{C_7}, V_{C_8}, I_{L_9}) + g_3 u_3 \\ y_3 = I_{L_9} \end{cases} \tag{4.69}$$

The Lie derivative of the output with respect to g_9 is:

$$\mathcal{L}_{g_3}(I_{L_9}) = -\frac{V_{C_8} - (R_{08} - R_{07}) I_{L_9}}{L_9}$$

Lie derivative is non-singular since $V_{C_8} \neq (R_{08} - R_{07}) I_{L_9}$ because of technological reasons, the voltage drop in the semiconductors are always smaller than the output

of the converter.Therefore, a nonlinear feedback control input can be written as:

$$u_3 = \mathcal{L}_{g_3}(I_{L_9})^{-1}\left[v_9 - \frac{1}{L_9}\left(V_{C_7} - V_{C_8} - R_{08}I_{L_9}\right)\right] \tag{4.70}$$

$$u_3 = \frac{L_9 v_9 - V_{C_7} + V_{C_8} + R_{08}I_{L_9}}{V_{C_8} - (R_{08} - R_{07})I_{L_9}} \tag{4.71}$$

where u_3 is the control input in (4.69) and v_9 is the additional input.

Since $I^*_{L_9}$ is the desired trajectory for I_{L_3}, it is possible to design the additional input v_9 in a linear manner with respect to the output I_{L_9} and hence a linear stable subspace is generated.

$$v_9 = -K_9(I_{L_9} - I^*_{L_9}) - K^{\alpha}_9\alpha_9 \tag{4.72}$$

$$\dot{\alpha}_9 = I_{L_9} - I^*_{L_9} \tag{4.73}$$

where K_9 and K^{α}_9 are positive constants.

4.4.3. Zero dynamics analysis

The states V_{C_7} and V_{C_8} are the zero dynamics in the PV system. The calculated equilibrium points are given by:

$$V^e_{C_7} = V_{PV} - R_7 I^*_{L_9} \tag{4.74}$$

$$V^e_{C_8} = \frac{V_{dc}}{2} \pm \frac{1}{2}\sqrt{V^2_{dc} + 4R_7 I^*_{L_9}(V_{C_7} - R_{07}I^*_{L_9})} \tag{4.75}$$

To analyze the zero dynamics local stability, the Jacobian linearization matrix $\mathcal{J}_C$ is presented:

$$\mathcal{J}_C = \begin{bmatrix} -\frac{1}{R_7C_7} & 0 \\ \frac{-I^*_{L_9}}{V^e_{C_8}-(R_{08}-R_{07})I^*_{L_9}} & -\frac{1}{R_8C_8} - \frac{I^*_{L_9}[V_{C_7}-(2R_{08}-R_{07})I^*_{L_9}]}{C_8[V^e_{C_8}-(R_{08}-R_{07})I^*_{L_9}]^2} \end{bmatrix}$$

In this case, one has that $I_{L_9} \geq 0$ is always positive, as a consequence $V_{PV} \geq V_{C_7}$. Therefore, there are only two possible cases in the matrix C parameters:

1. For $V_{C_7} - (2R_{08} - R_{07})I^*_{L_9} > 0$, the eigenvalues of matrix C is always negative, then the zero dynamics is locally stable.
2. For $V_{C_7} - (2R_{08} - R_{07})I^*_{L_9} < 0$: this condition is not physically possible, therefore this case is not considered in the stability analysis.

4.5. DC Load Subsystem

The DC load is represented mostly by electronic devices, that have a DC nature. Therefore, to avoid energy conversion, these kind of loads can be directly supplied in DC voltage. The general DC load in the Microgrid represents lights, ventilation, heating and electrical vehicles, as an aggregation of the power demand in the smart train station. The load shift power according to the required demand [202], where voltage deviation is not allowed to exceed the grid limits.

The DC load connected via a DC/DC converter is an adequate representation for modern DC distribution systems, since it represents a significant portion of the total load in DC networks [113]. The main load requirement is to maintain its voltage inside of the grid requirements (normally ±5%).

4.5.1. DC load model

The load converter is a buck one as depicted in Figure 4.5. The state-space model is introduced in (4.76)-(4.78):

$$\dot{V}_{C_{11}} = \frac{1}{R_{11}C_{11}}V_L - \frac{1}{R_{11}C_{11}}V_{C_{11}} + \frac{1}{C_{11}}I_{L_{13}} \tag{4.76}$$

$$\dot{V}_{C_{12}} = \frac{1}{R_{12}C_{12}}(V_{dc} - V_{C_{12}}) - \frac{1}{C_{12}}I_{L_{13}}u_4 \tag{4.77}$$

$$\dot{I}_{L_{13}} = -\frac{1}{L_{13}}V_{C_{11}} - \frac{R_{011}}{L_{13}}I_{L_{13}} + \frac{1}{L_{13}}\left[V_{C_{12}} - (R_{012} - R_{011})I_{L_{13}}\right]u_4 \tag{4.78}$$

where V_L is the load voltage, $V_{C_{11}}$ and $V_{C_{12}}$ are the voltages on capacitor C_{11} and C_{12}, respectively, and $I_{L_{13}}$ is the current on the inductor L_{13}. R_{11} and R_{12} are the resistances representing the cable losses, and R_{011} and R_{012} are the semiconductor losses plus the inductor losses. u_4 is the duty cycle of the converter. $V_{C_{11}}$, $V_{C_{12}}$ and $I_{L_{13}}$ are the state variables, u_4 is the control input and V_L and V_{dc} are seen as perturbations.

The load is represented on the Microgrid model as a variable current source I_L with a fixed resistance in parallel R_L, where variations in the current source represent the load demand variations, and are related to the load voltage as follows:

$$I_L = \frac{V_L}{R_L} + \frac{V_L - V_{C_{11}}}{R_{11}} \tag{4.79}$$

The current I_L is unknown, because V_L is the only measured variable from the load point of view. So, V_L is measured on the PCC of the DC load system. Therefore, the DC load control strategy is to control the voltage $V_{C_{11}}$ on the DC/DC converter, such that, the voltage on V_L is inside of the grid limits, since the cable losses (R_{11}) create voltage drop on V_L, which may overcome the grid limits.

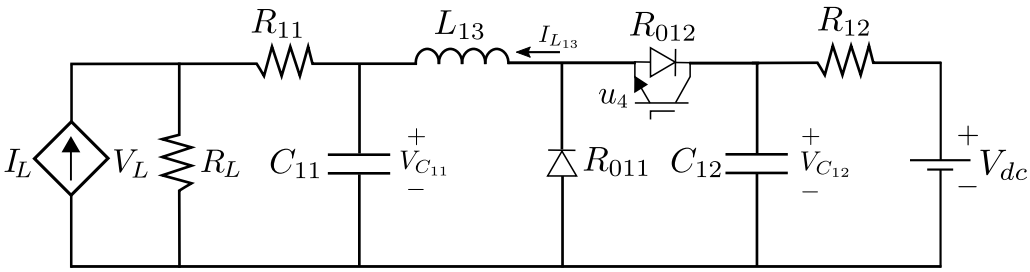

Figure 4.5: The buck converter of the DC load subsystem.

4.5.2. Backstepping control

The target in DC load subsystem is to provide constant voltage supply, even if there are power variations. The DC load reference is given by $V^*_{C_{11}}$, which is the desired value for V_L, since V_L is not directly controlled in this system. Here, one has the output control given by $y_4 = V_{C_{11}}$, then there is a square system where relative degree is 2. The DC load model can be represented as follows:

$$\begin{cases} \dot{V}_{C_{11}} = f_{11}(V_L, V_{C_{11}}) + g_{11} I_{L_{13}} \\ \dot{I}_{L_{13}} = f_{13}(V_{C_{11}}, V_{C_{12}}, V_{dc}) + g_{13}(V_{C_{12}}, I_{L_{13}}) u_4 \\ y_4 = V_{C_{11}} \end{cases} \tag{4.80}$$

In this case, the backstepping control strategy have straight forward application according to the system model as can be seen in (4.80), the control input is applied for $I_{L_{13}}$, which is used to control $V_{C_{11}}$. This control scheme is the usual approach, since the control input (u_4) appears in $I_{L_{13}}$ dynamics and and reference trajectory $I^*_{L_{13}}$ is computed to control voltage $V_{C_{11}}$. It is provided the desired linear dynamics for the output control $V_{C_{11}}$ called as the additional input v_{11}:

$$v_{11} = -K_{11}(V_{C_{11}} - V^*_{C_{11}}) - K^{\alpha}_{11}\alpha_{11} \tag{4.81}$$

$$\dot{\alpha}_{11} = V_{C_{11}} - V^*_{C_{11}} \tag{4.82}$$

where K_{11} and K^{α}_{11} are positive constants and α_{11} an auxiliary variable representing an integral term.

It is needed to find a reference trajectory for $I_{L_{13}}$, such that, one can obtain the desired dynamics for $V_{C_{11}}$ as presented in (4.81). By feedback linearization in equation (4.76), results:

$$I^e_{L_{13}} = \frac{1}{R_{11}}(V_{C_{11}} - V_L) - C_{11}\big[K_{11}(V_{C_{11}} - V^*_{C_{11}}) + K^{\alpha}_{11}\alpha_{11}\big] \tag{4.83}$$

With a desired trajectory $I^e_{L_{13}}$ designed to stabilize $V_{C_{11}}$ in $V^*_{C_{11}}$, a linear stable subspace is generated. As next step, $I^e_{L_{13}}$ is assigned as the feedback control law

ensuring closed-loop stability around the reference $V^*_{C_{11}}$: furthermore, as before, there is also a desired dynamic behaviour to impose:

$$v_{13} = -K_{13}(I_{L_{13}} - I^e_{L_{13}}) - K^\alpha_{13}\alpha_{13} \tag{4.84}$$

$$\dot{\alpha}_{13} = I_{L_{13}} - I^e_{L_{13}} \tag{4.85}$$

where K_{13} and K^α_{13} are positive constants and α_{13} an auxiliary variable representing an integral term. To select a proper control input, one can consider the following Lyapunov candidate:

$$W_{11,13} = \frac{1}{2}\left(V_{C_{11}} - V^*_{C_{11}}\right)^2 + \frac{K^\alpha_{11}}{2}\alpha^2_{11} + \frac{1}{2}\left(I_{L_{13}} - I^e_{L_{13}}\right)^2 + \frac{K^\alpha_{13}}{2}\alpha^2_{13} > 0 \tag{4.86}$$

Therefore, the Lyapunov derivative can be developed as follows:

$$\dot{W}_{11,13} = \left(V_{C_{11}} - V^*_{C_{11}}\right) v_{11} + K^\alpha_{11}\dot{\alpha}_{11} + \left(I_{L_{13}} - I^e_{L_{13}}\right)\left(\dot{I}_{L_{13}} - \dot{I}^e_{L_{13}}\right) + K^\alpha_{13}\dot{\alpha}_{13} \tag{4.87}$$

$$\begin{aligned}\dot{W}_{11,13} = &\left(V_{C_{11}} - V^*_{C_{11}}\right)\left[-K_{11}(V_{C_{11}} - V^*_{C_{11}}) - K^\alpha_{11}\alpha_{11}\right] + K^\alpha_{11}(V_{C_{11}} - V^*_{C_{11}}) + \\ &+ \left(I_{L_{13}} - I^e_{L_{13}}\right)\left[-\tfrac{1}{L_{13}}V_{C_{11}} - \tfrac{R_{011}}{L_{13}}I_{L_{13}} + \tfrac{1}{L_{13}}\left[V_{C_{12}} - (R_{012} - R_{011})I_{L_{13}}\right]u_4\right] + \\ &- \left(I_{L_{13}} - I^e_{L_{13}}\right)\dot{I}^e_{L_{13}} + K^\alpha_{13}(I_{L_{13}} - I^e_{L_{13}})\end{aligned} \tag{4.88}$$

The time derivative of $I^e_{L_{13}}$ is calculated in order to solve equation (4.87):

$$\dot{I}^e_{L_{13}} = \left[\frac{1}{R_{11}} - C_{11}K_{11}\right] v_{11} - C_{11}K^\alpha_{11}(V_{C_{11}} - V^*_{C_{11}}) \tag{4.89}$$

The derivative of the Lyapunov function is then used to obtain the proper control input, imposing the desired result for $\dot{W}_{11,13}$ as written next:

$$\dot{W}_{11,13} = -K_{11}\left(V_{C_{11}} - V^*_{C_{11}}\right)^2 - K_{13}(I_{L_{13}} - I^e_{L_{13}})^2 \leq 0 \tag{4.90}$$

by applying Barbalat's lemma it is possible to establish that $\dot{W}_{11,13} \to 0$ as $t \to \infty$: ergo $(V_{C_{11}} - V^*_{C_{11}}) \to 0$, $(I_{L_{13}} - I^*_{L_{13}}) \to 0$, and by signal chasing, that $\alpha_{11} \to 0$ and $\alpha_{13} \to 0$ [188].

Therefore, the proper control input u_4 is calculated such that equation (4.90) is satisfied and asymptotic stability is assured. The control input u_4 is written as:

$$u_4 = \frac{L_{13}v_4 + V_{C_{11}} + R_{011}I_{L_{13}}}{V_{C_{12}} - (R_{012} - R_{011})I_{L_{13}}} \tag{4.91}$$

where:

$$v_4 = v_{13} + \left(\frac{1}{R_{11}} - C_{11}K_{11}\right)v_{11} - C_{11}K^\alpha_{11}(V_{C_{11}} - V^*_{C_{11}}) \tag{4.92}$$

4.5.3. Zero dynamics analysis

The state $V_{C_{12}}$ is the zero dynamics here, where the local stability analysis is given.

$$\dot{V}_{C_{12}} = \frac{1}{R_{12}C_{12}}V_{dc} - \frac{1}{R_{12}C_{12}}V_{C_{12}} - \frac{1}{C_{12}}I^e_{L_{13}}u^*_4 \tag{4.93}$$

where $I^e_{L_{13}} = \frac{1}{R_{11}}(V^*_{C_{11}} - V_L)$ and:

$$u^*_4 = \frac{V^*_{C_{11}} + R_{011}I^e_{L_{13}}}{V_{C_{12}} - (R_{012} - R_{011})I^e_{L_{13}}} \tag{4.94}$$

To analyze the dynamics above, let us consider its linearization. The needed equilibrium points can be determined as follows:

$$V^e_{C_{12}} = \frac{-a_{12}}{2} \pm \frac{1}{2}\sqrt{a^2_{12} + 4\Delta_{12}} \tag{4.95}$$

where:

$$a_{12} = V_{dc} - (R_{012} - R_{011})I^e_{L_{13}}$$

$$\Delta_{12} = I^e_{L_{13}}\left[(R_{012} - R_{011})V_{dc} + R_{12}(V_{C_{11}} + R_{011}I^e_{L_{13}})\right]$$

The linearization of the $V_{C_{12}}$ dynamical equation is obtained with the eigenvalue of the linearized zero dynamics in (4.96).

$$\mathcal{J}_{12} = -\frac{1}{R_{12}C_{12}} + \frac{I^e_{L_{13}}}{C_{12}}\left[\frac{V^*_{C_{11}} + R_{011}I^e_{L_{13}}}{[V^e_{C_{12}} - (R_{012} - R_{011})I^e_{L_{13}}]^2}\right] \tag{4.96}$$

In the DC load case, we have that current is always positive: $I^e_{L_{13}} \geq 0$ (sense adopted in modelling from Figure 4.1). As a consequence we can also state that $V_L \leq V_{C_{11}}$ always. Given this physical considerations, let us now take into account all possible cases for the stability analysis:

1. When $V^*_{C_{11}} + R_{011}I^e_{L_{13}} < 0$, we may result in:

$$V_L > \frac{R_{11} + R_{011}}{R_{011}}V^*_{C_{11}} \qquad \therefore \qquad V_L > V_{C_{11}} \tag{4.97}$$

   which is not physically possible because $V_L \leq V_{C_{11}}$, then this case is not considered.

2. When $V^*_{C_{11}} + R_{011} I^e_{L_{13}} > 0$, we may result in:

$$V_L < \frac{R_{11} + R_{011}}{R_{011}} V^*_{C_{11}} \qquad \therefore \qquad V_L < V_{C_{11}} \tag{4.98}$$

Which is feasible, then following inequality is required to obtain local stability:

$$-\frac{1}{R_{12}C_{12}} + \frac{I^e_{L_{13}}}{C_{12}} \left[\frac{V^*_{C_{11}} + R_{011} I^e_{L_{13}}}{[V_{C_{12}} - (R_{012} - R_{011}) I^e_{L_{13}}]^2} \right] < 0 \tag{4.99}$$

Considering inequality (4.99), it is possible to find the region of stability for $I^e_{L_{13}}$, where eigenvalue of the linearized zero dynamics is negative assuring local stability for zero dynamics.

4.6. Regenerative Braking Subsystem

A train line can recover energy through regenerative braking when the train motor occasionally becomes a generator by producing a counter-torque in the electrical motor [11]. The braking energy recovery system is a renewable energy source, and the perturbation it introduces is different with respect to the usually considered ones. Indeed, it introduces a high level of current in a short time period [14–16] in a predictable way. However, this intermittent high power peak can cause instability in a Microgrid context; to avoid it, the supercapacitor has the duty to absorb the transient peak of energy [173–176]. As a consequence, the system is able to keep save operation and battery is less stressed.

A voltage source V_T models the train DC bus[3]; when the regenerative braking takes place, the voltage of the train line in the Parisian metro system have increment of 25% of the nominal value [14]. A buck converter is exclusively dedicated to the energy recovery, connecting the train line to the DC Microgrid. The demanded power of the train is fed by one or more others converters and they are independent: train's power supply is not included in the regenerative braking system, only the generated energy from braking is then absorbed. This system recovers the braking energy instead of wasting it, and also helps the train's grid to keep its voltage inside desired operational margins. The target of the converter is to keep its voltage to the constant value of the train line, resulting in a very high power injection in a few seconds when the regenerative energy is recovered.

[3]Voltage V_T represents the measured voltage on the train's coupling point

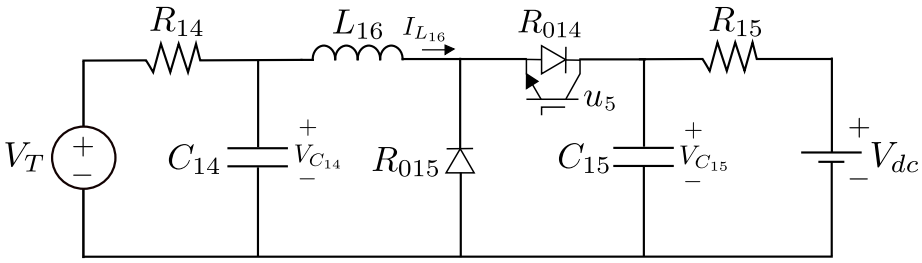

Figure 4.6: The buck converter of the train (regenerative braking) subsystem.

4.6.1. Regenerative braking model

Figure 4.6 represents the energy recovery subsystem. The state-space model of the regenerative energy subsystem including the buck converter is presented in (4.100)-(4.102):

$$\dot{V}_{C_{14}} = \frac{1}{R_{14}C_{14}}V_T - \frac{1}{R_{14}C_{14}}V_{C_{14}} - \frac{I_{L_{16}}}{C_{14}}u_5 \tag{4.100}$$

$$\dot{V}_{C_{15}} = \frac{1}{R_{15}C_{15}}V_{dc} - \frac{1}{R_{15}C_{15}}V_{C_{15}} + \frac{1}{C_{15}}I_{L_{16}} \tag{4.101}$$

$$\dot{I}_{L_{16}} = \frac{1}{L_{16}}V_{C_{14}}u_5 - \frac{1}{L_{16}}V_{C_{15}} - \frac{R_{014}}{L_{16}}I_{L_{16}} \tag{4.102}$$

here, V_T is the train's line voltage source, $V_{C_{14}}$ is the voltage on capacitor C_{14}, $V_{C_{15}}$ is the voltage on capacitor C_{15}, and $I_{L_{16}}$ is the current on inductor L_{16}. R_{14} and R_{15} are the resistances representing the cable losses, and R_{014} and R_{015} are the semiconductor losses plus the inductor losses. Here, the following consideration is made: $R_{014} = R_{015}$. u_5 is the duty cycle of the converter. $V_{C_{14}}$, $V_{C_{15}}$ and $I_{L_{16}}$ are the state variables, u_5 is the control input and V_T and V_{dc} are seen as perturbations.

The control target in the regenerative braking system is to regulate the voltage $V_{C_{14}}$ in a constant reference $V^*_{C_{14}}$, such that, it is possible to inject the power generated by the train braking due to the different voltage created between V_T and $V_{C_{14}}$. In this way, the generated current in the train can flow to the DC bus (which can be absorbed by the supercapacitor when needed). The straight forward control application for this subsystem is to define $V_{C_{14}}$ as the control control output and then the control input is calculated as follows:

$$u_5 = \frac{1}{I_{L_{16}}}\left[C_{14}v_{14} - \frac{1}{R_{14}(V_T - V_{C_{14}})}\right] \tag{4.103}$$

where v_4 is a additional control input to steer $V_{C_{14}} \to V^*_{C_{14}}$ by using linear techniques.

But, the control input calculated in (4.103) may result in a singularity when $I_{L_{16}}$ is zero, and there is also a non-minimum phase problem with unstable zero

dynamics[4]. The buck converter has non-minimum phase feature when the input voltage converter is chosen as the control output.

Therefore, singular perturbation analysis applied to design a control induced time-scale separation, considering $I_{L_{16}}$ as the output of the subsystem (4.100)-(4.102), and the two voltages are the zero dynamics. Subsequently, the system is divided into two lower order interconnected subsystems with different dynamics. Since the control target is to track a constant reference for $V_{C_{14}}$, similar considerations for the case of the supercapacitor subsystem are done, and dynamic feedback linearization is used [117, 118].

4.6.2. Regenerative braking control application

According to the control objective, it is defined the output as $y_5 = I_{L_{16}}$. It is considered that the system has one output and one input, thus the system can be represented as follows:

$$\begin{cases} \dot{I}_{L_{16}} = f_{16}(V_{C_{14}}, V_{C_{15}}, I_{L_{16}}) + g_{16}u_5 \\ y_5 = I_{L_{16}} \end{cases} \tag{4.104}$$

Let $\mathcal{L}_{g_{16}}(I_{L_{16}})$ be a 1×1 matrix where the Lie derivative of the output with respect to g_{16} is:

$$\mathcal{L}_{g_{16}}(I_{L_{16}}) = -\frac{V_{C_{15}}}{L_{16}}$$

with $\mathcal{L}_{g_{16}}(I_{L_{16}})$ being non-singular since $V_{C_{15}}$ is always positive by technological reasons, therefore, a nonlinear feedback control input can be calculated as follows:

$$u_5 = \frac{1}{V_{C_{14}}}\left[L_{16}v_{16} + V_{C_{15}} + R_{015}I_{L_{16}}\right] \tag{4.105}$$

where v_{16} is the additional input to be designed.

The additional input v_{16} can be designed in a linear manner with respect to the output $I_{L_{16}}$ and hence a linear stable subspace is generated.

$$v_{16} = -K_{16}(I_{L_{16}} - I^e_{L_{16}}) - K^{\alpha}_{16}\alpha_{16} \tag{4.106}$$

$$\dot{\alpha_{16}} = I_{L_{16}} - I^e_{L_{16}} \tag{4.107}$$

where K_{16} and K^{α}_{16} are positive constants calculated by pole allocation and α_{16} an auxiliary variable.

[4]Similar analysis as presented for the supercapacitor subsystem in subsection 4.2.2

4.6.3. Zero dynamics analysis

The states $V_{C_{14}}$ and $V_{C_{15}}$ presented in (4.100)-(4.102) are the zero dynamics in the system, where a stability study is presented for these dynamics.

$$\dot{V}_{C_{14}} = \frac{1}{R_{14}C_{14}}(V_T - V_{C_{14}}) - \frac{I^*_{L_{16}}}{C_{14}V_{C_{14}}}(V_{C_{14}} + R_{015}I^*_{L_{16}}) \tag{4.108}$$

$$\dot{V}_{C_{15}} = \frac{1}{R_{15}C_{15}}(V_{dc} - V_{C_{15}}) + \frac{1}{C_{15}}I^*_{L_{16}} \tag{4.109}$$

The calculated equilibrium points are given by:

$$V^e_{C_{14}} = \frac{V_T}{2} \pm \frac{1}{2}\sqrt{V_T^2 - 4R_{14}I^e_{L_{16}}(V^*_{C_{15}} + R_{05}I^e_{L_{16}})} \tag{4.110}$$

$$V^e_{C_{15}} = V_{dc} + R_{15}I^e_{L_{16}} \tag{4.111}$$

The stability analysis is made by linearization procedure, where the local stability of the zero dynamics is investigated. The matrix $\mathcal{J}_D$ is the Jacobian linearization matrix:

$$\mathcal{J}_D = \begin{bmatrix} -\frac{1}{R_{14}C_{14}} + \frac{I^e_{L_{16}}(V_{C_{15}}+R_{015}I^e_{L_{16}})}{C_{14}{V^e_{C_{14}}}^2} & -\frac{1}{C_{14}}\frac{I^e_{L_{16}}}{V_{C_{14}}} \\ 0 & -\frac{1}{R_{15}C_{15}} \end{bmatrix}$$

The eigenvalues of λ from matrix D can be written as:

$$\lambda_{1,2} = -\frac{a_3}{2} \pm \frac{1}{2}\sqrt{a_3^2 - 4b_3} \tag{4.112}$$

where:

$$a_3 = \frac{1}{R_{15}C_{15}} + \frac{1}{R_{14}C_{14}} - \frac{I^e_{L_{16}}}{C_{14}{V^e_{C_{14}}}^2}(V_{C_{15}} + R_{015}I^e_{L_{16}}) \tag{4.113}$$

$$b_3 = \frac{1}{R_{15}C_{15}}\left[\frac{1}{R_{14}C_{14}} - \frac{I^e_{L_{16}}}{C_{14}{V^e_{C_{14}}}^2}(V_{C_{15}} + R_{015}I^e_{L_{16}})\right] \tag{4.114}$$

In this case, current $I_{L_{16}}$ is always positive ($I_{L_{16}} \geq 0$), because the regenerative braking subsystem only injects energy into the Microgrid. Local stability can be determined when the eigenvalues are negative. Therefore, to assure local stability is assured when the following condition is satisfied:

$$\frac{1}{R_{14}C_{14}} - \frac{I^e_{L_{16}}}{C_{14}{V^e_{C_{14}}}^2}(V_{C_{15}} + R_{015}I^e_{L_{16}}) > 0 \tag{4.115}$$

From 4.115, the region of stability for current $I^*_{L_{16}}$ can be determined as follows:

$$-\frac{V_{C_{15}}}{2R_{015}} - \frac{\sqrt{\Delta_5}}{2R_{015}} < I^e_{L_{16}} < -\frac{V_{C_{15}}}{2R_{015}} + \frac{\sqrt{\Delta_5}}{2R_{015}} \tag{4.116}$$

where:

$$\Delta_5 = {V_{C_{15}}}^2 + 4\frac{R_{015}}{R_{14}}{V_{C_{14}}^e}^2$$

In conclusion, local stability for zero dynamics is assured when equations (4.116) is satisfied.

4.6.4. Reference calculation

The next procedure is to create the reference value $I_{L_{16}}^e$, which must be deduced from the desired $V_{C_{14}}^*$. Following the theory presented in [125], it is designed the controller such that $I_{L_{16}}$ quickly converges to $I_{L_{16}}^e$ and the dynamics of $V_{C_{14}}$ can be replaced thanks to singular perturbation as by a simplified model considering the convergence of $I_{L_{16}}$:

$$\dot{V}_{C_{14}} = \frac{1}{R_{14}C_{14}}V_T - \frac{1}{R_{14}C_{14}}V_{C_{14}} - \frac{1}{C_{14}}I_{L_{16}}^e u_5^* \tag{4.117}$$

where:

$$u_5^* = \frac{1}{V_{C_{14}}}[V_{C_{15}} + R_{015}I_{L_{16}}^e] \tag{4.118}$$

One would like to develop a control strategy for $I_{L_{16}}^e$ such that $V_{C_{14}}$ is stabilized at $V_{C_{14}}^*$. With the above conditions and since $(I_{L_{14}}^*)^2$ explicitly appears in (4.119), one may apply the dynamical feedback strategy, choosing $\dot{I}_{16}^e$ as the control input. Therefore, it is added an integrator in $I_{L_{16}}^e$ which yields a higher order system, resulting in full-state transformation with no zero dynamics:

$$\begin{cases} \dot{V}_{C_{14}} = \dfrac{1}{R_{14}C_{14}}(V_T - V_{C_{14}}) - \dfrac{I_{L_{16}}^e[V_{C_{15}} + R_{015}I_{L_{16}}^e]}{C_{14}V_{C_{14}}} \\ \dot{I}_{L_{16}}^* = v_t \end{cases} \tag{4.119}$$

The system above has the standard form (4.120), where v_t is the input control.

$$\begin{cases} \dot{V}_{C_{14}} = f_{14}(V_{C_{14}}, V_{C_{15}}, I_{L_{16}}) + g_{14}v_t \\ h_{14}(x) = V_{C_{14}} \end{cases} \tag{4.120}$$

Defining $V_{C_{14}}$ as the output, the relative degree is 2, consequently there are no remaining dynamics in this part. The following Lie derivatives can be deduced as:

$$\dot{V}_{C_{14}} = \mathcal{L}_{f_{14}}^1(V_{C_{14}}) \tag{4.121}$$

$$\ddot{V}_{C_{14}} = \left[-\frac{1}{R_{14}C_{14}} + \frac{V_{C_{15}}I^e_{L_{16}} + R_{015}{I^e_{L_{16}}}^2}{C_{14}{V_{C_{14}}}^2} \right] \dot{V}_{C_{14}} - \frac{1}{C_{14}V_{C_{14}}} I^e_{L_{16}} \dot{V}_{C_{15}} - \frac{1}{C_{14}V_{C_{14}}} (V_{C_{15}} + 2R_{015}I^e_{L_{16}}) \dot{I}^*_{L_{16}} \tag{4.122}$$

$$\ddot{V}_{C_{14}} = \mathcal{L}^2_{f_{14}} h_{14}(x) + \mathcal{L}_{g_{14}} L^1_{f_{14}}(V_{C_{14}}) v_t \tag{4.123}$$

By introducing a synthetic input θ_t, the input v_t can be designed as:

$$v_t = \frac{1}{\mathcal{L}_{g_{14}} \mathcal{L}^1_{f_{14}}(V_{C_{14}})} [\theta_t - \mathcal{L}^2_{f_{14}}(V_{C_{14}})] \tag{4.124}$$

where the synthetic input is chosen using linear techniques to give the desired dynamics for $V_{C_{14}}$.

$$\theta_t = -K_{14}(\dot{V}_{C_{14}} - \dot{V}^*_{C_{14}}) + K^\alpha_{14}(V_{C_{14}} - V^*_{C_{14}}) \tag{4.125}$$

The speed response of the voltage is defined by using the positive gains K_{14} and K^α_{14} by pole placement and $I^e_{L_{16}}$ can be easily determined by integrating the input $\int v_t dt = I^e_{L_{16}}$.

4.7. AC Grid-Connection

A connection with a main AC grid is included in the considered Microgrid, with the possibility to supply active and reactive power according with the grid demand. From the Microgrid point of view, it results as to supply an AC load, ensuring power supply to the main network. The AC grid connection is done through a three-phase AC bus connected with a VSC converter with output L-filter. In this case, the AC grid is considered as an infinite bus, where voltage and frequency are not controlled by the Microgrid, and the power variations are supported by the main grid. Next chapters will present a weak grid case[5], where frequency and voltage are taken into account for stability purposes.

4.7.1. AC grid model

The AC grid subsystem is depicted in Figure 4.7. The equations (4.126)-(4.128) represent the state-space model of the VSC interconnecting the Microgrid with the

[5]A weak grid can be composed of isolated system with low inertia properties.

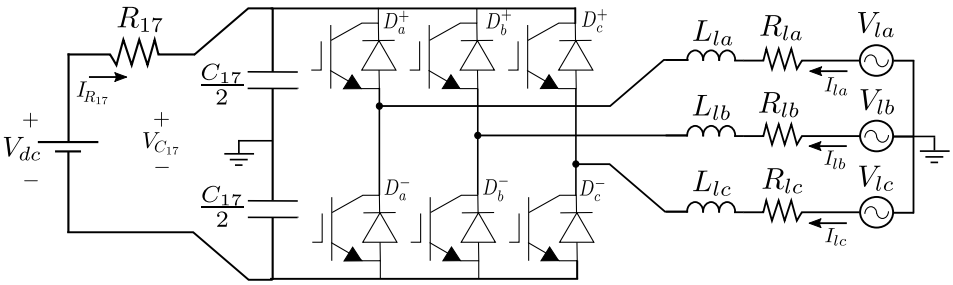

Figure 4.7: Voltage Source Converter (VSC) to AC grid-connection.

main grid:

$$\dot{I}_{ld} = -\frac{R_l}{L_l} I_{ld} + \omega_g I_{lq} + \frac{1}{2L_l} V_{C_{17}} u_6 - \frac{V_{ld}}{L_l} \tag{4.126}$$

$$\dot{I}_{lq} = -\frac{R_l}{L_l} I_{lq} - \omega_g I_{ld} + \frac{1}{2L_l} V_{C_{17}} u_7 - \frac{V_{lq}}{L_l} \tag{4.127}$$

$$\dot{V}_{C_{17}} = \frac{1}{R_{17} C_{17}} (V_{dc} - V_{C_{17}}) - \frac{3}{2C_{17} V_{C_{17}}} (I_{ld} V_{ld} + I_{lq} V_{lq}) \tag{4.128}$$

I_{ld} and I_{lq} are the direct and quadratic currents in the AC line, respectively, and V_{ld} and V_{lq} are the related direct and quadratic voltages on the AC grid using Park's transformation [203]. $V_{C_{17}}$ is the voltage on capacitor C_7, and R_{17} is the cable losses in the VSC and ω_g is the grid frequency. The modulation index u_6 and u_7 are the control inputs: they are bounded by $\sqrt{u_6^2 + u_7^2} \leq 1$. In this case, I_{ld}, I_{lq} and $V_{C_{17}}$ are the state variables, ω_g and V_{dc} are seen as perturbations.

In the following, I_{ld} and I_{lq} will be the outputs of the subsystems, and $V_{C_{17}}$ the zero dynamics. Feedback linearization is used to meet the control target, i.e., to let the outputs reach two decoupled current references I_{ld}^* and I_{lq}^*. They are obtained by given power references P_l^* and Q_l^*, as in [125].

The synchronous dq reference frame is chosen such that the d-axis is fixed to the AC side of the grid, i.e., $V_{ld} = \hat{V}_l$, which is the voltage amplitude and $V_{lq} = 0$, then decoupled control on P_l and Q_l can be realized [125].

$$P_l = \frac{3}{2} V_{ld} I_{ld} \tag{4.129}$$

$$Q_l = -\frac{3}{2} V_{ld} I_{lq} \tag{4.130}$$

According to (4.129) and (4.130) it is possible to control P_l and Q_l controlling I_{ld} and I_{lq} in the desired value. Therefore, one has the control objective explicit in (4.132) and (4.132).

$$I_{ld}^* = \frac{2}{3} \frac{P_l^*}{V_{ld}} \tag{4.131}$$

$$I_{lq}^* = \frac{2}{3} \frac{Q_l^*}{V_{ld}} \tag{4.132}$$

4.7.2. Feedback linearization

According to the control objective, it is defined the control outputs as $y_d = I_{ld}$ and $y_q = I_{lq}$. It is considered that the system has two outputs and two inputs, thus a square system is shown in (4.133).

$$\begin{cases} \dot{I}_{ld,q} = f_{ld,q}(I_{ld,q}, V_{ld,q}, V_{C_{17}}) + g_{ld,q}u_{6,7} \\ y_{d,q} = I_{ld,q} \end{cases} \tag{4.133}$$

Let the Lie derivatives $L_{g_{ld,q}}(I_{ld}, I_{lq})$ be a 2×2 matrix where the Lie derivative of the output with respect to $g_{ld,q}$ is:

$$\mathcal{L}_{g_{ld,q}}(I_{ld}, I_{lq}) = \frac{V_{C_{17}}}{2L_l}$$

The Lie derivatives are non-singular since $V_{C_{17}}$ is always positive, therefore, a nonlinear feedback control input can be written as:

$$u_6 = \frac{2}{V_{C_{17}}}\left[L_l v_{i_d} + R_l I_{ld} - \omega_g L_l I_{lq} + V_{ld}\right], \tag{4.134}$$

$$u_7 = \frac{2}{V_{C_{17}}}\left[L_l v_{i_q} + R_l I_{lq} + \omega_g L_l I_{ld} + V_{lq}\right], \tag{4.135}$$

where $u_{6,7}$ are the control input in (4.133) and v_{i_d,i_q} are the additional inputs.

Since $I^*_{ld,q}$ is the desired trajectory for $I_{ld,q}$, it is possible to design the additional input v_{i_d,i_q} in a linear manner with respect to the output $I_{ld,q}$ and hence a linear stable subspace is generated.

$$v_{i_d,i_q} = -K_{d,q}(I_{ld,q} - I^*_{ld,q}) - K^{\alpha}_{d,q}\alpha_{dq} \tag{4.136}$$

$$\dot{\alpha_{dq}} = I_{ld,q} - I^*_{ld,q} \tag{4.137}$$

where $K_{d,q}$ and $K^{\alpha}_{d,q}$ are positive constants calculated by pole allocation.

4.7.3. Zero dynamics analysis

The state $V_{C_{17}}$ is the zero dynamic in the VSC system.

$$\dot{V}_{C_{17}} = \frac{1}{R_{17}C_{17}}(V_{dc} - V^e_{C_{17}}) - \frac{3}{2C_{17}V^e_{C_{17}}}(I^*_{ld}V_{ld} + I^*_{lq}V_{lq}) \tag{4.138}$$

where:

$$u^*_6 = \frac{2}{V_{C_{17}}}\left[R_l I^*_{ld} - \omega_g L_l I^*_{lq} + V_{ld}\right] \tag{4.139}$$

$$u^*_7 = \frac{2}{V_{C_{17}}}\left[R_l I^*_{lq} + \omega_g L_l I^*_{ld} + V_{lq}\right] \tag{4.140}$$

The calculated equilibrium point is given by:

$$V_{C_{17}}^{e} = \frac{V_{dc}}{2} \pm \frac{1}{2}\sqrt{V_{dc}^{2} + 6R_{17}[V_{ld}I_{ld}^{*} + V_{lq}I_{lq}^{*}]} \tag{4.141}$$

The linearization of $V_{C_{17}}$ dynamic state is obtained by calculating the eigenvalue of the lineraized zero dynamics in (4.142).

$$\mathcal{J}_{17} = -\frac{1}{R_{17}C_{17}} + \frac{3}{2C_{17}}\frac{1}{{V_{C_{17}}^{e}}^{2}}(V_{ld}I_{ld}^{*} + V_{lq}I_{lq}^{*}) \tag{4.142}$$

As stated before $V_{lq} = 0$ from chosen reference frame, so I_{lq}^{*} has no influence on local stability and the eigenvalue of the lineraized zero dynamics becomes:

$$\mathcal{J}_{17} = -\frac{1}{R_{17}C_{17}} + \frac{3V_{ld}I_{ld}^{*}}{2C_{17}{V_{C_{17}}^{e}}^{2}} \tag{4.143}$$

One can easily see that $\mathcal{J}_{17}$ is always negative when $I_{ld}^{*} \leq 0$. Therefore, $V_{C_{17}}$ is locally stable when the Microgrid is absorbing active power from the AC grid.

When $I_{ld}^{*} > 0$, one has to analyze the region where the Jacobian is negative ($\mathcal{J}_{17} < 0$). From (4.143) results:

$$I_{ld}^{*} < \frac{2{V_{C_{17}}^{e}}^{2}}{3R_{17}V_{ld}} \tag{4.144}$$

Concluding, local stability is assured for zero dynamics $V_{C_{17}}$ for reactive power supply and active power supply when current I_{ld}^{*} respects equation (4.144).

4.7.4. PLL synchronization

The voltages in the AC side of the VSC converter can be written as follows:

$$\begin{cases} V_{ld} = \widehat{V}_l \cos(\omega_g t + \theta_0 - \rho(t)) \\ V_{lq} = \widehat{V}_l \sin(\omega_g t + \theta_0 - \rho(t)) \end{cases} \tag{4.145}$$

where $\widehat{V}_l$ is the peak voltage value, ω_g is the grid frequency, θ_0 is the phase angle of the fundamental component and $\rho(t) = \omega t + \varphi$ is the angle of the synchronous system calculated by PLL.

The adopted reference frame implies $V_{ld} = \widehat{V}$ and $V_{lq} = 0$ when $\rho(t) = \omega_g t + \theta_0$, which means that the converter is synchronized with the main grid. Thus, it is possible to design a controller for $\rho(t)$, such that $V_{lq} = 0$ in steady state [204, 205]. The Synchronous Reference Frame (SRF) PLL structure is shown in Figure 4.8,

with $G(s)$ being a linear controller that cancels the quadrature component of the voltage ($V_{lq} = 0$) by adjusting the value of $\rho(t)$. The linear controller $G(s)$ is written as follows:

$$G(s) = k_p \frac{1 + s\tau_i}{s\tau_i} \tag{4.146}$$

where k_p is the proportional gain and τ_i the time constant.

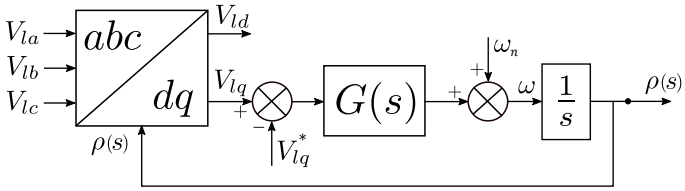

Figure 4.8: Block diagram of SRF-PLL.

The nonlinear dynamics of the synchronism structure is linearized around an operating point ($\bar{\rho} = \omega_n t + \theta_0$, where ω_n is the fundamental frequency), considering $\sin\mu \approx \mu$ when $\mu \approx 0$, and the grid frequency close enough to the fundamental frequency ($\omega_g \approx \omega_n$) [205]. Thus, based on the block diagram of the PLL, the tracked frequency is given as:

$$\omega = \widehat{V}_l(\omega_n t + \theta_0 - \rho(t)) \tag{4.147}$$

In this case, the PLL can be applied to synchronize the VSC with the main AC grid. The PLL controller is not designed from nonlinear control strategies, but traditional linearization is applied, since the focus here is the Microgrid as a whole. Therefore, no contribution on PLL synchronization is developed.

4.8. System Interconnection

4.8.1. The DC bus

The DC bus is the PCC among the devices, and it represents the interconnection of the different subsystems. This node is represented by the capacitor C_{10} in Figure 4.1. The cables inductance are not considered here, since for small distances as the proposed Microgrid, the inductance of the cables are not significant. Therefore, only resistance losses are considered. The dynamical behavior of V_{dc} is introduced as follows.

$$\begin{aligned}\dot{V}_{dc} = \frac{1}{C_{10}}\Bigg[&\frac{1}{R_2}(V_{C_2} - V_{dc}) + \frac{1}{R_5}(V_{C_5} - V_{dc}) + \frac{1}{R_8}(V_{C_8} - V_{dc}) + \\ &+\frac{1}{R_{12}}(V_{C_{12}} - V_{dc}) + \frac{1}{R_{15}}(V_{C_{15}} - V_{dc}) + \frac{1}{R_{17}}(V_{C_{17}} - V_{dc})\Bigg]\end{aligned} \tag{4.148}$$

V_{dc} is not directly controllable by any control inputs; then, it is considered it as a zero dynamics of the whole system. The control target is to fix a certain reference voltage V_{dc}^* for the DC bus; the control law of the supercapacitor subsystem will be developed for this purpose.

4.8.2. Hierarchical control structure

A hierarchical control structure is considered in this work [27, 95]. While the low-level controllers for the converters are here introduced, they need references supposed to be provided by a higher secondary level controller, which development is out of the scope of this work. The references for the voltages of DC bus, DC load and regenerative system are fixed and chosen *a priori*: they are V_{dc}^*, $V_{C_{11}}^*$ and $V_{C_{14}}^*$, respectively.

The current reference $I_{L_9}^*$ for the PV is given by the Incremental Conductance MPPT algorithm, in order to address the maximum power point for the PV. The reference of active and reactive powers to be provided to the AC grid are I_{ld}^* and I_{lq}^*, while the one for the battery is $I_{L_6}^*$. These references are supposed to be calculated with an optimal power flow controller, considering grid codes, the physical constraints of the devices given by their sizes and the needs of the Microgrids, as in [116, 123]. The reference vector is

$$r = [I_{L_6}^* \; I_{L_9}^* \; V_{dc}^* \; V_{C_{11}}^* \; V_{C_{14}}^* \; I_{ld}^* \; I_{lq}^*]. \tag{4.149}$$

Part of the contribution of this work relies on the development of control laws for stabilizing the dynamics of the whole Microgrid system introduced previously with respect to given references, introduced in (4.149). Furthermore, a complete rigorous analysis of the DC Microgrid is implemented, proving stability of the whole system and answering to the following Problem:

Problem 1. *Given the equations of the system model (4.1), (4.2), (4.3), (4.52), (4.53),(4.54), (4.66), (4.67), (4.68), (4.76), (4.77), (4.78), (4.100), (4.101), (4.102), (4.126), (4.127), (4.128) and (4.148), and supposing the given references in (4.149) to fulfill the steady-state stability conditions (i.e., to correctly satisfy power balance in steady-state), the development of dedicated control law u_1, u_2, u_3, u_4, u_5, u_6 and u_7 such to ensure grid stability is needed.*

4.8.3. Preliminaries

Consider the extended state x, the respective equilibrium point x^e, the output y and the error $\tilde{x} \triangleq x - x^e$:

$$x = [\ \xi_1\ \xi_2\ \eta\ \mu\ \zeta\ ]^T, \tag{4.150}$$

$$x^e = [\ \xi_1^e\ \xi_2^e\ \eta^e\ \mu^e\ \ \zeta^e\ ]^T, \tag{4.151}$$

$$y = [\, y_\mu\ y_{\xi_1}\ \ y_{\xi_2}\ ]^T, \tag{4.152}$$

where:

$$\xi_1 = [\, I_{L_6}\, \alpha_6\, I_{L_9}\, \alpha_9\, I_{ld}\, \alpha_d\, I_{lq}\, \alpha_q\,], \tag{4.153}$$

$$\xi_2 = \Big[\, V_{C_{11}}\, \alpha_{11}\, I_{L_{13}} \alpha_{13}\ V_{C_{14}}\, \dot{V}_{C_{14}}\, I_{L_{16}}\, \alpha_{16}\, \Big], \tag{4.154}$$

$$\eta = [\, V_{C_5}\, V_{C_8}\, V_{C_{12}}\, V_{C_{15}}\, V_{C_{17}}\, V_{dc}\,], \tag{4.155}$$

$$\mu = \Big[\, V_{C_2}\, \dot{V}_{C_2}\, I_{L_3}\, \alpha_3\, \Big], \qquad \zeta = [\, V_{C_1}\, V_{C_4}\, V_{C_7}\,], \tag{4.156}$$

$$\xi_1^e = \big[\, I_{L_6}^*\, 0\, I_{L_9}^*\, 0\, I_{ld}^*\, 0\, I_{lq}^*\, 0\, \big], \tag{4.157}$$

$$\xi_2^e = \big[\, V_{C_{11}}^*\, 0\, I_{L_{13}}^e\, 0\, V_{C_{14}}^*\, 0\, I_{L_{16}}^e\, 0\, \big], \tag{4.158}$$

$$\eta^e = \big[\, V_{C_5}^*\, V_{C_8}^*\, V_{C_{12}}^*\, V_{C_{15}}^*\, V_{C_{17}}^*\, V_{dc}^*\, \big], \tag{4.159}$$

$$\mu^e = \big[\, V_{C_2}^e\, 0\, I_{L_3}^e\, 0\, \big], \qquad \zeta^e = \big[\, V_{C_1}^*\, V_{C_4}^*\, V_{C_7}^*\, \big], \tag{4.160}$$

$$y_\mu = [y_1] = [I_{L_3}], \quad y_{\xi_2} = [\, y_4\ y_5\,] = [\, V_{C_{11}}\, I_{L_{16}}\ ], \tag{4.161}$$

$$y_{\xi_1} = [\, y_2\ y_3\ y_d\ y_q\,] = [\, I_{L_6}\, I_{L_9}\, I_{ld}\, I_{lq}\,]. \tag{4.162}$$

The equations of I_{L_J}, with $J = \{3, 6, 9, 13, 16, d, q\}$, and V_{C_I}, with $I = \{1, 2, 4, 5, 7, 8, 10, 11, 12, 14, 15, 17\}$, are introduced in (4.1)-(4.148), while the terms α_H, with $H = \{3, 6, 9, 11, 13, 16, d, q\}$, are integral terms ensuring zero error in steady-state

4.8.4. Stability analysis

The values of the equilibrium point are either provided by the higher level controller in (4.149), either obtained by solving the equations of the Microgrid (4.1)-(4.148), for V_{C_I}, $I = \{1, 4, 5, 7, 8, 12, 15, 17\}$, and (4.34), (4.60), (4.73), (4.107) and (4.137) in steady-state, given (4.149). Finally, the trajectories $V_{C_2}^e$, $I_{L_3}^e$, $I_{L_{13}}^e$ and $I_{L_{16}}^e$ are obtained by Lyapunov techniques considering the stability of the whole DC bus

connection ($V_{C_2}^e$), backstepping ($I_{L_{13}}^e$) and dynamical feedback linearization ($I_{L_3}^e$ and $I_{L_{16}}^e$) techniques to meet the control purpose:

$$\begin{aligned} V_{C_2}^e =& V_{dc} + \frac{K_{10}}{V_{dc}}(V_{dc}^{*\,2} - V_{dc}^2) - R_2\Psi_{dc} + \\ & - \frac{R_2}{V_{dc}}\left[\Psi_5 + \Psi_8 + \Psi_{12} + \Psi_{15} + \Psi_{17} + \Psi_W\right], \end{aligned} \tag{4.163}$$

$$I_{L_3}^e = \int \frac{1}{L_{g_2} L_{f_2}^1(V_{C_2})}[\theta_d - L_{f_2}^2(V_{C_2})]\, dt, \tag{4.164}$$

$$I_{L_{13}}^e = \frac{V_{C_{11}} - V_L}{R_{11}} - C_{11}\left[K_{11}(V_{C_{11}} - V_{C_{11}}^*) + K_{11}^{\alpha}\alpha_{11}\right], \tag{4.165}$$

$$I_{L_{16}}^e = \int \frac{1}{L_{g_{14}} L_{f_{14}}^1(V_{C_{14}})}[\theta_t - L_{f_{14}}^2(V_{C_{14}})]\, dt, \tag{4.166}$$

K_{10} is a positive constant calculated to improve the converge speed of the DC bus voltage. The η extended terms in (4.163) are expressed as follows, being part of the complete Lyapunov function detailed next.

$$\Psi_5 = (V_{C_5} - V_{C_5}^e)\left[\frac{V_{dc} - V_{C_5}}{R_5} + I_{L_6}(1 - u_2)\right], \tag{4.167}$$

$$\Psi_8 = (V_{C_8} - V_{C_8}^e)\left[\frac{V_{dc} - V_{C_8}}{R_8} + I_{L_9}(1 - u_3)\right], \tag{4.168}$$

$$\Psi_{12} = (V_{C_{12}} - V_{C_{12}}^e)\left[\frac{V_{dc} - V_{C_{12}}}{R_{12}} - I_{L_{13}}u_4\right], \tag{4.169}$$

$$\Psi_{15} = (V_{C_{15}} - V_{C_{15}}^e)\left[\frac{V_{dc} - V_{C_{15}}}{R_{15}} + I_{L_{16}}\right], \tag{4.170}$$

$$\Psi_{17} = (V_{C_{17}} - V_{C_{17}}^e)\left[\frac{V_{dc} - V_{C_{17}}}{R_{17}} - \frac{3(I_{ld}V_{ld} + I_{lq}V_{lq})}{2V_{C_{17}}}\right], \tag{4.171}$$

$$\begin{aligned} \Psi_{dc} =& \frac{V_{C_5} - V_{dc}}{R_5} + \frac{V_{C_8} - V_{dc}}{R_8} + \frac{V_{C_{12}} - V_{dc}}{R_{12}} + \\ & + \frac{V_{C_{15}} - V_{dc}}{R_{15}} + \frac{V_{C_{17}} - V_{dc}}{R_{17}}, \end{aligned} \tag{4.172}$$

$$\begin{aligned} \Psi_W =& -\frac{(V_{C_5} - V_{C_5}^e)^2}{R_5} - \frac{(V_{C_8} - V_{C_8}^e)^2}{R_8} - \frac{(V_{C_{12}} - V_{C_{12}}^e)^2}{R_{12}} \\ & - \frac{(V_{C_{15}} - V_{C_{15}}^e)^2}{R_{15}} - \frac{(V_{C_{17}} - V_{C_{17}}^e)^2}{R_{17}} \end{aligned} \tag{4.173}$$

where the Lie derivatives of the dynamical feedback approach (V_{C_2} and $V_{C_{14}}$) can be expressed as:

$$\mathcal{L}_{g_2}\mathcal{L}^1_{f_2}(V_{C_2}) = \frac{1}{C_2 V_{C_2}}(V_{C_1} - 2R_{01}I^e_{L_3}), \tag{4.174}$$

$$\mathcal{L}_{g_{14}}\mathcal{L}^1_{f_{14}}(V_{C_{14}}) = \frac{1}{C_{14}V_{C_{14}}}(V_{C_{15}} + 2R_{014}I^e_{L_{16}}), \tag{4.175}$$

and

$$\mathcal{L}^2_{f_2}(V_{C_2}) = \frac{I^e_{L_3}}{C_2 V_{C_2}}\dot{V}_{C_1} + \frac{\dot{V}_{dc}}{R_2 C_2} - \left[\frac{1}{R_2 C_2} + \frac{V_{C_1}I^e_{L_3} - R_{01}{I^e_{L_3}}^2}{C_2 {V_{C_2}}^2}\right]\dot{V}_{C_2}, \tag{4.176}$$

$$\mathcal{L}^2_{f_{14}}(V_{C_{14}}) = \frac{I^e_{L_{16}}}{C_{14}V_{C_{14}}}\dot{V}_{C_{15}} - \left[\frac{1}{R_{14}C_{14}} - \frac{V_{C_{15}}I^e_{L_{16}} + R_{014}{I^e_{L_{16}}}^2}{C_{14}{V_{C_{14}}}^2}\right]\dot{V}_{C_{14}}, \tag{4.177}$$

The synthetic inputs for dynamical feedback process are then written according to references $V^e_{C_2}$ and $V^*_{C_{14}}$ [6]:

$$\theta_d = -K_2(\dot{V}_{C_2} - \dot{V}^e_{C_2}) - K^\alpha_2(V_{C_2} - V^e_{C_2}), \tag{4.178}$$

$$\theta_t = -K_{14}(\dot{V}_{C_{14}}) - K^\alpha_{14}(V_{C_{14}} - V^*_{C_{14}}). \tag{4.179}$$

The control inputs are bounded: $u_i \in [0,1]$, $i \in \{1,2,3,4,5\}$, and $\sqrt{u_6^2 + u_7^2} \leq 1$. Consider the set Ω_{x^e} of all possible values of the equilibrium point x^e and the set Ω_K of all possible positive values of the gains K_i, K^α_i, $i \in \{3,6,9,10,11,13,16,d,q\}$, such that the physical constraints of the converters are not violate. Given $x^e \in \Omega_{x^e}$, let us consider the set Ω_{V_L} of all the possible values of V_L and I_L such that the condition of power balance is satisfied. Such condition can be expressed by:

$$\begin{aligned}&\frac{V^e_{C_2} - V^e_{dc}}{R_2} + \frac{V^e_{C_5} - V^*_{dc}}{R_5} + \frac{V^e_{C_8} - V^*_{dc}}{R_8} + \\ &+\frac{V^e_{C_{12}} - V^*_{dc}}{R_{12}} + \frac{V^e_{C_{15}} - V^*_{dc}}{R_{15}} + \frac{V^e_{C_{17}} - V^*_{dc}}{R_{17}} = 0.\end{aligned} \tag{4.180}$$

Consider furthermore the set $\Omega_{\tilde{x}}$ of any evolution of $\tilde{x}$ satisfying for each t the conditions:

$$\begin{aligned}V_{C_2} > 0\,;\ V_{C_5} > 0\,; \quad V_{C_8} - (R_{08} - R_{07})I_{L_9} > 0;\\ V_{C_{14}} > 0\,;\ V_{C_{17}} > 0; \quad V_{C_{12}} - (R_{012} - R_{011})I_{L_{13}} > 0.\end{aligned} \tag{4.181}$$

The main result can now be formulated as:

[6] It should be noted that $V^e_{C_2}$ is a time-varying reference to balance the DC bus according to system operation state and $V^*_{C_{14}}$ is a constant reference, resulting in the calculated inputs (4.178) and (4.179).

Theorem 2. *Given $x^e \in \Omega_{x^e}$, $V_L, I_L \in \Omega_{V_L}$, $K_i, K_i^\alpha \in \Omega_K$, the control laws u_1, u_2, u_3, u_4, u_5, u_6, u_7 introduced in (4.20), (4.59), (4.71), (4.91), (4.105), (4.134) and (4.135) solve the Problem 1, since there exist suitable functions $\vartheta \in K\mathcal{L}$ and $\gamma \in K$ such that:*

$$||\tilde{x}(t)|| \leq \vartheta(\tilde{x}(0), t) + \gamma(V_{dc}^*), \tag{4.182}$$

provided that $\tilde{x} \in \Omega_{\tilde{x}}$.

Proof. The proof is based on the development of a Lyapunov function W for the whole system $\tilde{x}$ (see [104], [91], [37]). Such Lyapunov function is composed by several Lyapunov functions:

$$W(\tilde{x}(t)) = W_{\tilde{x}} = W_{\tilde{\xi}_1} + W_{\tilde{\xi}_2} + W_{\tilde{\eta}} + W_{\tilde{\mu}} + W_{\tilde{\zeta}} > 0. \tag{4.183}$$

In the following, the proof is structured according to the introduction of the extended states ξ_1, ξ_2, η, μ and ζ. For each of them, a Lyapunov function is provided, aiming at showing stability for the overall system. $W_{\tilde{\xi}_1}$ and $W_{\tilde{\xi}_2}$ will be the first pieces, since their dynamics are directly controllable with respect to a fixed given reference. The focus will move on the zero dynamics involved on the systems' interconnection, with $W_{\tilde{\eta}}$, and how to control such interconnection, with $W_{\tilde{\mu}}$. Finally, stability analysis is provided for the remaining zero dynamics considered by $W_{\tilde{\zeta}}$.

Classical input-output feedback linearization technique is used to calculate the control inputs in (4.59), (4.71), (4.134), (4.135), according to the output y_{ξ_1} (see [188]). Consequently, the following Lyapunov function $W_{\tilde{\xi}_1}$ can be used to prove stability of ξ_1:

$$W_{\tilde{\xi}_1} = W_6 + W_9 + W_{d,q} > 0, \tag{4.184}$$

where:

$$W_j = \frac{1}{2}\left(I_{L_j} - I_{L_j}^*\right)^2 + \frac{K_j^\alpha}{2}\alpha_j^2 > 0, \quad j \in \{6, 9\} \tag{4.185}$$

$$W_{d,q} = \tfrac{1}{2}\left[(I_{ld} - I_{ld}^*)^2 + (I_{lq} - I_{lq}^*)^2 + K_d^\alpha \alpha_d^2 + K_q^\alpha \alpha_q^2\right] > 0. \tag{4.186}$$

Using the control inputs in (4.59), (4.71), (4.134), (4.135), the related time derivatives are calculated as:

$$\dot{W}_j = -K_j\left(I_{L_j} - I_{L_j}^*\right)^2 \leq 0, \quad j \in \{6, 9\} \tag{4.187}$$

$$\dot{W}_{d,q} = -K_d \left(I_{ld} - I_{ld}^*\right)^2 - K_q \left(I_{lq} - I_{lq}^*\right)^2 \leq 0. \tag{4.188}$$

From $\dot{W}_6 \leq 0$, it results $W_6(t) \leq W_6(0)$, which implies that $I_{L_6} - I_{L_6}^*$ and α_6 are bounded, thanks to Lyapunov theorem. Consequently, it can be shown that $\ddot{W}_6$ is bounded as well. Then $\dot{W}_6$ is uniformly continuous in time. At this point, by applying Barbalat's lemma it is possible to establish that $\dot{W}_6 \to 0$ as $t \to \infty$: ergo $(I_{L_6} - I_{L_6}^*) \to 0$ and $\alpha_6 \to 0$ [188]. The same is valid for $\dot{W}_9$ and $\dot{W}_{d,q}$ with respect to $\ddot{W}_9$ and $\ddot{W}_{d,q}$.

Asymptotic stability is then proved for the errors considered in (4.184), thanks to (4.187), (4.188) and Barbalat's lemma. In a similar way, the solution is presented for the remaining Lyapunov functions.

We continue the analysis by focusing on $W_{\tilde{\xi}_2}$:

$$W_{\tilde{\xi}_2} = W_{11,13} + W_{14} + W_{16}. \tag{4.189}$$

First, classical input-output feedback linearization is used for obtaining the control input in (4.91) that leads to a positive definite $W_{11,13}$ with a negative semidefinite $\dot{W}_{11,13}$, ensuring stability according to the same argumentations used for (4.185), (4.186), (4.187) and (4.188):

$$W_{11,13} = \tfrac{1}{2}\left(V_{C_{11}} - V_{C_{11}}^*\right)^2 + \tfrac{K_{11}^\alpha}{2}\alpha_{11}^2 + \tfrac{1}{2}\left(I_{L_{13}} - I_{L_{13}}^e\right)^2 + \tfrac{K_{13}^\alpha}{2}\alpha_{13}^2 > 0, \tag{4.190}$$

$$\dot{W}_{11,13} = -K_{11}\left(V_{C_{11}} - V_{C_{11}}^*\right)^2 - K_{13}\left(I_{L_{13}} - I_{L_{13}}^e\right)^2 \leq 0. \tag{4.191}$$

Next, dynamical feedback linearization is used to calculate the control input (4.105) based on (4.166); indeed, the reference $I_{L_{16}}^e$ in (4.166) is calculated in a way such there exists $W_{14} > 0$ with a $\dot{W}_{14} < 0$, where:

$$W_{14} = \frac{1}{2}K_{14}^\alpha\left(V_{C_{14}} - V_{C_{14}}^*\right)^2 + \frac{1}{2}\dot{V}_{C_{14}}^2 > 0. \tag{4.192}$$

This can be shown using a change of variable, where $z_1 = V_{C_{14}}$ and $z_2 = \dot{V}_{C_{14}}$. The resulting system would be:

$$\begin{cases} \dot{z}_1 = z_2, \\ \dot{z}_2 = \mathcal{L}_{f_{14}}^2 + \mathcal{L}_{g_{14}}\mathcal{L}_{f_{14}}^1 \dot{I}_{L_{16}}^e, \end{cases} \tag{4.193}$$

and, considering $\dot{I}_{L_{16}}^e$ as a control input, the chosen value in (4.166) allows to obtain a linear stable system with respect to the desired equilibrium;

$$\begin{cases} \dot{z}_1 = z_2 \\ \dot{z}_2 = -K_{14}z_2 - K_{14}^\alpha(z_1 - z_1^*). \end{cases} \tag{4.194}$$

From (4.194), it is possible to calculate the proper time derivative of the Lyapunov function in (4.192) such that

$$\dot{W}_{14} = -K_{14} z_2^2 < 0. \tag{4.195}$$

Then, the control input in (4.105) correctly operates the tracking of the calculated reference in (4.166), as it can be shown by calculating the time derivative of the following Lyapunov function W_{16}:

$$W_{16} = \frac{1}{2}\left(I_{L_{16}} - I_{L_{16}}^e\right)^2 + \frac{1}{2} K_{16}^{\alpha} \alpha_{16}^2 > 0, \tag{4.196}$$

$$\dot{W}_{16} = -K_{16}\left(I_{L_{16}} - I_{L_{16}}^e\right)^2 \leq 0. \tag{4.197}$$

In the same way as for (4.185) and (4.187), in the case of $\dot{W}_{16}$ asymptotic stability can be proven by Barbalat's lemma utilization with the calculation of $\ddot{W}_{16}$.

Voltage $V_{C_2}^e$ is seen as a control input that represents the remaining degree of freedom of the system: it is then designed with the purpose to control the interconnection of the whole system. To analyze the stability of such interconnection, the Lyapunov function $W_{\tilde{\eta}}$ is introduced to perform calculations of the reference for V_{C_2} to be applied by u_1 in order to control the interconnections:

$$\begin{aligned} W_{\tilde{\eta}} = & \frac{C_{10}}{2} V_{dc}^2 + \frac{C_5}{2}(V_{C_5} - V_{C_5}^e)^2 + \frac{C_8}{2}(V_{C_8} - V_{C_8}^e)^2 + \\ & + \frac{C_{12}}{2}(V_{C_{12}} - V_{C_{12}}^e)^2 + \frac{C_{15}}{2}(V_{C_{15}} - V_{C_{15}}^e)^2 + \frac{C_{17}}{2}(V_{C_{17}} - V_{C_{17}}^e)^2 > 0. \end{aligned} \tag{4.198}$$

Voltages V_{C_5}, V_{C_8}, $V_{C_{12}}$, $V_{C_{15}}$ and $V_{C_{15}}$ are the non-controlled dynamics that interconnect each device in the Microgrid DC bus, which are considered in the Lyapunov equation to assure voltage stability on the DC bus. $V_{C_5}^e$, $V_{C_8}^e$, $V_{C_{12}}^e$, $V_{C_{15}}^e$ and $V_{C_{17}}^e$ are their respective equilibrium points. The time derivative can be calculated as:

$$\dot{W}_{\tilde{\eta}} = V_{dc}\left[\frac{1}{R_2}(V_{C_2} - V_{dc}) + \Psi_{dc}\right] + \Psi_5 + \Psi_8 + \Psi_{12} + \Psi_{15} + \Psi_{17}, \tag{4.199}$$

where the term representing the available degree of freedom, i.e., V_{C_2}, is clearly indicated, and the others are defined in (4.167)-(4.172).

Then, by backstepping, supposing the dynamics of V_{C_2} matches its reference calculated in (4.163), the function $\dot{W}_{\tilde{\eta}}$ can be written as:

$$\begin{aligned} \dot{W}_{\tilde{\eta}} = & \frac{K_{10}}{R_2} V_{dc}^{*\,2} - \frac{K_{10}}{R_2} V_{dc}^2 - \frac{(V_{C_5} - V_{C_5}^*)^2}{R_5} - \frac{(V_{C_8} - V_{C_8}^*)^2}{R_8} + \\ & - \frac{(V_{C_{12}} - V_{C_{12}}^*)^2}{R_{12}} - \frac{(V_{C_{15}} - V_{C_{15}}^*)^2}{R_{15}} - \frac{(V_{C_{17}} - V_{C_{17}}^*)^2}{R_{17}}. \end{aligned} \tag{4.200}$$

The Lyapunov function in (4.198) results to be an ISS-like Lyapunov function [119, 190, 206], therefore the system is proven to be *input to state stable* and consequently it is robustly stable as explained at the end of the proof. The characterization of Input-to-State Stability properties are defined in [207], which is inserted in the Appendix.

Here, V_{C_2} is considered as the control input, and by tracking its reference trajectory $V_{C_2}^e$ in (4.163) it can regulate V_{dc} and assure stability for the considered dynamics. The extended state μ is studied to obtain convergence of V_{C_2} to $V_{C_2}^e$. Then, using the control input in (4.20), the trajectory in (4.164) and defining a Lyapunov function $W_{\tilde{\mu}}$ as:

$$W_{\tilde{\mu}} = W_2 + W_3, \tag{4.201}$$

where:

$$W_2 = \frac{1}{2}\left(V_{C_2} - V_{C_2}^e\right)^2 + \frac{1}{2}\left(\frac{dV_{C_2}}{dt} - \frac{dV_{C_2}^e}{dt}\right)^2 > 0, \tag{4.202}$$

$$W_3 = \frac{1}{2}\left(I_{L_3} - \int \frac{dI_{L_3}^e}{dt}\right)^2 + \frac{1}{2}K_3^{\alpha}\alpha_3^2 > 0. \tag{4.203}$$

Stability is proven with arguments similar to the ones used for (4.192), (4.193), (4.194) and (4.195), considering a state-dependent trajectory and its time derivatives $\dot{V}_{C_2}^e$ and $\ddot{V}_{C_2}^e$, obtaining:

$$\dot{W}_2 < 0 \ \ ; \ \ \dot{W}_3 = -\left(I_{L_3} - \int \frac{dI_{L_3}^e}{dt}\right)^2 \leq 0. \tag{4.204}$$

Finally, the focus on the states that represent the remaining zero dynamics of the system. To show their stability, the Lyapunov function $W_{\tilde{\zeta}}$ is used and the controlled dynamics are considered already on their equilibrium point:

$$W_{\tilde{\zeta}} = W_1 + W_4 + W_7, \tag{4.205}$$

$$W_j = \frac{1}{2}C_j\left(V_{C_j} - V_{C_j}^*\right)^2 > 0, \ \ j \in \{1, 4, 7\}. \tag{4.206}$$

$$\dot{W}_j = -\frac{1}{R_j}\left(V_{C_j} - V_{C_j}^*\right)^2 < 0, \ \ j \in \{1, 4, 7\}, \tag{4.207}$$

assuring asymptotic stability for these zero dynamics.

From (4.184), (4.189), (4.198), (4.201), (4.205), we can state that there exist functions $\underline{\alpha}, \overline{\alpha} \in K_\infty$ such that $\underline{\alpha}(|\tilde{x}|) \leq W_{\tilde{x}}(\eta) \leq \overline{\alpha}(|\tilde{x}|)$ for $W_{\tilde{x}}$ in (4.183). From (4.187), (4.188), (4.191), (4.195), (4.197), (4.200), (4.204), (4.207), we can state that:

$$\dot{W}_{\tilde{x}}(\tilde{x}, V_{dc}^*) \leq -\beta_{\tilde{x}}(|\tilde{x}|) + \gamma_{\tilde{x}}(|V_{dc}^*|), \tag{4.208}$$

with $\beta_{\tilde{x}}, \gamma_{\tilde{x}} \in K_\infty$ and V_{dc}^* playing the role of a virtual input [187, 190, 206]. From (4.208), inequality in (4.182) follows. □

Remark 6. *ISS stability is practically accepted for the proposed application domain [208, 209]. However, stronger stability results can be derived from the proposed analysis by passivity based considerations, as in [113, 210].*

Remark 7. *The domain of attraction and the convergence to the equilibrium can be better defined as depending on the proposed Lyapunov function and the control gains, according to [191, 192]. Numerical methods as the one proposed in [211] can be used for computing the reachable set.*

4.9. Simulation Results

The DC Microgrid model for the Microgrid proposed in Figure 4.1 has been implemented with the *SimPowerSystems* toolbox of *Matlab/Simulink*. Simulink's toolbox *SimPowerSystem* allows to model a realist power system including power electronics devices[7] like IGBT, MOSFET, and GTO, sources, loads, and basic elements like resistances, capacitors, and inductors providing a powerful simulation environment. Besides that, control algorithms can be easily developed on Simulink environment, which makes Simulink environment the standard platform for simulation of complex systems like Microgrids.

The simulations are focused on showing the transient behavior of the system and the proposed nonlinear control performance. The used parameters' values are introduced in table 4.1. In this simulation example, the DC bus is modeled as capacitor with a small capacitance (representing fast voltage dynamics) and the desired voltage on DC bus is $V_{dc}^* = 630\ V$. The DC voltage reference value is chosen according to the devices architecture and grid standard. In the same way, the converters configuration were chosen according to voltage levels in each part of the grid.

The considered supercapacitor is composed of 4 parallel and 18 series cells with 9 $m\Omega$ of equivalent DC series resistance, resulting in 50 F of total capacitance, 420 V rated voltage and has 1.225 kWh of nominal energy capacity. The battery is an ion-lithium one with 380 kWh of energy capacity and 160 kW of power capacity with nominal voltage of 380 V. The current capacity is 1000 Ah and nominal discharge current is 434 A, with 3.8 $m\Omega$ of internal resistance.

[7] Electronic devices are detailed modeled including the ripples generated by their switching.

The PV array model is is a monocrystalline Kyocera KC60 composed by 15 modules in series and 100 modules in parallel of 60 W, which generates 90 kW in nominal conditions (1000 W/m^2 irradiation and 25°C temperature) and the open circuit voltage is 342 V. The MPPT algorithm used is the incremental conductance one.

The main load requirement is to maintain its voltage inside of the grid requirements (normally ±5%). The DC load reference voltage is $V^*_{C_{11}} = 500\ V$, the power demand is time-varying one with 62.5 kW of maximum consumption. The train line is modeled as a voltage source represented by V_T with 750 V nominal voltage. When the regenerative braking takes place the voltage increases up to 800 V, injecting about 0.5MW with duration of 8 seconds in the Microgrid.

The VSC converter L-filter grid has an impedance of $L_l = 0.5\ mH$ and $R_l = 2\ m\Omega$. The AC grid has 10 MVA short-circuit power and the nominal frequency of the grid is $f_n = 50\ Hz$ ($\omega_n = 2\pi f_n$) and the rms voltage on the PCC is 400 V. The Microgrid provide active and reactive power supply to the AC grid, where the maximum power supplied to the AC side of the grid is 100 kVA, which is given by the VSC nominal power. AC grid is not used to help the stabilization of the DC bus, but is supported by the DC grid.

The switching frequency of the DC/DC converters is 10 kHz, while the one of the VSC converter is 20 kHz. Here a simulation of the introduced nonlinear control laws is presented, and a comparison with the classical linear technique is proposed. The simulation time is 30 s: during this time, both the conditions of having or not having regenerative energy from the braking recovery system is proposed.

4.9.1. The proposed nonlinear control

Here the proposed nonlinear control is shown to be capable to stabilize the DC Microgrid. The gains of the nonlinear controllers are provided in Table 4.2, and are computed considering the pole placement of the linear controller (presented next) provided in the Appendix, and are tuned experimentally so that the poles are allocated to present a good control performance with a time constant of 50ms for current and 100ms for voltage variables. Figure 4.9 introduces the incident irradiation on the PV system and the current variation in the DC load, respectively. They represent, in a realistic way, the time varying disturbances impacting the system. These variations are used to test the control system performance when several nonlinearities characteristics take place. Panel temperature is kept constant during the simulation time; the DC load current values are negative since the load

Table 4.1: Microgrid parameters

Supercap	**Battery**	**PV**	**Load**	**Train**	Value
R_1	R_4	R_7	R_{11}	R_{14}	0.1 Ω
C_1	C_4	C_7	C_{11}	C_{14}	10 mF
R_2	R_5	R_8	R_{12}	R_{15}	0.1 Ω
C_2	C_5	C_8	C_{12}	C_{15}	10 mF
L_3	L_6	L_9	L_{13}	L_{16}	3.3 mH
R_{01}	R_{04}	R_{07}	R_{011}	R_{014}	10 $m\Omega$
R_{02}	R_{05}	R_{08}	R_{012}	R_{015}	10 $m\Omega$
VSC	Value	**AC grid**	Value	**DC bus**	Value
R_{17}	0.1 Ω	R_l	2 $m\Omega$	C_{10}	10 μF
C_{17}	50 mF	L_l	0.5 mH		

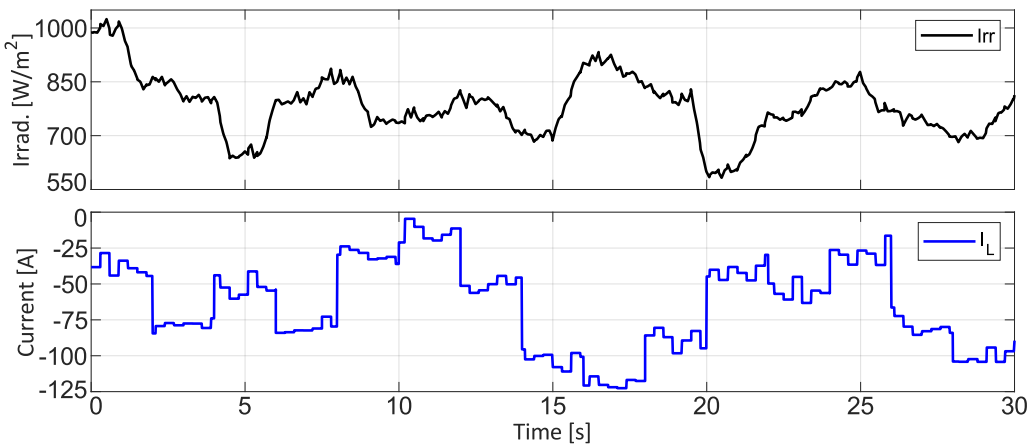

Figure 4.9: The PV incident irradiance and the demanded DC load current, respectively.

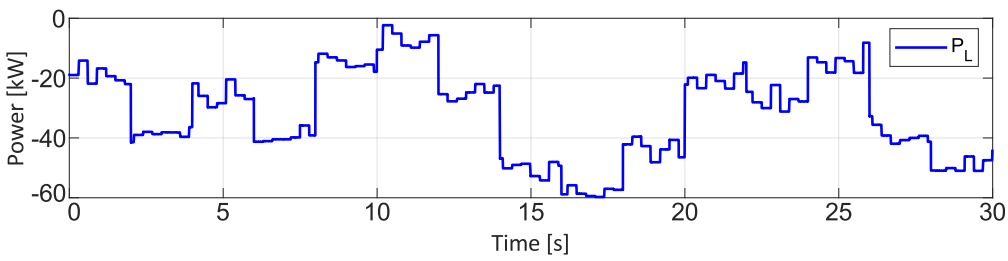

Figure 4.10: The power demand in the DC load in kW.

is absorbing power from the Microgrid and represents the power variations in DC load demand. The power variations in the DC load (in kW) is depicted in Figure 4.10.

The voltages V_S, V_B, V_{PV}, V_T, of supercapacitor, battery, PV array, and train, respectively, are depicted in Figure 4.11. While V_S has important variations, highlighting the charge and discharge of the supercapacitor, V_B is not affected by the same problems as expected, since the references provided by the higher level

Table 4.2: Gains' parameters for the nonlinear controller.

Supercap.	$K_3 = 3000$	$K_3^\alpha = 50000$	$K_2 = 500$	$K_2^\alpha = 10000$
Battery	$K_6 = 1515.15$	$K_6^\alpha = 3030.30$		
PV array	$K_9 = 3030.30$	$K_9^\alpha = 6060.60$		
DC load	$K_{13} = 3030.30$	$K_{13}^\alpha = 6060.60$	$K_{11} = 100$	$K_{11}^\alpha = 1000$
Train	$K_{16} = 1200$	$K_{16}^\alpha = 200000$	$K_{14} = 1050$	$K_{14}^\alpha = 50000$
VSC	$K_{d,q} = 10000$	$K_{d,q}^\alpha = 100000$		

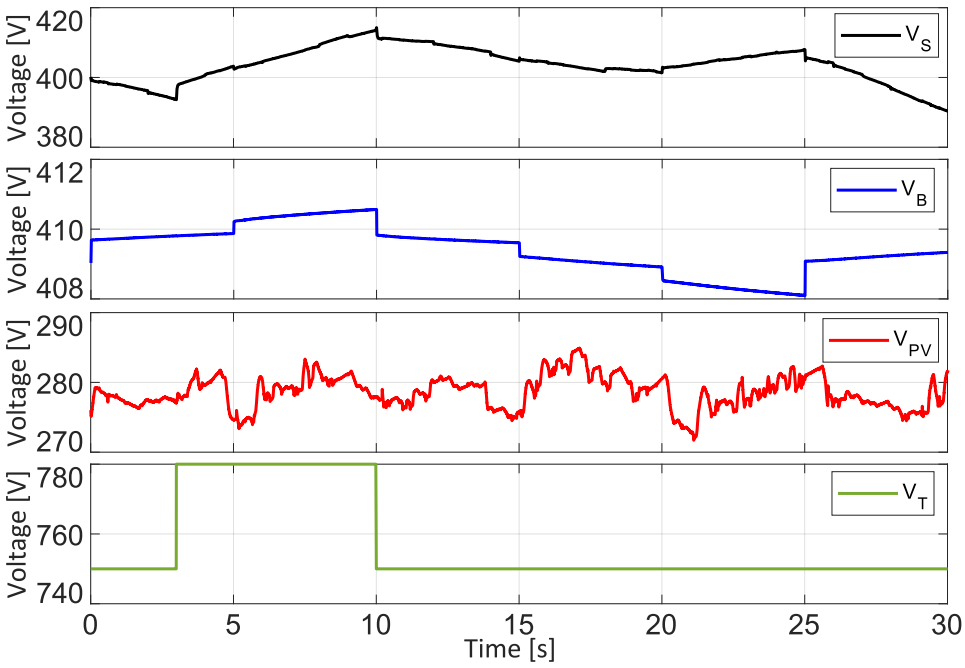

Figure 4.11: The voltages V_S, V_B, V_{PV}, V_T, of the supercapacitor, battery, PV array, and train, respectively.

controller allow for a lower charge/discharge rate. The voltage V_{PV} varies according to the incident irradiation in Figure 4.9. The voltage V_T produces a high voltage peak in a short time period due to the regenerative braking.

The currents I_{L_3}, I_{L_6} and I_{L_9}, respectively related to the supercapacitor, battery and PV array subsystem, are depicted in Figure 4.12. They are shown to correctly follow their references given by the higher level controller, as for $I_{L_6}^*$ from the power flow model or $I_{L_9}^*$ by the MPPT algorithm, or calculated such that to keep DC bus voltage stability, as for $I_{L_3}^e$, which depends on the desired value of $V_{C_2}^e$ for V_{C_2} (see Figure 4.13). A zoom on V_{C_2} voltage dynamics is introduced in Figure 4.14, where the fast convergence of voltage is highlighted with small overshoots, despite the high variations in reference $V_{C_2}^e$ during transients. So, even for fast disturbances, introduced by the irradiation profile and the DC load power demand, depicted in Figure 4.9, the convergence of V_{C_2} is guaranteed.The reference $V_{C_2}^e$ is calculated

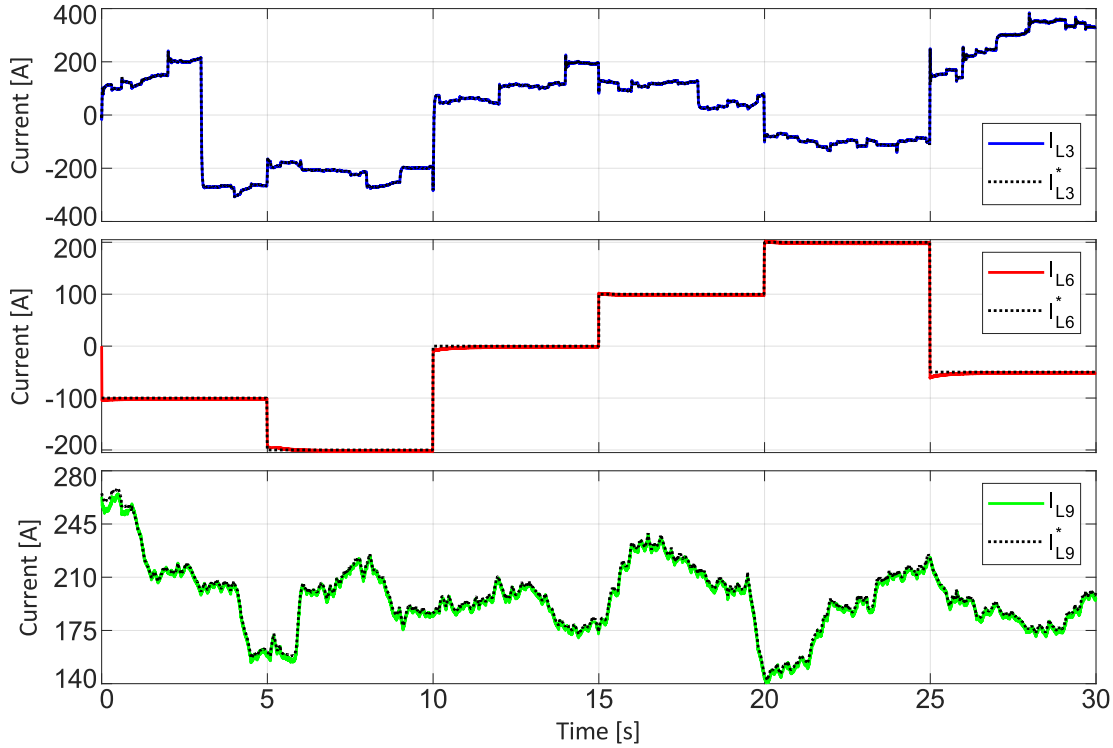

Figure 4.12: The currents I_{L_3}, I_{L_6}, I_{L_9} and their references $I^e_{L_3}$, $I^*_{L_6}$, $I^*_{L_9}$.

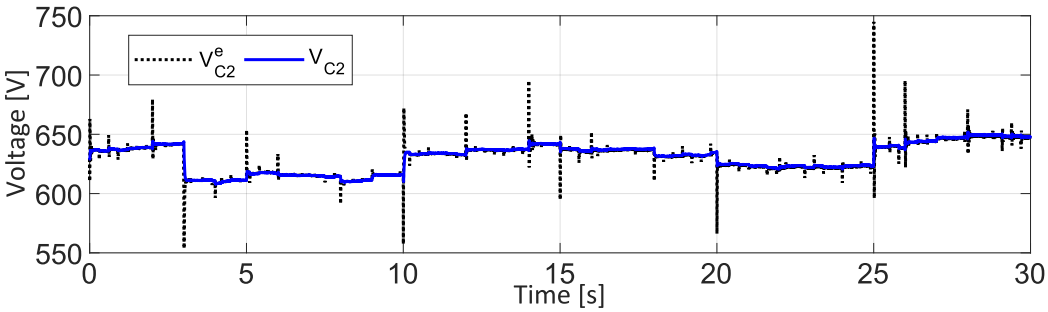

Figure 4.13: The voltage V_{C_2} and its nominal reference $V^e_{C_2}$.

for having a proper regulation of the voltage in the DC bus, and it is a function of several state variables, as shown in (4.163), and on the way it is controlled, as shown in (4.164).

Here, the derivative $\dot{V}^e_{C_2}$ is obtained by taking the time derivative of V_{C_2} in (4.163) to be applied in the control input (4.178). It is not computed by a numerical derivative block. Therefore, the noise effects caused by derivatives blocks are eliminated, which improves the performance of control.

The obtained reference $V^e_{C_2}$, together with the consequent dynamics of I_{L_3}, is shown to correctly being capable to perform DC bus voltage regulation to the desired value V^*_{dc} in Figure 4.15. The effects of such fast control response to the

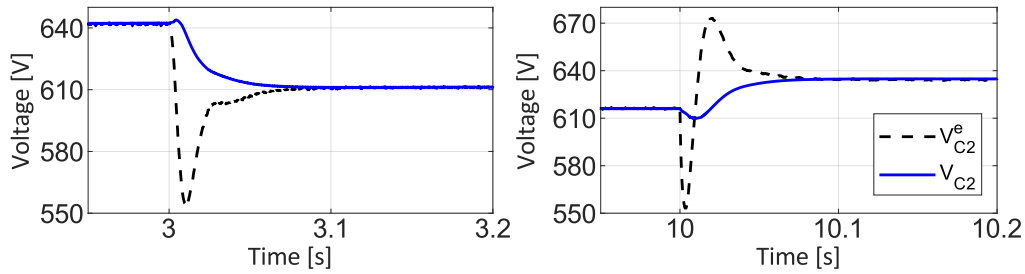

Figure 4.14: A zoom on V_{C_2} voltage dynamics, showing its convergence and settling times.

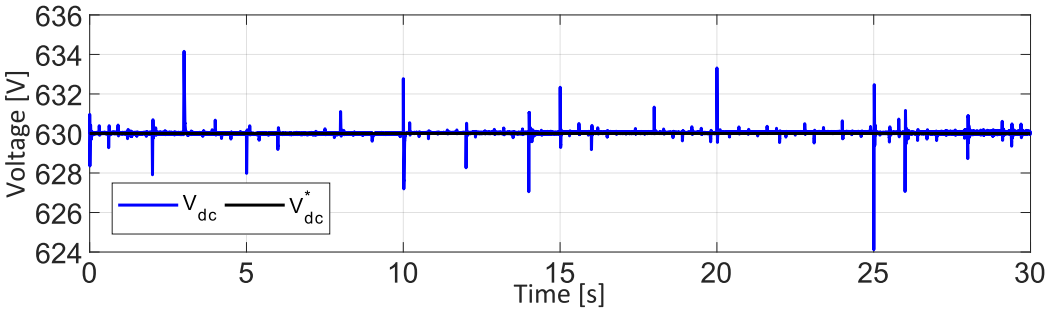

Figure 4.15: The DC bus voltage V_{dc} and its reference V_{dc}^*.

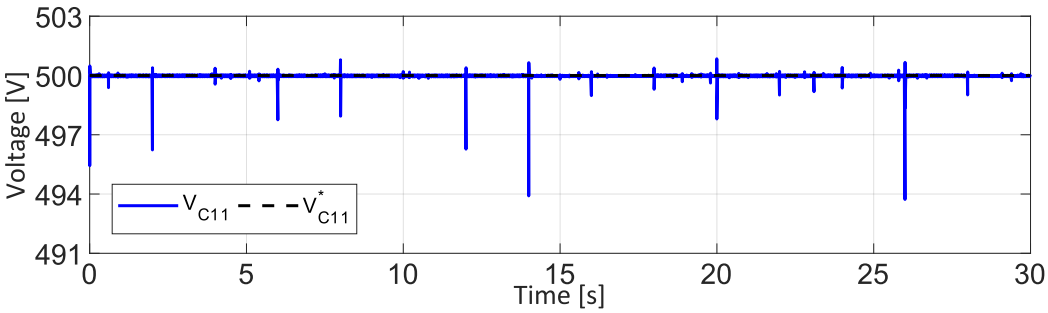

Figure 4.16: The DC load voltage $V_{C_{11}}$ and its reference $V_{C_{11}}^*$.

grid variations are such that the transient peaks are lower than 2.4% of the nominal value.

To better highlight the quality of the proposed control action, a more detailed description of the involved power sources and power load are needed. The DC load profile has been introduced in Figure 4.9. Figure 4.16 shows the effectiveness of the proposed control action for DC load voltage regulation, resulting in the requested current $I_{L_{13}}$ depicted in Figure 4.17. It is calculated according to the current demanded by DC load. The obtained load voltage successfully meets the grid code requirements ($\pm 5\%$). Figure 4.17 also describes the renewable power profile of the braking regenerative system, $I_{L_{16}}$, which has a high peak about 350 A during a few seconds of energy recovery and the current flowing to the AC grid through the VSC, $I_{R_{17}}$ according the AC power demand given by the secondary control. The profiles of the current $I_{L_{16}}$ and its reference $I_{L_{16}}^e$ are a consequence of the desired

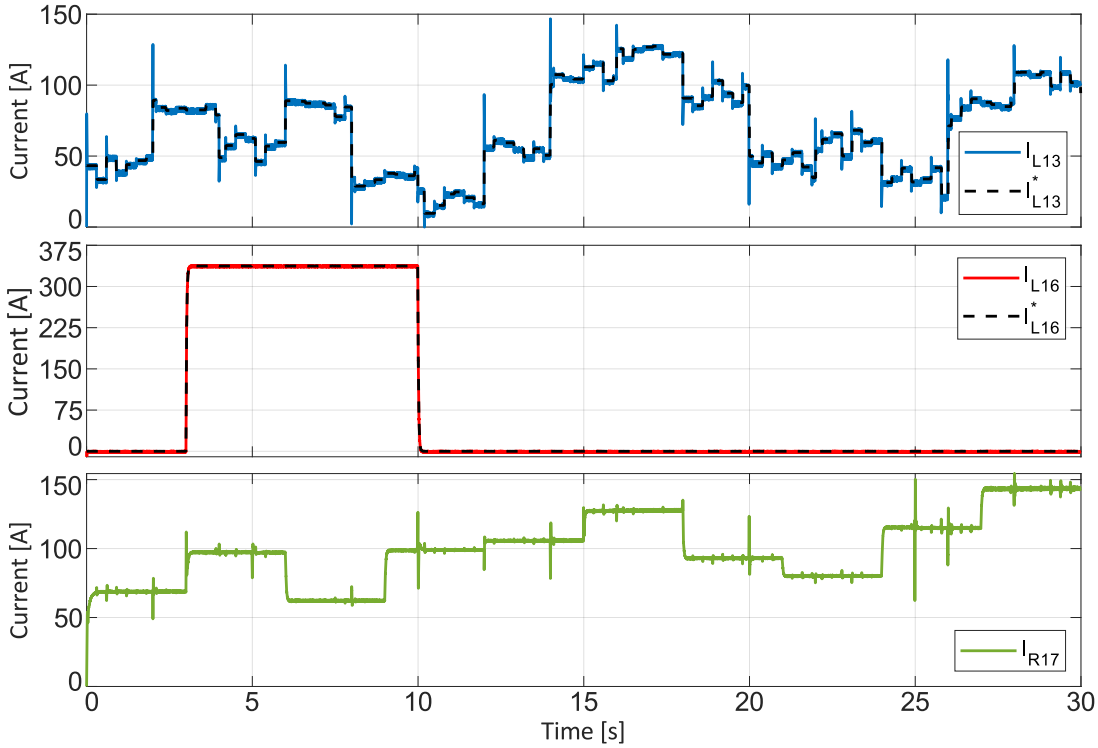

Figure 4.17: The currents $I_{L_{13}}$, $I_{L_{16}}$ and $I_{R_{17}}$ with their respective references $I^e_{L_{13}}$ and $I^e_{L_{16}}$.

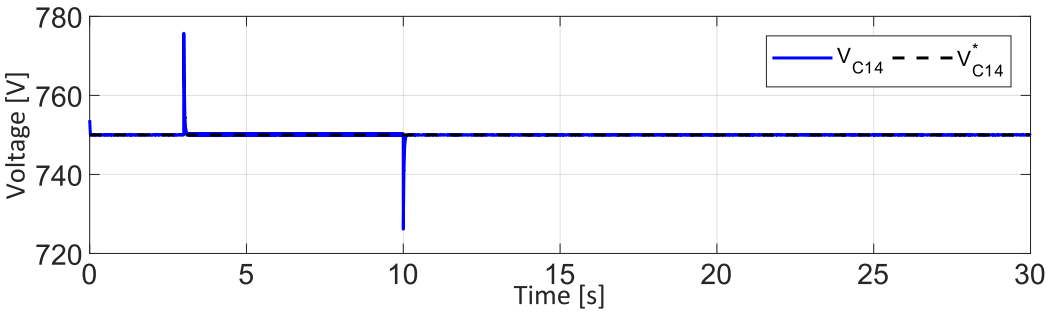

Figure 4.18: The voltage $V_{C_{14}}$ and its reference $V^*_{C_{14}}$ ensuring the injection of power from the regenerative braking system.

reference for $V_{C_{14}}$, i.e., $V^*_{C_{14}}$, and the proper control of such dynamics (see Figure 4.18). Indeed, since V_T increases very fast during brake recovery peaks, to control the voltage $V_{C_{14}}$ to a constant reference $V^*_{C_{14}}$ equal to the same value of V_T when there is no regenerative energy means to absorb the whole injected power, obtaining a desired current profile as the one of $I^e_{L_{16}}$ in Figure 4.17. To better understand the possible risks of grid instability due to it, it is important to remark that the injected regenerative power is much higher than the one normally provided by the PV array.

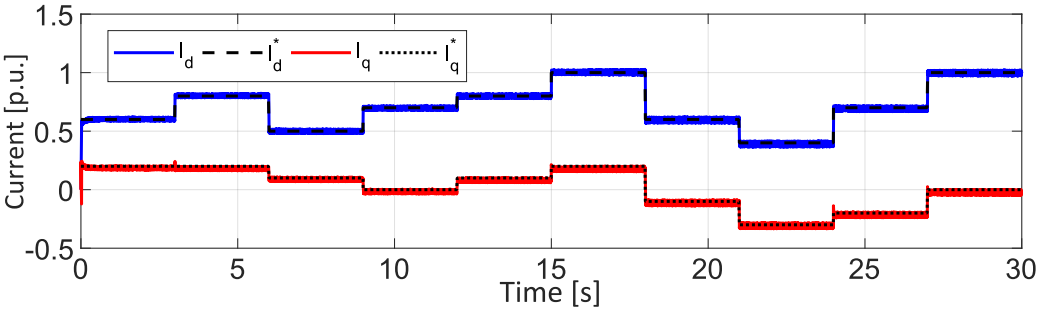

Figure 4.19: The direct and quadrature currents I_{ld} and I_{lq} with their references I^*_{ld} and I^*_{lq}, respectively.

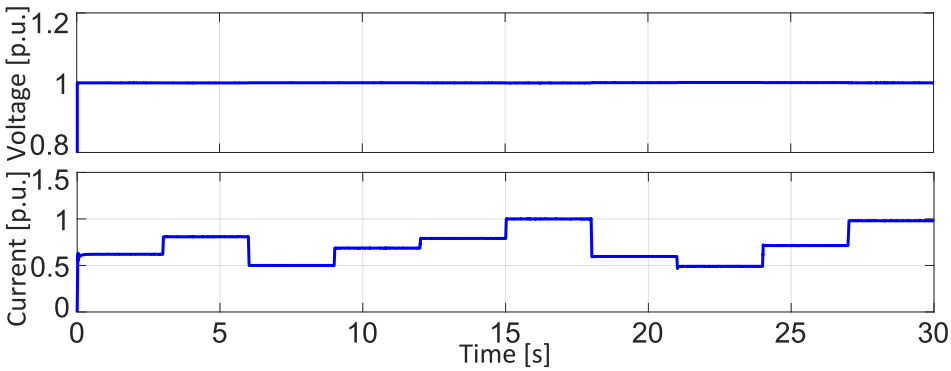

Figure 4.20: The AC bus voltage and the injected current into AC grid in $[p.u.]$.

The current $I_{R_{17}}$ in Figure 4.17 is given by the required direct (I_{ld}) and quadratic (I_{lq}) current to supply the AC grid[8]. Figure 4.19 introduces the references I^*_{ld} and I^*_{lq} given by the second level controller, and shows how their are perfectly tracked by the related dynamics, these currents are shown in per unit ($S_{base} = 100kVA$ and $V_{base} = 400V$). Figure 4.20 depicts rms voltage and current in the AC side of the main grid in per unit. The current injected in AC grid is directly related to the desired active and reactive power injected in the grid as shown in (4.131) and (4.132) respectively. The AC voltage is kept constant since the AC bus is considered to be a strong grid.

Finally, the zero dynamics are introduced to verify their stability. The voltage dynamics V_{C_1}, V_{C_4} and V_{C_7} are depicted in Figure 4.21. Their variations are related to the dynamics of V_S, V_B, V_{PV} and I_{L_3}, I_{L_6}, I_{L_9} in Figure 4.11 and 4.12, according to the power injected/absorbed by the devices. The remaining zero dynamics are depicted in Figure 4.22. They are the output voltages of the converters connecting the devices (battery, PV, DC load, train and AC grid) into the Microgrid by the DC bus. As for the ones previously described, their dynamical behavior depends on the ongoing power flow. Figure 4.22 characterizes their stable behavior.

[8] $I_{R_{17}}$ is the current in the DC side of VSC converter to supply the AC grid

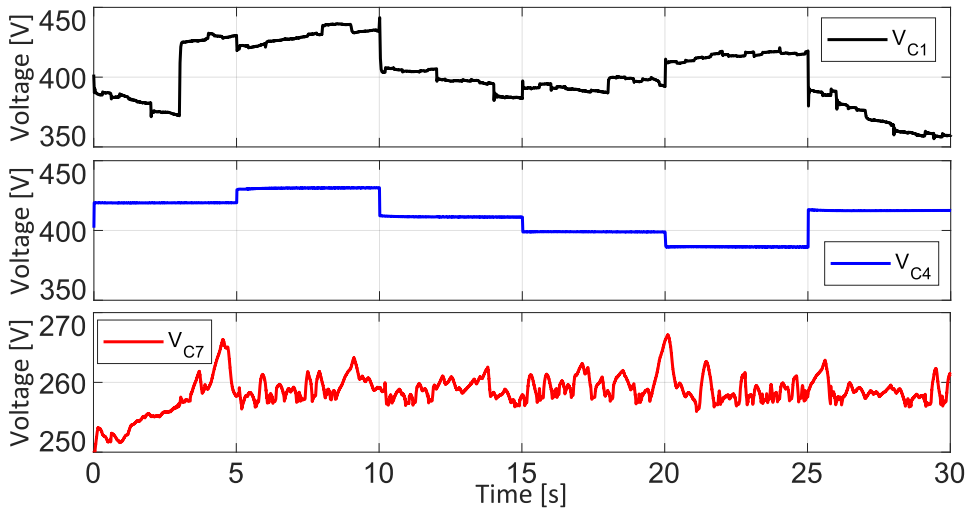

Figure 4.21: The dynamics of V_{C_1}, V_{C_4} and V_{C_7}, respectively.

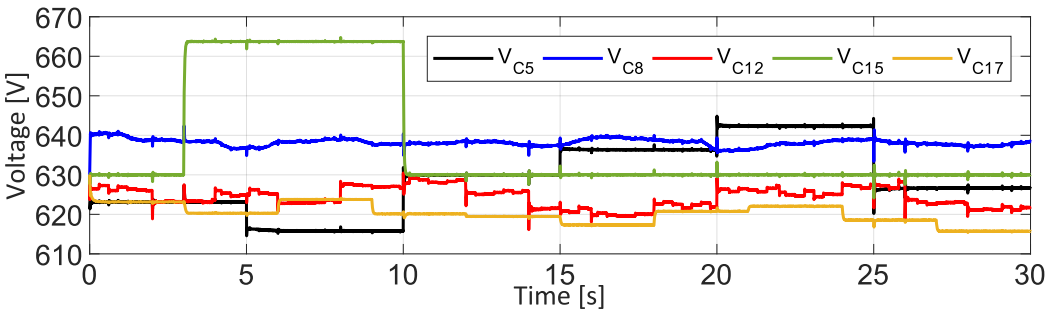

Figure 4.22: The output voltages V_{C_5}, V_{C_8}, $V_{C_{12}}$, $V_{C_{15}}$ and $V_{C_{17}}$ on the Microgrid converters (zero dynamics).

Here, the boundary layer dynamics obtained from the singular perturbation analysis are compared with the real voltage dynamics measured in simulations to provide an evaluation of the limitations between the computed and measured values. The Figure 4.23 shows the measured voltages V_{C_2} and $V_{C_{14}}$ compared to the computed voltages in (4.45) and (4.119), called in the figure as $V_{C_{2n}}$ and $V_{C_{14n}}$, respectively. One may concluded that the measured and computed variables are similar besides very small deviations, which makes feasible the application of the computed variables in the nonlinear control law. The zoom depicted in the last part of the figure highlights that the error between the measured variable and the computed one is irrelevant, showing that the boundary layer model can precisely describe the behavior of the controlled dynamics.

Once that the whole dynamics are introduced, and a full knowledge of the disturbances acting on the Microgrid has been acquired, it is opportune to better highlight the success of the proposed control action. Indeed, Figure 4.15 shows how the proposed nonlinear control performs voltage stability according to the grid codes and with a proper margin of error under the whole set of adverse circumstances,

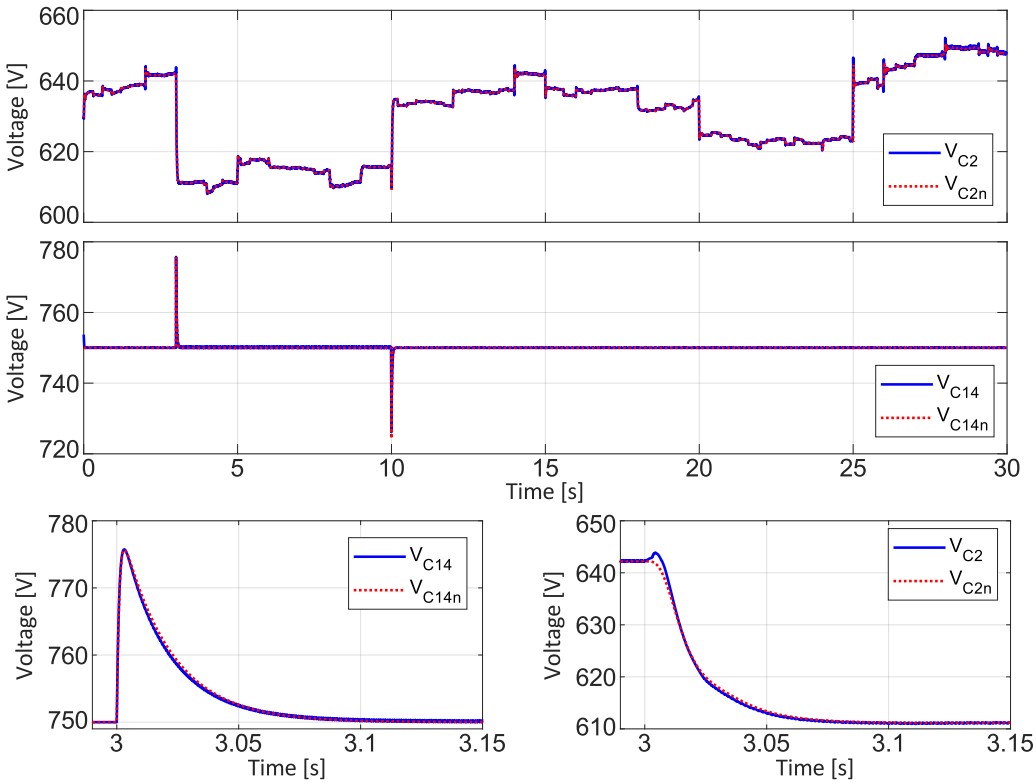

Figure 4.23: The computed (in red) and simulated (in blue) voltages V_{C_2} and $V_{C_{14}}$ with a zoom in the respective variables.

as the regenerate power input, AC and DC load power variations, PV and battery operating point variations. In the next, a further remark about the importance of dealing with nonlinear control is proposed.

4.9.2. A control comparison: Linear vs Nonlinear

A very common control strategy applied to power converters and to Microgrids in general, both in academia and in industry, is the linear PI technique. However, in this work the importance of using nonlinear techniques is addressed. This because the PI technique works around a linearized operation point, which suffers of great limitations when compared to nonlinear control techniques. In this section, a comparison between the two control strategies is done to compare the control performance and the related limitations. The linear PI control law design is detailed in the Appendix, presenting the block diagrams of each converter and the tuning of the control gains according to the desired convergence speed.

Since DC bus voltage stability is the most important requirement, the comparison in Figure 4.24 will focus on this dynamics, which is the key for the good interconnection of the subsystems. Figure 4.24 compares the different voltage

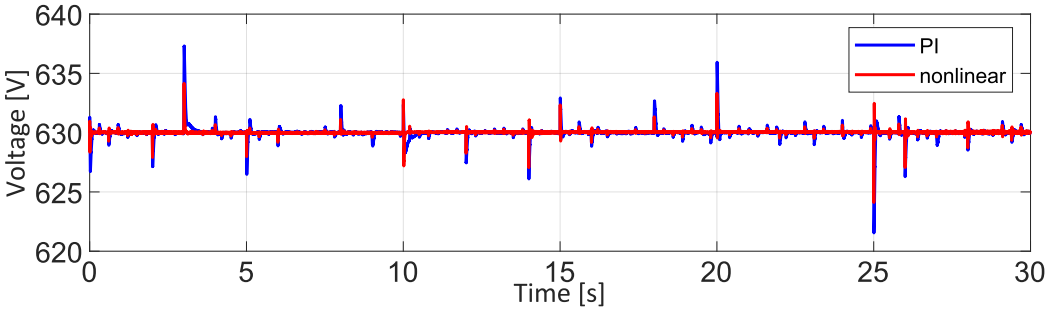

Figure 4.24: A comparison of the DC bus dynamics when the whole system is controlled by simple PI (blue curve) and by the introduced nonlinear technique (red curve).

behavior in the DC bus when using the proposed nonlinear controller (in red) and the classical PI controller (in blue). As it is possible to state, when implementing the introduced nonlinear control, the DC bus dynamics presents smaller variations with respect to the ones with the simpler PI control: indeed, the PI control has higher overshoots. This is better highlighted in Figure 4.25, where a zoom of the comparison for the two most critical transients is depicted. It is clearly shown that the nonlinear control has a smaller overshoot and a faster convergence rate than the PI control. Also, since the nonlinear control considers the different nonlinearities, it has a larger operating region and there is no need to tune the gains continuously according to the different operating point.

Therefore, the proposed nonlinear control is shown to better perform when dealing with the system interconnection. A better controller is very important for improving energy efficiency, which is relevant for renewable energy systems integration in a Microgrid. But the most interesting point on this comparison is the fact that in an extensive set of simulations carried out exploring the effects of several disturbances, it was necessary to re-adjust the PI parameters for each case. While in the same simulations the nonlinear control has always kept the same tuning. In the same way, the nonlinear tuning is a easy pole placement problem for all elements, where the tuning gains interaction are manifested on the DC bus control, while for the PI it is necessary to use one of the standard methods like root locus, but with complex interference between one controller setting to the others. Indeed, this much easier tuning procedure, and the fact that it is valid for the whole operation region are part of the most interesting advantages of the nonlinear control.

The behavior of the controlled dynamics in the Microgrid is introduced in Figure 4.26. The comparison between the PI strategy and the proposed nonlinear control for the controlled variables highlight the performance of each controller. The PI controller has a slower behavior during the highest transients, due to the regenerative

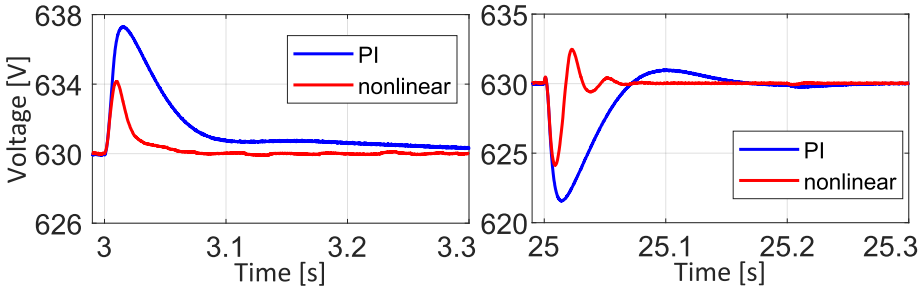

Figure 4.25: A zoom on V_{dc} to compare PI and nonlinear control in the most critical transients.

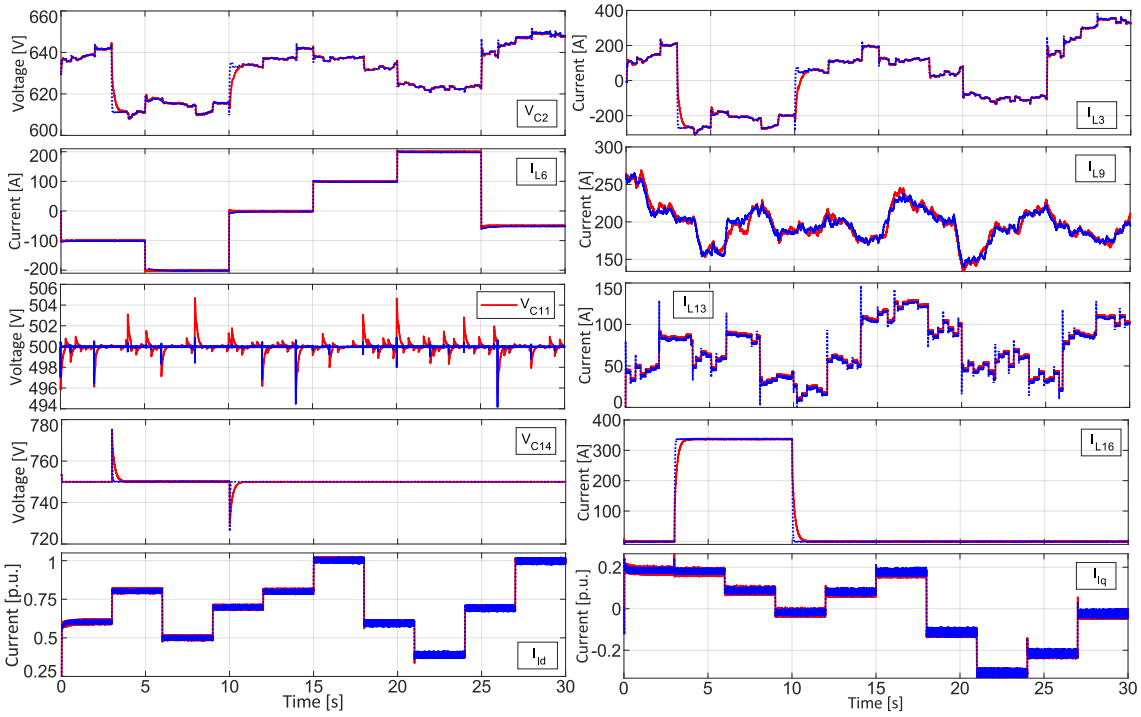

Figure 4.26: The controlled variables in the Microgrid, comparing the PI controller in red and the nonlinear controller in blue.

braking period, which is clearly seen in voltages V_{C_2}, $V_{C_{14}}$ and in currents I_{L_3}, $I_{L_{16}}$. During this period, the nonlinear controller proves more to robust strong variations.

Figure 4.26 also shows that voltage $V_{C_{11}}$ have higher overshoots and slower convergence for the PI controller. The voltage $V_{C_{14}}$ is well controlled for both strategies, but the PI controller has slower convergence during transients. Current I_{L_9} have different behavior for each control strategy, which indicate that the MPPT algorithm influences the control strategy differently. Current I_{L_6} present similar behavior for each control strategy, but the nonlinear controller is slightly better, since the PI controller have small overshoots during transients. Currents I_{ld} and I_{lq} also have similar behavior for both strategies, but PI controller presents higher ripples. Therefore, the nonlinear control presents a greater control response in general.

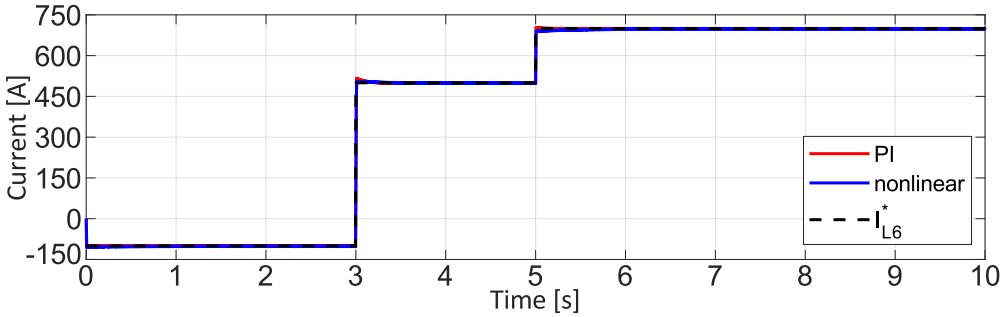

Figure 4.27: The stronger variations in the battery current.

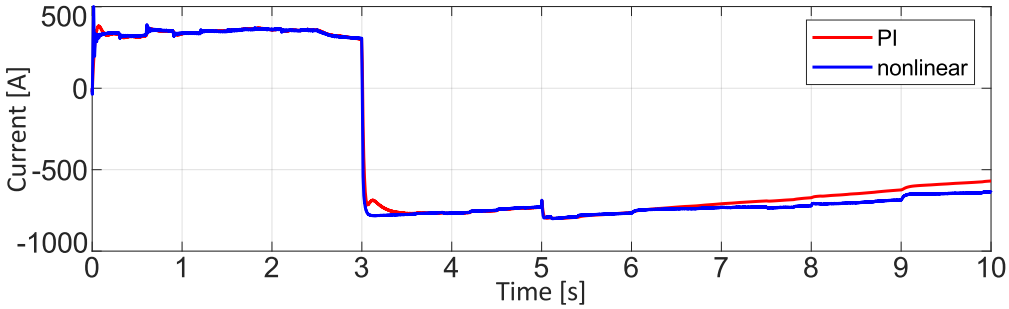

Figure 4.28: The supercapacitor current variation to regulate the power mismatch in the DC bus.

To better understand the operating limits of the system, extreme variations are made so that the system's stability margins are tested. In this case, the battery changes its reference from $-150A$ to $500A$ in 3 seconds, which is exactly the beginning of the regenerative braking. Then, in 5 seconds of simulation the reference goes up to $700A$ in the battery as shown in the Figure 4.27. Then, the supercapacitor assumes this power imbalance and performs a sudden current variation, absorbing around $800A$ from 3 seconds, as shown in Figure 4.28.

These variations cause a very large power imbalance, which is quickly absorbed by the supercapacitor, a large transient peak is generated. The voltage overshoot is up to $660V$ for the PI controller presenting slower convergence when compared with the nonlinear controller with overshoot peak about $645V$, the power balance is again reached shortly after. However, the PI controller cannot attain the power balance and the voltage on the DC bus starts to increase, showing that there is more power being injected into the bus than absorbed. The power is quickly balanced by the nonlinear controller, which keep the DC bus voltage controlled, without large voltage transients, where stability is assured. The voltage in the DC bus is depicted in Figure 4.29, where the instability of the PI controller is highlighted and the robustness of the nonlinear controller is confirmed.

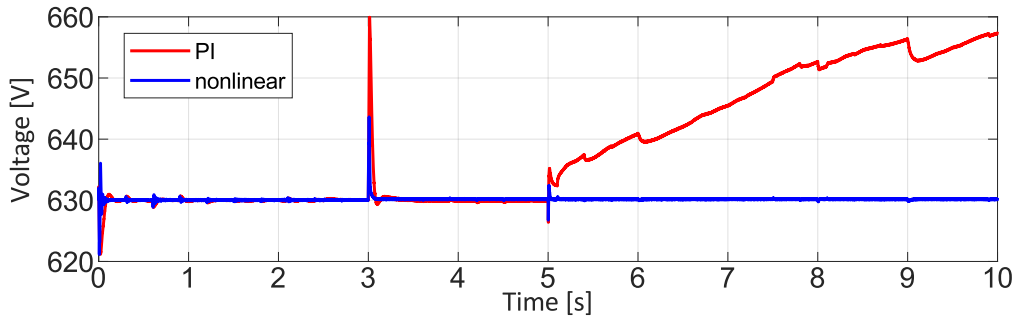

Figure 4.29: The behavior of the DC bus voltage for the PI controller in red and nonlinear controller in blue, when strong variations takes place.

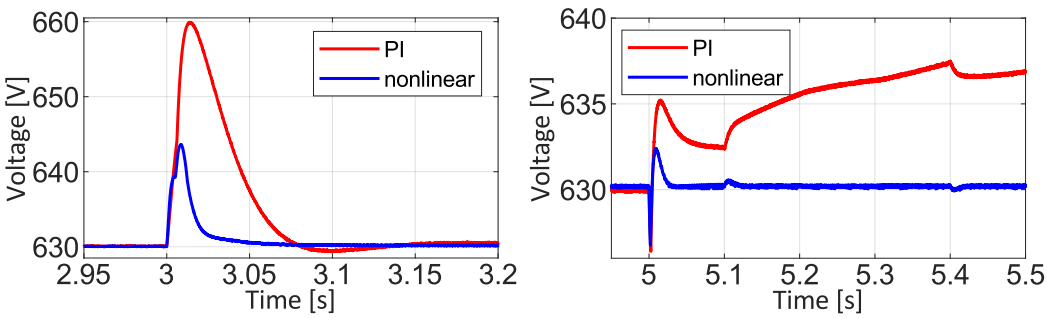

Figure 4.30: A zoom on V_{dc} to highlight the PI controller diverging towards the power imbalance caused by the battery.

Figure 4.30 present a zoom to show the impact of the power imbalance in the DC bus, where the stronger transients are introduced. The divergence of the PI controller is also emphasized in the second part of the figure, after the 5 seconds of simulation.

4.9.3. Robustness

Simulations to the purpose to test the robustness of the proposed control laws are here introduced. The presence of errors for the value of the grid parameters as resistances, inductors and capacitors is treated. Two cases are described: in the first one, the parameters have a value of -20% smaller than nominal one, while in the second case the value is $+20\%$ larger than the nominal value. The considered grid parameters are: R_2, C_1, C_2, L_3 for supercapacitor; R_5, C_4, C_5, L_6 for battery; R_8, C_7, C_8, L_9 for PV array; $R_{12}, C_{11}, C_{12}, L_{13}$ for DC load; $R_{15}, C_{14}, C_{15}, L_{16}$ for train braking; and R_{17}, C_{17} for VSC converter.

The simulations are performed for both the PI and the proposed nonlinear control, in order to better introduce a proper comparison. Figure 4.31 introduces the behavior of the DC bus voltage V_{dc} considering the parametric errors: as it is possible to state, the transients present higher peaks for both control techniques, but

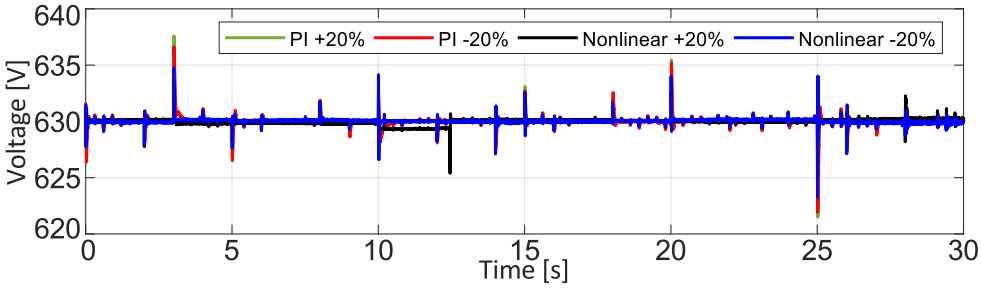

Figure 4.31: The voltage V_{dc} when comparing PI and nonlinear control with parametric errors of +20% and −20%.

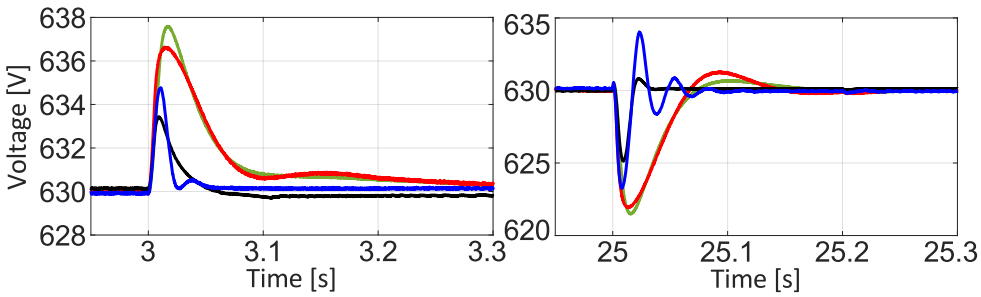

Figure 4.32: A zoom on V_{dc} of Figure 4.31 to compare PI and nonlinear control in the most critical transients.

the nonlinear approach has better performances compared with the PI one because of the smaller overshoots.

A zoom on the highest transients in the proposed robustness test for both control strategies is depicted in Figure 4.32. It is clearly possible to see that the proposed nonlinear strategy presents smaller overshoots and a faster response than the traditional PI strategy even with considerable parametrical errors. One can conclude that the nonlinear controller shows good robustness properties in these simulations. The robust behavior of the proposed nonlinear control is a result from the ISS properties applied in this strategy, which assures good response even with strong parametrical errors. However, PI control is also robust against parametric errors.

The improvements of the nonlinear controller over the PI can be better remarked in Figure 4.33, where the parametric errors are extended to be of +25% higher than the nominal value. As it is possible to see, in this case the voltage on the DC bus for the PI control diverges after the regenerative train braking takes place, while the nonlinear controller keeps a good performance. This behavior is highlighted in Figure 4.34, where a first zoom of Figure 4.33 in the most critical transient is proposed, still highlighting the better control performance of the nonlinear control versus the PI, and with a second zoom on the beginning of the unstable behavior of

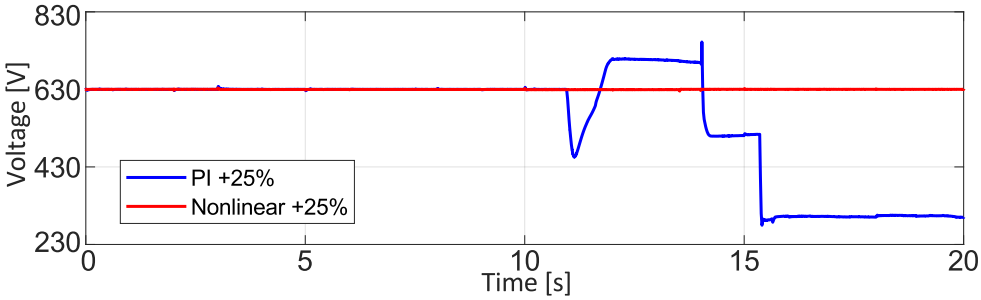

Figure 4.33: The voltage V_{dc} in case of +25% higher parametric error than the nominal value.

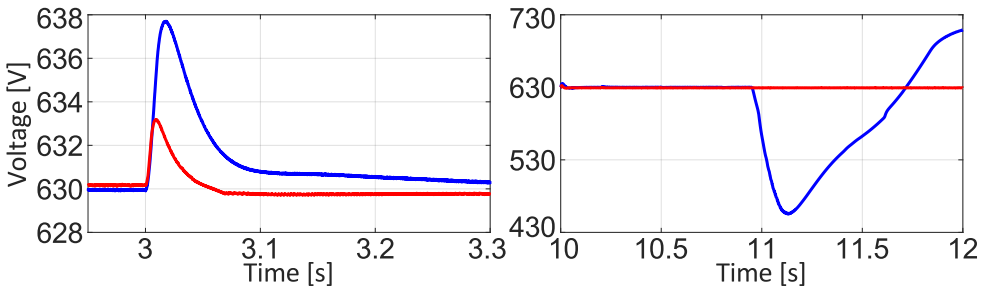

Figure 4.34: A zoom of Figure 4.33 in the highest transients, showing the unstable behavior of PI control after the high peak transient due to the regenerative braking.

the PI strategy. An interesting point to be addressed is the fact that the PI needs to re-adjust the control gains and parameters to keep following the grid reference and to correctly perform stability, while the nonlinear gains can work in a broader region of attraction and consequently need less tuning. Therefore, it is possible to conclude that the nonlinear controller can stand larger disturbances, like the braking energy recovery, and that it is able to operate in a wider region with more robust performances towards parametrical errors when compared with the standard PI control.

4.10. Different Approaches for DC Bus Control

4.10.1. Fixed reference for V_{C_2}

Different from previous results, one may propose here a fixed reference value V_{dc}^* as desired reference for V_{C_2} instead of a time-varying $V_{C_2}^e$ used to exactly steer the voltage of the DC grid. This will induce a small steady state error in V_{dc}, which is the voltage drop in R_2 (cable loss). This happens because the capacitor's voltage will not be driven to the desired bus voltage in a direct way. Nevertheless, the trade off between this small error (proportional to the resistance of the cables connecting V_{C_2} and V_{dc}) and a greatly simplified control design is very convenient.

In this case, the regenerative braking from trains and the grid-connection are not included in the stability proof and in simulations for simplification purposes. But, they can be easily inserted on the bus interconnection. The model of the DC Microgrid for this approach is presented in Figure 4.35.

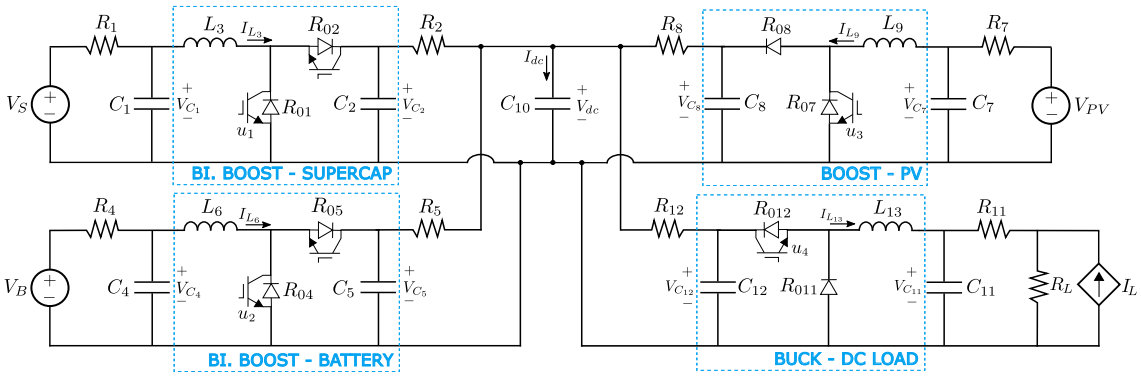

Figure 4.35: The considered DC Microgrid.

DC bus voltage dynamic is rewritten according to Figure 4.35.

$$\dot{V}_{dc} = \frac{1}{C_{10}}\left[\frac{1}{R_2}(V_{C_2} - V_{dc}) + \frac{1}{R_5}(V_{C_5} - V_{dc}) + \right.$$
$$\left. + \frac{1}{R_8}(V_{C_8} - V_{dc}) + \frac{1}{R_{12}}(V_{C_{12}} - V_{dc})\right] \tag{4.209}$$

The behavior of V_{dc} dynamic must be analyzed to verify its convergence, when V_{C_2} is controlled to V_{dc}^*. Then, V_{dc} dynamic is not controlled by any control input, and this V_{dc}'s dynamic can be calculated as follows:

$$\dot{V}_{dc} = \frac{1}{C_{10}}\left[\frac{1}{R_2}(V_{dc}^* - V_{dc}) + \frac{1}{R_5}(V_{C_5}^e - V_{dc}) + \right.$$
$$\left. + \frac{1}{R_8}(V_{C_8}^e - V_{dc}) + \frac{1}{R_{12}}(V_{C_{12}}^e - V_{dc})\right] \tag{4.210}$$

where $V_{C_5}^e$, $V_{C_8}^e$ and $V_{C_{12}}^e$ were presented in (4.62), (4.75) and (4.95), respectively.

The equilibrium point of V_{dc} is calculated to provide steady-state value, which varies according to the other devices of the Microgrid (PV, battery and DC load).

$$V_{dc}^e = R_{eq}\left[\frac{V_{dc}^*}{R_2} + \frac{V_{C_5}^e}{R_5} + \frac{V_{C_8}^e}{R_8} + \frac{V_{C_{12}}^e}{R_{12}}\right] \tag{4.211}$$

where:

$$R_{eq} = \frac{R_2R_5R_8R_{12}}{R_5R_8R_{12} + R_2R_8R_{12} + R_2R_5R_{12} + R_2R_5R_8} \tag{4.212}$$

It is clearly seen in (4.211) that the closer the voltages $V_{C_5}^e$, $V_{C_8}^e$ and $V_{C_{12}}^e$ are to reference V_{dc}^* the smaller DC bus error in steady-state. The reference V_{dc}^* given by

controlling $V_{C_2} \to V_{dc}^*$ in equation (4.211) implies that the error in steady state is around this value.

To analyze the local convergence of V_{dc} dynamics, let us consider the eigenvalue of the linearization:

$$J_{10} = -\left[\frac{1}{R_2} + \frac{1}{R_5} + \frac{1}{R_8} + \frac{1}{R_{12}}\right] \tag{4.213}$$

Indeed, the Jacobian J_{10} is always negative, then the equilibrium point of V_{dc} is locally stable around this equilibrium value V_{dc}^e.

4.10.1.1. Simulation results

Simulations results using the same parameters configuration in Table (4.1) for the DC Microgrid is provided here. Voltage V_{C_2} from the supercapacitor subsystem is controlled in a fixed reference, which is the desired DC bus voltage $V_{C_2}^* = V_{dc}^*$. This approach simplifies the control design to regulate the DC bus in the Microgrid and its stability analysis as previously presented. The following simulation results expose the convenience and simplicity of this strategy, where the system can operate with some limitations.

The voltage reference is $V_{C_2}^* = 630V$. This approach does not control V_{dc} directly, but it provides DC grid voltage regulation by maintaining V_{dc} in a granted region (with an error smaller than 5%) with smooth oscillations. To understand the influence of the resistance between the supercapacitor subsystem and DC bus, the value of R_2 is changed composing three different scenarios: 1) $R_2 = 0.1\Omega$, 2) $R_2 = 0.5\Omega$ and 3) $R_2 = 0.05\Omega$.

Figure 4.36 introduces the dynamical behaviour of the voltage V_{C_2} with respect to its reference $V_{C_2}^*$ where the three proposed scenarios are shown. It is clear that the voltage remains with the same dynamics considering the variation of R_2, but as larger is R_2, smaller is the overshoots and the ripples in V_{C_2}. The voltage has some small transients according to variation on the other devices of the grid (PV, DC load and battery), with maximum error about 0.4%. The ripples are caused by the converter switching; nevertheless, they can be considered moderate.

The calculated voltage V_{C_2} in (4.45) is depicted in Figure 4.37. This is the simplified dynamic for V_{C_2}, considering I_{L_3} already on its equilibrium point $I_{L_3}^e$, from singular perturbation analysis. This variable is used to design the control strategy of the DC bus voltage. As shown in Figure 4.37, the voltage is well controlled in V_{dc}^*, but for smaller values of R_2, the voltage have higher overshoots with more oscillation, which may bring instability to the grid.

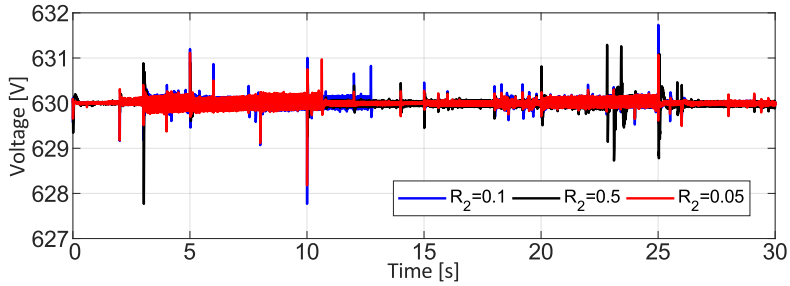

Figure 4.36: V_{C_2} voltage behavior for different values of R_2.

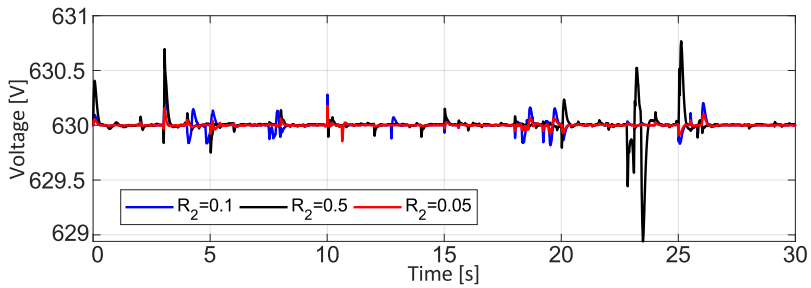

Figure 4.37: Calculated voltage V_{C_2} from equation (4.45) for different values of R_2.

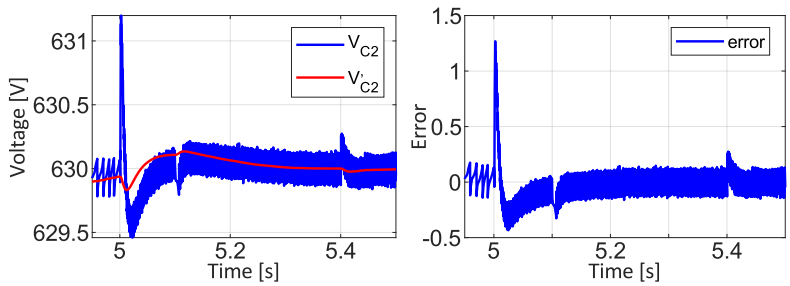

Figure 4.38: Voltage V_{C_2} with the calculated value from equation (4.45) and the error between those variables.

Figure 4.38 presents a comparison between the calculated[9] (in red) and measured (in blue) voltage V_{C_2}. The behavior of both signals are quite similar, since the error is very small in transients (0.15% maximum). The error is zero in steady-state, besides the ripple in the measured voltage as depicted in the figure. Then, it is possible and reasonable to use the calculated V_{C_2} instead of the measured one to calculate $I^*_{L_3}$ as made in subsection 4.2.6.

The DC bus voltage is depicted in Figure 4.39, where the three scenarios are simulated to highlight the dynamical behavior of V_{dc}. As expected, the lower the value of R_2, the smaller the steady-state error of V_{dc}, the more accurate the control of the bus voltage, since V_{C_2} approaches DC bus voltage. In the third case

[9]The proposed control strategy uses the calculated voltage V_{C_2}, obtained in (4.45) instead of the measured value. This calculation is given by the obtained simplified dynamics of V_{C_2} from singular perturbation analysis where I_{L_3} is already considered in its equilibrium point.

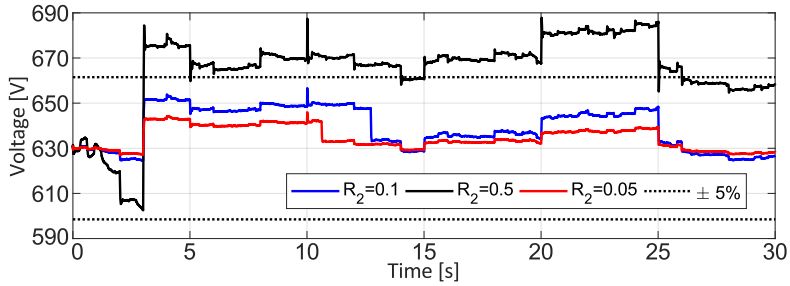

Figure 4.39: DC bus voltage (V_{dc}) profile for different values of R_2.

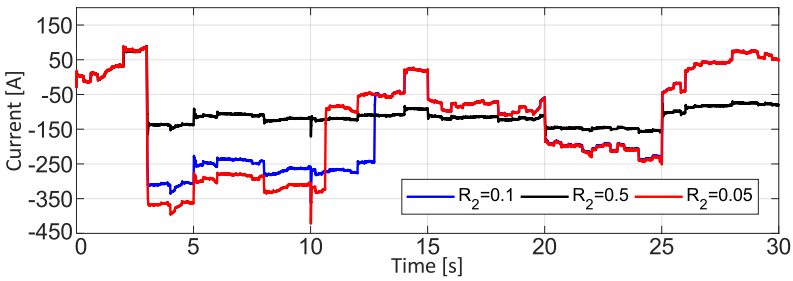

Figure 4.40: Controlled current I_{L_3} on the supercapacitor subsystem for different values of R_2.

scenario, where $R_2 = 0.5\Omega$, the behavior of V_{dc} conflicts with grid requirements. Grid requirements generally allow voltage variations of a maximum of 5% relative to the nominal value. It is clearly seen that the value of resistor R_2 must be considered in this control approach to meet network requirements.

Figure 4.40 shows the behavior of I_{L_3} current according to simulated variations in Microgrid. The influence of resistance R_2 is evident, because the lower the cable losses between the supercapacitor and the DC bus, more current can be injected to keep the DC bus controlled, reducing the error on voltage V_{dc}. However, in the case where resistance value is equal to $R_2 = 0.5\Omega$, the variations of current I_{L_3} are much smaller, indicating that the supercapacitor is not varying enough to regulate bus voltage, resulting in poor control performance.

4.10.1.2. Control robustness test

The Input to State Stability (ISS) results from stability analysis assure robustness properties for the designed control law. Therefore, simulations with the purpose to test the robustness of the proposed control laws are performed in this subsection. The robustness is tested by introducing errors in the components parameters of the Microgrid grid, where the considered parameters are inductors, capacitors and resistors. In real Microgrid systems, it is very common to have uncertainties in these parameters, therefore the proposed control strategy should be able to have

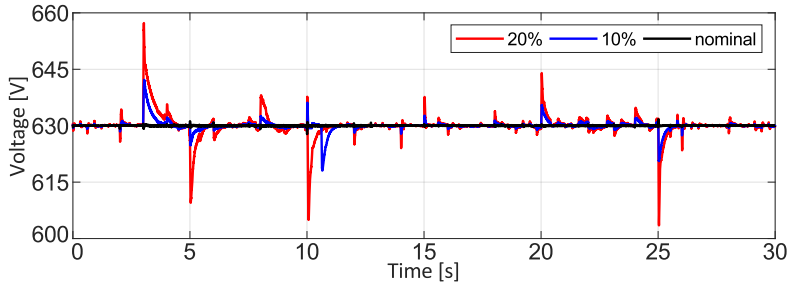

Figure 4.41: Voltage V_{C_2} with parameters uncertainties 10% and 20%.

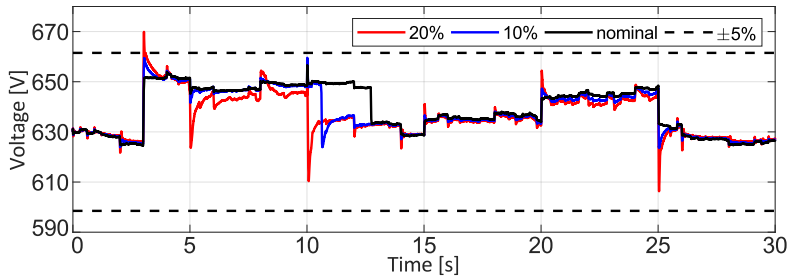

Figure 4.42: Voltage on the DC bus with parameters uncertainties 10% and 20%.

a good performance in the presence of this uncertainties. In simulations, 2 cases are described: the first case, the parameters are 10% smaller than the nominal one, and the second case the parameters are 20% smaller than the nominal value. The parameters considered with uncertainties are presented in Table 4.1 and they are: $R_2, C_1, C_2, L_3,\ R_5, C_4, C_5, L_6,\ R_8, C_7, C_8, L_9,\ R_{12}, C_{11}, C_{12}$ and L_{13}.

The parametrical robustness test made for voltage V_{C_2} is depicted in Figure 4.41. In this case, the transients present considerable higher peaks as the parametrical errors increase. In the first scenario (10% error), the higher transient peaks are about 2.1%, and the second scenario is the worse case, with transient peaks about 4.5% of the nominal.

The profile of the DC bus voltage V_{dc} is depicted in Figure 4.42 where the parametrical errors are analyzed. For voltage V_{dc}, the results with parametrical errors are quite similar, which indicates that even in uncertainties problems, the voltage profile remains stable. But, for the second scenario, the voltage has a peak that exceeds the limits allowed by general grid requirements[10].

The simulations highlight the robustness of the proposed control strategy, since the system remains stable even when high parametrical errors takes place (considered 20%). Concluding, the control have good robustness properties and great

[10]Usually, network regulation allows a maximum variation in steady-state of 5% in the voltage profile. In Brazil, the voltage limits established by Prodist Module 8 are 5% above and 7% below the nominal for traditional distribution systems.

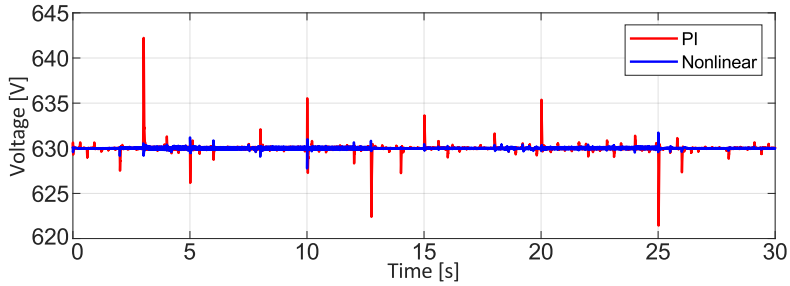

Figure 4.43: Voltage V_{C_2} controlled by nonlinear control (in blue) and linear control (in red).

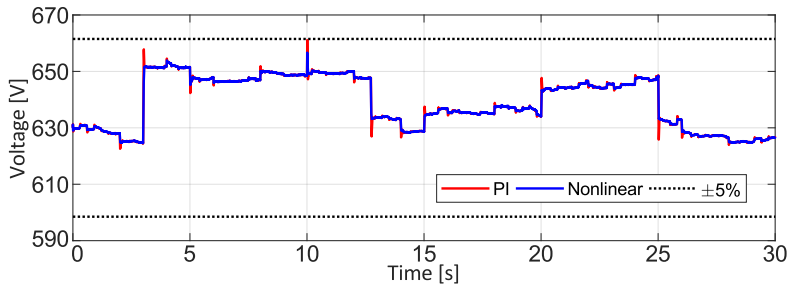

Figure 4.44: A comparison on the DC bus voltage (V_{dc}) between the proposed nonlinear and linear control.

performance, but the level of uncertainties should be investigated to ensure that the voltage is within the allowed limits.

4.10.1.3. Comparison with PI control

The proposed control strategy is also compared with standard control techniques to highlight the benefits of the nonlinear strategy. Voltage V_{C_2} profile is depicted in Figure 4.43, where the nonlinear control in blue line is compared with linear PI control in red line. The PI control strategy have higher overshoots compared with the nonlinear approach. The highest transient overshoot in the PI control is about 2% error. Therefore, nonlinear control presents much better control performance.

Figure 4.44 introduces the comparison between nonlinear control and linear PI control for DC bus voltage V_{dc}. Here, it is possible to notice that the voltage has the same profile for both control strategies, but the linear control presents some peaks that are very close to the allowed limits. The nonlinear control is able to work in a wide operation region, with no need of gains re-adjustment. On the other hand, the linear control strategy works only around one operation point, and then the control gains must be redesigned to keep the stability of the system.

4.10.2. Simplification on C_2 dynamics

As previously discussed, the DC bus Voltage dynamics is the sum of all currents flowing trough the devices of the grid. The current flowing on the DC bus from Figure 4.35 is written as follows:

$$I_{dc} = I_{R_2} + I_{R_5} + I_{R_8} + I_{R_{12}} \tag{4.214}$$

The currents that flows to the DC bus are composed of the voltage drop over the output resistance as exemplified next:

$$I_{R_2} = \frac{1}{R_2}(V_{C_2} - V_{dc}) = I_{L_3}(1 - u_1) - C_2\dot{V}_{C_2} \tag{4.215}$$

The simplification of C_2 dynamics eliminates the non-minimal phase feature of the DC/DC converter. In this case, the current I_{L_3} is seen as the control input to control directly control the voltage V_{dc}. Therefore, ff we neglect the converter switching and the transient current on capacitor C_2, the current from the supercapacitor subsystems becomes: $I_{R_2} = I_{L_3}$. In fact, this consideration despises some terms of the equation, which is expressed as follows:

$$I_{R_2} - I_{L_3} = -u_1 I_{L_3} - C_2\dot{V}_{C_2} \tag{4.216}$$

This may result in a very convenient simplification of V_{dc} dynamics, where current I_{L_3} explicity appears on voltage V_{dc}.

$$\dot{V}_{dc} = \frac{1}{C_{10}}\left[I_{L_3} + \frac{1}{R_5}(V_{C_5} - V_{dc}) + \frac{1}{R_8}(V_{C_8} - V_{dc}) + \frac{1}{R_{12}}(V_{C_{12}} - V_{dc})\right] \tag{4.217}$$

With this simplification, one may propose a Lyapunov function candidate to control $V_{dc} \to V_{dc}$ using I_{L_3} as the degree of freedom that will result in a much simpler control strategy:

$$W = \frac{C_{10}}{2}V_{dc}^2 + \frac{C_5}{2}(V_{C_5} - V_{C_5}^e)^2 + \frac{C_8}{2}(V_{C_8} - V_{C_8}^e)^2 + \frac{C_{12}}{2}(V_{C_{12}} - V_{C_{12}}^e)^2 > 0 \tag{4.218}$$

when its time derivative ($\dot{W}$) is investigated, I_{L_3} is seen as the control input to bring stability for the whole grid.

$$\begin{aligned}\dot{W} = V_{dc}\Bigg[I_{L_3} + \frac{1}{R_5}(V_{C_5} - V_{dc}) + \frac{1}{R_8}(V_{C_8} - V_{dc}) + \\ + \frac{1}{R_{12}}(V_{C_{12}} - V_{dc}) + \Psi_5 + \Psi_8 + \Psi_{12}\Bigg]\end{aligned} \tag{4.219}$$

To obtain a stable grid-connection, it is analyzed the time derivative of W where the desired expression for $\dot{W}$ is presented as follows:

$$\dot{W} = -\frac{1}{R_2}(V_{dc}^2 - V_{dc}^{*\,2}) + \Psi_{W_1} \tag{4.220}$$

with:

$$\Psi_{W_1} = -\frac{(V_{C_5} - V_{C_5}^e)^2}{R_5} - \frac{(V_{C_8} - V_{C_8}^e)^2}{R_8} - \frac{(V_{C_{12}} - V_{C_{12}}^e)^2}{R_{12}} \tag{4.221}$$

The Lyapunov function (4.218) then results to be an ISS-like Lyapunov function with equilibrium point in V_{dc}^* with same properties as the previous results [190,206]. Here, I_{L_3} is the control input that can regulate V_{dc} in the desired value and assure asymptotic stability for those dynamics. Therefore, the following control input is assigned to be the desired $I_{L_3}^*$, such that one obtains (4.220) as the time-derivative of the Lyapunov function.

$$\begin{aligned} I_{L_3}^* = \frac{1}{V_{dc}}\Bigg[-\frac{1}{R_2}(V_{dc}^2 - V_{dc}^{*\,2}) + \Psi_{W_1} + \Psi_5 + \Psi_8 + \Psi_{12} + \\ -V_{dc}\left(\frac{1}{R_5}(V_{C_5} - V_{dc}) + \frac{1}{R_8}(V_{C_8} - V_{dc}) + \frac{1}{R_{12}}(V_{C_{12}} - V_{dc})\right)\Bigg] \end{aligned} \tag{4.222}$$

4.10.2.1. Simulation results

The simplification on C_2 dynamics approach was tested in simulations using the same parameters of Table 4.1, and the same inputs for irradiation profile and DC load demand from Figure 4.9.

The currents I_{L_3}, I_{L_6}, I_{L_6} and $I_{L_{12}}$ are depicted in Figure 4.45. Currents I_{L_6}, I_{L_9} and $I_{L_{12}}$ from battery, PV and DC load present the same dynamics from previous simulations, since they have the same inputs. But current I_{L_3} is now following a different control reference $I_{L_3}^*$ to directly regulate the voltage V_{dc}.

The DC bus voltage is regulated with steady-state error from ISS results, but the voltage profile can be considered satisfactory since, the DC grid remains stable over many grid perturbations. The DC load is properly supplied as the voltage $V_{C_{11}}$ is controlled in $V_{C_{11}}^*$. Figure 4.46 presents the controlled voltages in the Microgrid.

In this control strategy, V_{C_2} is considered a zero dynamics. The output voltage converters present a stable behavior in simulations as depicted in Figure 4.47

4.10.3. DC bus generalization: Thévenin equivalent

For generalization purposes, one may consider that the voltage of the output capacitor of the PV array, the battery and the load are considered as piecewise constant plus a slowly time-varying disturbance. As the supercapacitor is allocated exclusively to perform voltage stabilization in the DC bus, it will only act when there is a power mismatch on power balance. The proposal is to design equivalent dynamics for the other devices of the Microgrid, when many different devices are integrated in

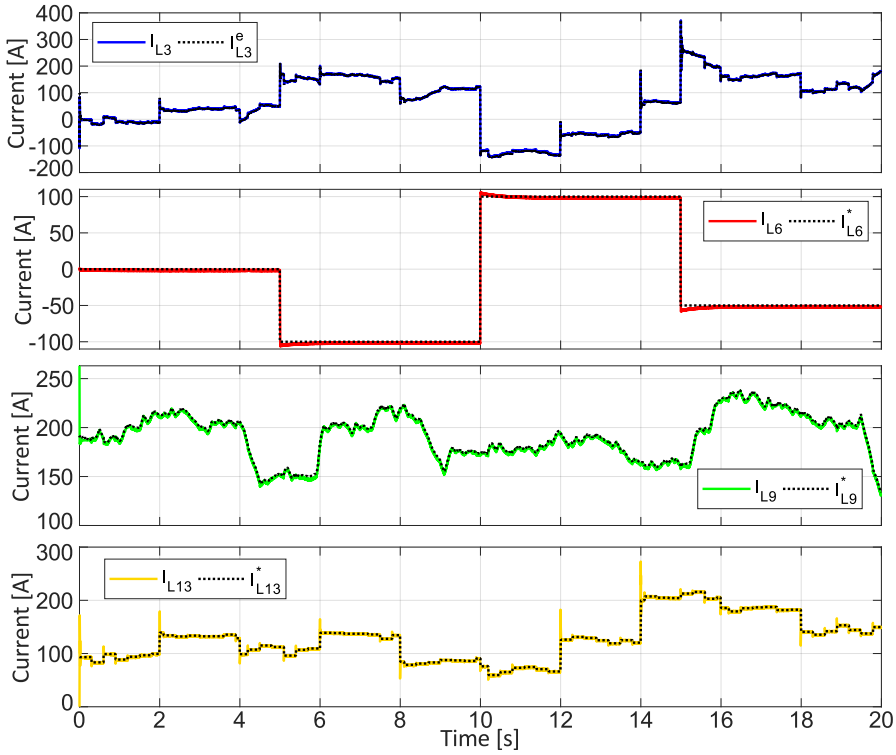

Figure 4.45: The controlled currents I_{L_3}, I_{L_6}, I_{L_9} and $I_{L_{12}}$.

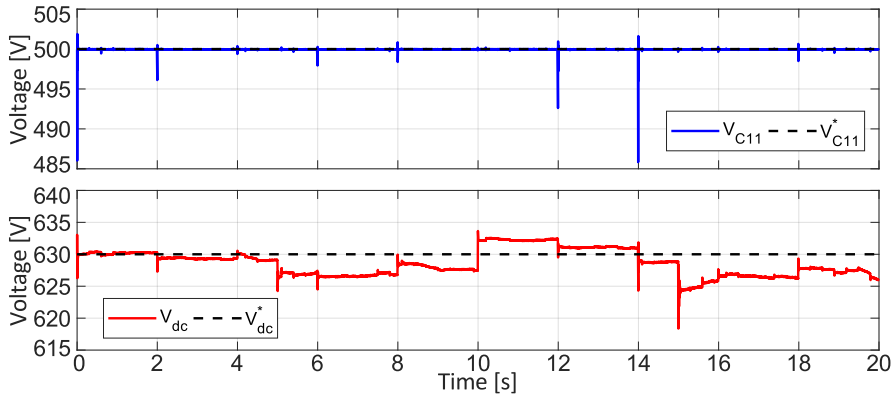

Figure 4.46: The controlled voltages $V_{C_{11}}$ and V_{dc}.

the system. This generalization approach is to study the DC bus dynamics compared with many other devices in the Microgrid.

This because the battery is controlled in a time-scale of seconds according to power flow regulation, while the load is in general a sum of switching elements in addition to slowly (seconds) varying ones. Finally, in the PV case, the disturbances come from the solar radiance, where the solar variations is much slower than the voltage control time-scale. The time varying disturbances will be neglected; the effect of this will be an additive disturbance in a linear stable closed loop system, which will be compensated by the robustness of the controller. Nevertheless, there

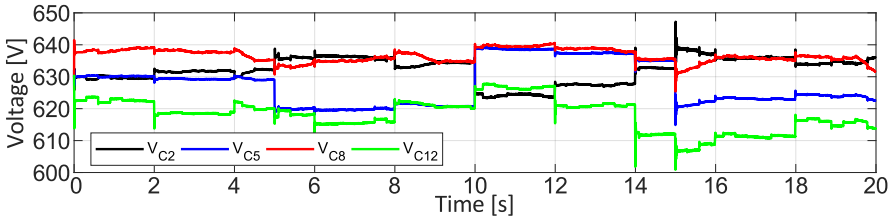

Figure 4.47: Zero dynamics V_{C_2}, V_{C_5}, V_{C_8}, and $V_{C_{12}}$.

will be an arbitrarily small slowly varying disturbance that will not bring the system outside of the operation margin defined around the desired equilibrium point.

From the hierarchical point of view, the secondary control target is to perform the power flow trough the battery subsystem. In general, the DC bus is always balanced, unless there are errors in the power flow calculation, where the supercapacitor take place to act. The DC bus voltage can be considered always around the region the operation point of the grid even under stronger power imbalance, then a equivalent approach can be applied.

One can apply Thévenin theorem on those devices to obtain an equivalent circuit. The DC bus is the coupling point for the integrated devices in the system, modeled as a capacitance. The Thévenin equivalent circuit is used to substitute PV, battery and load by a voltage source V_{th} and a resistance R_{th}.

Thévenin voltage V_{th} is calculated according to PV, battery and load system in open circuit.

$$V_{th} = R_{th}\left[\frac{V_{C_5}}{R_5} + \frac{V_{C_8}}{R_8} + \frac{V_{C_{12}}}{R_{12}}\right] \tag{4.223}$$

where V_{C_5}, V_{C_8} and $V_{C_{12}}$ are converters' output voltage on PV, battery and load. They are considered according to generalization assumption; consequently, the resulting voltage V_{th} can be considered piecewise constant plus slowly time-varying as well. In this approach, other devices included in the DC bus can be inserted the equivalent circuit. Figure 4.48 depicts the Thévenin equivalent circuit on the Microgrid.

The equivalent Thévenin resistance R_{th} is calculated as

$$R_{th} = \frac{R_5 R_8 R_{12}}{R_5 R_8 + R_5 R_{12} + R_8 R_{12}} \tag{4.224}$$

where R_5, R_8 and R_{12} are the cable losses of the converters on PV, battery and DC load respectively.

Figure 4.49 depicts the Microgrid's simplified electrical model due to the considerations done above. The system is composed by the converter that is

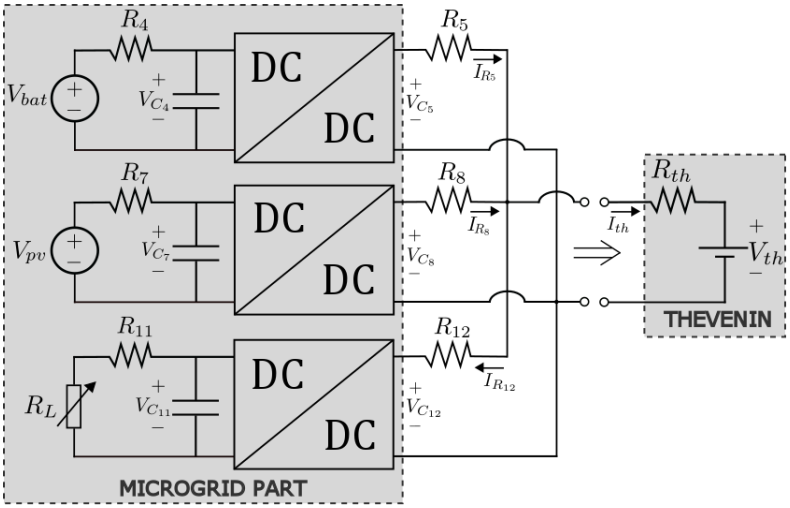

Figure 4.48: Thévenin equivalent circuit for the DC Microgrid.

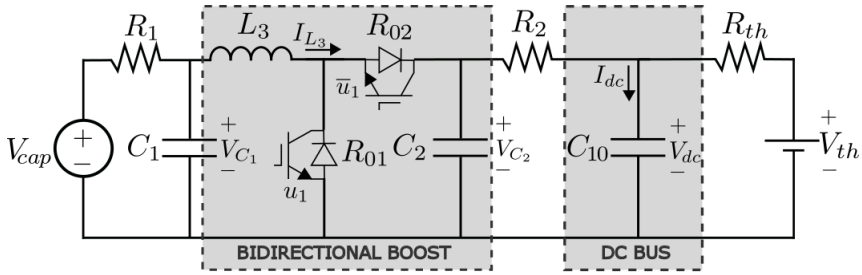

Figure 4.49: The simplified electrical model of the DC Microgrid.

connected to the supercapacitor, a capacitor representing the DC bus and the Thévenin equivalent circuit.

The equivalent circuit is expressed using state space average model as follows:

$$\dot{V}_{dc} = \frac{1}{C_{10}R_2}(V_{C_2} - V_{dc}) + \frac{1}{C_{10}R_{th}}(V_{th} - V_{dc}) \tag{4.225}$$

with this simplification, the control strategy to control the DC bus of the Microgrid can be easily developed even when many devices are inserted into the grid working around the operational point, but the stability analysis becomes limited due to the assumptions made.

One may proposed a Lyapunov function without considering the zero dynamics of the system, since they are proven to be locally stable in previous sections. Equivalent Thévenin voltage is assumed to be piecewise constant where its dynamics are not considered. Therefore, a Lyapunov function candidate can be written as follows:

$$W_{10} = \frac{C_{10}}{2}(V_{dc} - V_{dc}^*)^2 + \frac{K_{10}^{\alpha}}{2}\alpha_{10}^2 \tag{4.226}$$

where $\dot{\alpha}_{10} = V_{dc} - V_{dc}^*$, is a auxiliary variable for a integral term.

The derivative of W_{10} is written as follows, where V_{C_2} is seen as the degree of freedom of this system.

$$\dot{W}_{10} = (V_{dc} - V_{dc}^*)\left[\frac{1}{R_2}(V_{C_2} - V_{dc}) + \frac{1}{R_{th}}(V_{th} - V_{dc}) + K_{10}^{\alpha}\alpha_{10}\right] \tag{4.227}$$

hence, V_{C_2} is calculated, such that, the system is asymptotically stable with the following Lyapunov derivative:

$$\dot{W}_{10} = -K_{10}(V_{dc} - V_{dc}^*)^2 \tag{4.228}$$

The control input $V_{C_2}^*$ is given as follows.

$$V_{C_2}^* = R_2\left[-K_{10}(V_{dc} - V_{dc}^*) - K_{10}^{\alpha}\alpha_{10} - \frac{1}{R_{th}}(V_{th} - V_{dc}) + \frac{V_{dc}}{R_2}\right] \tag{4.229}$$

Concluding, the system is asymptotically stable considering a region around the operating point.

4.10.3.1. Simulation results

The Thévenin equivalent approach was tested in simulations using the same parameters of Table 4.1, and the same inputs for irradiation profile and DC load demand from Figure 4.9. In this case, the Thévenin voltage is given in Figure 4.50, where the behavior of the battery, PV array and the DC load subsystems are expressed in the equivalent voltage V_{th}.

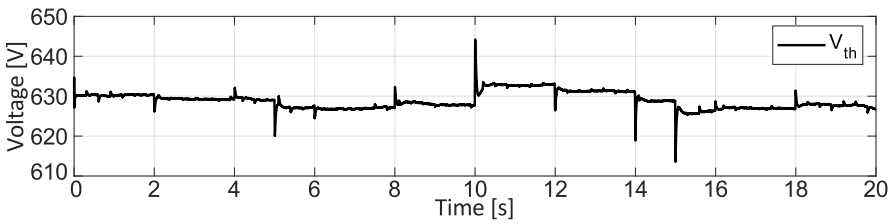

Figure 4.50: The equivalent Thévenin voltage (V_{th}) for the Microgrid part (battery, PV and DC load).

The currents I_{L_3}, I_{L_6}, I_{L_6} and $I_{L_{12}}$ are depicted in Figure 4.51. Currents I_{L_6}, I_{L_9} and $I_{L_{12}}$ from battery, PV and DC load present the same dynamics from previous simulations, since they have same inputs. But current I_{L_3} follows the reference to regulate the voltage V_{C_2}. Therefore the behavior of voltage $V_{C_2} \rightarrow V_{C_2}^*$ is different from last results as depicted in Figure 4.52.

The DC bus voltage is controlled in a fixed reference, with good transient performance, which means small overshoots and fast convergence. Reference computed

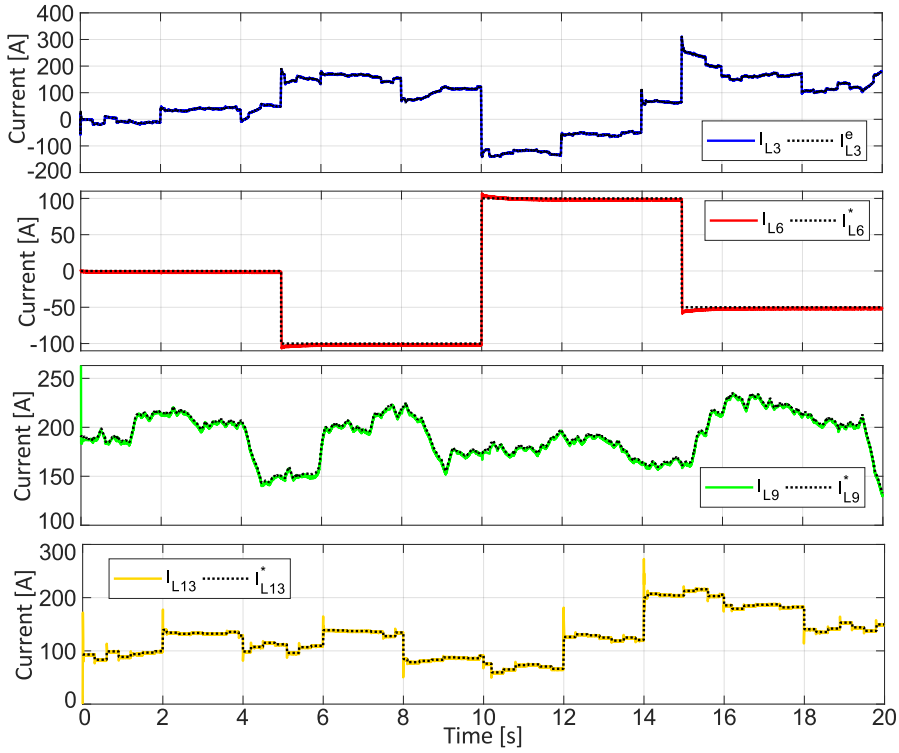

Figure 4.51: The controlled currents I_{L_3}, I_{L_6}, I_{L_9} and $I_{L_{13}}$ in the equivalent Thévenin approach.

in (4.229) is well tracked and provides satisfactory DC bus regulation. Similarly voltage $V_{C_{11}}$ controlled assuring proper power supply for the DC load.

Finally, the zero dynamics voltages representing the grid interconnection is depicted in Figure 4.53. Voltages remain stable towards the variations of the system as expected from local stability analysis.

4.11. Conclusions

This chapter addresses the problem of controlling a Hybrid AC/DC Microgrid with grid-connection, renewables sources and different ESS. The proposed Microgrid is used to absorb the train braking regenerative power, that constitutes a very large and sudden peak of power that is difficult to address by classical linear controllers. This Microgrid is also used to integrate distributed generation as PV arrays. The proposed system is based on two energy storages with different time-scale, i.e., a battery and a supercapacitor. The Microgrid is then completed with a variable DC load (that represents the aggregation of all DC loads as lights, heating and electric vehicles) and a connection with the AC grid. The proposed DC Microgrid is controlled by low-level distributed nonlinear controllers. For each subsystem

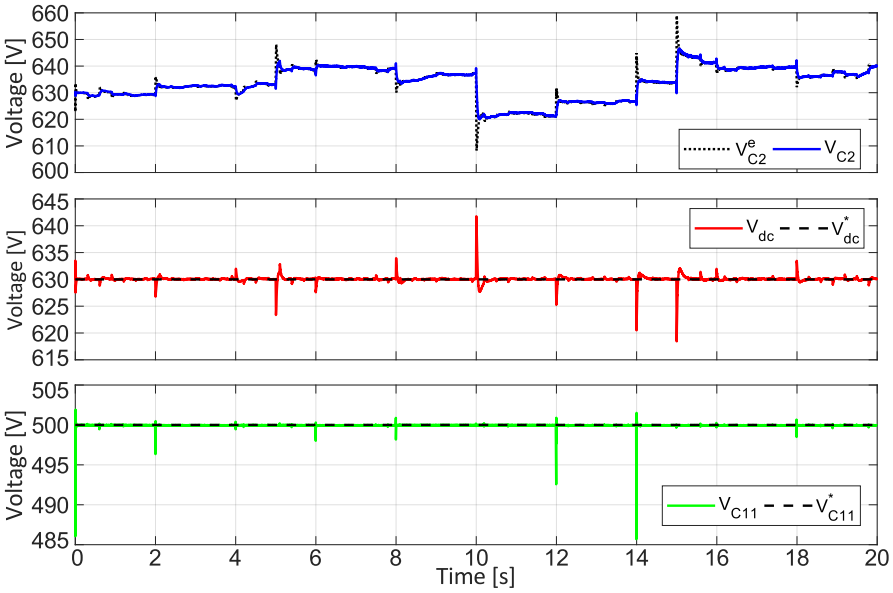

Figure 4.52: The controlled voltages V_{C_2}, V_{dc} and $V_{C_{11}}$.

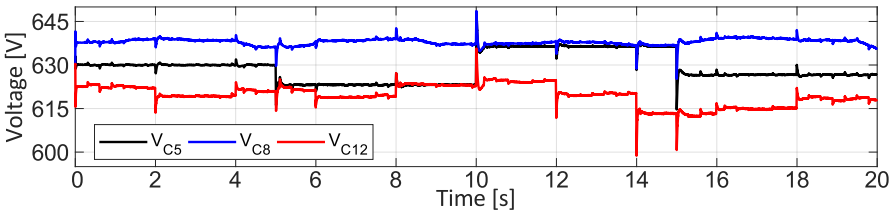

Figure 4.53: Zero dynmics V_{C_5}, V_{C_8}, and $V_{C_{12}}$.

composing the Microgrid and for each related target, a control strategy is provided according to a hierarchical control structure and a System of Systems approach.

The nonlinear control laws are developed according to a rigorous analysis based on an ISS-like Lyapunov function, which provides the possibility to let the Microgrid operate under several adverse circumstances, as for example the high perturbations brought by the train's braking recovery energy system or the load variations. Both theoretical and numerical results show the capability of the proposed approach to handle the complex scenarios given by the mix of different renewable sources, loads and storage devices.

CHAPTER 5

Ancillary Services for AC Microgrids

5.1. Chapter Introduction

In this chapter it is presented a strategy for the interconnection of an AC and a DC Microgrids. In particular it is developed algorithms to provide inertial, frequency and voltage support (ancillary services) for an AC Microgrid (weak grid) composed of diesel generators and loads. In addition, it is presented an adaptive variable synthetic inertia strategy for stabilizing this AC grid face to strong variations on loads and productions, brought by electric vehicles and possibly other renewable energy sources. In the proposed structure there is a DC Microgrid connected to the AC one by a Voltage Source Converter (VSC). The VSC converter is driven as a Virtual Synchronous Machine (VSM), where the control strategy follows a swing equation such that the converter emulates a synchronous machine, including inertial support. A rigorous stability analysis is based on Lyapunov technique assuring proper stability conditions for the adaptive inertia, such that frequency stability is improved and power oscillations reduced. This strategy can be exploited in low inertia systems like Microgrids or grids with high penetration of renewables. Simulation results illustrate the performance of the proposed control and a comparison with classical droop control.

5.2. Power System Stability

Power system stability has been an important issue for proper system operation. Instability problems may cause oscillations and instability on the system states, or even cause major problems as blackouts. The continuing growth and ramification of

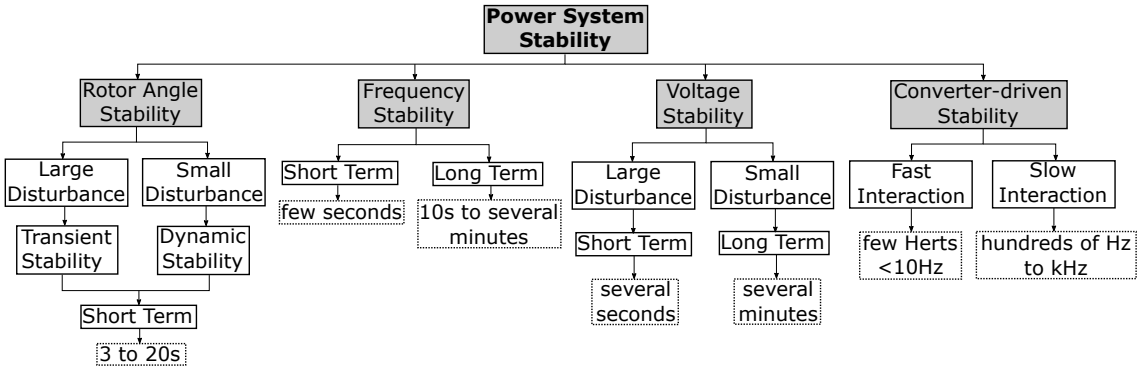

Figure 5.1: Power system stability classification.

power systems, the integration of distributed generation based on power converters and electronic loads, and the highly stressed operation of the system has brought different forms of stability problems. For example, with the advance of Microgrids technologies, voltage and frequency stability become important concerns. The definition of power system stability is given in [104]:

"Power system stability is the ability of an electric power system, for a given initial operating condition, to regain a state of operating equilibrium after being subjected to a physical disturbance, with most system variables bounded so that practically the entire system remains intact."

The definition can be extended to different interconnected power systems, because nowadays many systems have been interconnected to each other to improve its operation and reliability, like the Brazilian National System or the European system. But the complexity of a huge system like this brings thousands of variables to deal with, where the stability problem can not be easily addressed. The assessment of power system stability is split according to different phenomena and variables involved (angle, frequency or voltage), the scale of the perturbation (small or large signal) and the time range (long and short term) as depicted in Figure 5.1 extracted from [104]. This definition has been updated for the new paradigms related to the large scale integration of high power's converters in traditional power systems, which deal with fast and slow frequency-related interactions in [212].

Power systems are mainly composed by synchronous generators sharing power to feed load demand. Rotor angle stability is related to synchronizing those generators in the power network, where dynamic stability deals with oscillations and control interaction among the generators and transient stability is the capacity of those machines to support large disturbances as partial disconnections of loads, black-outs or short-circuits. Transient stability is related to the robustness of the grid in face of large disturbances on the grid [213, 214].

Frequency stability is one of the most important issues of power systems, since it is related to the balance between the generation and the consumption of power in the system. The power mismatch can cause excursions of frequency, accelerating or braking the generators, since the synchronized machines works with the same speed. With current advances in power electronics, the physical interpretation of frequency has became a great issue, since for power converters the frequency is not a dynamic state that respond to power balance, but it is a constant reference [215].

In the same way, voltage stability is the ability to maintain the equilibrium between load and supply, related to the ability to transfer the generated power to the load. Low voltage conditions implies in large current responses to keep system's power supply. Voltage stability is often a problem to be locally addressed according to power grid requirements (grid codes) [134].

Following the Power system Stability classification, this work is focused on voltage and frequency stability, for Microgrids mainly composed of power converters and the necessary ancillary services to maintain stability of the system, which are the actions taken to assure this stability [216].

5.2.1. Frequency stability and control

Frequency stability is defined in [104] as:

"Frequency stability refers to the ability of a power system to maintain steady frequency following a severe system upset resulting in a significant imbalance between generation and load. It depends on the ability to maintain/restore equilibrium between system generation and load, with minimum unintentional loss of load."

The frequency in a traditional power system is given by the rotational speed of the synchronous generators that composes the system. Those machines transforms the mechanical input power from a prime mover to electrical current injected in the grid. A balanced system transmits the same amount of power generated by the machine, otherwise it will be stored/supplied by the rotating masses of the generators. The Swing Equation[1] describes the angular speed deviation caused by the unbalance between the electrical power output and the mechanical power input. The Swing Equation is written as follows:

$$\dot{\omega} = \frac{1}{2H}(P_m - P_e) \tag{5.1}$$

where ω is the rotating frequency of the generator (network), P_m is the mechanical power input and P_e is the electrical power output. H is the inertia constant of

[1] Also known as the equation of motion, it is primordial to power stability analysis.

the network. The power unbalance generates a frequency deviation, changing the operation point of the grid. Then, bring the frequency back to the desired operational value can be one of the targets for ancillary services [213].

Frequency control reserve is the amount of active power kept available to compensate a frequency drop, usually caused by a load shift. On the other hand, the negative frequency control act to decreases the frequency. The frequency reserve is essential to maintain system stability even with sudden power load change, avoiding great excursions of frequency [134].

An interesting power system feature is the natural frequency regulation after a power unbalance. It comes from the self-regulating load and the stored energy in the rotating mass (inertia) from the generation units and the loads (motors) [217]. Concerning frequency stability, there are two types of power loads:

- Static load: are generally represented by algebraic equations, having suitably chosen power to voltage sensitivity, where the frequency dependency can be neglected. Then, the power output of the load is not changed for a frequency deviation.
- Dynamic load: are modelled with algebraic and differential equations where the power output varies according to a frequency deviation [218]. They are called as self-regulating load, since they can attenuate a frequency deviation from a damping effect, given by the ratio between frequency deviation and active power variation (D_L).

The inertial contribution of rotating mass from (generators and motor loads) is very important for frequency stability, since it can hold frequency deviation while the controllers from generation respond from a disturbance. The power stored in a rotating mass is given by:

$$P_{kinect} = J\omega\frac{d\omega}{dt} \tag{5.2}$$

where J is the moment of inertia of the machine rotor and ω is the mechanical speed. From this equation it is seen that the inertial contribution is function of the derivative of frequency, called *Rate of Change of Frequency (RoCoF)*, and the moment of inertia J. This concept of natural frequency response is part of an inertial response of a power system [213].

Grid's evolution has brought large penetration of power converters in the network, where the angular speed of the electrical machines are not coupled with the frequency of the system. Then, the lack of inertia in this kind of grid may lead to higher Rate of Change of Frequency (RoCoF) than classical values. As

a consequence, system's operation and protection may suffer from poor inertial response. This important issue will be detailed in the virtual inertia subsection.

5.2.1.1. Primary control

Power system have a natural frequency response from the accumulated energy of rotating masses, but it is not enough to maintain frequency stability. The natural response limits the frequency deviation, but when a bigger disturbance takes place, action is needed to decrease/increase the energy generation and keep stability.

Standard in frequency control adopt three levels of control to keep the balance between generation and load. The primary control is a local automatic control to adjust the active power generation and the controllable loads to counteract frequency variations, bringing the system to a new operation point within few seconds. They are designed to react to large generation changing or load shifts. The small deviations of frequency can be attenuated by the primary control, then large frequency deviation (off-normal) is dealt by the secondary control to restore nominal frequency. The speed governor performs this control in the region of synchronization of the generation units. The prime mover has a speed regulator that uses the mechanical power to maintain the rotating mass inside an operation range [102,214].

Demand side also contributes with frequency control by connecting or disconnecting a group of loads according to frequency thresholds, but they are not always taken into account for primary control response. A distributed primary frequency control can be advantageous since a generator unit can not surpass the active power supply limits from a frequency drop, therefore other units must share the increase on power demand.

There are many different approaches for speed governors, that can also be applied in power converters for modern grid operation. The different strategies can be cited as isochronous regulation, droop control and virtual inertia.

5.2.1.2. Isochronous control

The isochronous regulation is featured by constant frequency, where the governor adjusts the input to eliminate the frequency deviation. Figure 5.2 presents the block diagram of the isochronous governor, where the integral term guarantees the elimination of steady-state error in frequency by actuating the valve.

In the isochronous operation mode, a load increase will firstly cause a frequency drop given by the generator's inertia, and then, as response, the mechanical power increase to compensate the frequency deviation until the mechanical power reaches

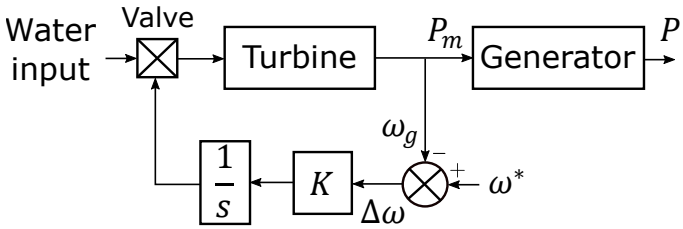

Figure 5.2: Isochronous governor block diagram.

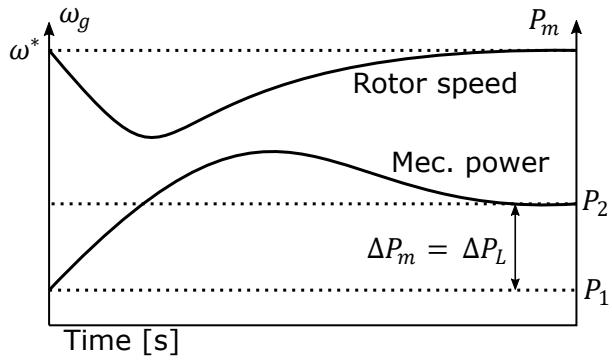

Figure 5.3: Frequency response in the isochronous mode.

the new load demand point. Finally, the frequency is back to its reference. This example is illustrated in Figure 5.3 extracted from [213].

The operation of the isochronous control in an isolated system is considered satisfactory, but when two or more generators are sharing the same load, there is control conflict and the system becomes unstable. Therefore in this case, only one generator is chosen to respond the load changes and perform frequency regulation, while the others are set to constant power supply [219].

5.2.1.3. Frequency droop control

A droop characteristic is obtained by inserting proportional gain in the rotational speed reference, causing a frequency deviation in steady-state. Figure 5.4 shows the block diagram for droop strategy. The frequency-power curve is changed as a sloped line given by:

$$m_p = \frac{\Delta f}{\Delta P} \tag{5.3}$$

The droop control is better applied in multigenerator power sharing because they present a speed drop feature, i.e., a decrease of load will cause an increase of the speed and vice-versa. Therefore, they have a stable load share compared with isochronous control. The frequency deviation rate is usually given in percentage, where the

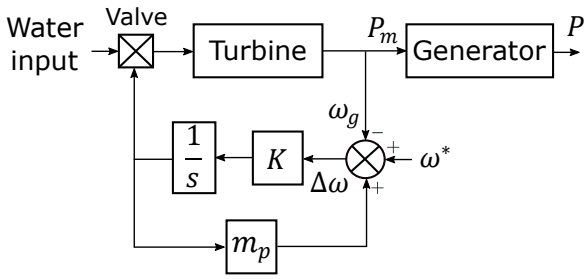

Figure 5.4: Droop governor block diagram.

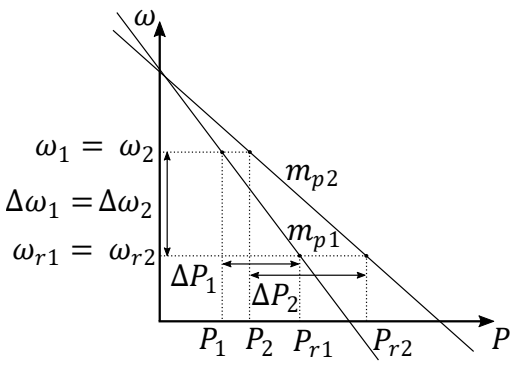

Figure 5.5: Power sharing scheme of droop control in steady-state.

maximum power deviation[2] is linked with the maximum frequency deviation by a proportional relation [131].

Droop control is able to allow the generators to contribute with power supply in different levels, according to their power rate, to provide the balance of power in the system. But, in this case, there will be always a non-zero frequency deviation. Because, there is only one operation point where the frequency is stabilized in its nominal value. The power-frequency relation ($P - \omega$) is seen in Figure 5.5. The droop coefficient (m_p) provides the proportional contribution of each generator for a given frequency deviation. This coefficient can be designed according to the nominal available power (P_{nom}) and the frequency deviation limits ($\Delta\omega_{max}$) [135]. The droop coefficient equation is written as follows:

$$m_p = \frac{\Delta\omega_{max}}{P_{nom}} \tag{5.4}$$

with $\Delta\omega_{max} = \omega_{nl} - \omega_{fl}$, being ω_{nl} the non-load frequency of the machine and ω_{fl} the full-load frequency.

In a multigeneration example, the equivalent frequency characteristic of the whole system (λ) will depend on the droop coefficient (m_p) of each generator and

[2]Primary power reserve in nominal conditions.

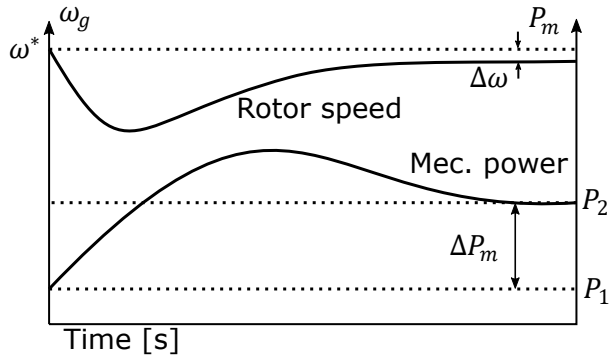

Figure 5.6: Frequency response in the droop control mode.

the variation of the load power output (D_L).

$$\lambda = D_L + \frac{1}{m_{p1}} + \frac{1}{m_{p2}} + ... + \frac{1}{m_{pn}} \tag{5.5}$$

$$\lambda = D_L + \frac{1}{m_{eq}} \tag{5.6}$$

λ is the network frequency characteristic, D_L is the natural response of frequency sensitive load and m_{pi} is the droop coefficient of $i-th$ generator of the system. The sum of the inverse of each droop coefficients results in an equivalent droop given by $1/m_{eq}$ [56].

Therefore, the steady state equation that relates frequency and active power is given as:

$$\omega_g = \omega^* - m_p(P_m - P^*) \tag{5.7}$$

where ω_g is the grid frequency, P_m is the power in the generator, P^* is the active power set point and ω^* is the grid frequency reference [129].

From equation (5.7), the behavior of the frequency in response to a load change can be described as is shown in Figure 5.6 extracted from [213]. After a load increase, the frequency will drop and the mechanical power is increased as a response to the frequency deviation, but in this case, the frequency end up with a steady-state error given by $\Delta\omega$.

5.2.1.4. Load reference setpoint

The Automatic Generation Control (AGC) is used to eliminate the steady state error in frequency. In this case a load reference setpoint is inserted as input in the proportional gain of the droop control. The effect of the load reference set point is to distribute the proportion of load for each generation unit. Therefore, the output power of the generation unit can be shifted by changing the load reference. The load

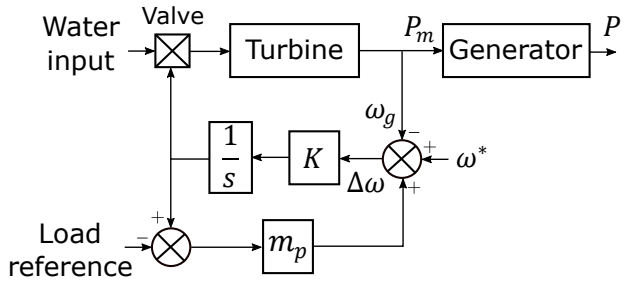

Figure 5.7: Block diagram of a droop governor with load reference setpoint.

reference is usually computed by a secondary centralized controller [213]. Figure 5.7 shows the block diagram of this scheme.

The calculation of the load reference of AGC is necessary to bring frequency to its nominal value, as a consequence, the AGC is able to restores the power reserves caused by the droop control. Therefore, equation (5.8) can find the Load reference by using an integral term in frequency assuring zero steady-state error.

$$\Delta P_{AGC} = -\int (\omega_g - \omega^*)dt \tag{5.8}$$

where ΔP_{AGC} is the power variation of the load reference setpoint and ω^* is the frequency reference. Hence, frequency ω_g can be computed as the average value of frequency in the generation units according to their power and inertia.

5.2.1.5. Secondary and tertiary control

The secondary frequency control is based on a centralized approach to meet the power production of the generators units to restore the frequency to the nominal value and interacts with other systems to accomplish the balance target. While the primary level only avoids frequency excursion and reduces the frequency deviation, the secondary brings the frequency back to the original equilibrium point, i.e., the nominal value of the frequency. This control scheme is mainly applied in interconnected large systems, because a faster response is needed, and usually dispensable in isolated systems. The AGC designates the combination of dispatching and secondary control, where the time range of this level of control is few seconds to minutes [134].

Tertiary control refers to manual changes in the dispatching set of the generations units and application of optimization methods according to economical purposes. This level of control is applied to restore the primary and secondary reserves, managing the optimal operation of transmission lines.

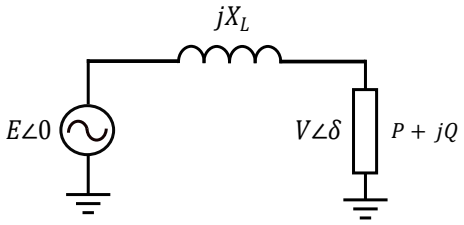

Figure 5.8: A generator connected to a load through a transmission line.

5.2.2. Voltage stability and control

Voltage stability is related with the power system's capacity to transport power through the buses of the system considering the loads and the losses of the system. Definition of voltage stability is given in [104] as:

"Voltage Stability refers to the ability of a power system to maintain steady voltages at all buses in the system after being subjected to a disturbance from a given initial operating condition."

There is close link between reactive power and voltage, mainly in transmission networks[3]. Therefore, a great part of voltage stability is related to the system ability to provide or absorb reactive power. In practice, it is not interesting to transmit reactive power, since this increases the transmission losses. The main problems in voltage stability are related to a voltage drop occurrence when active and reactive power are flowing through inductive reactances in transmission networks. Voltage stability is assured when $Q - V$ relation is positive, i.e., the bus voltage magnitude increases as the reactive power injection also increases, otherwise the system becomes unstable.

Considering a simple radial system where the transmission is lossless as presented in Figure 5.8, the transmitted active and reactive power are given as:

$$P = -\frac{E.V}{X_L}\sin(\delta); \tag{5.9}$$

$$Q = \frac{E.V}{X_L}\cos(\delta) - \frac{V^2}{X_L} \tag{5.10}$$

where E and V are the generator's voltage magnitude and in the same way, the voltage magnitude on load side terminal, X_L is the transmission line reactance and δ is the angle difference between the two sources (power angle) [214].

The relation between voltage and reactive power can be derived from (5.10), where the following condition is obtained:

$$P^2 + QS_{sc} \leq \frac{S_{sc}^2}{4} \tag{5.11}$$

[3]Mainly in inductive power lines.

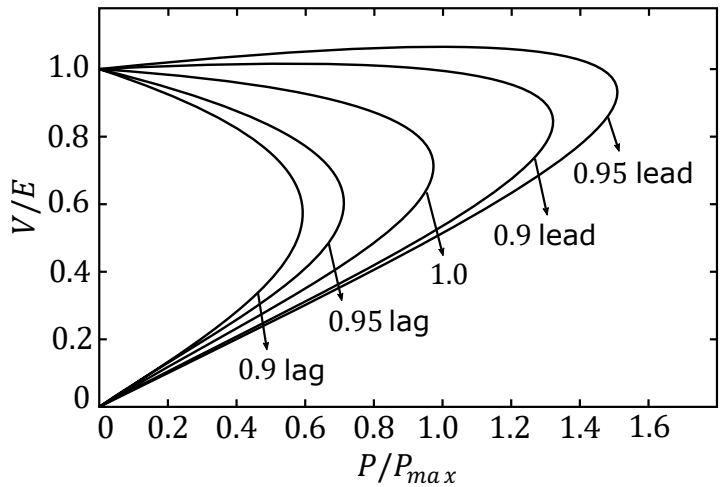

Figure 5.9: $P - V$ curve characteristics for different power factors.

The short-circuit power of the system is defined as: $S_{sc} = E^2/X_L$. The maximum power transmission when power factor is one ($Q = 0$) is $P_{max} = S_{sc}/2$ and the maximum reactive power transmission when power factor is zero ($P = 0$) is $Q_{max} = S_{sc}/4$. So, the reactive power transmission is more restricted than active power. Also, the active power capacity is related with reactive power injection, for example looking again at equation (5.11), when the system is absorbing reactive power (negative value for Q), the active power maximum is increased. As a conclusion, there is a maximum value to transmit active power through an impedance from a voltage source (generation unit), which occurs when the voltage drop in the line is equal to load voltage (V) [56].

For this reason, reactive power compensation is usually realized on the load side using shunt and series capacitors, and tap changing transformers. Recently, the evolution in power electronics has brought Flexible AC Transmission Systems (FACTS), where voltage and reactive power control is improved. At the same time, the grid evolution through power electronic devices, the reducing number of synchronous machines in the grid, together with the increasing load demand bring some impacts to voltage stability [220].

A traditional way to illustrate the relation between voltage and power is to use the $P - V$ curve presented in Figure 5.9 adapted from [104]. Here, it is possible to relate the voltage drop according to active power transmission for different power factors. P_{max} is the maximum power transfer with unity power factor.

The inflection point in the curves represent the critical operational points, where the voltage becomes unstable. Therefore, the satisfactory region of operation is above the critical point. As one can see, a sudden change in power factor (sudden variation

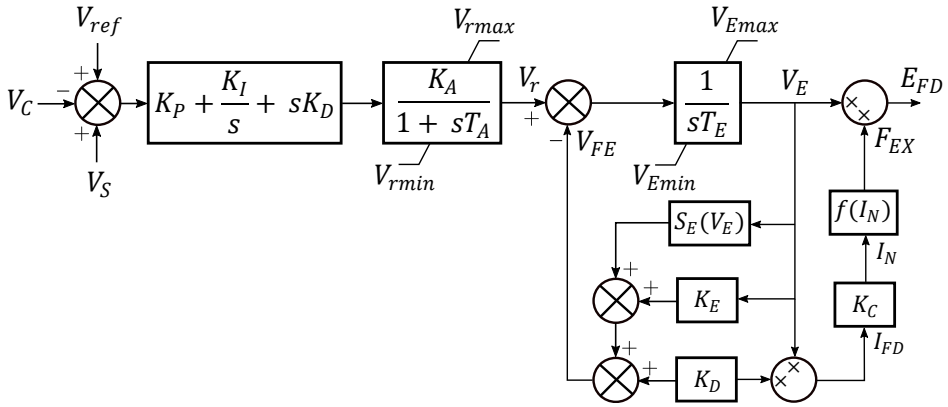

Figure 5.10: Block diagram of the voltage regulator and exciter.

in reactive power) can bring the system to an unstable region (below critical point), which may cause a voltage collapse.

Many other factors can contribute to voltage instability as: power transfer levels; load characteristics; strength of transmission line; reactive power compensating devices; reactive power capability limits; etc. These factors expose the complexity that power systems deal with to maintain system operation.

5.2.2.1. Automatic Voltage Regulator (AVR)

Traditionally, the voltage control is organized in a three level's hierarchy. The primary voltage control has the target to maintain the voltage in a given bus at its desired level. Usually, primary voltage control is done by an Automatic Voltage Regulator (AVR) implemented in synchronous generators of the considered system. The Automatic Voltage Regulator (AVR) controls the voltage in the rotor's excitation. AVR is composed by voltage sensor, amplifier, exciter and generator, where a PID controller is inserted in the control loop to perform voltage regulation [219]. A example of an AC8B excitation model of the synchronous machine extracted from [221] is depicted in Figure 5.10.

In the block diagram, the voltage error is given by the subtraction of reference voltage V_{Ref} and measured voltage V_C, then a voltage V_S from a Power System Stabilizer (PSS) is summed when grid-connected. The result is applied to PID controller connected to the regulator transfer function, with gain K_A and time constant T_A. Therefore, the output voltage of the regulator V_R is inserted in the excitation model as an input, where the desired voltage excitation E_{FD} is calculated. K_D is the demagnetizing factor and K_E is the exciter constant.

5.2.2.2. Voltage droop control

As presented in droop control subsection for frequency control, a relation between active power and frequency ($P - f$) is built. Here, considering a power system with high value X/R relation, where the losses are negligible considering the system reactance, a direct relation between reactive power and voltage magnitude ($Q - V$) can be shown. The coefficient that relates reactive power with voltage magnitude is written as:

$$m_q = \frac{\Delta V}{\Delta Q} \tag{5.12}$$

where the voltage droop coefficient (m_q) provides a proportional contribution of reactive power for a given voltage deviation [60]. In this case, the voltage droop feature will cause a steady state error on the voltage level, since a change on reactive power supply implies in a new operational point for the voltage, but will always be a non-zero voltage deviation. The coefficient m_q can be designed according to the voltage limits requirements (ΔV_{max}) and the nominal reactive power capacity (Q_{nom}) as given next:

$$m_q = \frac{\Delta V_{max}}{Q_{nom}} \tag{5.13}$$

where $\Delta V_{max} = V_{max} - V_{min}$ according to the grid limits and Q_{nom} is given by the capability curve of the generator or power converter.

Therefore, the steady-state equation for voltage droop equation is written as:

$$V = V^* - m_q(Q_m - Q^*) \tag{5.14}$$

where V is the grid voltage amplitude, V^* is the nominal voltage set, Q_m is the filtered reactive power, Q^* is the reactive power set point. Figure 5.11 depicts the behavior described in (5.13), exhibiting the voltage droop feature for different coefficients (m_q) [135]. In island system operation, the reactive power reference is considered $Q^* = 0$ [128].

As droop control has a better performance for power sharing, multiple units can share the responsibility of reactive power supply to voltage regulation purposes. The generation units can contribute with reactive power supply in different levels, according to their capacity. $Q - V$ droop control have been widely applied in power converters that integrate renewable sources and ESS, since it allows the voltage support by a simple relation with reactive power. Even in Microgrids mainly composed of power converters, the voltage control can be easily designed by droop control approach [129, 135].

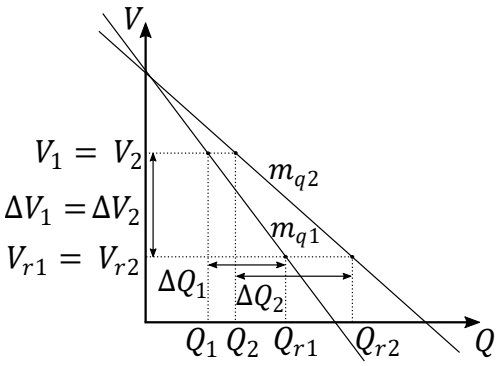

Figure 5.11: Different coefficients of the voltage droop control scheme.

5.2.2.3. Secondary and tertiary control

Secondary control is based on a centralized automatic approach to manage the reactive power injection within a regional voltage zone by coordinating the action of the local controllers. This level of control is related to the capability of a generator supply an extra-mandatory quantity of reactive power, such that a group of buses in the grid is maintained at desired operation. The improvement of the voltage regulation can be done by the integral of the voltage error, which results in a reactive power reference to the service provider. Tertiary control is based on optimization techniques to calculate the reactive power flow in the entire system [134].

5.3. Ancillary Services in Brazil

The main responsibility of a Transmission System Operator (TSO) is to provide electric power from generators to the consumers through transmission lines meeting the standardized network requirements (obligations of control areas and transmitting utilities) to maintain the proper and reliable operation of the system interconnection. In this context, the specific services and functions provided to maintain and support the power supply in the grid are called ancillary services. The ancillary services support the grid to maintain continuous and reliable operation of the system, properly supplying the loads while keeping stability and security. Traditionally, the ancillary services are provided by generators controlled by the TSO, however the integration of power electronic based equipment in the network expanded the possibility of ancillary services provision. Therefore, power electronic devices and generators non-controlled by the TSO are now able to participate on the support to the grid in several operation modes, which has created a new opportunity in the energy market [222–224].

The ancillary services provision in Brazil is still very limited because of regulation aspects and restricted to the generation units controlled by the TSO (composed of hydroelectric and thermoelectric plants). There are some generation units able to operate as synchronous compensators, which provide reactive power compensation through a formal contract with the national TSO. These are centralized thermoelectric plants used as operational power reserves. Therefore, power plants non-controlled by the TSO cannot perform ancillary services, which greatly restrict theses services in Brazil [225–227].

The normative resolution in [225] made in 2018 updates the version introduced in 2015 for ancillary services provision, where the TSO is in charge of identifying the generation units capable of carrying out the ancillary services related to power reserve dispatch, opening the possibility for different generation units. The limitation of the prices offered for such services and the operating restrictions related to the load curve, operating time and minimum operating power were also discussed. Aspects of fees and service unavailability, as well as forms of payment were also considered.

According to [226], the ancillary services' provision in Brazil includes the following supports: a) Primary frequency control, performed by all generating units integrating the national electrical grid; b) Secondary frequency control, where only the plants that are part of the Automatic Generation Control, requested by the TSO are able to participate; c) Reactive power support, performed by generation units integrating the network and by plants that operate as synchronous compensators, under prior authorization from the National Electrical Energy Agency (ANEEL); d) Black-start, performed by all generation units integrating the network and by plants in compliance with ANEEL and on demand from the TSO with the support of previous studies; Special Protection System, performed by existing plants in operation with the support of studies performed by operator with prior authorization from ANEEL, in addition to proof of technical feasibility; and Complementary power reserve dispatch, performed by centrally dispatched thermoelectric plants.

In this context, the report in [227] proposes a normative review for ancillary services provision based on the reduction of the regularization of the reservoirs of hydroelectric power plants and the high penetration of intermittent renewable sources. It addresses the need to adapt the spatial and temporal allocation of energy resources and the current load of the electrical system so that requirements can be sized, equipment allocation made and guidelines of contracting services can be defined. The planning of the requirements of ancillary services identified by the planning and operation of the electrical system aims to encourage the provision of services, identify costs in order to minimize the operational cost, and

operate efficiently. It is also proposed to encourage the expansion of existing services (mentioned above) and the insertion of new services such as:

1. Development of new services for reactive power compensation using photovoltaic plants, reactive power support for wind power plants and even in the distribution system, which could be applied through tariffs already established;
2. Inertia as an ancillary service through power electronics equipment, aiming at reducing the connection of thermal plants, but it may bring losses to the system, or the use of thermal plants to increase inertia that avoids the installation of electronic equipment for this purpose;
3. Load modulation by distribution agents, performed through the dispatching of power plants not operated by the national TSO, but by the local distributor;
4. Paying for ancillary service provision: payment through system services charges using the principle of causality, where the TSO identifies the causers of the need to provide the service, which can bring improvements to the electrical planning, or even the bilateral payment between consumer and the provider, raising the need for the development of an ancillary services market.

Thus, in the Brazilian scenario, there are still many barriers to the diversification of ancillary services provision, being restricted to large generation units controlled by the national TSO. In addition, the regulations updates presented are limited to proposals and introduce possible advantages and disadvantages to be discussed, being distant from an imminent implementation. According to these reports, the greatest barriers to the accomplishment of the rendering of ancillary services are presented in the increase of complexity in the identification of costs, operation and verification of services.

Nowadays, ESS have the ability (according to their size and technology) to perform most kinds of ancillary services presented here according to their nominal power limitation. Thus, ESS can be applied for primary frequency regulation (which represents the most restricted ancillary service in ANEEL), in view of the availability of the power electronics equipment required for this purpose. However, due to the lack of regulation in Brazil and the restriction of generation units authorized by the national TSO, ESS are very restricted for ancillary services provision in Brazilian power grid. These limitations highlight the urgent need to develop new operating strategies for the system, maintaining the operational requirements with the installation of new equipment for this purpose. The adaptation of economic

regulation tools must be considered, as well as carry out studies to identify costs (valuation of the service) for these services.

A crucial factor is the identification and verification of the service provision. It is necessary to develop tools to validate these services, and to track the operator or the local consumer that receives the service. Technological adaptation costs and equipment deterioration costs combined with massive insertion of power electronics' devices and ICT equipment make the valuation of ancillary service provision quite complex. Other aspects, such as cause and effect relationships are also widely discussed as in the case of harmonic mitigation and should be taken into account to create a new resolution for ancillary services. In addition, the size of the storage system limits its use for services requiring a large amount of energy, such as secondary (or even primary) reserve.

The development of a market for ancillary services in distribution is very relevant from a technical point of view for Brazil, considering that the main current power quality problems are faced in the distribution system. The report in [225] proposes that the modulation of loads can be carried out by distribution dealership for the dispatch of plants not operated by the national TSO, demonstrating the relevance of the high penetration of energy resources directly installed in the distribution system (mainly PV and ESS).

The distribution system has undergone a revolution in recent years, known as Smart-Grids, which results in a multitude of possibilities for ancillary services in the context of the distribution system. Therefore, consumers can also perform services to improve the network operation. This reflects in the creation of a new market that brings economic growth in the energy market, also improving the operation of the distribution system as a whole. The use of renewable resources for ancillary services provision enhances the effort to change the energy matrix, bringing more technical and economic benefits for this type of generation, expanding the operation field of renewables to solve power quality issues.

Electric vehicles can also become an excellent contribution to the ancillary services through Vehicle to Grid (V2G) concept, since they bring a larger dispatching capacity. In conclusion, there is great technical feasibility for developing an ancillary services market in the context of distribution systems, which would further drive the modernization of the distribution system and the energy market economy, the main challenges being the development of regulations and valuation for ancillary services in Brazil.

5.4. Power Converters Issues

Recent grid evolution has brought the integration of renewable energy sources, ESS and loads based on power electronics. Further, the HVDC advances and MTDC are more present in large interconnected grids. Those equipment are also based on power converters. On the other hand, Microgrids like isolated systems, or small independent grids located in urban centers are composed mainly of power converters to transform energy and operate the system [228, 229].

In all of these cases, power converters are the key technology for grid components. But power converters have different behavior than synchronous machines. Synchronous machines have an inherent energy storage from their rotational mass[4], being able to naturally respond to a load perturbation contributing to system stability, while power converters are directly affected by their controllers with fast response and very low natural energy stored[5]. Therefore, power converters do not have the natural ability to contribute to frequency stability in the active power sense [133, 230].

In Microgrids context, power converters use the measured voltage of the network to estimate the phase angle of the grid, being able to synchronize with the main grid to generate the voltage output, i.e., grid-following converters. The main issue related to power converters in Microgrids is the difficulty to implement isolated operation called as grid forming converters. Grid-forming converters are a great concern in academia and industry, where numerous studies have been carried out to develop useful strategies to proper operate electrical grids only composed of power electronics technologies. In this context, droop control approach has been widely applied, since it allows power share among power converters with a distributed control approach.

A crucial issue in power electronics technology is the lack of inertia and interactions between control as stated by the United Kingdom Transmission System in [231]. In fact, the high penetration of power electronics based technologies decrease the inertia of the system, bringing frequency stability problems and reduction of transient stability margins.

The AC/DC power converters like VSC are mostly controlled by Pulse Width Modulation (PWM) and traditional control schemes in grid-following operation make these converters behave as current sources[6]. The Phased Locked Loop (PLL)

[4]Synchronous generators store kinetic energy proportional to moment of inertia J and their angular speed, with time response of few seconds as seen in Section 5.2.1.

[5]The capacitors of power converters can store electrostatic energy in order of milliseconds.

[6]Usually, VSC have outer voltage control loop and an inner control loop, which is the current control loop

is used to synchronize the converter with the grid by estimating the phase angle of the network, where the calculation of the voltage reference depends on the grid impedance. Therefore, the control performance is affected by grid impedance, which makes these control schemes sensitive to grid condition. So, it is necessary to design a good interaction between the PLL, voltage and current control loops, PWM switching frequency and the output filter. The match of bandwidth of the controllers can be a very complex task. Usually, current control loop bandwidth is twenty times smaller than the PWM frequency and filter frequency is designed accordingly [232, 233].

Other important issues can be related to power electronics in power systems, where countries in Europe are dealing as priorities [56]:

1. Decrease of inertia, related to frequency stability;
2. Wrong participation of power converters devices in frequency regulation (control errors);
3. Reduction of transient stability margins due to decreased short-circuit capacity of power converters
4. Resonance and oscillations caused by power electronics;
5. Power electronics controller interaction among the devices (active and passive) in the grid.

In this scenario, new ancillary services and grid support are needed to fulfill the stability requirements for power system operation and reliability. A suitable solution is to develop new control strategies for power converters changing the original feature of power converters to provide ancillary services to the network and reduce the power electronics impacts [234].

Traditional power systems composed of synchronous generators have a well established time-scale separation considering the dynamics of the system. Usually, the time constant for frequency and voltage regulation are related to slow dynamics of turbines (about $10s$) and governors (about $1s$), compared with faster dynamics of the exciter (about $50ms$), which can deal with the network line dynamics (time constants about $1 - 30ms$). Besides that, the time constant of the swing equation and flux linkages will be given by the flux and swing dynamics. So, in conventional systems, the controllers are typically designed considering its operational margins and can assure the stability of the whole system. However, in low inertia systems, the fast dynamics of power converter-based generation bring interactions among different controllers, affecting the time-scale separation and increasing complexity [235].

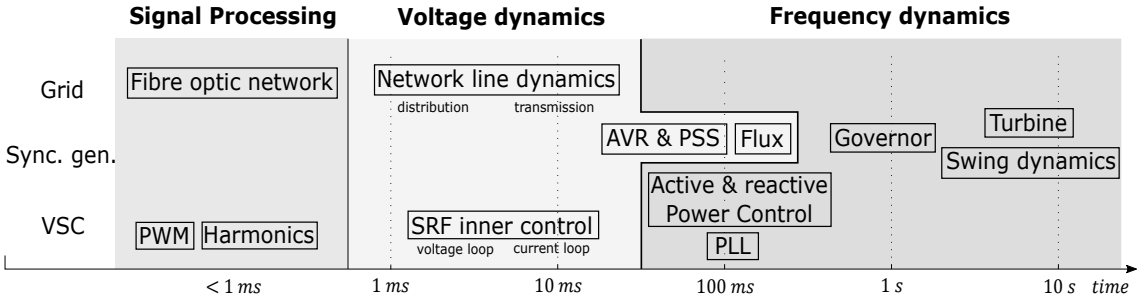

Figure 5.12: Time-scale separation of power system dynamics considering conventional synchronous generators and power converters integration.

The time-scale separation of power systems including power converter-based generation and the dynamics characteristics of low inertia are introduced in Figure 5.12, adapted from [235]. It is presented the physical and control dynamics, considering three different time-scales: signal processing, voltage dynamics and frequency dynamics. The voltage and frequency dynamics are related to the controllers designed for these purposes. First, the signal processing is associated to the fastest interactions ($< 1ms$), which may include PWM signals and harmonics from converters, and fibre optic network communication of the electrical grid. Then, the voltage dynamics are associated with large range time-scale interactions ($> 1ms$ to $< 100ms$), which includes the network line dynamics, the AVR, PSS and linkage flux dynamics of synchronous machines, and the SRF inner control loops of converters. The frequency dynamics are associated with the slowest interactions ($> 10ms$ to $10s$), including the Active and reactive Power Control, PLL of power converters, and the Governor, Turbine and swing dynamics of synchronous machines [213, 235, 236].

In this sense, the controllers and LPF of power converters have faster dynamics than synchronous generator controllers, resulting in control interactions and causing stability issues, since they have different time constants as shown in Figure 5.12. So, power converters can potentially impact in the frequency regulation in low inertia systems, affecting frequency dynamics and the associated fast transients. The result is the deterioration of protection schemes that consider the limitation of frequency Nadir and RoCoF due to incompatible control strategies interacting with the main grid under high penetration of power electronic-based generators. The transmission line dynamics also interact with the dynamics of power converters' controllers, where the fast behavior of these dynamics can amplify the interactions. Therefore, when the X/R impedance ratio is high enough, the time constant of the line is able to suppress the gap between faster dynamics of power converters and slow dynamics of synchronous generators, acting as a buffer, improving the system stability. However,

in distribution lines, the lower X/R relation restricts the operation and control of voltage and frequency, hindering system's stability. In this case, virtual impedance application may be a feasible solution for these stability issues.

5.4.1. Inertial response and low inertia issues

Since power converters based generations are not able to provide natural frequency response (primary control), the reliability of renewable generators and Microgrids can be dramatically reduced. Consequently, the frequency response of the system as a whole can be affected, which is an European concern [233].

A reduced inertia may cause higher frequency excursions during and after a contingency and also increase the Rate of Change of Frequency (ROCOF). RoCoF is used to indicate load disconnections (Load Shed) and in protection schemes to detect the disconnection of generations units. Therefore, faster frequency ancillary services, inertial response emulation and increase the grid code requirements of RoCoF were proposed by [237, 238].

The power response of an inertial system (natural or virtual) depends on its inertial time response (H) and the derivative of frequency as:

$$\Delta P_{p.u.} = -\frac{2H}{f_0}\frac{df}{dt} \tag{5.15}$$

where f is the measured frequency and f_0 is the nominal grid frequency.

The inertial power variation ($\Delta P_{p.u.}$) is proportional to the RoCoF, then its maximum is just after a frequency perturbation and it goes to zero when a new equilibrium point is reached. Considering a perturbation, as load increase or a generation loss, in a power system with primary reserve to contain the frequency drop. The behavior the frequency deviation and the inertial power variation are depicted in Figure 5.13 from [56]. In this, case, the frequency Nadir is reduced when the inertial support takes place, which means that inertial power helps to improve frequency variations.

This is a natural response of synchronous machines, but power electronic devices may apply this phenomenon as a virtual inertia approach. The synthetic inertial response after a contingency can be a great solution to lack of inertia due to interfaced connection, since it results in an equivalent behavior of a synchronous machine. The main difficulty in this process is to measure the frequency, when it is not possible to use the angular velocity of a synchronous machine (Power converters based grids). Therefore, the PLL can be used for frequency measurement in this case.

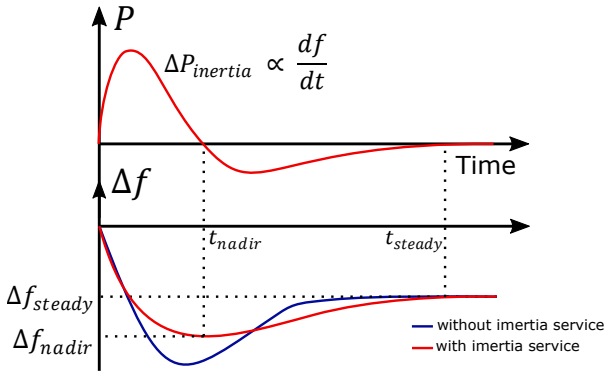

Figure 5.13: Inertial response scheme with a primary control.

5.4.2. Frequency problems in weak power systems

An important issue in weak grids and Microgrids is the severe effect on frequency stability caused by power converters when operating these systems. The reduction of system's inertia affects the frequency deviation face to disturbances causing increase in frequency changes even in strong grids, since the renewables has arrived. The Electricity Reliability Council of Texas (ERCOT) has reported a continuous decline in the inertial response of its system and recommends additional inertial response [239]. Also, the European Network of Transmission System Operators for Electricity (ENTSO-E) has reported frequency violations growth related to large renewable integration in the grid [240]. So, frequency problems have a straight relation to renewable penetration and power converters based grids.

Frequency limits are imposed by TSO, and these limits are well defined in grid codes. For example, the IEEE recommends a tight frequency operating standard of $\pm 0.036\ Hz$ for grid-connected systems, but for off-grid operation in Microgrids and isolated systems, the limits are redefined to fit limitations of this kind of operation. In the North American Reliability Corporation (NERC) the recommendation is to start load shedding when the frequency drops bellow 59.3 Hz to re-balance the system[7]. For variations lower than 57 Hz or higher than 61.8 Hz, the NERC recommendation is to disconnect generators units. To highlight the regulatory differences between grid-connected and isolated modes, Table 5.1 is introduced from [57]. Generally speaking, the limits for the isolated mode are relaxed compared with grid-connected mode, allowing variations of $\pm 1.5 Hz$ in frequency, and up to $\pm 9\ Hz$ for critical periods according to ISO 8528-5 standard, which provides a guideline for frequency in off-grid context.

[7]Nominal frequency in this case is 60 Hz.

Table 5.1: Microgrid operation standard for frequency levels.

Grid-connected	**Island mode**
Frequency: main grid task	Freq. primary controller by VSC
Small number of critical deviation	Low inertia with critical deviations
IEEE	**ISO 8528-5**
Recommended range: $\pm 0.036\ Hz$	Nominal range: $\pm 1.5\ Hz$
NERC	Critical range: $\pm 9\ Hz$
Freq. < 59.3 load shedding	Recovery time: $10\ s$
Freq. < 57 or > 61.8 disconnect generator	Maximum RoCoF: $0.6\ Hz/s$
EN50160	
49.5 to 50.5 Hz for 95% of a week	
47 to 52 Hz for 100% of a week	

A virtual inertia approach as a solution for power converters impacts related to grid integration and Microgrids solutions is presented in next section.

5.5. Virtual Inertia

Virtual or synthetic inertia consists in emulate the energy stored from rotational mass (inertia) of synchronous generators in power electronic devices, such that the power converter is able to have natural frequency response. The definition of Synthetic Inertia from ENTSO-E is [240]:

"A facility provided by a Power Park Module or HVDC System to replace the effect of Inertia of a Synchronous Power Generating Module to a prescribed level of performance."

The concept of virtual inertia implementation through power converters was first appeared in [241]. Then, the concept of synchronverters has been developed [63], subsequently called as Virtual Synchronous Machine (VSM)[8] in [242]. These are composed by power converters that mimic or behave like synchronous machines. In this way, it is much easier to integrate such systems to the power network, providing a framework that practitioners are well acquainted [57,69,70]. These VSM have raised much interest in recent years and have been widely applied to improve frequency stability and to provide inertial support in weak grids and Microgrids [243–245].

Virtual inertia uses a combination of control strategies, DER (as renewables and storage systems) and power converters to emulate the inertia of conventional synchronous machines. The control algorithm of virtual inertia approach can be

[8]Note that VSM is said as the VSC operating as a synchronous machine.

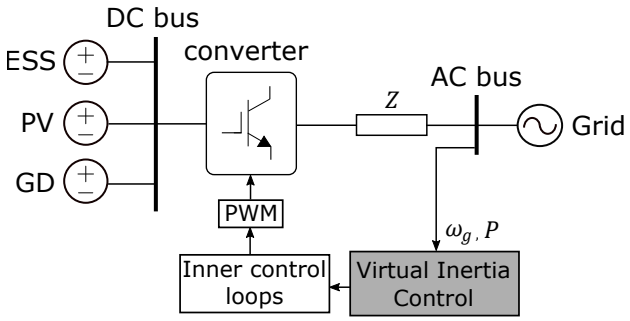

Figure 5.14: The concept of virtual inertia.

inserted in the power converter, where the equations are written and the signal is sent to the converter. Therefore, the power converter becomes the crucial device able to emulate inertia based on a control scheme. PV's and ESS with VSC converters (inverters), wind turbines with back-to-back converters and even HVDC links with multilevel converters can apply the virtual inertia approach to contribute with inertial response for the grid. The key element to emulate inertia in this case is the available energy from DER to proper inject power following inertial feature [57, 133, 246].

VSM reproduces the dynamic properties of a real synchronous generator in a power electronics unit, in order to achieve the inherent advantages of a synchronous machine for stability improvement. It can be applied in strong grids on power converters based integration or in Microgrids. The idea of virtual inertia is illustrated in Figure 5.14 adapted from [57].

Many studies have been carried out concerning the application of virtual inertia in power converters, such as integration of DER [70], improvements in Microgrids [73] and isolated power systems [75]. In [76], a comparison on the dynamics between virtual inertia and droop control strategy is done, pointing out the similarities and the advantages of each control strategy, as well as the relevance of inertia properties. As the next step, new propositions on virtual inertia emerged, for example, in [67], where the parameters of VSM can be controlled, and then, VSM with alternating moment of inertia is developed. The damping effect of the alternating inertia scheme is investigated by transient energy analysis. In [247, 248], an improvement on frequency regulation is reached based on adaptive virtual inertia, where the inertia constant varies according to the frequency deviation. In this case, inertia constant and damping parameters become time-varying variables. As result, the frequency nadir has great improvement, reducing frequency excursions, where the control strategy matches the advantages of large inertia and small inertia properties.

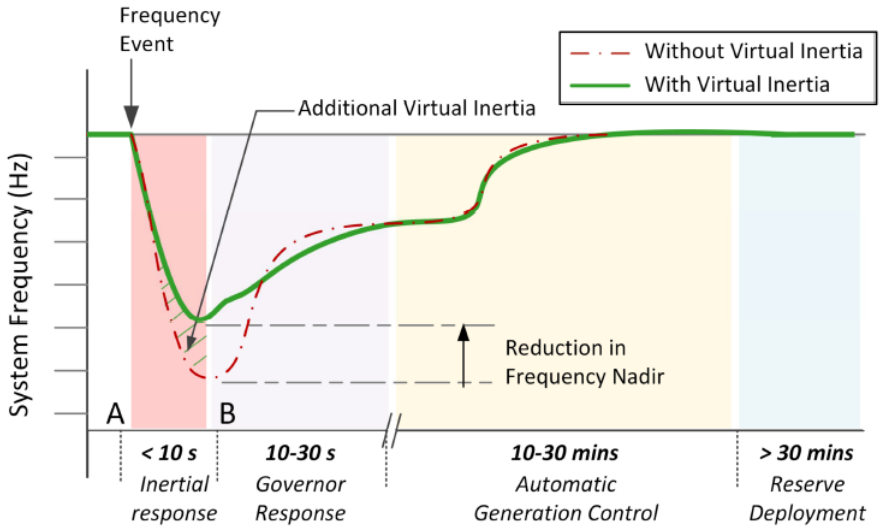

Figure 5.15: Time range of frequency response stages.

The time range of the hierarchical frequency response with virtual inertia is depicted in Figure 5.15 extracted from [57]. Section AB is given by the inertial response, with less than ten seconds duration, where is clearly seen the main contribution of virtual inertia. The frequency Nadir[9] is greatly reduced along with high RoCoF thanks to inertial behavior created. Virtual inertia feature can also improve the governor response, highlighting its contribution to primary control in general. Therefore, virtual inertia must operate in a short time range in autonomous way like inertial response from synchronous generators. The advantage here is that the inertial time response (H) can be adjusted as needed[10], and even can become a state variable to behave such that frequency stability is improved. This approach greatly enhance system stability, mainly in Microgrids context, where frequency stability is critical and then enable better penetration of power electronics in general.

The present section is dedicated to these systems, but now acknowledging that if they act as synchronous machines, they are not limited to this behaviour, and can provide extended support than a physical machine does. In this way, it was studied the contribution that VSM may bring to the overall inertia of a power grid, and how they can provide ancillary services, in particular frequency support and inertial response.

[9]Frequency Nadir measures the minimum post contingency frequency.
[10]The comparison can also be done with moment of inertia J.

5.5.1. Virtual inertia topologies

The basic concepts of virtual inertia in the literature are quite similar, even because as shown above, its definition is related to its effect and not by the means to obtain it. Hence, there are various topologies distinguishing by their model and application strategy. A topology may mimic the exact behavior of a synchronous machine, by applying the mathematical model of such machine, while other approaches applies directly the swing equation of synchronous machines to simplify the implementation on power converters, and yet others incorporate a responsive DER to respond to frequency changes. Next, the main topologies described in literature are discussed.

5.5.1.1. Synchronverters topology

Synchronverters developed in [63] are based on the dynamical equations of synchronous machines from the network point-of-view. Such control strategy allows a traditional operation of the power system without major changes in the operational infrastructure. The electrical torque (T_e), terminal voltage (e) and reactive power (Q) result from the equations written in the converter such that, a synchronous generator behavior is captured. A frequency droop strategy is applied to regulate the output power from the converter. The equations to model the synchronverter are:

$$T_e = M_f i_f i_g \sin\theta \tag{5.16}$$

$$e = \dot{\theta} M_f i_f \sin\theta \tag{5.17}$$

$$Q = -\dot{\theta} M_f i_f i_g \cos\theta \tag{5.18}$$

where M_f is the magnitude of the mutual inductance between the field coil and the stator coil, i_f is the field excitation current, θ is the angle between the rotor axis and one of the phases of the stator winding, and i_g is the stator current.

Figure 5.16 presents the block diagram of the proposed control scheme presented in [63], where i and v are the current and voltage feedback to used to solve the equation within the controller. J is the moment of inertia and D_p is the damping factor, which are arbitrary control parameters used to impose desired behaviour. The design of these parameters is intrinsically related to the stability properties of the system and will dictate the RoCoF, frequency nadir and power injection limits to keep the grid requirements.

The frequency and the voltage loops are used to generate the control inputs: mechanical torque T_m, given by the active power reference P^* from the swing

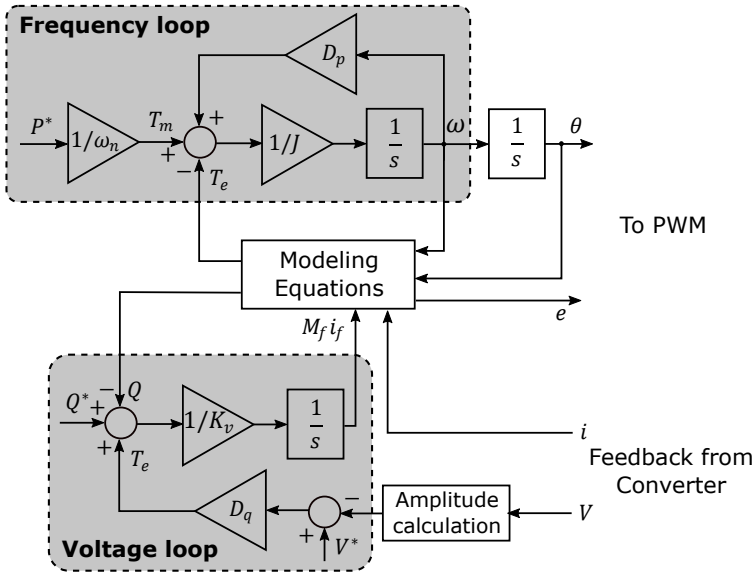

Figure 5.16: Control diagram of a synchronverter.

equation and excitation variable $M_f i_f$, given by the desired voltage amplitude in the terminal v^* and the reactive power reference Q^* from the droop strategy. The voltage loop have a droop constant D_q, where the measured reactive power is compared to its reference (Q^*). The resulted signal is then integrated with a gain K_v to eliminate steady-state error, resulting in $M_f i_f$. With $M_f i_f$, it is possible to generate e, which is the first control output for the converter related to the modulation index (voltage amplitude regulation). A virtual angular frequency is generated (ω) from the swing equation loop, hence its integral θ can be calculated to be the reference for PWM, which is the second control output of the converter related to power injection.

In the synchronverter topology, PLL is only used for initial synchronization and frequency measurement purposes, since the frequency loop from swing equation generates a natural ability to attain synchronism with the terminal voltage. A self-synchronized version of this approach is introduced in [249], greatly improving the stability performance, because PLL application may lead to instabilities in weak grids. In the synchronverter topology, the frequency derivative is not necessary for the control implementation, which is a great advantage since frequency derivative computation may bring noise and poor control performance. Another great advantage is the fact that voltage source implementation allows grid-forming operation for isolated systems. Synchronous motors can also be obtained when this topology is applied to the power electronic based loads (rectifiers), helping with inertial response in the load side [250]. Concluding, synchronverters is seen as a great solution for power converters based application in power systems to improve system's stability.

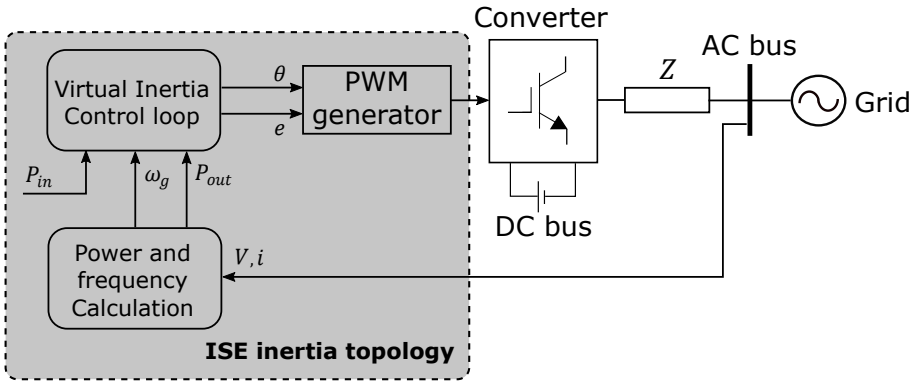

Figure 5.17: General control scheme of ISE lab topology for virtual inertia.

5.5.1.2. ISE topology

The ISE lab topology is based on the swing equation of a synchronous machine, where the power-frequency relation is used to emulate the inertial response of the system [242]. In this strategy, the voltage v and current i on the output converter is measured to compute the grid frequency ω_g (which can be done by the PLL) and the active power output P_{out}. The swing equation of this approach is written as follows, where the phase angle θ can be computed to generate the signal for PWM:

$$P_{in} - P_{out} = J\omega_m \frac{d\omega_m}{dt} + D_p(\omega_m - \omega_g) \tag{5.19}$$

where $\theta = \int \omega_m dt$, P_{in} in the active power input given by the prime mover and ω_m is the virtual rotor speed.

A governor model is used in this case to control the grid frequency (ω_g) to its reference ω^*. The prime mover power input reference P_{in} is computed by a first order system with gain K and time constant T_d, where P_0 is the active power reference received from a higher level controller. The prime mover equation is presented next in frequency domain:

$$P_{in}(s) = P_0(s) + \frac{K}{1 + T_d s}(\omega^*(s) - \omega_g(s)) \tag{5.20}$$

The voltage reference (e), can be implemented via $Q - V$ droop control to generate the amplitude reference for the PWM. Similarly, $P - f$ droop control may be applied to generate the power reference P_{in} instead of a prime mover approach. The general scheme of ISE VSM is illustrated in Figure 5.17 from [57].

As in the synchronverter approach, frequency derivative is not required in the present case, what improves the control performance, avoids signal pollution and can be applied for grid forming units. Nevertheless, a poor design of swing equation parameters (J and D_p) may result in oscillatory behavior and instability problems.

5.5.1.3. Virtual synchronous generators

VSG is a Frequency-Power response based topology that emulates the inertial response feature of synchronous generators focused on frequency deviation improvement. It is a simple way to insert inertial characteristics in power converter units[11], since it is not necessary to incorporate the detailed equation of synchronous generators. VSG can be easily compared with standard droop controllers, but here, they can also provide dynamic frequency control unlike droop controllers that only have steady-state performance. The dynamic frequency control is realized by frequency derivative measurement, where the system reacts from a power imbalance [65,251]. So, VSG provides a power output (P_{vsg}) according to frequency deviation, which equation is written as follows:

$$P_{vsg} = K_D \Delta\omega + K_I \frac{d\Delta\omega}{dt} \tag{5.21}$$

where $\Delta\omega$ is the frequency deviation and $d\Delta\omega/dt$ is the RoCoF. The gains K_D and K_I represents the damping factor and the inertial constant respectively, refereed from synchronous generator model.

The inertial constant (K_I) impact the RoCoF improving the dynamic frequency response, which is a suitable solution for isolated systems where the RoCoF may have high values, harming system stability. Therefore, this approach can be applied to enhance RoCoF values, and the damping constant (K_D) have the same effects of a $P - f$ droop controller. In this topology, a PLL must be used to measure frequency deviation and RoCoF, which can be challenging, since the harmonic distortions and voltage variations may lead to poor control performance, while, in the other topologies, PLL is not really necessary. The VSG scheme is depicted in Figure 5.18 adapted from [57].

VSG can be seen as a dispatchable current source, where P_{vsg} is used to calculate the current reference for power converter control loop. Equation (5.22) presents the current reference I_d^* related to active power injection:

$$I_d^* = \frac{2}{3} \frac{V_d P_{vsg} - V_q Q}{V_d^2 + V_q^2} \tag{5.22}$$

where V_d and Vq are the voltages in dq reference frame from Park transformation, Q is the measured reactive power.

[11]Power converter units can be understand as a generalization for DER integrated via power converters.

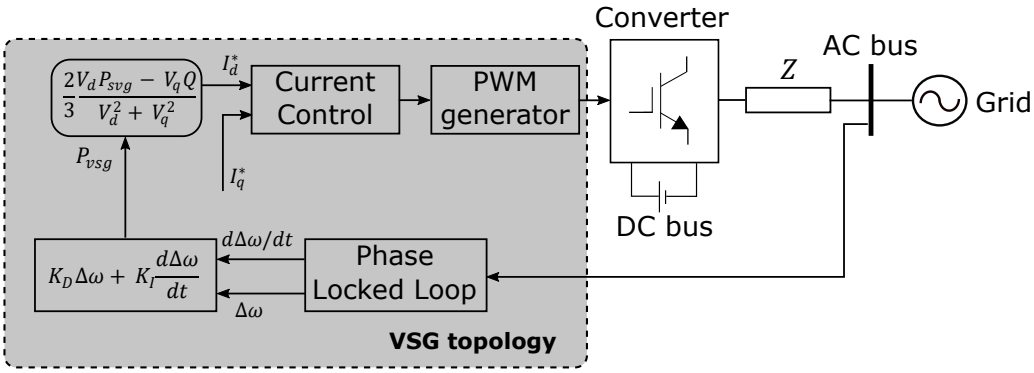

Figure 5.18: General control scheme of VSG topology for virtual inertia.

The reactive power can also be controlled by calculating current reference I_q^* related to reactive power injection:

$$I_q^* = \frac{2}{3}\frac{V_d Q^* - V_q P}{V_d^2 + V_q^2} \tag{5.23}$$

where Q^* is the reactive power reference, which may be obtained by a droop control strategy, and P is the measured active power in the grid.

VSG topology is used by the European VSYNC group, because of the simplicity and effectiveness features of this approach. When applied as current sources as described in equations (5.22) and (5.23), VSG approach is not able to operate as grid-forming unit. Also, the inertia is not emulated during power input variations, but only in frequency variations. And the main problem of this approach is the complexity to compute and measure frequency deviations and RoCoF, since the derivative operation involves noise pollution and stability issues[12]. Stability problems can also be noticed, when cascaded control loops are used, such as PI controllers with an inner-current loop and an outer-voltage loop for converters. This happens because the tuning gains of these controllers may be complex to tune, which results in inaccurate control performance [253].

5.5.1.4. Droop based topology

The droop control is a well known approach used for power sharing both in strong grids or Microgrids without necessary communication among the distributed generation units, which contributes for an easy application. The designed control loop is composed by $P - f$ and $Q - V$ droops considering an electrical grid with inductive impedance ($X >> R$) and large amount of inertia, which is the case

[12]PLL performance problems can also be cited here, since may bring steady state errors and instability mainly in weak grids application. So, this approach requires robust PLL implementation [252].

for conventional power system with high voltage transmission lines. In the classical case, equations (5.7) and (5.14) model the droop relation. But, when dealing with Microgrids composed of medium and low voltage lines, in many cases the impedance is not inductive ($X \approx R$) and the active and reactive power decoupling is not true. Then, the traditional droop relation ($P - f$ and $Q - V$) is not applicable. In fact, in resistive lines, the reactive power will depends on the phase angle (or frequency) and the voltage is related to the real power exchange. Therefore, an opposite droop is addressed by $P - V$ and $Q - f$ droops [254].

As mentioned before, droop strategy has only steady state properties, with no dynamical contribution to frequency or voltage regulation, which results in slow transient response with improper active power sharing. In addition, droop control is not able to bring the system back to the original equilibrium point of the system [127, 255].

Another approach to provide virtual inertia is to insert a delay in the active power response, to emulate the inertial behavior of a synchronous machine [256, 257]. In droop control applications, the measured output power is filtered to avoid noise and high frequency components from power converter switching. Usually, a low-pass filter with a suitable time constant is applied, so the filter will induce a slower behavior in active and reactive power that can be compared with the inertial behavior of a synchronous machine [74, 258]. Consequently, the droop control with a well designed filter may be used for virtual inertia purposes. A standard low-pass filter for active power can be described as follows:

$$P^*_{out}(s) = \frac{1}{1 + sT_f} P_m(s) \tag{5.24}$$

where P^*_{out} is the filtered output active power measured in the system, and T_f is the filter time constant.

According to [259], applying the filter dynamics (5.24) in the frequency droop equation (5.7), we may result in the following expression that presents a virtual inertial component:

$$P^*_{out} - P_m = \frac{1}{m_p}(\omega^* - \omega_g) + \frac{T_f}{m_p}\frac{d\omega_g}{dt} \tag{5.25}$$

where the derivative term is equivalent to the inertial response, which results in a LPF with analogous function of a virtual inertia approach. It is necessary to correctly tune the parameters of the droop regulator to obtain a small signal behavior of a synchronous machine [259].

5.5.2. Weak grid modelling

A strong grid is generally modelled by an infinite bus that is capable to attain stability even in front of strong perturbations. The infinite bus is then modelled by an ideal AC voltage source with constant parameters, therefore, the terminal voltage and frequency can be always maintained at fixed values. For distributed generation integration in strong grids using power converters, the converter is responsible only for active and reactive power, while voltage and frequency stability is assured by the main grid.

In weak grids, voltage and frequency stability is not assured, therefore the power converter connected to this grid must be able to provide voltage and frequency support for the system. The AC bus may be modelled as a capacitor, presented in Figure 5.19, where V_c is the system's terminal voltage, and represented by the capacitor's dynamics.

The electrical model used in this section was developed in two parts: The Microgrid with an output LC filter, and the VSM model. It is proposed a VSM using an adaptive virtual inertia approach to improve frequency stability and reduce power oscillations in the grid. The variable inertia scheme is incorporated in a VSC converter connected to an AC Microgrid composed by a diesel generator and loads. The DC side of the grid is formed by a DC Microgrid able to provide energy (ancillary services) to the AC side of the grid. The DC side of the grid was detailed on Chapter IV, being summarized here as voltage V_{dc}. The electrical model of the system is depicted in Figure 5.19.

The VSC converter has a LC filter, represented by L_c and C_c, connected to the Point of Common Coupling (PCC) with the AC Microgrid. The line impedance is represented by L_l and the active losses are given by R_l. The state space model of the system can be written as:

$$\dot{I}_{c,d} = -\frac{R_c}{L_c} I_{c,d} + \omega_g I_{c,q} + \frac{1}{2L_c} V_{dc} m_d - \frac{V_{c,d}}{L_c} \tag{5.26}$$

$$\dot{I}_{c,q} = -\frac{R_c}{L_c} I_{c,q} - \omega_g I_{c,d} + \frac{1}{2L_c} V_{dc} m_q - \frac{V_{c,q}}{L_c} \tag{5.27}$$

$$\dot{V}_{c,d} = \frac{I_{c,d}}{C_c} - \frac{I_{l,d}}{C_c} + \omega_g V_{c,q} \tag{5.28}$$

$$\dot{V}_{c,q} = \frac{I_{c,q}}{C_c} - \frac{I_{l,q}}{C_c} - \omega_g V_{c,d} \tag{5.29}$$

$$\dot{I}_{l,d} = -\frac{R_l}{L_l} I_{l,d} + \omega_g I_{l,q} + \frac{V_{c,d}}{L_l} - \frac{V_{l,d}}{L_l} \tag{5.30}$$

$$\dot{I}_{l,q} = -\frac{R_l}{L_l} I_{l,q} - \omega_g I_{l,d} + \frac{V_{c,q}}{L_l} - \frac{V_{l,q}}{L_l} \tag{5.31}$$

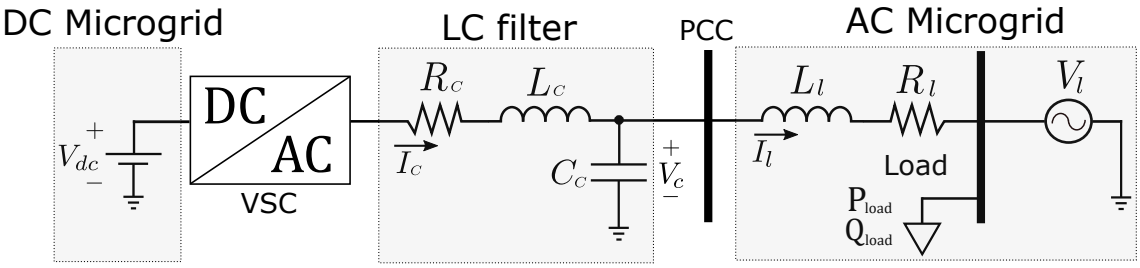

Figure 5.19: Virtual Synchronous Machine (VSM) connected to an AC Microgrid based on diesel generation.

From Park transformation we have: $V_{c,dq}$ the voltage on the LC filter capacitor C_c, $I_{c,dq}$ the current on the LC filter inductor L_c. $I_{l,dq}$ are the line current. The DC/AC converter modulation indexes are m_d and m_q. V_l is the voltage on the diesel generator and P_{load} and Q_{load} are the active and reactive power of the load in the AC Microgrid respectively. The angular speed is given by ω_g, where $\omega_g = 2\pi f_g$.

5.5.3. Proposed virtual inertia

A VSM can act to provide transient power sharing and primary control frequency support independently, using only local measurements. VSM can also be implemented with no need of PLL, being used just for sensing the grid frequency or during initial machine starting[13]. As result, VSM are conceptually simple thanks to intuitive interpretation as synchronous machines responses [57, 75]. The VSM is implemented to provide voltage reference output where the power flow is related to inertia emulation and the angle from the swing equation, while voltage amplitude and reactive power control is made separately by the modulation index in the converter. The VSM scheme is introduced in Figure 5.20, where the direct application of VSM concept is built. The voltage amplitude and the phase angle are directly used to generate the PWM signal in the converter [259].

To develop a VSM it is necessary to implement the swing equation of a Synchronous Machine in the VSC control structure as detailed in [63]. In the following, is presented the general swing equation of a synchronous machine applied for VSM implementation, where the inertia acceleration is represented by the power balance and a damping factor:

$$\dot{\tilde{\omega}} = \frac{1}{H}[P_{ref} - P - D_p(\omega_{vsm} - \omega_g)] \tag{5.32}$$

[13]The swing equation of VSM allows interactions with the grid frequency, influencing its behavior.

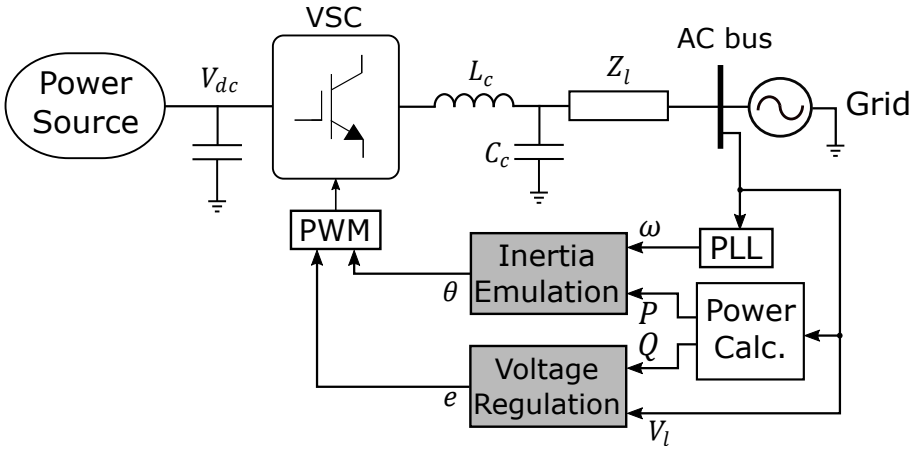

Figure 5.20: VSM general control scheme for a Microgrid integration.

where $\tilde{\omega} = \omega_{vsm} - \omega_g$ is the frequency deviation, ω_{vsm} is the VSM's frequency, H the virtual inertia coefficient and D_p the damping factor. P_{ref} is the active power droop reference and P is the measured power into the AC grid.

The inertia coefficient is defined in [213]:

$$H = \frac{J\omega_o^2}{2S_{nom}} \tag{5.33}$$

where S_{nom} is the nominal apparent power of the VSC converter, ω_o is nominal grid value and J is the emulated moment of inertia. In (5.33) it is evident the inverse ratio between moment of inertia and its time constant. H unit is given in seconds, therefore, the larger the inertia coefficient, the lower the frequency deviation and the longer the accommodation time, and vice-versa, the smaller the inertia coefficient, the higher the frequency deviation and the shorter the accommodation time. This idea is going to be used for variable inertia formulation.

5.5.4. Droop control strategy

Here, the droop control strategy is applied to implement the VSM on the Microgrid's VSC and the application of variable virtual inertia to provide ancillary services.

The power reference is calculated by an active power-frequency droop strategy, included in the swing equation (5.32), relating active power with angular speed deviation as follows:

$$P_{ref} = P^* - K_\omega[\omega_{vsm} - \omega^*] \tag{5.34}$$

where P^* is the desired active power to be injected/absorbed into the grid. K_ω is the $P - f$ droop gain and ω^* is the angular speed reference, i.e., $\omega^* = \omega_o$. In this

case, the angular speed ω_{vsm} computed in (5.32) can be integrated to obtain VSM angle $\delta_{vsm} = \int \omega_{vsm} dt$.

Voltage reference is also calculated by a reactive power-voltage droop strategy, where the voltage is controlled at the PCC (LC filter voltage on capacitor C_c). From synchronous reference frame, voltage $V_{c,d}$ reefers to the voltage module, and then to regulate the voltage amplitude, the following droop equation is presented:

$$V_{c,d_{ref}} = V^*_{c,d} - K_q[Q - Q^*] \tag{5.35}$$

$V^*_{c,d}$ is the desired voltage amplitude and Q^* is the desired reactive power injected/absorbed into the grid, with K_q the droop gain for reactive power. The converter voltage $V_{c,d}$ is controlled to reach $V_{c,d_{ref}}$ using a PI controller, and the PLL is used to measure the grid frequency ω_g, therefore one can consider $V_{c,q} = 0$.

Equations (5.34) and (5.35) are known as the droop reference for respectively the Active Power and Voltage, and represent primary ancillary services. They are seen as a higher level control for the overall power grid.

Here, the control system is used to directly generate the voltage references for PWM signals driving the power electronic conversion. Modulation indexes (m_d and m_q) provides the signal reference to obtain the desired sinusoidal waveform for voltage and current output (V_c and I_c) on the VSC converter, such that, control targets like ancillary services are accomplished.

According to control target, frequency (ω_{vsm}) and voltage ($V_{c,d}$) are chosen as the control output. Modulation indexes (m_d and m_q) provide the reference to generate the PWM signals, where m_d and m_q are transformed into phasor signal with amplitude m and phase θ, chosen as the control inputs. The angle is given by θ_{vsm} from the swing equation in (5.32) and voltage reference $V_{c,d_{ref}}$ is given by the droop strategy in (5.35):

$$\frac{V_{dc}}{2} m\angle\theta = V_{c,d_{ref}}\angle\theta_{vsm} \tag{5.36}$$

The signal obtained in (5.36) is the reference signal for the PMW modulation, making possible to emulate inertia in a VSC.

5.5.5. Stability analysis

The stability analysis of the virtual inertia can be compared with the conventional stability analysis of synchronous machines. The swing equation can be

rewritten considering the total inertia of the system and defining $\tilde{\omega} = \omega_{vsm} - \omega_g$:

$$M\dot{\tilde{\omega}} = P_m - P_{max}\sin(\delta) - D\tilde{\omega} \tag{5.37}$$

where δ is the power angle, $P_{max} = |V_{vsm}||V_g|/X_{eq}$ is the maximum power for the diesel and the VSC converter. D is the equivalent damping factor and M is the equivalent inertia coefficient given by [260]:

$$M = \frac{H_{vsm}H_{diesel}}{H_{vsm} + H_{disel}} \tag{5.38}$$

H_{vsm} and H_{diesel} is the inertia coefficient of the VSM and the diesel generator respectively.

The equivalent input power is given by:

$$P_m = \frac{H_{diesel}P_{vsm} - H_{vsm}P_g}{H_{vsm} + H_{diesel}} \tag{5.39}$$

If the damping term is neglected and the swing equation in (5.37) is multiplied by $\tilde{\omega}$, the following equation is arranged [214]:

$$M\tilde{\omega}\dot{\tilde{\omega}} - (P_m - P_{max}\sin\delta)\tilde{\omega} = 0 \tag{5.40}$$

To find a positive function, equation (5.40) is integrated from its equilibrium point ($\delta^e = \bar{\delta}$, $\tilde{\omega}^e = 0$):

$$W_{vi} = \int_0^{\tilde{\omega}} M\tilde{\omega}d\tilde{\omega} - \int_{\bar{\delta}}^{\delta}(P_m - P_{max}\sin\delta)d\delta = C \tag{5.41}$$

where C is a positive constant.

The Lyapunov function candidate is given by the the energy function of the system [214]:

$$W_{vi} = \tfrac{1}{2}M\tilde{\omega}^2 - [P_m(\delta - \bar{\delta}) + P_{max}(\cos\delta - \cos\bar{\delta})] = E_k + E_p \tag{5.42}$$

where the kinetic energy is given by $E_k = \frac{1}{2}M\tilde{\omega}^2$ and potential energy given by $E_p = -[P_m(\delta - \bar{\delta}) + P_{max}(\cos\delta - \cos\bar{\delta})]$, with respect to the equilibrium point ($\delta^e = \bar{\delta}$, $\tilde{\omega}^e = 0$). The energy function is positive definite around the considered equilibrium point.

The time derivative of the Lyapunov function can be calculated as follows:

$$\dot{W}_{vi} = \frac{\partial E_k}{\partial\tilde{\omega}}\frac{d\tilde{\omega}}{dt} + \frac{\partial E_p}{\partial\delta}\frac{d\delta}{dt} \tag{5.43}$$

Therefore,

$$\dot{W}_{vi} = \tilde{\omega} M \dot{\tilde{\omega}} - (P_m - P_{max} \sin \delta)\tilde{\omega} - D\tilde{\omega}^2 \tag{5.44}$$

The result is a negative definite function of the time derivative of the Lyapunov function [261].

$$\dot{W}_{vi} = -D\tilde{\omega}^2 < 0 \tag{5.45}$$

where is proven that the energy of the system is dissipated proportionally to the damping factor and the frequency deviation. Therefore, the given equilibrium point is asymptotically stable [213, 214].

5.5.6. Simulation results

The proposed model was built on *Matlab/Simulink* using *SimScape Electrical - SimPowerSystems* toolbox. The converter that interfaces a DC Microgrid is connected to an AC one composed of a diesel generator and loads as depicted in Figure 5.19. The diesel generator in the AC Microgrid has a Governor (speed control) to control the frequency and active power. The control parameters of the governor are presented as follows: Regulator gain $K = 150$ and time constant $T_{reg} = 0.1s$, actuator time constant $T_{act} = 0.25s$ and engine time delay $T_d = 0.024s$. The AVR is implemented to control voltage and reactive power [262]. The AVR parameters are presented as follows: Voltage regulator gain $K_{va} = 400$, time constant $T_{va} = 0.02s$ and low-pass filter time constant $T_r = 0.02s$.

The VSM and the AC grid parameters are presented in Table 5.2. The nominal frequency of the grid is $f_n = 50Hz$ and the nominal power of the diesel generator is $S_{diesel} = 2MVA$ with $V_l = 400V$ rms nominal voltage, 2 pairs of poles and inertia coefficient of $H_{diesel} = 3s$. The Q-V droop coefficient is $K_q = 0.3$.

Table 5.2: Microgrid parameters

VSC	$S_{nom} = 1MVA$	$f_s = 20kHz$	$\hat{V}_{c,nom} = 400V$
LC Filter	$R_c = 20m\Omega$	$L_c = 0.25mH$	$C_c = 150\mu F$
VSM	$K_w = 20$	$D_p = 50$	$H_o = 2s$
AC grid	$R_l = 0.1\Omega$	$L_l = 0.01mH$	$V_{l,nom} = 400V$

Here, the VSM has a nominal power of $S_{vsm} = 1MVA$ and same nominal rms voltage as the grid $V_{vsm} = 400V$, where these values are the base for per unit transformation. The active and reactive power load demand of the Microgrid is introduced in Table 5.3.

Table 5.3: The AC load power demand.

Time $[s]$	0	4	12	23	31
Active power $[MW]$	0.5	1	1.8	1.8	1.3
Reactive Power $[kW]$	50	100	200	150	100

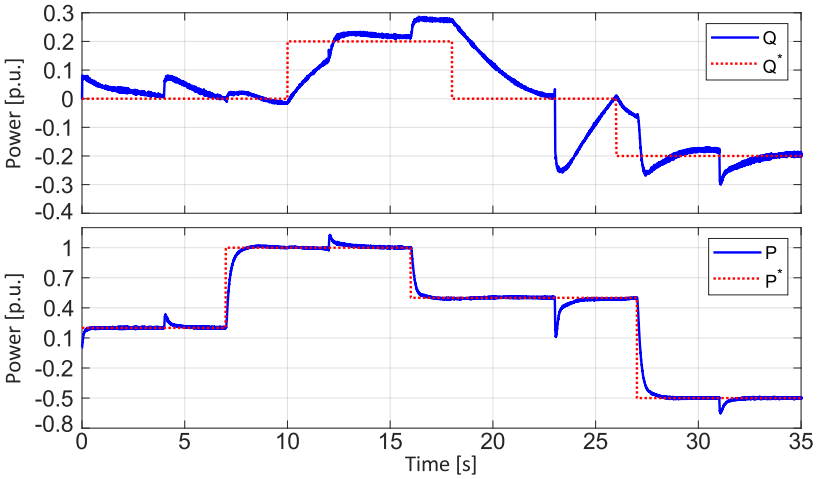

Figure 5.21: The controlled active and reactive power in the VSC converter of the Microgrid.

Active power (P) and reactive power (Q) injected by the VSC converter are controlled in their references (P^* and Q^*), given by a higher control level, according to power dispatch schedule. The controlled active and reactive power are presented in Figure 5.21. Active power is well controlled, following the reference with small overshoots during the load changes. The reactive power is controlled to maintain the voltage regulated in the desired value, and the reactive power reference is given by a secondary control. The steady state errors are due to the droop control feature.

The active and reactive power supplied by the diesel generator is depicted in Figure 5.22, where the power variation are done to control the frequency given by the machine governor. Voltage and machine excitation are regulated by the AVR control. In the figure is clearly seen that the power response of the synchronous machine is slower than the power variations in the VSM.

The voltage on the PCC is controlled according the $P - V$ voltage droop. The voltage amplitude, given by $V_{c,d}$ is introduced in Figure 5.23, where the overshoots are caused mainly during the load changes and the reactive power reference changes. But, even with deviations, the voltage operates within the established limits

The frequency of the VSM and its reference are depicted in Figure 5.24. The diesel generator has a governor to track the frequency in the desired value, therefore,

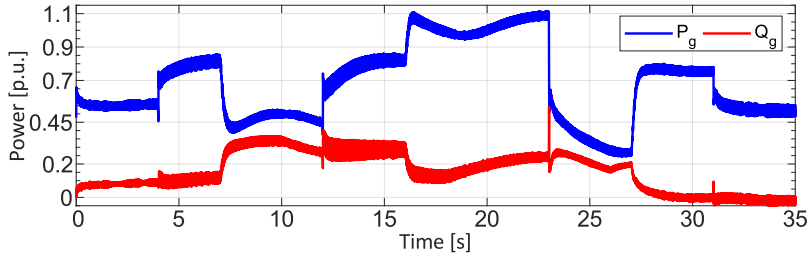

Figure 5.22: The active and reactive power supplied by the diesel generator.

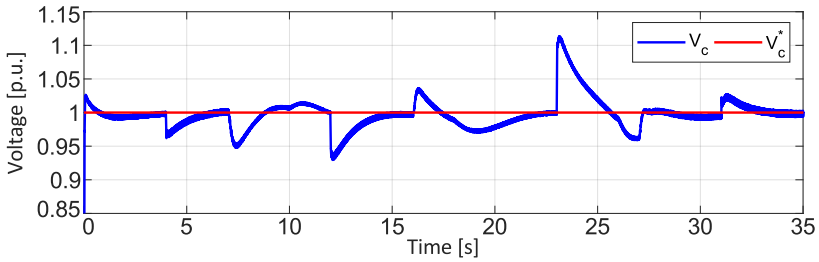

Figure 5.23: The voltage amplitude profile on the PCC.

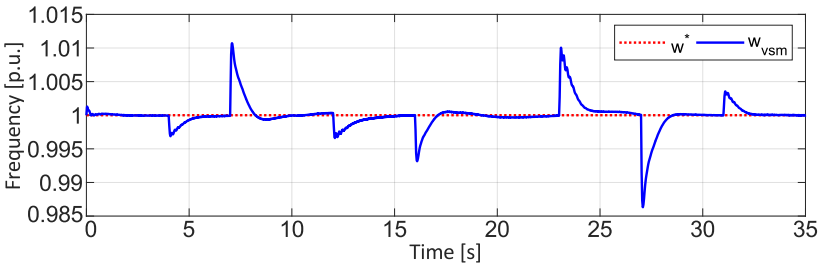

Figure 5.24: The controlled frequency from the VSM approach.

there is no error in steady state. The virtual inertia with the droop equation provide the power sharing with the VSM. As result, the frequency have some transient overshoots during load changes and when the active power injection dispatch changes in the VSM, but remains with good transitory behavior, and quick response to disturbances.

Next, the frequency deviation (Δw) and the frequency RoCoF is introduced in Figure 5.25, where the operational margins of the grid can be analyzed, as the maximum frequency deviation and the rate of change of frequency.

5.5.7. Isolated operation

In the context of Microgrid operation, errors and failures may exist. In the event of a diesel generator failure, the Microgrid converter must be able to operate stand alone, controlling the frequency and voltage in the network within the established grid requirements. In this case, it is possible to use the concept of virtual inertia and droop control to maintain the operation of the system. Here, the isolated operation

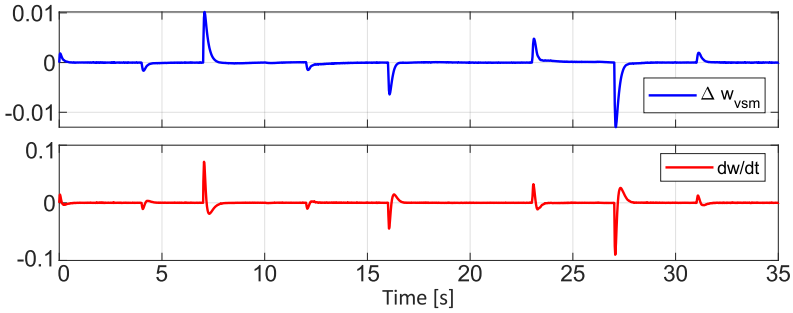

Figure 5.25: The frequency deviation (Δw) and RoCoF.

Table 5.4: The AC load power demand in isolated operation.

Time $[s]$	0	4	12	23	31
Active power $[MW]$	0.5	1	1.8	1	0.5
Reactive Power $[kW]$	50	100	200	100	50

is called when only the VSM is supplying the AC loads from the DC side of the Microgrid, i.e., no rotating machines are connected into the system.

In the isolated operation, considering the VSM, the P and Q dispatch is provided, such that the frequency and the voltage is controlled. Therefore, the reference values of the droop equations (5.34) and (5.35) are set to zero ($P^* = 0$ and $Q^* = 0$). The swing equation of the VSM becomes:

$$\dot{\tilde{\omega}} = \frac{1}{H}[P_{ref} - P - D_p(\omega_{vsm} - \omega^*)] \tag{5.46}$$

where $\tilde{\omega} = \omega_{vsm} - \omega^*$. The swing equation in (5.46) can be applied for isolated operation of the Microgrid. And the droop equations can be expressed as follows:

$$P_{ref} = -K_\omega[\omega_{vsm} - \omega^*] \tag{5.47}$$

$$V_{c,d_{ref}} = K_v[V_{c,d} - V_{c,d}^*] - K_q Q \tag{5.48}$$

where K_v is the voltage droop coefficient.

The simulation of the isolated operation is built considering the same Microgrid parameters of previous simulations. Table 5.4 presents the load variation during these simulations. The power generated in the VSM is to attend the load demanded power of the Microgrid, such that the frequency and the voltage are regulated. The active and reactive power injected by the VSM is introduced in Figure 5.26. The power response is slower than the traditional control of power converters, to emulate the behavior of a synchronous machine.

The voltage on the PCC and the grid frequency are presented in Figure 5.27. The voltage and the frequency present steady state errors due to droop control behavior.

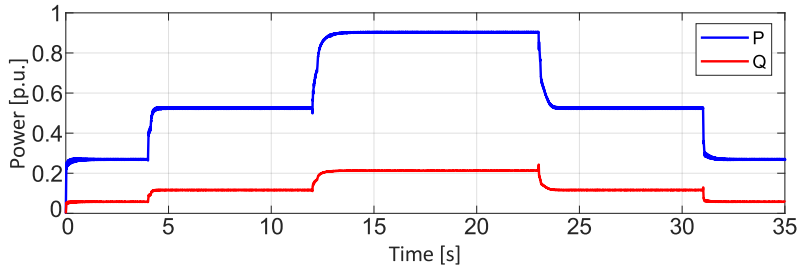

Figure 5.26: The active and reactive power from the VSM in the isolated operation.

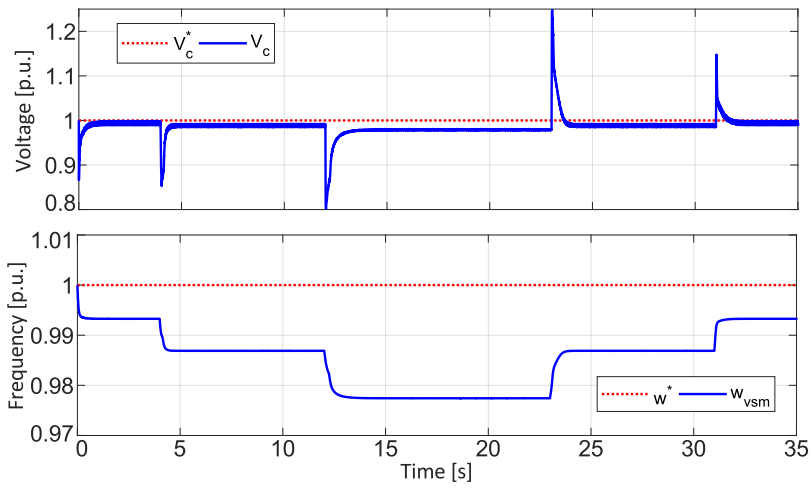

Figure 5.27: The voltage profile and the grid frequency in the isolated operation.

Therefore, when the load increase the power demand, the voltage and frequency stabilize below their references, which can be seen during 12 and 23 seconds of simulation. The transient overshoots are caused by the load change, with larger variations when compared to the system operating with the diesel generator, where the smallest value of frequency is 48.7 Hz. In this case, the voltage and the frequency varies according to the operating condition of the system.

The frequency deviation and the RoCoF are depicted in Figure 5.28. In this case, the frequency deviation are much larger than in previous simulations with the diesel generator in operation, and also has a steady state error. But the frequency RoCoF have smaller peaks compared with the previous simulations.

A integral term from a secondary level control can be inserted in the system to eliminate the steady state error of the frequency and the voltage of the system, improving the operating margins and power quality. Therefore, the droop equations are written as follows:

$$P_{ref} = -K_{\omega}[\omega_{vsm} - \omega^*] - K_{\omega}^{\alpha}\alpha_{\omega} \tag{5.49}$$

$$V_{c,d_{ref}} = K_v[V_{c,d} - V_{c,d}^*] - K_q Q - K_v^{\alpha}\alpha_v \tag{5.50}$$

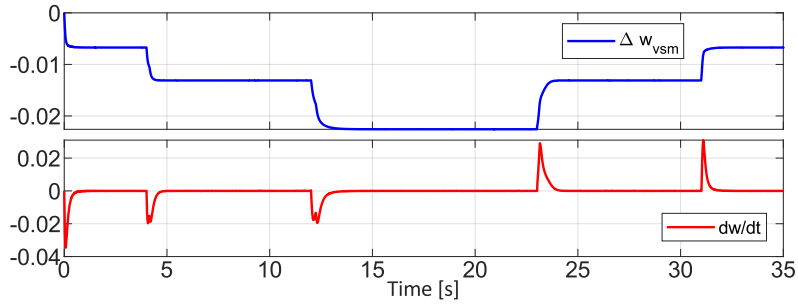

Figure 5.28: Frequency deviation and RoCoF in isolated operation.

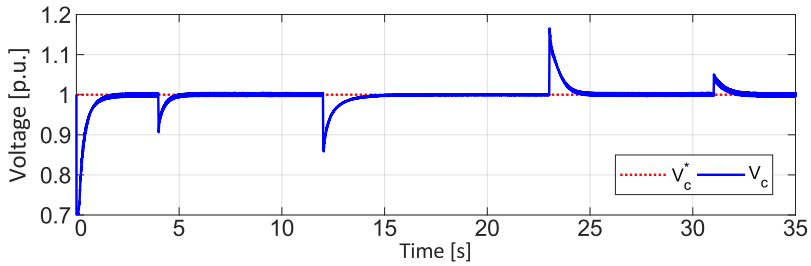

Figure 5.29: Voltage profile on PCC applying the integral term.

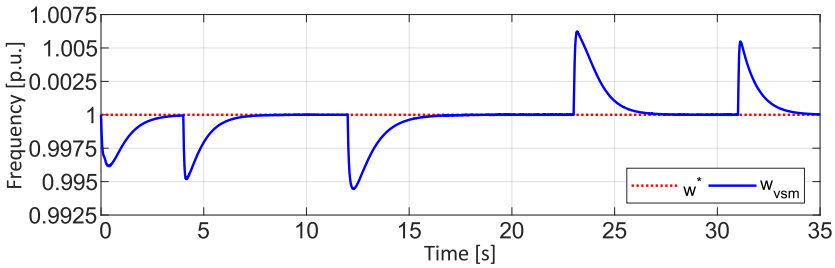

Figure 5.30: Frequency response with the integral term (secondary control).

where the integral gains are K_ω^α and K_v^α, the integral terms are given as $\alpha_\omega = \int(\omega_{vsm} - \omega^*)dt$ and $\alpha_v = \int(V_{c,d} - V_{c,d}^*)dt$.

The following simulations show the behavior of the system when the integral terms representing the secondary controller are employed. The Microgrid parameters are kept the same and the load variations are presented according to Table 5.4.

The voltage profile on the PCC is introduced in Figure 5.29, where the steady state error is eliminated by the secondary control, improving the voltage profile. The same behavior is seen frequency, where the steady state error is eliminated, leaving only the transient overshoots during load changes. The transients levels can be reduced according to the secondary control arrangement. The frequency behavior with the integral term is introduced in Figure 5.30.

The frequency deviation and the RoCoF are presented in Figure 5.31, where frequency deviation is reduced without steady state error.

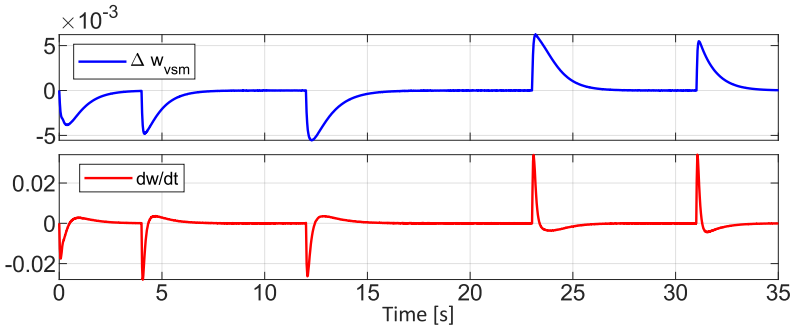

Figure 5.31: Frequency deviation and RoCoF when the integral term is applied.

Table 5.5: The power demand in the AC load, considering the DC Microgrid dynamics.

Time $[s]$	0	4	12	20	25
Active power $[kW]$	40	90	140	90	40
Reactive Power $[kW]$	5	15	20	15	5

5.5.8. Dynamics of the DC Microgrid

In this subsection the DC part of the Microgrid is analyzed, considering the proposed control strategy to the AC side of the grid. Therefore, the proposed virtual inertia approach applied in the VSC converter together with the AC side of the Microgrid (AC load and diesel generator) is inserted in the DC bus of the DC Microgrid, composing the complete system proposed in Figure 3.15. . Simulations are carried out to show the operation of the whole system. The parameters of the VSC converter is sized according to the Microgrid power. The nominal power of the VSM and the diesel generator here is $P_{nom} = 100kVA$, the nominal voltage is $V_{nom} = 400V$, where the control gains are adapted for this configuration. The variation in the power load demand is introduced in Table 5.5.

The active and reactive power from the VSM are depicted in Figure 5.32. The steady state errors refers to the droop strategy feature, where the power is shared with the diesel generator. The mechanical power of the diesel is presented in Figure 5.33, that complements the power injected from the DC side of the Microgrid to properly supply the AC loads.

The voltage on the PCC and the grid frequency are depicted in Figure 5.34. The voltage and frequency are well controlled, with no steady state error, but with some transient overshoots during load changes. The controlled DC bus voltage is introduced in Figure 5.35. The DC bus is kept stable throughout the simulation period, where the largest transients in the voltage are caused by large load variations in the AC grid. The stability of the DC bus is ensured by the supercapacitor in the

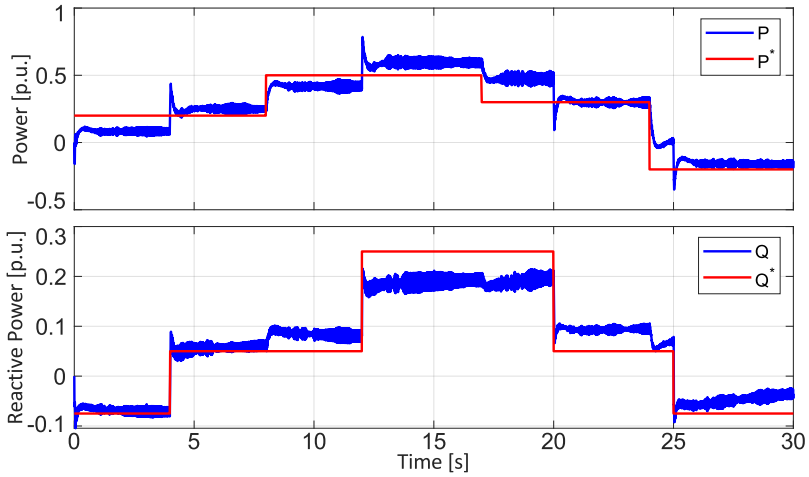

Figure 5.32: Active and reactive power injected by the VSC converter from the DC side of the grid.

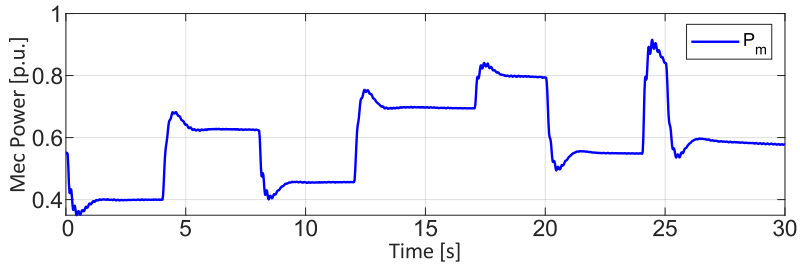

Figure 5.33: The mechanical power in the diesel generator.

DC side of the grid, dealing with all devices in the DC Microgrid bus (PV, battery, train braking and DC load) as seen in Chapter 4.

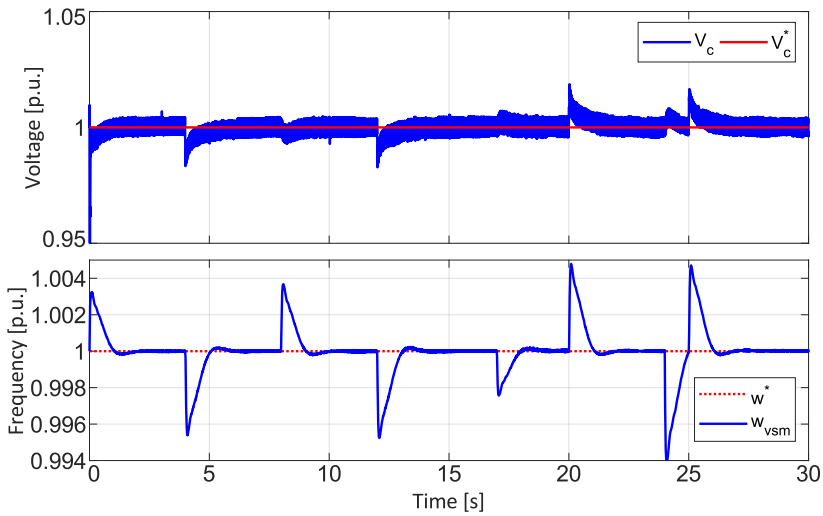

Figure 5.34: The voltage on the PCC and the frequency of the grid.

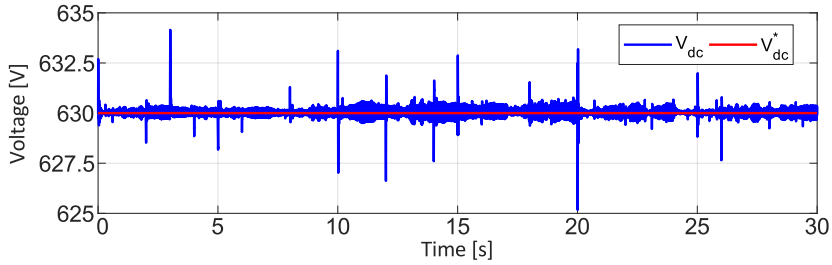

Figure 5.35: The DC bus voltage of the Microgrid considering the virtual inertia approach.

5.6. Adaptive Virtual Inertia Formulation

The inertia coefficient is the key to inertial support and the frequency regulation in the ancillary services provision context. The inertia coefficient indicates the amount of energy that can be stored in the rotating mass of synchronous machine. So, the higher the inertia coefficient, the smaller the frequency deviation, requiring a large disturbance to generate a higher frequency deviation. Now, when the coefficient of inertia is small, the frequency is more susceptible to errors, easily leaving its point of operation in face of disturbances.

Moving forward, the inertia emulated in power converters can be treated as a time varying variable, which can behave to favor the provision of ancillary services, such that, the operation of the system is improved [67, 242, 247]. The inertia is not fixed according to the rotating mass value, but it varies strategically according to the frequency behavior. The idea is to minimize the frequency deviation when the frequency moves from a equilibrium point, by increasing the inertia coefficient. Then, when the frequency return to the equilibrium point, the inertia coefficient is decreased to reach faster the new equilibrium point.

Based on [247], a variable inertia coefficient is given:

$$H \approx H_o + K_M \tilde{\omega} \dot{\tilde{\omega}} \tag{5.51}$$

One may propose a proper time-varying inertia coefficient, from adaptive control theory that precisely define the inertia variation:

$$H \triangleq H_o + K_M \tilde{\omega} \frac{1}{H_0} (P_{ref} - P_{max} sin(\delta) - D_p \tilde{\omega}) \tag{5.52}$$

where H_o is a constant inertia coefficient, kept in steady-state and K_M is interpreted as a positive gain that presents its influence during frequency transients. The inertia coefficient is saturated in order to have $H_{min} \leq H \leq H_{max}$ for suitable constants H_{min} and H_{max} assuring the desired behavior of the electric grid. The angular speed deviation ($\tilde{\omega}$) and its derivative ($\dot{\tilde{\omega}}$) play a important role to change significantly the inertia value during transients.

The variable inertia coefficient proposed in (5.52) is replaced in the swing equation in (5.32). Therefore, an improved inertial support can be implemented in the VSC converter of the Microgrid [247].

To explain the action of the proposed variable inertia coefficient, one may remark that:

1. When $\tilde{\omega} > 0$ and $\dot{\tilde{\omega}} > 0$ or $\tilde{\omega} < 0$ and $\dot{\tilde{\omega}} < 0$, the machine is in accelerating process, which means that angular speed is deviating from its original value. Therefore, the inertia should increase to minimize frequency deviation (inertial support).
2. When $\tilde{\omega} < 0$ and $\dot{\tilde{\omega}} > 0$ or $\tilde{\omega} > 0$ and $\dot{\tilde{\omega}} < 0$, the machine is in decelerating process, which means that angular speed is returning to its steady-state value. Therefore, the inertia should decrease to allow fast return to a new equilibrium point.

This way, it is possible to damp frequency and power oscillation more efficiently than keeping constant inertia.

5.6.1. Stability analysis

Here, the stability analysis of the proposed adaptive virtual inertia is developed, where asymptotic stability of the system is proven. The swing equation of the proposed virtual inertia variation is restructured as a function of the power angle δ, remarking that $\dot{\delta} = \omega_{vsm} - \omega_g$. Equation (5.32) is rewritten as follows [261]:

$$H\ddot{\delta} = P_{ref} - P_{max}sin(\delta) - D_p\dot{\delta} \tag{5.53}$$

where $\delta = \delta_{vsm} - \delta_g$ is the power angle difference between the diesel generator and the VSC, $P_{max}sin(\delta)$ is the maximum available power[14]. Remembering that $\tilde{\omega} = \omega_{vsm} - \omega_g$, and multiplying the last equation by $\tilde{\omega}$, one may obtain:

$$\tilde{\omega}H\dot{\tilde{\omega}} - \tilde{\omega}P_{ref} + \tilde{\omega}P_{max}\sin\delta + D_p\tilde{\omega}^2 = 0 \tag{5.54}$$

The energy variation of the system from a given equilibrium point ($\delta^e = \bar{\delta}$; $\tilde{\omega}^e = 0$) can be calculated by integrating equation (5.55) as:

$$H\int_0^{\tilde{\omega}} \tilde{\omega}d\omega - P_{ref}\int_{\bar{\delta}}^{\delta} d\delta + P_{max}\int_{\bar{\delta}}^{\delta} \sin(\delta)d\delta = C \tag{5.55}$$

where C is a positive constant.

[14]The maximum available power is the nominal power of the VSC or the diesel generator, depending on the power angle δ.

The dissipated energy (damping term) is not considered, obtaining then a well known Lyapunov candidate, considering just potential (E_p) and kinetic (E_k) energy introduced in [214].

$$W_{avi} = \frac{1}{2}H\tilde{\omega}^2 - P_{ref}(\delta - \bar{\delta}) - P_{max}[\cos(\delta) - \cos(\bar{\delta})] \tag{5.56}$$

The time-derivative of the Lyapunov candidate is expressed in (5.57) from the energy function of the system [213]:

$$\dot{W}_{avi} = \frac{\partial E_k}{\partial \tilde{\omega}}\frac{d\tilde{\omega}}{dt} + \frac{\partial E_p}{\partial \delta}\frac{d\delta}{dt} \tag{5.57}$$

where E_k represents the kinetic energy and E_p is the potential energy.

Therefore, considering the inertia coefficient H as time varying, the time-derivative of the Lyapunov candidate can be computed as:

$$\dot{W}_{avi} = \frac{1}{2}\tilde{\omega}^2\frac{dH}{dt} + H\tilde{\omega}\dot{\tilde{\omega}} - P_{ref}\dot{\delta} + P_{max}\sin(\delta)\dot{\delta} \tag{5.58}$$

Substituting (5.53) in (5.58):

$$\dot{W}_{avi} = \frac{1}{2}\tilde{\omega}^2\frac{dH}{dt} + \tilde{\omega}[P_{ref} - P_{max}\sin\delta - D_p\tilde{\omega}] - \tilde{\omega}P_{ref} + \tilde{\omega}P_{max}\sin(\delta) \tag{5.59}$$

Therefore, it results:

$$\dot{W}_{avi} = \frac{1}{2}\tilde{\omega}^2\frac{dH}{dt} - D_p\tilde{\omega}^2 \tag{5.60}$$

The time derivative of the proposed adaptive inertia coefficient is investigated, since it explicitly appears in (5.60), where its computation is developed as follows:

$$\begin{aligned}\dot{H} \triangleq\ & \frac{K_M}{H_0^2}[P_{ref} - P_{max}\sin(\delta) - D_p\tilde{\omega}]^2 \\ & + \frac{K_M\tilde{\omega}}{H_0}\left[-\tilde{\omega}P_{max}\cos(\delta) + \frac{D_p^2}{H_0}\tilde{\omega} - \frac{D_p}{H_0}[P_{ref} - P_{max}\sin(\delta)]\right]\end{aligned} \tag{5.61}$$

Developing equation (5.61), one may obtain:

$$\begin{aligned}\dot{H} =\ & \frac{K_M}{H_0^2}[P_{ref} - P_{max}\sin(\delta) - D_p\tilde{\omega}]^2 - \frac{K_M}{H_0}\tilde{\omega}^2P_{max}\cos(\delta) + \frac{K_MD_p^2}{H_0^2}\tilde{\omega}^2 \\ & - \frac{K_MD_p}{H_0^2}\tilde{\omega}[P_{ref} - P_{max}\sin(\delta)]\end{aligned} \tag{5.62}$$

Therefore, considering the adaptive inertia coefficient in (5.62), the Lyapunov's function time derivative becomes:

$$\begin{aligned}\dot{W}_{avi} =\ & -D_p\tilde{\omega}^2 + \frac{1}{2}\tilde{\omega}^2\left[\frac{K_M}{H_0^2}[P_{ref} - P_{max}\sin(\delta) - D_p\tilde{\omega}]^2\right. \\ & \left. - \frac{K_M}{H_0}P_{max}\cos(\delta)\tilde{\omega}^2 + \frac{K_MD_p^2}{H_0^2}\tilde{\omega}^2 - \frac{K_MD_p}{H_0^2}\tilde{\omega}[P_{ref} - P_{max}\sin(\delta)]\right]\end{aligned} \tag{5.63}$$

and can be developed as:

$$\begin{aligned}\dot{W}_{avi} &= -D_p\tilde{\omega}^2 + \frac{K_M}{2H_0^2}[P_{ref} - P_{max}\sin(\delta) - D_p\tilde{\omega}]^2\tilde{\omega}^2 \\ &+ \left[\frac{K_M D_p^2}{2H_0^2} - \frac{K_M}{2H_0}P_{max}\cos(\delta)\right]\tilde{\omega}^4 - \frac{K_M D_p}{2H_0^2}[P_{ref} - P_{max}\sin(\delta)]\tilde{\omega}^3\end{aligned} \tag{5.64}$$

It is easy to see that inside a given operation region $\|\tilde{\omega}\| \leq \tilde{\omega}_{max}$, $\|(\delta - \bar{\delta})\| \leq \tilde{\delta}_{max}$, for K_M properly chosen such that dH/dt is smaller than $2D_p$, one obtains a negative semi-definite function ($\tilde{\omega}_{max}$, $\tilde{\delta}_{max}$ and C_1 suitable constants):

$$\dot{W}_{avi} = -C_1\tilde{\omega}^2 \tag{5.65}$$

Indeed, for K_M smaller than a limit value: $dH/dt < 2D_p + C_1$, where K_M can be of several thousands of unities for typical values, equation (5.65) together with (5.56) assure boundedness of all states. From this, calling upon La Salle's theorem, one may now conclude that the system is asymptotically stable inside the region $\mathcal{D} = \{\tilde{\omega}, \delta \mid \dot{W}_{avi}(\tilde{\omega}, \delta) \leq 0\}$.

5.6.2. Simulation results

The simulations are performed to present the effectiveness of the proposed control strategy. In this case, the load demand profile is depicted in Figure 5.36, where the active and reactive power variation are shown. Large load variations were considered in simulations, up to 50% of the total load, to analyze the virtual inertia response under large disturbances. The maximum power consumption is $P_{max} = 2.3MW$ and $Q_{max} = 0.25MVA$.

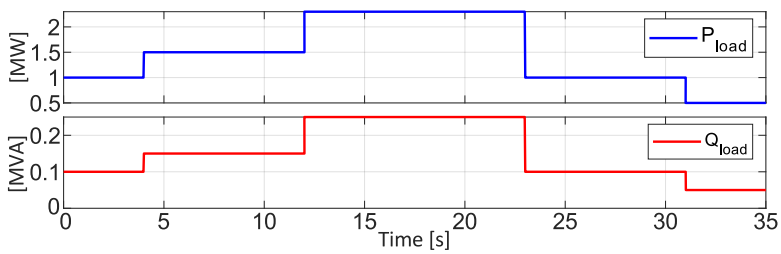

Figure 5.36: AC load profile in the Microgrid.

The VSM is controlled to dispatch active power to assist the diesel generator on the power supply. Figure 5.37 presents the desired power P^* to be injected into the Microgrid by the VSM and measured active power P.

Next is presented the reactive power injected into the grid according to the desired voltage and reactive power profile. The control of voltage and reactive power

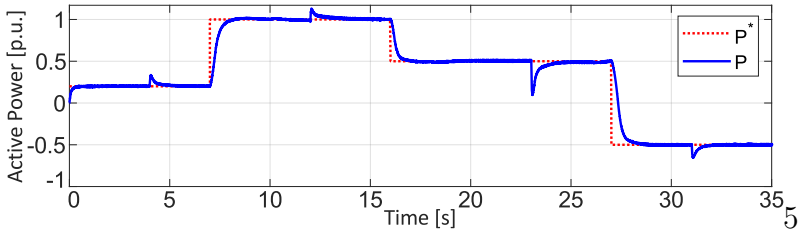

Figure 5.37: The injected power P into the grid and its desired power dispatch P^*.

is made by the droop control presented in (5.35). The reactive power behavior does not go exactly to the desired reactive power profile (Q^*), since the voltage has also to be controlled to a desired value. Then, reactive supply changes to steer the voltage to its reference as depicted in Fig 5.38.

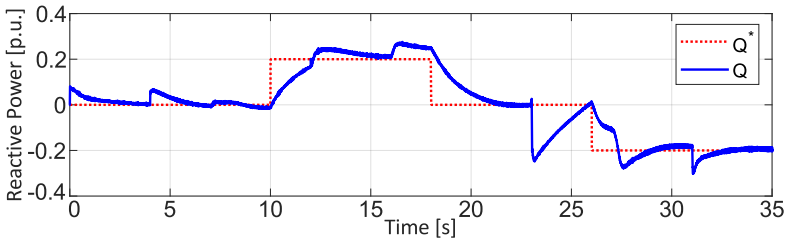

Figure 5.38: The injected reactive power Q into the grid and its desired power dispatch Q^*.

The voltage profile on the PCC (after LC filter) is depicted in Figure 5.39. The voltage is well controlled by the droop to its desired value, even with some transient and steady-state deviations. They are caused by the coupling between active power and voltage, since in this Microgrid we have low X/R relation, which means that the grid is resistive (common in isolated systems).

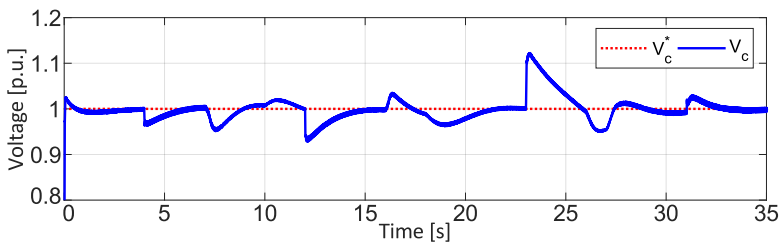

Figure 5.39: Voltage profile on the PCC.

Once the active power was properly regulated by the VSM as shown in Figure 5.37, the frequency of the grid should be controlled, such that system stability is attained. It means balance the injected power by the generator with the load demanded power. But, in this case, there is a low inertia system represented by the diesel generator, where the stability can be compromised by a large load change. Therefore, the VSM is used to assure frequency stability in the AC Microgrid, by

using a virtual inertia. Moreover, a variable inertia is proposed here to improve frequency stability and provide inertial support.

The $I_{d,q}$ currents of the VSM are depicted in Figure 5.40, where the current $I_{l,d}$ is varies according to the active power demand and current $I_{l,q}$ change such that the reactive power is controlled. The mechanical power of the synchronous machine is depicted in Figure 5.41, which is the power input to supply the power demand.

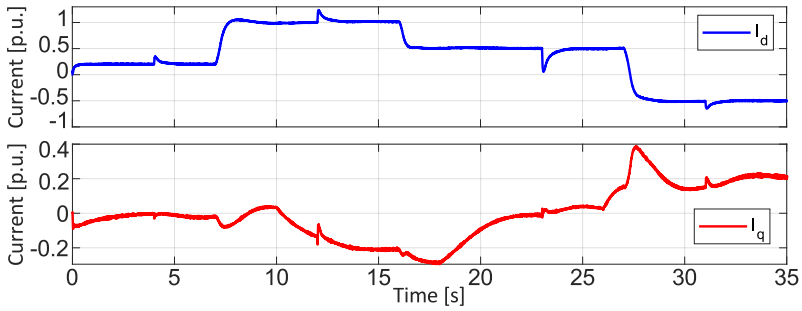

Figure 5.40: The $I_{d,q}$ currents of the VSM.

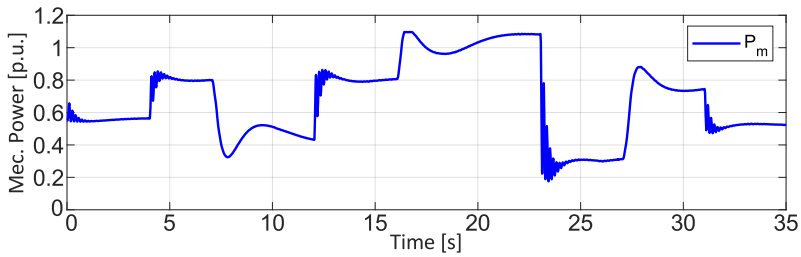

Figure 5.41: The mechanical power input of the synchronous machine.

Figure 5.42 depicts the behavior of the grid frequency ω_g, with the angular speed ω_{vsm} produced by the VSM and the angular speed reference ($\omega^* = 1\ p.u.$). The transient variations outcome from load variations (in 4, 12, 23 and 31 seconds of simulation time) and active power reference changes (in 7, 16 and 27 seconds). As expected, the bigger the power change, the larger the frequency excursion in the grid.

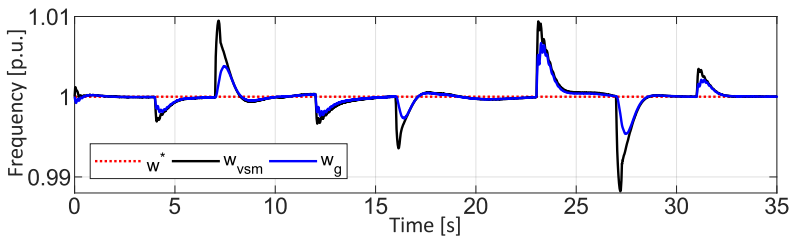

Figure 5.42: Grid frequency ω_g with the angular speed on the VSM (ω_{vsm}) and frequency reference ω^*.

The variable inertia calculated in (5.52), is then applied in the VSM control law. Again, the main idea is to have an inertia coefficient H that varies according to frequency deviation $\tilde{\omega}$ and angular acceleration $\dot{\tilde{\omega}}$. Therefore, when VSM is accelerating, the inertia increases to minimize frequency deviation and when VSM is decelerating, the inertia decreases to speed-up reaching steady-state. The behavior of the variable inertia coefficient can be seen in Figure 5.43. The transient behavior of the inertia is a consequence of $\dot{\tilde{\omega}}$ and $\tilde{\omega}$ as shown in Figure 5.44, where the zoom presents the largest transients in these variables.

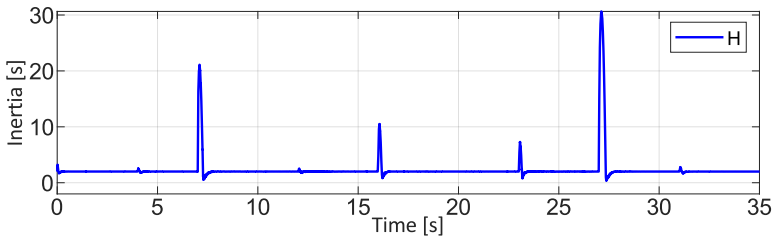

Figure 5.43: Inertia coefficient behavior varying during frequency transients.

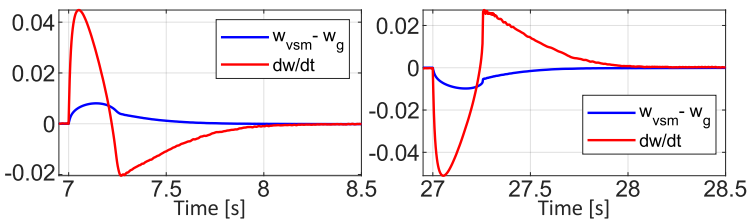

Figure 5.44: Zoom in frequency deviation $\tilde{\omega}$ and in angular acceleration $\dot{\tilde{\omega}}$ during the largest transients.

5.6.3. Comparison with droop control

To perform a complete analysis of the proposed control strategy, a comparison with well know techniques is required. Droop control strategy is widely used in Microgrids to share load demand among generators to balance the power and to assure frequency and voltage stability. Therefore, a comparison between virtual inertia strategy and droop control is developed here.

The droop control is developed as follows:

$$P_{droop} = P^* - K_p(\omega_g - \omega^*) \tag{5.66}$$

where P_{droop} is the resultant power reference in this strategy and K_p is the droop coefficient that relates active power with frequency variation. The coefficient is chosen ($K_p = 5$) according to the limits of power and frequency.

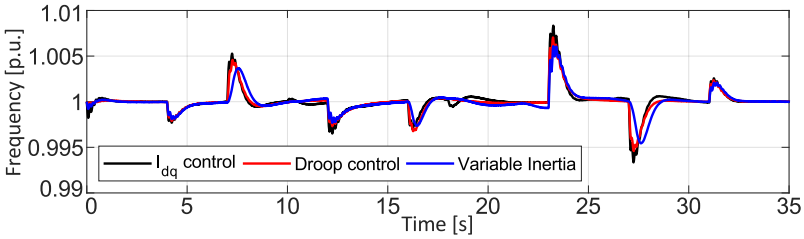

Figure 5.45: Frequency of the grid considering different control approaches.

To perform the comparison, the traditional $I_{d,q}$ control is also developed, where these currents are controlled, such that, active and reactive power are controlled on the desired values (P^* and Q^*). In this case, the only control target is to reach references, given by the following relations:

$$I^*_{c,d} = \frac{P^*}{V_{cd}} \; ; \qquad I^*_{c,q} = \frac{Q^*}{V_{cd}} \tag{5.67}$$

Figure 5.45 presents the behavior of the frequency for each control strategy. The frequency response for standard $I_{d,q}$ control is considered the worse case, since it has highest overshoots and more oscillations. The variable inertia presents best transient response, which improves frequency stability and provides inertial support. The droop control presents a worse frequency behavior compared with virtual inertia strategy, since the transient variations are larger and more oscillatory than the virtual inertia approach. Also, the droop control is not able to perform inertia support, which may result in instability problems.

The main result here is the improvement in inertial support given by the virtual inertia approach, and not only improvement in frequency deviations. The virtual inertia approach may introduce robustness properties for frequency perturbations, therefore, the frequency remains stable in large load changes or shifts in the power set-points. This approach may reduce the fast-control interference of power converters related to stability issues. One can see that, the frequency oscillations are reduced for the virtual inertia when compared with the droop controller, and it is also possible to adjust the inertia coefficient of the system to provide a suitable frequency behavior, reducing power oscillations, since the coefficient parameters (inertia coefficient and damping factor) from the swing equation of synchronous machine can be tuned according to the system conditions. In this thesis, the inertia coefficient and damping factor parameters are chosen according to classical values from synchronous machines, but a study to optimize the choice of these parameters can be very interesting.

A zoom in the largest transient of frequency is depicted in Figure 5.46, where is clearly seen that droop control and $I_{d,q}$ control present almost the same behavior

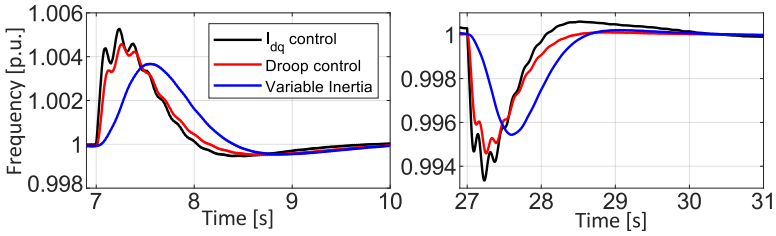

Figure 5.46: Zoom in the frequency tramsients to compare the control strategies.

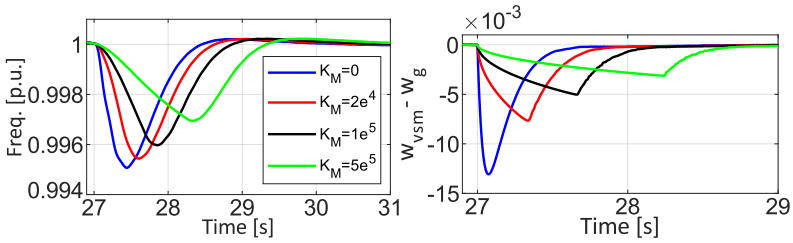

Figure 5.47: Grid frequency on left and frequency deviation on right for different variation in the inertia coefficients.

with no inertial support while the virtual inertia approach reduces the frequency deviation in the grid during load changes and power perturbations, improving frequency Nadir and RoCoF.

5.6.4. Comparison of different inertia coefficients

In this subsection, a comparison between constant inertia coefficient and a variable one is made. The idea is to compare how the frequency deviation changes when the inertia is fixed and how is the response for changing the coefficient K_M in the variable inertia approach. Four different scenarios are simulated, first with constant inertia (which means $K_M = 0$), second $K_M = 2e^4$, third $K_M = 1e^5$ and fourth $K_M = 5e^5$, where for the proposed values of K_M, equation (5.65) is always valid.

As coefficient K_M increases, the frequency deviation decreases, improving the transient frequency response in the Microgrid. This is clearly shown in Figure 5.47, where the four scenarios are presented with a zoom.

Figure 5.48 presents how the moment of inertia changes according to the coefficient K_M, making possible larger inertia coefficients to reduce frequency deviations, improving frequency Nadir and RoCoF. Also is presented how the angular acceleration behaves in these cases. All of these figures are zoomed in to depict the largest transient during simulations.

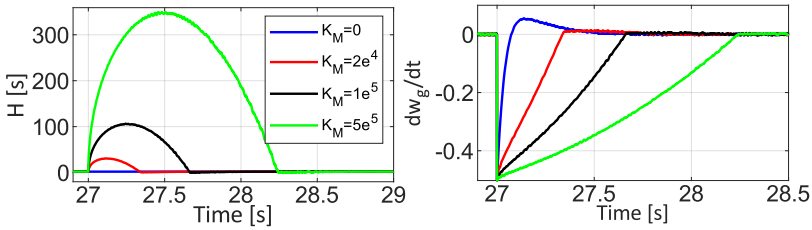

Figure 5.48: Inertia coefficient on the left and angular acceleration on the right over different values of K_M.

Table 5.6: The AC load power demand for two synchronous machines scenario.

Time $[s]$	0	4	15	23	33
Active power $[MW]$	1.3	1.8	2.3	1.0	0.5
Reactive Power $[kW]$	100	150	250	100	50

5.6.5. Additional simulation results

The results of the proposed adaptive virtual inertia control can be diversified, creating different network configurations and analyzing their control performance. To do this, one more synchronous generator was inserted in the AC bus of Microgrid, to operate in parallel with the others already existed generators in the system. The additional synchronous machine have $1MVA$ and $400V$ of nominal voltage directly connected in the AC bus of the Microgrid. The power dispatch in the synchronous machine is made according to the load demand supposing a secondary controller, and the local controller is given by droop scheme for power sharing. The voltage control is made by the local AVR of the machine. The AC load demand for this case is presented in Table 5.6.

Therefore, the power flow of the Microgrid can be seen trough the active and reactive power of each generator. The active and reactive power of both synchronous machines is presented in Figure 5.49. The controlled active and reactive power of the VSM are depicted in Figure 5.50, where the active power assume negative values in few moments to absorb the energy from the other generators.

The voltage on the PCC and the frequency of the grid is depicted in Figure 5.51. The voltage and frequency have good control performance, with no steady state error. The Frequency deviation and the RoCoF is improved by the adaptive virtual inertia.

Finally, a comparison between the fixed coefficient of inertia and the proposed adaptive inertia is developed for the isolated operation, i.e., without the presence of diesel generators. The comparison of the frequency behavior for both cases is depicted in Figure 5.52. The frequency transients in the adaptive inertia are

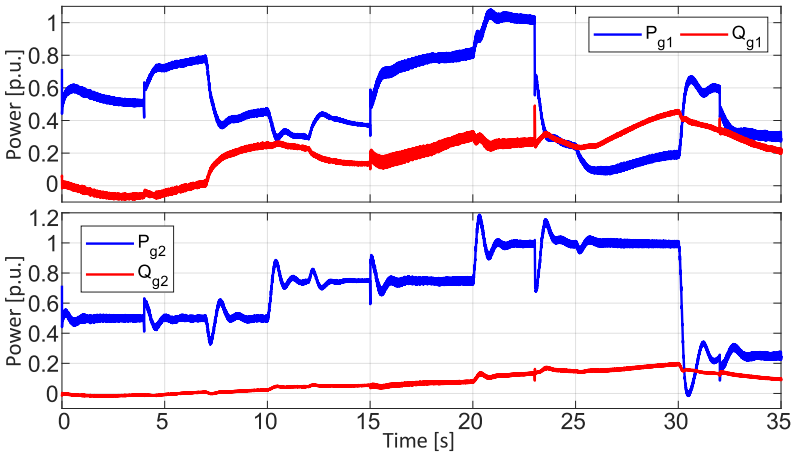

Figure 5.49: Active and reactive power flow of the generator 1 ($2MVA$) and the inserted generator 2 ($1MVA$), respectively.

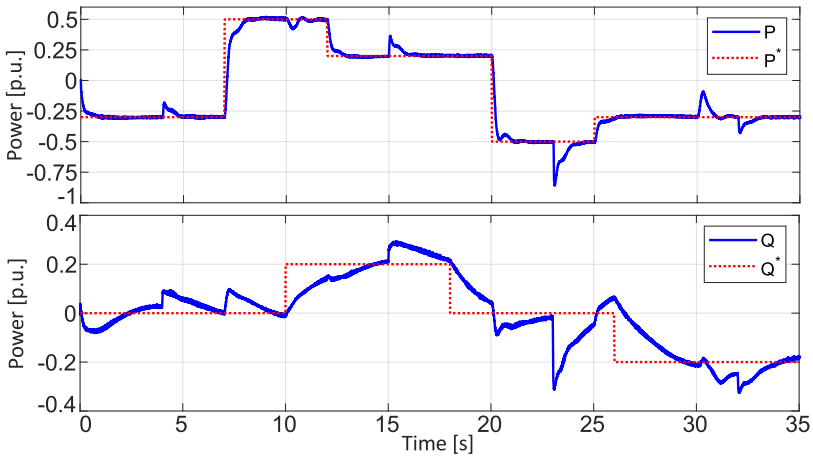

Figure 5.50: Controlled active and reactive power in the VSM.

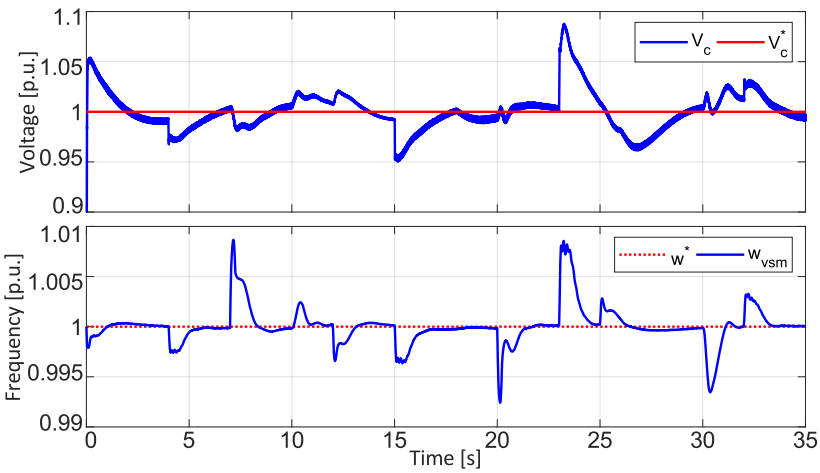

Figure 5.51: Voltage on the PCC and grid frequency with two generators connected in the AC bus of the Microgrid.

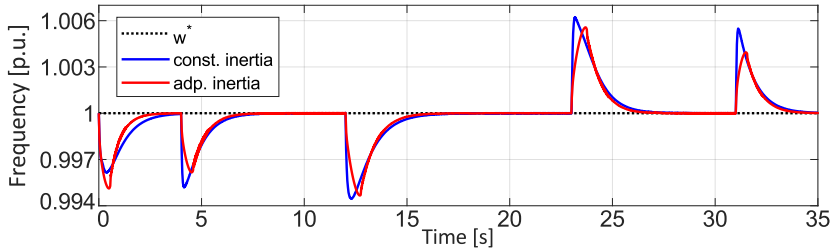

Figure 5.52: The comparison between fixed inertia and adaptive inertia approach for the system in isolated operation.

considerably reduced when compared to the fixed inertia coefficient. The convergence speed, in this case, are the same for both control strategies. Thus, the proposed adaptive inertia actually improves the inertial support.

5.7. VSM with Voltage and Current Control

Virtual Synchronous Machine application can be done through a reduced order synchronous machine model, where the active power balance is associated to the system inertia and the swing equation provides the power angle. Then, the voltage regulation is related with reactive power control from a droop equation independent of the inertia emulation [259]. The direct implementation of VSM concept is developed in subsection 5.4.3, where voltage amplitude regulation and the phase angle are straightly inserted as the PWM signal of the power converter. In this case, the voltage and current saturation, the over-current protection, and the interaction of the control loops are not included in this structure. Here, the voltage control loop is implemented following the reactive power control, with a inner current control loop. This strategy allows a more flexible VSM implementation, which may include protection schemes with saturation in the control outputs, but a proper tuning of the controllers is required [259, 263].

The proposed adaptive virtual inertia is implemented in this section considering the design of a nonlinear control strategy for voltage control loop and the inner current control loop, such that, the operation of the VSC converter is improved. The voltage control can enhance performance of the system assuring the stabilization of other state variables of the system, i.e. voltage and current. A virtual impedance is inserted to improve the controllability of the system, where the X/R ratio is compared to classical power systems, and then the decoupling between active and reactive power is reached, accordingly the $(P - f)$ and $(Q - V)$ relation can be applied. A nonlinear control strategy based on singular perturbation analysis with

explicit time-scale separation is developed for voltage and current control [15], in this case the current is controlled, such that, the voltage tracks its reference, where a simplified controller is obtained. A rigorous stability analysis is conducted for the overall control and the virtual inertia, assuring asymptotic stability.

The state space model of the AC Microgrid given in (5.26)-(5.31), where the control induced time-scale separation based on singular perturbation for the voltage and current control loops are developed, followed by their stability analysis.

The scheme of the proposed control strategy is introduced in Figure 5.53, and is composed by the active and reactive power control, given by the droop controllers. The active power control provides the power reference for the swing equation of the virtual inertia to generate the power angle of the converter. The virtual impedance is inserted to provide the reference for the voltage control loop, improving damping, power sharing and decoupling of active and reactive power flows. The voltage control loop provides the references for the current control loop, where the voltage is allocated to have slower dynamics than current control loop, such that, a control induced time-scale separation is created. The current control loop results in the modulation indexes, which is provided to the PWM signal.

Remark 8. *In this case, the synchronism between the diesel generator and the VSC converter results from the virtual swing equation, similar to conventional synchronous machines in parallel, where the Phase-Looked Loop (PLL) is not necessary. In any case, the PLL can be used for frequency measurement purposes.*

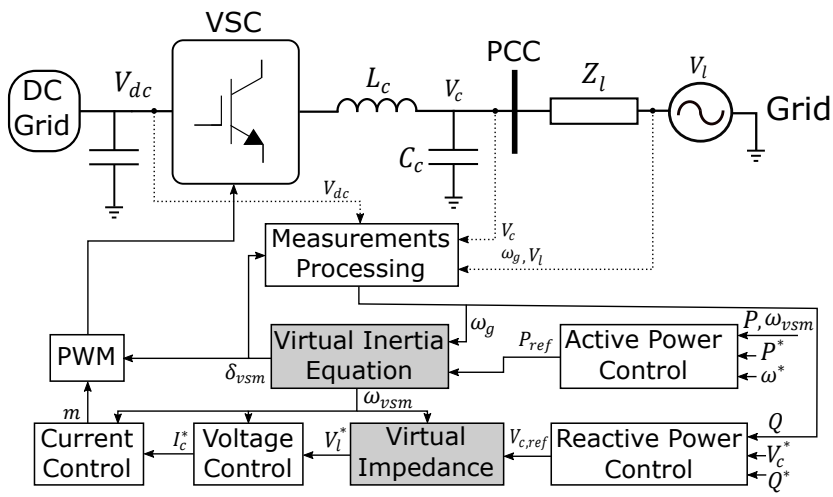

Figure 5.53: Proposed virtual inertia control scheme for the Microgrid using virtual impedance.

[15]This is the similar development of the control strategy designed in subsection 4.2.3 from Chapter 4.

5.7.1. Active and reactive power control

The power reference is calculated by an active power-frequency droop strategy, included in the swing equation (5.32), relating active power with angular speed deviation as given in (5.34) where P^* is the desired active power to be injected/absorbed into the grid.

Voltage reference is computed by a reactive power-voltage droop strategy, where the voltage is controlled at the PCC (LC filter voltage on capacitor C_c). From synchronous reference frame, voltage $V_{c,d}$ refers to the voltage module, and then to regulate the voltage amplitude, the droop equation in (5.35) is applied, with $V^*_{c,d}$ is the desired voltage amplitude and Q^* is the desired reactive power injected/absorbed into the grid,

The converter's voltage $V_{c,d}$ is controlled to reach $V_{c,d_{ref}}$, and the PLL is used to measure the frequency of the grid ω_g, therefore we may consider $V^*_{c,q} = 0$ from the synchronous reference frame. Equations (5.34) and (5.35) are the droop reference for respectively the Active Power and Voltage, and represent primary ancillary services. They are seen as a higher level control for the overall power grid.

5.7.2. Virtual impedance

The voltage amplitude reference from the droop equation in (5.35) is summed with a virtual impedance, given by a virtual resistance (R_v) and a virtual inductance (L_v). The voltage reference including the virtual impedance is written as follows:

$$V^*_{c,d} = V_{c,d_{ref}} - (R_v - \omega_g L_v) I_{l,q} \tag{5.68}$$

$$V^*_{c,q} = 0 - (R_v + \omega_g L_v) I_{l,d} \tag{5.69}$$

where the quadrature voltage reference is zero ($V_{c,q_{ref}} = 0$) from the synchronous reference frame.

The virtual impedance is used to modify the dynamics and steady-state features of the Virtual Synchronous Machine. The displacement of the phase angle between the PCC voltage (V_l) and the converter output voltage (V_c) caused by the virtual power flow, allows the VSM to improve voltage control in the converter instead of the actual voltage in the PCC. It reduces the sensitivity to disturbances in the grid and emulates the synchronous impedance quasi-stationary characteristics in synchronous generators [256, 264, 265].

5.7.3. Voltage and current control

The voltage control loop is designed via a control induced time-scale separation, to artificially make the currents' dynamics much faster than the voltages' dynamics, then we may create a singular perturbation condition. In this case, a reduced model for voltages V_{cd} and V_{cq} is obtained.

The first step is to design a current control loop, in which the currents $I_{c,d}$ and $I_{c,q}$ track their respective references $I^*_{c,d}$ and $I^*_{c,q}$ yet to be designed. Applying feedback linearization to currents $I_{c,d}$ and $I_{c,q}$, the control inputs are calculated as follows:

$$m_d = \frac{2}{V_{dc}}[L_c v_{id} + R_c I_{c,d} - \omega_g L_c I_{c,q} + V_{c,d}] \tag{5.70}$$

$$m_q = \frac{2}{V_{dc}}[L_c v_{iq} + R_c I_{c,q} + \omega_g L_c I_{c,d} + V_{c,q}] \tag{5.71}$$

where the additional control inputs are chosen using linear techniques to give the desired dynamics for $I_{c,dq}$:

$$\begin{aligned}
v_{id} &= -K_{id}(I_{c,d} - I^*_{c,d}) - K^{\alpha}_{id}\alpha_{id} \\
\dot{\alpha}_{id} &= I_{c,d} - I^*_{c,d} \\
v_{iq} &= -K_{iq}(I_{c,q} - I^*_{c,q}) - K^{\alpha}_{iq}\alpha_{iq} \\
\dot{\alpha}_{iq} &= I_{c,q} - I^*_{c,q}
\end{aligned}$$

Here, α_{dq} are an auxiliary dynamics representing integral terms to ensure zero error in steady-state. The gains K_{id} and K_{iq} are positive constants calculated by pole placement to regulate the speed convergence of the current [36, 117].

Now defining:

$$\xi_I = \left[\left(I_{c,d} - I^*_{c,d}\right)\ \alpha_{id}\ \left(I_{c,q} - I^*_{c,q}\right)\ \alpha_{iq}\right]^T$$

it is standard to define symmetric matrices $P_I,\ Q_I > 0$ such that we obtain the Lyapunov's function and its derivative:

$$W_i = \xi_I^T P_I \xi_I \tag{5.72}$$

$$\dot{W}_i = -\xi_I^T Q_I \xi_I \tag{5.73}$$

that assure exponential stability for this subsystem.

Then, applying control input (5.70)-(5.71) in (5.26)-(5.27) respectively, the boundary layer model for the voltages' dynamics is obtained as:

$$\dot{V}_{c,d} = \frac{I^*_{c,d}}{C_c} - \frac{I_{l,d}}{C_c} + \omega_g V_{c,q} \tag{5.74}$$

$$\dot{V}_{c,q} = \frac{I^*_{c,q}}{C_c} - \frac{I_{l,q}}{C_c} - \omega_g V_{c,d} \tag{5.75}$$

where from singular perturbation analysis, we consider that $I_{c,dq}$ has already reached $I^*_{c,dq}$ on the voltages dynamics (the current is allocated to be much faster than the voltages).

The dq currents' references $I^*_{c,d}$ and $I^*_{c,q}$ will be used as virtual control inputs, such that, the voltages $V_{c,dq}$ reach their references $V^*_{c,dq}$. This backstepping procedure is completed by feedback linearization, leading to:

$$I^*_{c,d} = C_c v_{vd} + I_{l,d} - \omega_g C_c V_{c,q} \tag{5.76}$$

$$I^*_{c,q} = C_c v_{vq} + I_{l,q} + \omega_g C_c V_{c,d} \tag{5.77}$$

with the additional control inputs $v_{v,dq}$ chosen to generate a linear stable subspace expressed as:

$$\begin{aligned}
v_{vd} &= -K_{vd}(V_{c,d} - V^*_{c,d}) - K^{\alpha}_{vd}\alpha_{vd} \\
\dot{\alpha}_{vd} &= V_{c,d} - V^*_{c,d} \\
v_{vq} &= -K_{vq}(V_{c,q} - V^*_{c,q}) - K^{\alpha}_{vq}\alpha_{vq} \\
\dot{\alpha}_{vq} &= V_{c,q} - V^*_{c,q}
\end{aligned}$$

where K_{vd} and K_{vq} are positive gains computed by pole placement, such that the explicit time-scale separation is ensured. $\alpha_{v,dq}$ are the integral terms to eliminate steady-state errors.

Therefore, by control inputs (5.70) and (5.71) based on (5.76) and (5.77), the system in (5.74)-(5.75) becomes linear. Now defining:

$$\xi_V = \left[\left(V_{c,d} - V^*_{c,d}\right)\ \alpha_{vd}\ \left(V_{c,q} - V^*_{c,q}\right)\ \alpha_{vq}\right]^T$$

it is standard to define symmetric matrices $P_V,\ Q_V > 0$ such that we obtain the Lyapunov's function and its derivative:

$$W_v = \xi_V^T P_V \xi_V \tag{5.78}$$

$$\dot{W}_v = -\xi_V^T Q_V \xi_V \tag{5.79}$$

that assure exponential stability for this boundary layer subsystem. Now, using singular perturbation analysis [188], we can assure that the full system is also exponentially stable.

Therefore, there is a Lyapunov function for the whole system, composed of the previous Lyapunov functions:

$$W = W_v + W_i + W_{avi} > 0 \tag{5.80}$$

From (5.78), (5.72) and (5.65) we can state that:

$$\dot{W} = \dot{W}_v + \dot{W}_i + \dot{W}_{avi} \leq 0 \tag{5.81}$$

where, in conjunction with Barbalat's Lemma, asymptotic stability is proven for all states, but δ that is only kept stable. This last result is equivalent to the case of standard synchronous machines.

5.7.4. Simulation results

Active power (P) and reactive power (Q) injected by the VSC converter are controlled to their references (P^* and Q^*), given by a higher control level, according to power dispatch schedule. Initially, the load demand in the simulation is $1MW$ and $0.1MVA$, where the VSC supplies $0.2MW$ and $0MVA$ and the diesel generator complements the power supply. Therefore, a load increase of 1 MW and $0.1MVA$ occurs after 5 seconds of simulation. In 10 seconds the active power reference of the VSC converter changes to $0.7MW$ and in 15 seconds the reactive power reference changes to $0.2MVA$. Then, in 20 seconds a load reduction of $1MW$ and $0.1MVA$ takes place and finally in 25 seconds the active power reference changes to $-0.5MW$.

The controlled active and reactive power are presented in Figure 5.54. Active power is controlled, following the reference with overshoots during the load changes and have fast response to reference changes. The reactive power is controlled to follow its reference, with overshoots during load changes and changes in power reference. The virtual impedance greatly improves the capacity of the system to provide reactive power regulation in the grid by the VSC converter. The larger the virtual impedance, the greater the amount of reactive power that can be controlled, assuring the decouple between active and reactive power. This is because, the virtual impedance acts as a buffer to reduce the gap between the fast dynamics of power converters and synchronous machines. On the other hand, they impose bounds in the droop feedback coefficients to guarantee the system stability.

The active and reactive power supplied by the diesel generator is depicted in Figure 5.55, where the power varies to stabilize the frequency following the machine governor, such that, the power balance is assured. Voltage and machine excitation are regulated by the AVR control. In the figure, it is clearly seen that the power

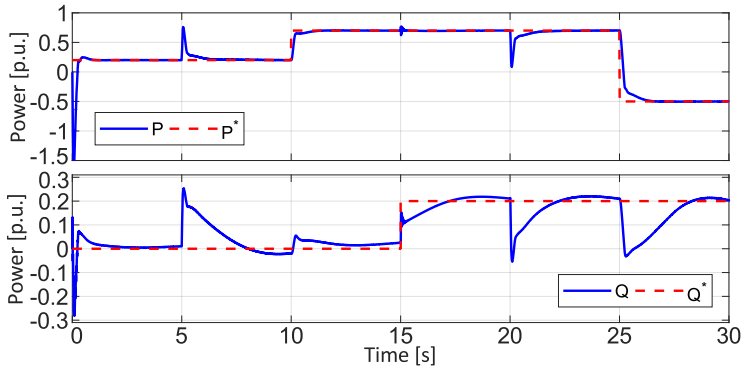

Figure 5.54: The controlled active and reactive power in the VSC converter of the Microgrid.

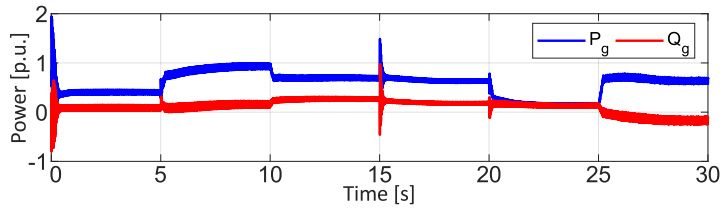

Figure 5.55: The controlled active and reactive power in the diesel generator to allow power balance.

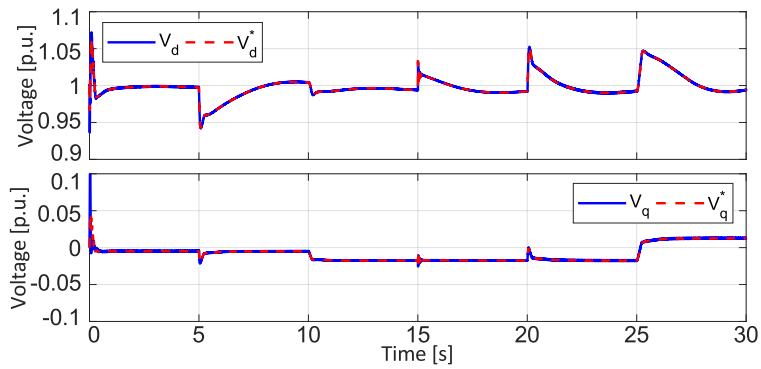

Figure 5.56: The controlled voltage of the grid in the PCC.

response of the synchronous machine is slower than the power variations in the VSM.

The voltage profile is depicted in Figure 5.56, where voltage V_d shows the voltage amplitude in the PCC, and the quadrature voltage V_q is set to zero for the synchronous reference frame. The reference V_d^* is given by the droop control in combination with the virtual impedance inserted to improve the controllability of the voltage and decouple the active and reactive power relation, resulting in a high X/R as traditional power systems. The voltages are well controlled with fast transient response and very small overshoots, which results in a good voltage profile. The steady state errors are caused because of the droop feature.

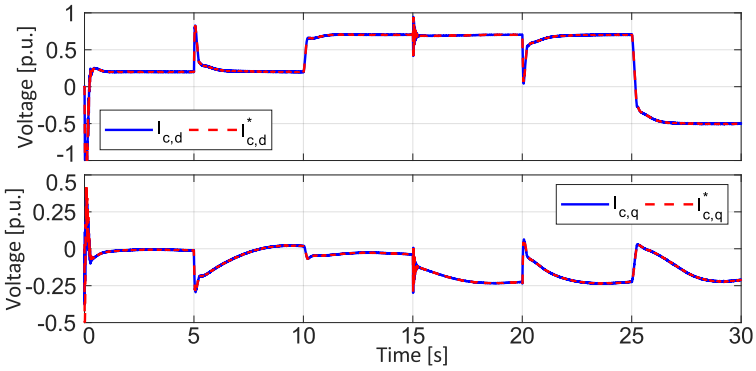

Figure 5.57: The controlled currents of the VSC converter.

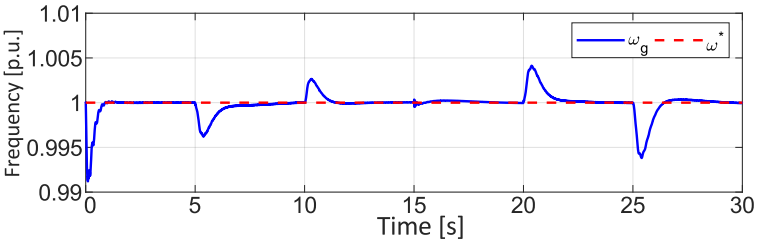

Figure 5.58: Frequency of the grid and its reference.

The direct and quadrature currents are presented in Figure 5.57, where the currents are controlled with fast response without overshoots. The references are given such that, the voltage V_d and V_q are controlled in the desired reference from singular perturbation analysis.

The frequency of the Microgrid is presented in Figure 5.42, where the proposed virtual inertia is used to reduce frequency deviation and to improve frequency RoCoF. The transient variations respond to load variations (in 5 and 20 seconds of simulation time) and power reference changes (in 10, 15 and 25 seconds). As expected, the bigger the power change, the larger the frequency excursion in the grid. The droop control developed in the VSC converter would result in steady state error in frequency, but governor of the diesel generator manages to eliminate the steady state error.

The adaptive inertia calculated in (5.52) is then applied in the VSM control law. The main idea is to have an inertia coefficient H that varies according to frequency deviation $\tilde{\omega}$ and angular acceleration $\dot{\tilde{\omega}}$. Therefore, when VSM is accelerating, the inertia increases to minimize frequency deviation and when VSM is decelerating, the inertia decreases to speed-up reaching steady-state. The behavior of the adaptive inertia coefficient can be seen in Figure 5.59. The transient behavior of the inertia is a consequence of $\dot{\tilde{\omega}}$ and $\tilde{\omega}$ as shown in Figure 5.60, where the zoom presents the largest transients in these variables.

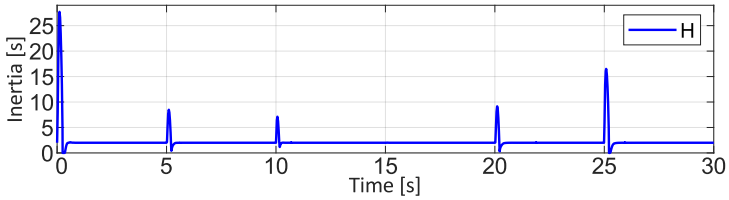

Figure 5.59: Inertia coefficient behavior varying during frequency transients.

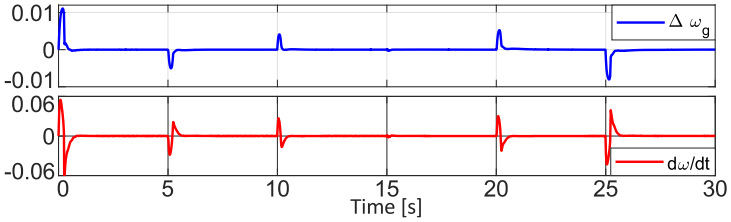

Figure 5.60: Zoom in frequency deviation $\tilde{\omega}$ and in angular acceleration $\dot{\tilde{\omega}}$ during the largest transients.

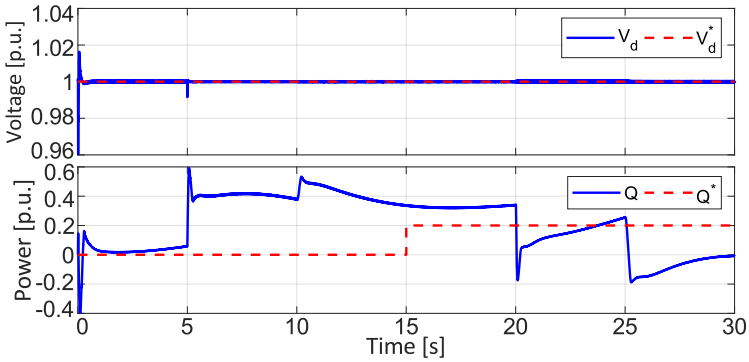

Figure 5.61: Zoom in frequency deviation $\tilde{\omega}$ and in angular acceleration $\dot{\tilde{\omega}}$ during the largest transients.

5.7.5. Fixed voltage reference

To guarantee a fixed voltage level on the PCC, the voltage reference is set to $1p.u.$, and it is removed the droop loop for sharing reactive power. Thus, the reactive power is adjusted only by the synchronous machine, and the VSC converter is able to maintain the voltage within a fixed reference value, which can improve the power quality on the PCC.

The voltage profile with reference fixed to $1p.u.$ and the reactive power supplied by the synchronous generator is introduced in Figure 5.61. It is possible to notice that the voltage remains stable without deviations or overshoots, presenting good control performance. The reactive power has a slower behavior, because it is provided by the diesel generator, and one can see that the system is able to correctly fulfill the load demand.

5.7.6. Parameters variation

To better understand the effect of parameters for the virtual inertia application, in this section there are tested several changes in the VSM parameters, in order to analyze the difference in the frequency response of the network. The concerned parameters are the fixed inertia constant H_0, the damping coefficient D_p, and the coefficient droop K_w. Two cases are simulated, in the first case both parameters are increased by 50% of the nominal value, and in the second case a reduction of 50% of the parameters is made.

Figure 5.62 depicts the values of frequency, coefficient of inertia, frequency deviation and frequency RoCoF respectively, where only the transient periods are presented. It is clearly shown that in the first case (50% increase) the frequency variations are considerably reduced, that is, the frequency nadir is improved and the frequency deviation together with the frequency RoCoF is also improved, however the response speed is slightly reduced. This happens because the coefficient of inertia has greater variations during transients, acting more to prevent frequency deviation. In the second case, the frequency variation increases and has some oscillations during the transient. The frequency deviation and RoCoF also increases, since the impact of adaptive inertia is reduced, however the convergence time is faster as shown in the figure. In this way, it is possible to reach a compromise between the strength of the VSM's performance for different Microgrid applications, aiming to improve inertial support.

Another important comparison is in relation to constant K_M referring to the transient term of adaptive inertia during transients, which must be adjusted in order to obtain an improvement in the frequency response and respecting the stability condition in (5.65). Thus, variations were made in the constant K_M for comparison with constant inertia coefficient ($K_M = 0$). The idea is to compare how the frequency deviation changes when the inertia is fixed and how is the response for coefficient K_M in the adaptive inertia approach. Four different scenarios are simulated, first with constant inertia (which means $K_M = 0$), second $K_M = 5e^4$, third $K_M = 5e^5$ and fourth $K_M = 5e^6$, where for the proposed values of K_M, condition (5.65) is always valid.

As coefficient K_M increases, the frequency deviation decreases, improving the transient frequency response in the Microgrid. This is clearly shown in Figure 5.63, where the four scenarios are presented in detail. The figure presents how the moment of inertia changes according to the coefficient K_M, making possible larger inertia

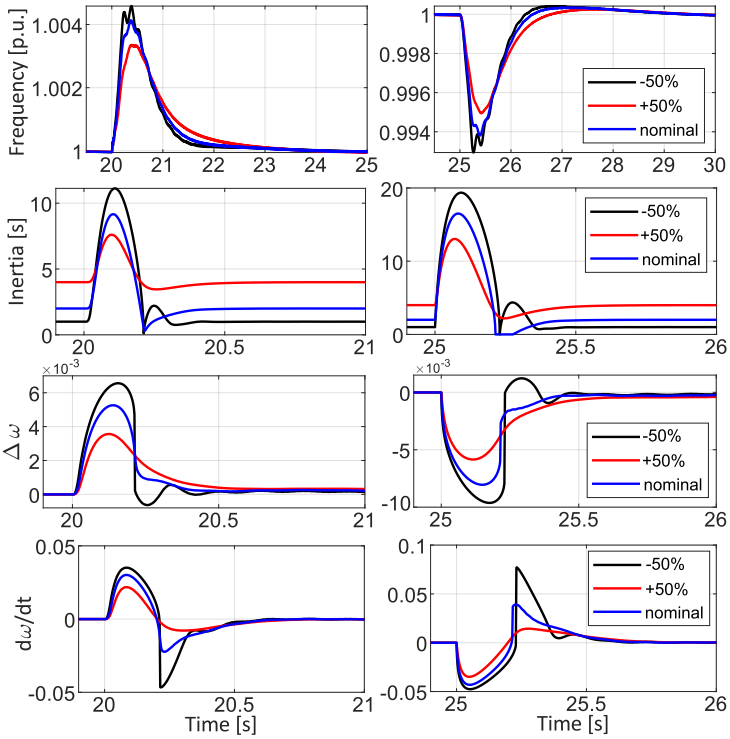

Figure 5.62: Comparison among different VSM parameters considering the response of the grid frequency.

coefficients to reduce frequency deviations, improving frequency Nadir and RoCoF. Also it is presented how the angular acceleration behaves in these cases.

5.7.7. Control strategy comparison

One last way to analyze the performance of the proposed control using adaptive virtual inertia is to compare with conventional control strategies. For this purpose, the conventional droop control was performed in the proposed Microgrid, where the voltage droop equation is the same as in (5.35), and the frequency droop is presented as follows:

$$\omega_{droop} = \omega^* + K_p(P^* - P) \tag{5.82}$$

where the active power droop coefficient is $K_p = 0.1$. The second strategy carried out is the current control I_{dq}, where the power references (P^* and Q^*) are associated directly with the direct and quadrature current as written:

$$I^*_{c,d} = \frac{P^*}{V_{cd}} \; ; \qquad I^*_{c,q} = \frac{Q^*}{V_{cd}} \tag{5.83}$$

The common parameters and gains of the controllers were kept the same for comparison purposes.

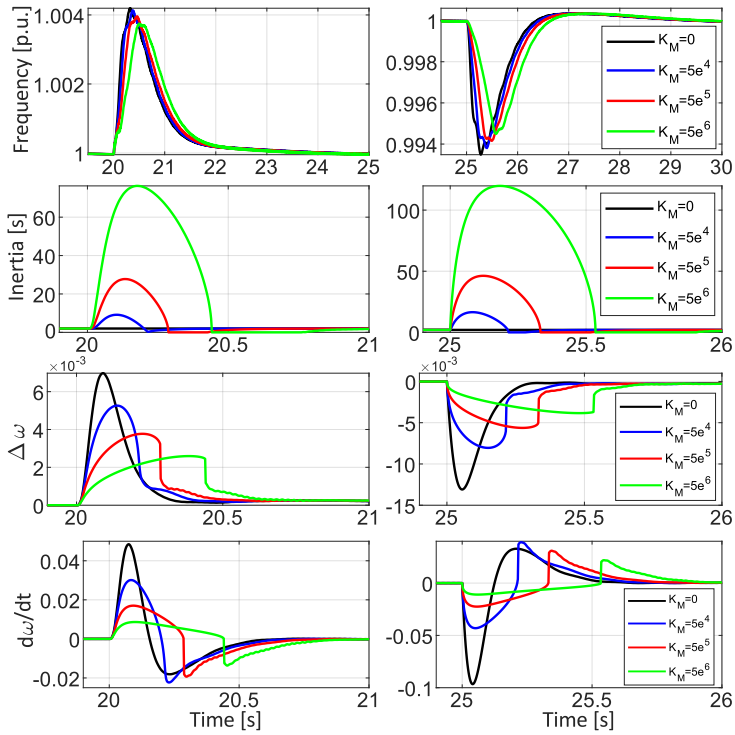

Figure 5.63: Comparison among different VSM parameters considering the response of the grid frequency.

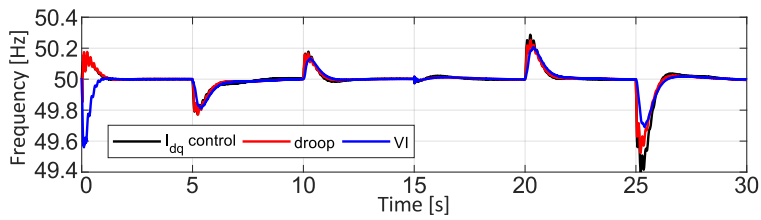

Figure 5.64: A comparison among different control approaches in the frequency behavior.

The comparison among the proposed adaptive virtual inertia (VI), the droop control and the current control is depicted in Figure 5.64, where the frequency profile is exhibited. A zoom showing the strongest transient variations is introduced in Figure 5.65. The droop control performs slightly better than current I_{dq} control. The convergence time is similar for both control strategies, however the frequency variation is evidently reduced in the virtual inertia strategy. A reduction in frequency oscillation during the transient is also noticed. Therefore, the virtual inertia approach presents an improvement in the frequency RoCoF, providing an inertial support more suitable for the Microgrid.

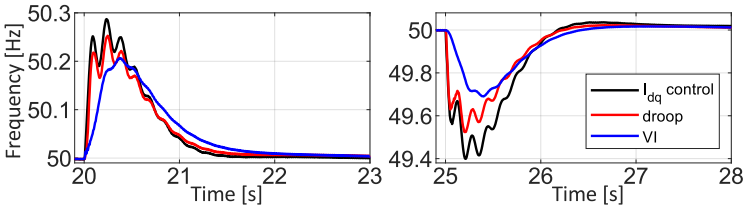

Figure 5.65: A zoom in the frequency for different control strategies.

5.8. Conclusions

This chapter proposes a variable virtual inertia scheme applied to a VSC converter to improve frequency stability and reduce power oscillations in a low inertia AC Microgrid. The AC Microgrid is composed by a diesel generator and loads, plus a VSC converter interfacing it to a DC Microgrid. The proposed scheme is analysed through a Lyapunov function that assures asymptotic stability for the whole system under the proposed variable inertia.

This approach, in large part inspired by adaptive control, assures through a Lyapunov function, asymptotic stability of the overall system. Simulation results illustrate the great contribution such Variable Synthetic Inertia can bring to a low inertia system. In particular, this approach can contribute to solve the problems brought by renewables in modern power systems, and allow much larger penetration of such intermittent energies.

The voltage and current control loop are designed based on a control induced time-scale separation, where singular perturbation analysis is applied, then in this case the tuning of controller parameters is much simpler than traditional linear control with outer PI voltage loop cascaded with PI for inner current. This scheme can explicitly include flexible protection strategies and control saturations for voltage and currents by saturating the regulators output, and in the same time is not dependent of PLL tracking and has great capability for island operation.

Simulation results shows that VSM helps the system providing frequency regulation and inertial support. This approach is compared to similar ones, and it is shown its improvement compared to classical droop control, since that one presents no inertia support. In addition, the analysis of the variation of parameters allows to understand their influence on the system's response in a more comprehensive way. Therefore, one can conclude that variable inertia of Virtual Synchronous Machine is a good strategy to provide ancillary services for low inertia systems like Microgrids.

CHAPTER 6

General Conclusions

In the last decades, the development of Microgrids has become a very important research topic, aiming to find a better way to integrate renewables and assure a more reliable operation of new power electronic devices in power systems. Microgrids provide a great solution considering the constant growth of load demand and the grid modernization through Smart Grid concepts. The impact of DER based on power electronics is an important power system concern, since it affects many aspects of power systems, breaking the radiality of distribution grids, the creation of bidirectional current flux in distribution feeders, and drastically reducing inertia and thereby the natural regulation capacity of the system. Hence, DC grids are considered a relevant solution in power systems, since the DC nature of power electronic devices bring technological and economical advantages. For example it allows the reduction of converter stages in the grid, since many elements are naturally DC, and allow an easier power flux control that is not dependent on phase angles or reactive power.

In this thesis it is introduced the design and control of a hybrid AC/DC Microgrid to integrate different renewable sources, energy storage systems and loads for reliable operation and stability of the whole system. The stabilization of the Microgrid buses by power flow balance and the provision of ancillary services is assured by the proposed control strategy, where a rigorous stability study is made.

In Chapter 1, a brief introduction on Microgrids and energy transition challenges is introduced. There, it is mentioned the impacts of the high penetration of DER into the network, the intermittent feature of renewables, the reduction of inertia because of power electronic technologies and the transformation of the grid from centralized generation to a heterogeneous distributed system. Furthermore, the importance of energy storage system for power systems to reduce the impact of renewables balancing the power flow, to improve power quality and reliability, and

to provide grid support as many other services are exposed. Finally, the new trends in Microgrids structures are presented to solve power system issues, where virtual inertia approach is highlighted.

In Chapter 2, it was presented an overview on Microgrid control, operation and stability aspects, where real application examples and management strategies are introduced. Standard control structures related with island or grid-connected operation modes are developed to highlight the challenges for Microgrid operation. The main aspects of DC and AC Microgrids are compared, where the simplifications and improvements that can be achieved through a DC network are introduced, as well as the middle ground to be taking into account with the traditional AC systems that are already standardized in the distribution systems. The particular stability problems in Microgrids are pointed out, such as control solutions that are developed to maintain the proper operation of the system, maintaining the power quality indexes and system reliability. Also, the limitation of the conventional controllers are exposed, presenting the need to develop reliable control strategies suitable to assure the proper operation of the system facing the Microgrid challenges.

In Chapter 3, the Microgrid components are described: PV systems with intermittent feature where a MPPT algorithm allows the system to work in the maximum power point; different kind of energy storage systems as batteries and supercapacitors to be composed into a Hybrid Energy Storage System to improve their operation in transients and long term stability. The rail regenerative braking review is also provided, motivated by industrial collaborations. Since these introduce a large amount of power in short periods, the integration of this energy recovered from trains is done based on more specific equipment that are able to withstand this peculiar problem, and by a suited control strategy. In this work, a supercapacitor connected through a bidirectional converter, is able to absorb this large amount of power during the breaking recovery, and reduce the strong power fluctuation. Last part of the chapter presents the proposed Microgrid where the voltage level and power converters' configuration is drawn.

In Chapter 4, the nonlinear dynamical model of the proposed Microgrid is introduced, where the average state space model of the whole system is obtained. A number of elements are connected to the Microgrid: two different renewable energy sources (photovoltaic panels and braking energy recovery from the trains), two kinds of storage acting at different time-scales (a battery and a supercapacitor), a DC load and the connection with the main AC grid. Then, a low-level distributed nonlinear controller, based on System-of-Systems approach is developed for the DC Microgrid integrated in a grid-connected Train Station. Feedback linearization and

backstepping approaches are employed in the Microgrid devices. For supercapacitor and train subsystems, the non-minimal phase problem of boost/buck converters, according to their chosen control output, is solved by a control induced explicit time scale separation, which is then addressed by a singular perturbation analysis. Therefore, a dynamical feedback linearization is applied using singular perturbation properties, assuring the proper control of such subsystems. A Lyapunov function for the overall system, considering the interconnected devices of the Microgrid, is used to ensure the stability of the whole system. The stability analysis results in Input to State Stability properties for the Microgrid, therefore the system may have proper operation inside the stability region and have good robustness properties from ISS results. The simulations highlight the performance of the proposed control, with parametric robustness tests and a comparison with traditional linear controller (PI), emphasizing the better performance of the proposed nonlinear controller. The transient behavior is much better and the control gains tuning much easier with the nonlinear control. Last, a not-static DC bus voltage is proposed to perform the grid stabilization, which results in a much simpler control law, besides the limitation of this approach. In addition, it was proposed a simplification on the DC bus current's dynamic, neglecting small terms. In this way, it was possible to develop a simpler Lyapunov function. Simulation tests of both propositions are made showing the performance of the system.

In Chapter 5, the AC side of the Microgrid is better detailed, as well as ancillary services provision necessary to assure its stability. The dynamical model of the AC grid is developed including the connection of the DC Microgrid trough a Voltage Source Converter. A review on power system stability, focused on voltage and frequency stability is provided, pinpointing the stability issues brought by the increase number of power converters in the grid and the energy transition in general. The lack of inertia in such systems is highlighted, where the virtual inertia approach is proposed here to improve system stability and power sharing. The virtual inertia is implemented in the Microgrid and the performance of the system is tested by simulations, where voltage regulation is made by droop control. In this way, it is assured the provision of ancillary services for a weak grid, as AC Microgrids are. A comparison with droop control strategy is made, where the inertial support and the dynamic frequency response for virtual inertia control is highlighted in simulations. Therefore, an adaptive virtual inertia is proposed where the inertia constant becomes a time varying control parameter of the system, which adaptation can be designed to improve frequency stability and inertial support. A stability analysis of the adaptive virtual inertia is carried out where asymptotic stability

is assured via La Salle theorem. Simulation results show the effectiveness of the proposed adaptive inertia, where a comparison with droop solution and standard current control is conducted.

This thesis aims to study solutions for Microgrids, considering the current power systems' trends. The use of DC systems is proposed, highlighting several beneficial characteristics, as simpler converter topologies and control design, and the fact that there is no more complex variables as reactive power and frequency regulation. Also, current trends for AC grids are exposed, in particular virtual inertia to improve power sharing in isolated systems, and improve frequency stability by proving support for inertial and primary control in Microgrids. In the same way, it is discussed new trends in ancillary services, such as inertial support, in response to the high penetration of power electronics, providing a framework for Microgrid evolution in the future SmartGrids solutions.

6.1. Main Results

The main contributions of this thesis can be summarized as:

1. Development of nonlinear control strategy for each converter of the Microgrid based on backstepping and feedback linearization.
2. Design a nonlinear control strategy to solve the non-minimal phase problem of DC/DC converters according to the chosen control output. The control induced time-scale separation design and dynamical feedback is used to develop a controller for the boost converter for the supercapacitor and the buck converter for the train braking recovery system.
3. Integration of regenerative braking system from trains, which is an original renewable energy source in a Microgrid, assuring proper operation of the system, considering the power fluctuations feature of braking energy recovery.
4. A rigorous stability analysis of the whole Microgrid considering all interconnected devices, where Input to State Stability is obtained. The proof is formally done with constructive Lyapunov functions where stability of the whole system is assured under mild conditions. The stability analysis guarantee the dynamic performance of the system and operation.
5. Development of a control strategy for power sharing and frequency stability improvement based on virtual inertia approach for AC Microgrids or weak grids. The proposition of adaptive virtual inertia to improve inertial response of Microgrids, where the inertia constant is variable. A stability analysis is

conducted to prove the asymptotic stability of adaptive virtual inertia in power converters application.

6. A comparison with traditional droop control strategy is performed via simulations, where the enhanced response of the adaptive virtual inertia is highlighted, since the droop control approach is not able to provide inertial support and have poor transient response features.

6.2. Future Works

The thesis approach brought several contributions related to Microgrid's control and ancillary services' provision for weak grids. However, there still exist many issues to be investigated.

1. DC grids are not yet widespread in conventional distribution systems. There are still many research issues to be solved for their widespread use. Protection schemes for DC grids are still difficult remaining technical challenge, as well as voltage level issues and the lack of commercial solutions for DC/DC power converters to easily interconnect DC systems, opening up the possibility of building networks purely DC. A next step is to develop mixed protection and control schemes in power converters to improve feasibility of DC systems. Also, the study of mixed AC/DC hybrid systems can be a good compromise between classical and DC grids.
2. Train station model can be more detailed to include real aspects of regenerative train braking. In this work, the train impedance is fixed, but in real application, the losses vary according to the train position. Also, the electric train drive could be included to match the braking of one train with the acceleration of another as is generally done.
3. Different results can be derived from stability analysis by passivity based considerations and the implementation of adaptive control schemes considering different proposals from the one made in this thesis.
4. The inclusion of inductance characteristics in the cables of the DC side of the Microgrid (not included in the thesis) will bring different dynamics to the system, where a novel system design and control is required. Also, filtering aspects may result from this analysis and a Lyapunov function of the inductance current dynamics may be considered.
5. The adaptive virtual inertia may also be applied in the damping factor of the swing equation, where stronger results can be achieved. The parameters choice for inertia coefficient and damping factor is an interesting topic of

study, where the optimization of these parameters can be achieved considering the operational margins of different power systems like weak grids or Microgrids. The proper parameterization of virtual inertia can really improve the stability properties of the system.

6. An experimental test bench of the proposed Microgrid system needs to be addressed for practical validation of the control schemes and gain tuning. In the following they will be tested in a real subway station. Also, unbalanced voltage networks and PLL issues may be addressed to consider a more realistic grid.
7. Finally, future works on the development of a secondary and tertiary control level for the proposed Microgrid is required. It is important to understand the behavior of the system and the interaction of the control hierarchy among the different layers. This will also allow the possibility of including economic aspects and to aim at sustainability in addition to reliability and power quality.

Bibliography

[1] T. Basso, S. Chakraborty, A. Hoke, and M. Coddington, "Ieee 1547 standards advancing grid modernization," in *2015 IEEE 42nd Photovoltaic Specialist Conference (PVSC)*, June 2015, pp. 1–5.

[2] M. E. El-Hawary, "The smart grid state-of-the-art and future trends," *Electric Power Components and Systems*, vol. 42, no. 3-4, pp. 239–250, 2014.

[3] V. C. Gungor, D. Sahin, T. Kocak, S. Ergut, C. Buccella, C. Cecati, and G. P. Hancke, "Smart grid technologies: Communication technologies and standards," *IEEE Transactions on Industrial Informatics*, vol. 7, no. 4, pp. 529–539, Nov 2011.

[4] C. W. Potter, A. Archambault, and K. Westrick, "Building a smarter smart grid through better renewable energy information," in *2009 IEEE/PES Power Systems Conference and Exposition*, March 2009, pp. 1–5.

[5] J. Romero Aguero and A. Khodaei, "Grid modernization, der integration utility business models - trends challenges," *IEEE Power and Energy Magazine*, vol. 16, no. 2, pp. 112–121, MARCH 2018.

[6] D. Tan and D. Novosel, "Energy challenge, power electronics amp; systems (peas) technology and grid modernization," *CPSS Transactions on Power Electronics and Applications*, vol. 2, no. 1, pp. 3–11, 2017.

[7] X. Li and S. Wang, "A review on energy management, operation control and application methods for grid battery energy storage systems," *CSEE Journal of Power and Energy Systems*, pp. 1–15, 2019.

[8] A. A. Akhil, G. Huff, A. B. Currier, B. C. Kaun, D. M. Rastler, S. B. Chen, A. L. Cotter, D. T. Bradshaw, and W. D. Gauntlett, *DOE/EPRI 2013 electricity storage handbook in collaboration with NRECA*. Sandia National Laboratories Albuquerque, NM, 2013.

[9] P. F. Ribeiro, B. K. Johnson, M. L. Crow, A. Arsoy, and Y. Liu, "Energy storage systems for advanced power applications," *Proceedings of the IEEE*, vol. 89, no. 12, pp. 1744–1756, 2001.

[10] D. Cornic, "Efficient recovery of braking energy through a reversible DC substation," in *Electrical Systems for Aircraft, Railway and Ship Propulsion*, Oct 2010, pp. 1–9.

[11] K. Itani, A. De Bernardinis, Z. Khatir, A. Jammal, and M. Oueidat, "Regenerative braking modeling, control, and simulation of a hybrid energy storage system for an electric vehicle in extreme conditions," *IEEE Transactions on Transportation Electrification*, vol. 2, no. 4, pp. 465–479, Dec 2016.

[12] J. W. Dixon and M. E. Ortuzar, "Ultracapacitors + dc-dc converters in regenerative braking system," *IEEE Aerospace and Electronic Systems Magazine*, vol. 17, no. 8, pp. 16–21, Aug 2002.

[13] Y. Yoshida, H. P. Figueroa, and R. A. Dougal, "Comparison of energy storage configurations in railway microgrids," in *2017 IEEE Second International Conference on DC Microgrids (ICDCM)*, June 2017, pp. 133–138.

[14] L. Galaï-Dol, A. De Bernardinis, A. Nassiopoulos, A. Peny, and F. Bourquin, "On the use of train braking energy regarding the electrical consumption optimization in railway station," in *Transportation Research Procedia*, vol. 14. Elsevier, 2016, pp. 655–664.

[15] L. Galaï-Dol and A. de Bernardinis, "AC or DC grid for railway stations?" in *PCIM Europe 2016; International Exhibition and Conference for Power Electronics, Intelligent Motion, Renewable Energy and Energy Management*, May 2016, pp. 1–8.

[16] S. Nasr, M. Iordache, and M. Petit, "Smart micro-grid integration in DC railway systems," in *IEEE PES Innovative Smart Grid Technologies, Europe*, Oct 2014, pp. 1–6.

[17] P. Tielens and D. Van Hertem, "Grid inertia and frequency control in power systems with high penetration of renewables," in *Young Researchers Symposium in Electrical Power Engineering, Date: 2012/04/16-2012/04/17, Location: Delft, The Netherlands*, 2012.

[18] F. Zare and D. Kumar, "Harmonics analysis of industrial and commercial distribution networks with high penetration of power electronics converters," in *2016 Australasian Universities Power Engineering Conference (AUPEC)*. IEEE, 2016, pp. 1–6.

[19] F. Kienle and C. de Schryver, "100% green computing at the wrong location?" 2012.

[20] N. Khan, S. Dilshad, R. Khalid, A. R. Kalair, and N. Abas, "Review of energy storage and transportation of energy," *Energy Storage*, p. e49, 2019.

[21] E. O. Ogunniyi and H. Pienaar, "Overview of battery energy storage system advancement for renewable (photovoltaic) energy applications," in *2017 International Conference on the Domestic Use of Energy (DUE)*, April 2017, pp. 233–239.

[22] J. C. Beardsall, C. A. Gould, and M. Al-Tai, "Energy storage systems: A review of the technology and its application in power systems," in *2015 50th International Universities Power Engineering Conference (UPEC)*, Sept 2015, pp. 1–6.

[23] S. Kotra and M. K. Mishra, "Energy management of hybrid microgrid with hybrid energy storage system," in *2015 International Conference on Renewable Energy Research and Applications (ICRERA)*, Nov 2015, pp. 856–860.

[24] K. Takeda, C. Takahashi, H. Arita, N. Kusumi, M. Amano, and A. Emori, "Design of hybrid energy storage system using dual batteries for renewable applications," in *2014 IEEE PES General Meeting | Conference Exposition*, July 2014, pp. 1–5.

[25] U. Energy, "Doe microgrid workshop report," 2018.

[26] T. Dragicevic, J. C. Vasquez, J. M. Guerrero, and D. Skrlec, "Advanced lvdc electrical power architectures and microgrids: A step toward a new generation of power distribution networks." *IEEE Electrification Magazine*, vol. 2, no. 1, pp. 54–65, March 2014.

[27] D. E. Olivares, A. Mehrizi-Sani, A. H. Etemadi, C. A. Cañizares, R. Iravani, M. Kazerani, A. H. Hajimiragha, O. Gomis-Bellmunt, M. Saeedifard, R. Palma-Behnke, G. A. Jiménez-Estévez, and N. D. Hatziargyriou, "Trends in microgrid control," *IEEE Transactions on Smart Grid*, vol. 5, no. 4, pp. 1905–1919, July 2014.

[28] W. Jing, C. H. Lai, S. H. W. Wong, and M. L. D. Wong, "Battery-supercapacitor hybrid energy storage system in standalone dc microgrids: areview," *IET Renewable Power Generation*, vol. 11, no. 4, pp. 461–469, 2017.

[29] J. J. Justo, F. Mwasilu, J. Lee, and J.-W. Jung, "Ac-microgrids versus dc-microgrids with distributed energy resources: A review," *Renewable and Sustainable Energy Reviews*, vol. 24, pp. 387–405, 2013.

[30] E. Unamuno and J. A. Barrena, "Hybrid ac/dc microgrids—part ii: Review and classification of control strategies," *Renewable and Sustainable Energy Reviews*, vol. 52, pp. 1123–1134, 2015.

[31] J. G. de Matos, F. S. F. e Silva, and L. A. d. S. Ribeiro, "Power control in ac isolated microgrids with renewable energy sources and energy storage systems," *IEEE Transactions on Industrial Electronics*, vol. 62, no. 6, pp. 3490–3498, June 2015.

[32] L. A. de Souza Ribeiro, O. R. Saavedra, S. L. de Lima, and J. G. de Matos, "Isolated micro-grids with renewable hybrid generation: The case of lençóis island,"," *IEEE Transactions on Sustainable Energy*, vol. 2, no. 1, pp. 1–11, Jan 2011.

[33] L. E. Zubieta, "Are microgrids the future of energy?: Dc microgrids from concept to demonstration to deployment," *IEEE Electrification Magazine*, vol. 4, no. 2, pp. 37–44, June 2016.

[34] L. A. d. S. Ribeiro, O. R. Saavedra, S. L. Lima, J. G. de Matos, and G. Bonan, "Making isolated renewable energy systems more reliable," *Renewable Energy*, vol. 45, pp. 221–231, 2012.

[35] R. H. Lasseter, "Smart distribution: Coupled microgrids," *Proceedings of the IEEE*, vol. 99, no. 6, pp. 1074–1082, 2011.

[36] A. Iovine, S. B. Siad, G. Damm, E. D. Santis, and M. D. D. Benedetto, "Nonlinear control of an ac-connected dc microgrid," in *IECON 2016 - 42nd Annual Conference of the IEEE Industrial Electronics Society*, Oct 2016, pp. 4193–4198.

[37] ——, "Nonlinear control of a dc microgrid for the integration of photovoltaic panels," *IEEE Transactions on Automation Science and Engineering*, vol. 14, no. 2, pp. 524–535, April 2017.

[38] T. Dragičević, X. Lu, J. C. Vasquez, and J. M. Guerrero, "Dc microgrids—part i: A review of control strategies and stabilization techniques," *IEEE Transactions on power electronics*, vol. 31, no. 7, pp. 4876–4891, 2015.

[39] L. Mariam, M. Basu, and M. F. Conlon, "Microgrid: Architecture, policy and future trends," *Renewable and Sustainable Energy Reviews*, vol. 64, pp. 477–489, 2016.

[40] V. Nasirian, S. Moayedi, A. Davoudi, and F. L. Lewis, "Distributed cooperative control of dc microgrids," *IEEE Transactions on Power Electronics*, vol. 30, no. 4, pp. 2288–2303, April 2015.

[41] D. Kumar, F. Zare, and A. Ghosh, "Dc microgrid technology: System architectures, ac grid interfaces, grounding schemes, power quality, communication networks, applications, and standardizations aspects," *Ieee Access*, vol. 5, pp. 12 230–12 256, 2017.

[42] T. Dragičević, X. Lu, J. C. Vasquez, and J. M. Guerrero, "Dc microgrids—part i: A review of control strategies and stabilization techniques," *IEEE Transactions on power electronics*, vol. 31, no. 7, pp. 4876–4891, 2016.

[43] N. Yang, B. Nahid-Mobarakeh, F. Gao, D. Paire, A. Miraoui, and W. Liu, "Modeling and stability analysis of multi-time scale dc microgrid," *Electric Power Systems Research*, vol. 140, pp. 906–916, 2016.

[44] S. M. Ashabani and Y. A. r. I. Mohamed, "New family of microgrid control and management strategies in smart distribution grids; analysis, comparison and testing," *IEEE Transactions on Power Systems*, vol. 29, no. 5, pp. 2257–2269, Sept 2014.

[45] E. Rokrok, M. Shafie-Khah, and J. P. S. Catalão, "Comparison of two control strategies in an autonomous hybrid microgrid," in *2017 IEEE PES Innovative Smart Grid Technologies Conference Europe (ISGT-Europe)*, Sept 2017, pp. 1–6.

[46] A. P. N. Tahim, D. J. Pagano, and E. Ponce, "Nonlinear control of dc-dc bidirectional converters in stand-alone dc microgrids," in *2012 IEEE 51st IEEE Conference on Decision and Control (CDC)*, Dec 2012, pp. 3068–3073.

[47] C. Wang, X. Li, L. Guo, and Y. W. Li, "A nonlinear-disturbance-observer-based dc-bus voltage control for a hybrid ac/dc microgrid," *IEEE Transactions on Power Electronics*, vol. 29, no. 11, pp. 6162–6177, 2014.

[48] S. Parhizi, H. Lotfi, A. Khodaei, and S. Bahramirad, "State of the art in research on microgrids: A review," *Ieee Access*, vol. 3, pp. 890–925, 2015.

[49] T. Morstyn, B. Hredzak, and V. G. Agelidis, "Control strategies for microgrids with distributed energy storage systems: An overview," *IEEE Transactions on Smart Grid*, vol. 9, no. 4, pp. 3652–3666, July 2018.

[50] J. M. Guerrero, J. C. Vasquez, J. Matas, L. G. De Vicuña, and M. Castilla, "Hierarchical control of droop-controlled ac and dc microgrids—a general approach toward standardization," *IEEE Transactions on industrial electronics*, vol. 58, no. 1, pp. 158–172, 2011.

[51] A. Bidram and A. Davoudi, "Hierarchical structure of microgrids control system," *IEEE Transactions on Smart Grid*, vol. 3, no. 4, pp. 1963–1976, 2012.

[52] P. Tielens and D. Van Hertem, "The relevance of inertia in power systems," *Renewable and Sustainable Energy Reviews*, vol. 55, pp. 999–1009, 2016.

[53] W. Winter, K. Elkington, G. Bareux, and J. Kostevc, "Pushing the limits: Europe's new grid: Innovative tools to combat transmission bottlenecks and reduced inertia," *IEEE Power and Energy Magazine*, vol. 13, no. 1, pp. 60–74, 2014.

[54] F. Milano, F. Dörfler, G. Hug, D. J. Hill, and G. Verbič, "Foundations and challenges of low-inertia systems," in *2018 Power Systems Computation Conference (PSCC)*. IEEE, 2018, pp. 1–25.

[55] National Grid ESO, "Interim report into the low frequency demand disconnection (lfdd) following generator trips and frequency excursion on 9 aug 2019," in *Technical report*, 2019.

[56] J. Rodrigues Lima, "Variable speed pumped storage plants multi-time scale control to allow its use to power system stability," Ph.D. dissertation, Paris Saclay, 2017.

[57] U. Tamrakar, D. Shrestha, M. Maharjan, B. P. Bhattarai, T. M. Hansen, and R. Tonkoski, "Virtual inertia: Current trends and future directions," *Applied Sciences*, vol. 7, no. 7, p. 654, 2017.

[58] E. Barklund, N. Pogaku, M. Prodanovic, C. Hernandez-Aramburo, and T. C. Green, "Energy management in autonomous microgrid using stability-constrained droop control of inverters," *IEEE Transactions on Power Electronics*, vol. 23, no. 5, pp. 2346–2352, 2008.

[59] A. Engler and N. Soultanis, "Droop control in lv-grids," in *2005 International Conference on Future Power Systems*. IEEE, 2005, pp. 6–pp.

[60] H. Han, X. Hou, J. Yang, J. Wu, M. Su, and J. M. Guerrero, "Review of power sharing control strategies for islanding operation of ac microgrids," *IEEE Transactions on Smart Grid*, vol. 7, no. 1, pp. 200–215, 2015.

[61] U. B. Tayab, M. A. B. Roslan, L. J. Hwai, and M. Kashif, "A review of droop control techniques for microgrid," *Renewable and Sustainable Energy Reviews*, vol. 76, pp. 717–727, 2017.

[62] T. Vandoorn, J. De Kooning, B. Meersman, and L. Vandevelde, "Review of primary control strategies for islanded microgrids with power-electronic interfaces," *Renewable and Sustainable Energy Reviews*, vol. 19, pp. 613–628, 2013.

[63] Q.-C. Zhong and G. Weiss, "Synchronverters: Inverters that mimic synchronous generators," *IEEE Transactions on Industrial Electronics*, vol. 58, no. 4, pp. 1259–1267, 2010.

[64] J. Driesen and K. Visscher, "Virtual synchronous generators," in *2008 IEEE Power and Energy Society General Meeting-Conversion and Delivery of Electrical Energy in the 21st Century*. IEEE, 2008, pp. 1–3.

[65] M. Torres and L. A. Lopes, "Virtual synchronous generator control in autonomous wind-diesel power systems," in *2009 IEEE Electrical Power & Energy Conference (EPEC)*. IEEE, 2009, pp. 1–6.

[66] Y. Hirase, O. Noro, E. Yoshimura, H. Nakagawa, K. Sakimoto, and Y. Shindo, "Virtual synchronous generator control with double decoupled synchronous reference frame for single-phase inverter," *IEEJ Journal of Industry Applications*, vol. 4, no. 3, pp. 143–151, 2015.

[67] J. Alipoor, Y. Miura, and T. Ise, "Power system stabilization using virtual synchronous generator with alternating moment of inertia," *IEEE journal of Emerging and selected topics in power electronics*, vol. 3, no. 2, pp. 451–458, 2014.

[68] Y. Chen, R. Hesse, D. Turschner, and H.-P. Beck, "Improving the grid power quality using virtual synchronous machines," in *2011 international conference on power engineering, energy and electrical drives*. IEEE, 2011, pp. 1–6.

[69] T. V. Van, K. Visscher, J. Diaz, V. Karapanos, A. Woyte, M. Albu, J. Bozelie, T. Loix, and D. Federenciuc, "Virtual synchronous generator: An element of future grids," in *2010 IEEE PES Innovative Smart Grid Technologies Conference Europe (ISGT Europe)*. IEEE, 2010, pp. 1–7.

[70] S. D'Arco, J. A. Suul, and O. B. Fosso, "A virtual synchronous machine implementation for distributed control of power converters in smartgrids," *Electric Power Systems Research*, vol. 122, pp. 180–197, 2015.

[71] A. W. dos Santos Serra, J. G. de Matos, L. A. de Souza Ribeiro, and L. S. Pinheiro, "Implementation of a virtual synchronous machine to improve the dynamic response of inverters," in *IECON 2019-45th Annual Conference of the IEEE Industrial Electronics Society*, vol. 1. IEEE, 2019, pp. 3912–3918.

[72] S. D'Arco, J. A. Suul, and O. B. Fosso, "Control system tuning and stability analysis of virtual synchronous machines," in *2013 IEEE Energy Conversion Congress and Exposition*. IEEE, 2013, pp. 2664–2671.

[73] K. Shi, H. Ye, W. Song, and G. Zhou, "Virtual inertia control strategy in microgrid based on virtual synchronous generator technology," *IEEE Access*, vol. 6, pp. 27 949–27 957, 2018.

[74] S. D'Arco and J. A. Suul, "Equivalence of virtual synchronous machines and frequency-droops for converter-based microgrids," *IEEE Transactions on Smart Grid*, vol. 5, no. 1, pp. 394–395, 2013.

[75] S. D'Arco, J. A. Suul, and O. B. Fosso, "Small-signal modeling and parametric sensitivity of a virtual synchronous machine in islanded operation," *International Journal of Electrical Power & Energy Systems*, vol. 72, pp. 3–15, 2015.

[76] J. Liu, Y. Miura, and T. Ise, "Comparison of dynamic characteristics between virtual synchronous generator and droop control in inverter-based distributed generators," *IEEE Transactions on Power Electronics*, vol. 31, no. 5, pp. 3600–3611, 2015.

[77] C. K. Sao and P. W. Lehn, "Control and power management of converter fed microgrids," *IEEE Transactions on Power Systems*, vol. 23, no. 3, pp. 1088–1098, 2008.

[78] J. M. Guerrero, P. C. Loh, T.-L. Lee, and M. Chandorkar, "Advanced control architectures for intelligent microgrids—part ii: Power quality, energy storage, and ac/dc microgrids," *IEEE Transactions on industrial electronics*, vol. 60, no. 4, pp. 1263–1270, 2012.

[79] P. Nahata, R. Soloperto, M. Tucci, A. Martinelli, and G. Ferrari-Trecate, "A passivity-based approach to voltage stabilization in dc microgrids with zip loads," *Automatica*, vol. 113, p. 108770, 2020.

[80] R. Jadeja, A. Ved, T. Trivedi, and G. Khanduja, "Control of power electronic converters in ac microgrid," in *Microgrid Architectures, Control and Protection Methods*. Springer, 2020, pp. 329–355.

[81] J.-O. Lee and Y.-S. Kim, "Frequency and state-of-charge restoration method in a secondary control of an islanded microgrid without communication," *Applied Sciences*, vol. 10, no. 5, p. 1558, 2020.

[82] C. Bordons, F. Garcia-Torres, and M. A. Ridao, *Model Predictive Control of Microgrids*. Springer, 2020.

[83] A. Parisio, E. Rikos, and L. Glielmo, "A model predictive control approach to microgrid operation optimization," *IEEE Transactions on Control Systems Technology*, vol. 22, no. 5, pp. 1813–1827, 2014.

[84] A. Parisio, E. Rikos, G. Tzamalis, and L. Glielmo, "Use of model predictive control for experimental microgrid optimization," *Applied Energy*, vol. 115, pp. 37–46, 2014.

[85] J. C. Vasquez, J. M. Guerrero, J. Miret, M. Castilla, and L. G. De Vicuna, "Hierarchical control of intelligent microgrids," *IEEE Industrial Electronics Magazine*, vol. 4, no. 4, pp. 23–29, 2010.

[86] M. Arnold, R. R. Negenborn, G. Andersson, and B. De Schutter, "Model-based predictive control applied to multi-carrier energy systems," in *2009 IEEE Power & Energy Society General Meeting*. IEEE, 2009, pp. 1–8.

[87] T. Morstyn, B. Hredzak, R. P. Aguilera, and V. G. Agelidis, "Model predictive control for distributed microgrid battery energy storage systems," *IEEE Transactions on Control Systems Technology*, vol. 26, no. 3, pp. 1107–1114, 2017.

[88] M. Sechilariu, B. C. Wang, and F. Locment, "Supervision control for optimal energy cost management in dc microgrid: Design and simulation," *International Journal of Electrical Power & Energy Systems*, vol. 58, pp. 140–149, 2014.

[89] G. J. Prinsloo, "Synthesis of an off-grid solar thermal cogeneration and intelligent smartgrid control system for rural applications," Ph.D. dissertation, Stellenbosch: Stellenbosch University, 2018.

[90] S. Tselepis, "Greek experience with microgrids: Results from the gaidouromantra site, kythnos island," in *Vancouver 2010 Symposium on Microgrids*, vol. 22, 2010.

[91] A. Iovine, L. Galai-Dol, E. De Santis, M. D. Di Benedetto, and G. Damm, "Distributed nonlinear control for a microgrid embedding renewables, train's energy recovery system and storages," in *PCIM Europe 2017; International Exhibition and Conference for Power Electronics, Intelligent Motion, Renewable Energy and Energy Management*, May 2017, pp. 1–8.

[92] A. H. Hajimiragha and M. R. D. Zadeh, "Research and development of a microgrid control and monitoring system for the remote community of bella coola: Challenges, solutions, achievements and lessons learned," in *2013 IEEE International Conference on Smart Energy Grid Engineering (SEGE)*, 2013, pp. 1–6.

[93] M. Soshinskaya, W. H. Crijns-Graus, J. M. Guerrero, and J. C. Vasquez, "Microgrids: Experiences, barriers and success factors," *Renewable and Sustainable Energy Reviews*, vol. 40, pp. 659–672, 2014.

[94] A. Hirsch, Y. Parag, and J. Guerrero, "Microgrids: A review of technologies, key drivers, and outstanding issues," *Renewable and sustainable Energy reviews*, vol. 90, pp. 402–411, 2018.

[95] L. Meng, Q. Shafiee, G. F. Trecate, H. Karimi, D. Fulwani, X. Lu, and J. M. Guerrero, "Review on Control of DC Microgrids and Multiple Microgrid Clusters," *IEEE Journal of Emerging and Selected Topics in Power Electronics*, vol. 5, no. 3, pp. 928–948, Sept 2017.

[96] "Ieee standard for the specification of microgrid controllers," *IEEE Std 2030.7-2017*, pp. 1–43, 2018.

[97] S. Sen and V. Kumar, "Microgrid control: A comprehensive survey," *Annual Reviews in control*, vol. 45, pp. 118–151, 2018.

[98] M. Farrokhabadi, C. A. Cañizares, J. W. Simpson-Porco, E. Nasr, L. Fan, P. A. Mendoza-Araya, R. Tonkoski, U. Tamrakar, N. Hatziargyriou, D. Lagos *et al.*, "Microgrid stability definitions, analysis, and examples," *IEEE Transactions on Power Systems*, vol. 35, no. 1, pp. 13–29, 2019.

[99] M. Farrokhabadi, C. A. Cañizares, and K. Bhattacharya, "Frequency control in isolated/islanded microgrids through voltage regulation," *IEEE Transactions on Smart Grid*, vol. 8, no. 3, pp. 1185–1194, 2015.

[100] X. Wang, F. Blaabjerg, M. Liserre, Z. Chen, J. He, and Y. Li, "An active damper for stabilizing power-electronics-based ac systems," *IEEE Transactions on Power Electronics*, vol. 29, no. 7, pp. 3318–3329, 2013.

[101] M. Cespedes and J. Sun, "Impedance modeling and analysis of grid-connected voltage-source converters," *IEEE Transactions on Power Electronics*, vol. 29, no. 3, pp. 1254–1261, 2013.

[102] H. Bevrani, *Robust power system frequency control.* Springer, 2009, vol. 85.

[103] H. Bevrani, B. François, and T. Ise, *Microgrid dynamics and control.* John Wiley & Sons, 2017.

[104] P. Kundur, J. Paserba, V. Ajjarapu, G. Andersson, A. Bose, C. Canizares, N. Hatziargyriou, D. Hill, A. Stankovic, C. Taylor, T. V. Cutsem, and V. Vittal, "Definition and classification of power system stability ieee/cigre joint task force on stability terms and definitions," *IEEE Trans. on Power Systems*, vol. 19, no. 3, pp. 1387–1401, Aug 2004.

[105] A. Bindra, "Pulsewidth modulated controller integrated circuit: Four decades of progress [a look back]," *Power Electronics Magazine, IEEE*, vol. 1, no. 3, pp. 10–44, Sept 2014.

[106] L. Hou and A. N. Michel, "Stability analysis of pulse-width-modulated feedback systems," *Automatica*, vol. 37, no. 9, pp. 1335 – 1349, 2001.

[107] V. A. Boicea, "Energy storage technologies: The past and the present," *Proceedings of the IEEE*, vol. 102, no. 11, pp. 1777–1794, Nov 2014.

[108] M. Tucci, S. Riverso, J. C. Vasquez, J. M. Guerrero, and G. Ferrari-Trecate, "A decentralized scalable approach to voltage control of dc islanded microgrids," *IEEE Transactions on Control Systems Technology*, vol. 24, no. 6, pp. 1965–1979, Nov 2016.

[109] M. Tucci, S. Riverso, and G. Ferrari-Trecate, "Line-independent plug-and-play controllers for voltage stabilization in dc microgrids," *IEEE Transactions on Control Systems Technology*, vol. 26, no. 3, pp. 1115–1123, May 2018.

[110] M. Cucuzzella, S. Trip, C. De Persis, X. Cheng, A. Ferrara, and A. van der Schaft, "A robust consensus algorithm for current sharing and voltage regulation in dc microgrids," *IEEE Transactions on Control Systems Technology*, pp. 1–13, 2018.

[111] E. Lenz, D. J. Pagano, and V. Stramosk, "Nonlinear control applied to a dc-dc power converter and the load sharing problem in a dc microgrid," *IFAC Proceedings Volumes*, vol. 47, no. 3, pp. 534–539, 2014.

[112] S. K. Sahoo, A. K. Sinha, and N. Kishore, "Control techniques in ac, dc, and hybrid ac-dc microgrid: a review," *IEEE Journal of Emerging and Selected Topics in Power Electronics*, vol. 6, no. 2, pp. 738–759, 2017.

[113] D. I. Makrygiorgou and A. T. Alexandridis, "Stability analysis of dc distribution systems with droop-based charge sharing on energy storage devices," *Energies*, vol. 10, no. 4, p. 433, 2017.

[114] P. Magne, B. Nahid-Mobarakeh, and S. Pierfederici, "General active global stabilization of multiloads dc-power networks," *IEEE Transactions on Power Electronics*, vol. 27, no. 4, pp. 1788–1798, 2012.

[115] A. P. N. Tahim, D. J. Pagano, E. Lenz, and V. Stramosk, "Modeling and stability analysis of islanded dc microgrids under droop control," *IEEE Transactions on Power Electronics*, vol. 30, no. 8, pp. 4597–4607, 2015.

[116] A. Iovine, T. Rigaut, G. Damm, E. De Santis, and M. D. Di Benedetto, "Power management for a dc microgrid integrating renewables and storages," *Control Engineering Practice*, vol. 85, pp. 59 – 79, 2019.

[117] F. Perez, A. Iovine, G. Damm, and P. Ribeiro, "DC microgrid voltage stability by dynamic feedback linearization," in *2018 IEEE International Conference on Industrial Technology (ICIT)*, Feb 2018, pp. 129–134.

[118] F. Perez, A. Iovine, G. Damm, L. Galai-Dol, and P. Ribeiro, "Regenerative braking control for trains in a dc microgrid using dynamic feedback linearization techniques," *IFAC-PapersOnLine*, vol. 52, no. 4, pp. 401–406, 2019.

[119] A. Iovine, M. Jimenez Carrizosa, G. Damm, and P. Alou, "Nonlinear Control for DC MicroGrids enabling Efficient Renewable Power Integration and Ancillary Services for AC grids," *IEEE Transactions on Power Systems*, pp. 1–1, 2018.

[120] F. Perez, G. Damm, P. Ribeiro, F. Lamnabhi-Lagarrigue, and L. Galai-Dol, "A nonlinear distributed control strategy for a dc microgrid using hybrid energy storage for voltage stability," in *2019 IEEE 58th Conference on Decision and Control (CDC)*. IEEE, 2019, pp. 5168–5173.

[121] S. Siad, G. Damm, L. G. Dol, and A. d. Bernardinis, "Design and control of a dc grid for railway stations," in *PCIM Europe 2017; International Exhibition and Conference for Power Electronics, Intelligent Motion, Renewable Energy and Energy Management*, 2017, pp. 1–8.

[122] S. B. Siad, A. Malkawi, G. Damm, L. Lopes, and L. G. Dol, "Nonlinear control of a dc microgrid for the integration of distributed generation based on different time scales," *International Journal of Electrical Power & Energy Systems*, vol. 111, pp. 93–100, 2019.

[123] M. Jiménez Carrizosa, A. Arzandé, F. Dorado Navas, G. Damm, and J. C. Vannier, "A Control Strategy for Multiterminal DC Grids With Renewable Production and Storage Devices," *IEEE Transactions on Sustainable Energy*, vol. 9, no. 2, pp. 930–939, April 2018.

[124] J. C. Gonzalez-Torres, G. Damm, V. Costan, A. Benchaib, and F. Lamnabhi-Lagarrigue, "Transient stability of power systems withembedded vsc-hvdc links: Stability margins analysis and control," *IET Generation, Transmission & Distribution*, 2020.

[125] Y. Chen, G. Damm, A. Benchaib, and F. Lamnabhi-Lagarrigue, "Feedback linearization for the DC voltage control of a VSC-HVDC terminal," in *European Control Conference (ECC)*, June 2014, pp. 1999–2004.

[126] Y. Chen, W. Huang, Y. Li, H. Rao, S. Xu, and G. Damm, "Nonlinear control design for multi-terminal voltage-sourced converter high voltage direct current systems with zero dynamics regulation," in *2019 4th IEEE Workshop on the Electronic Grid (eGRID)*, 2019, pp. 1–8.

[127] K. De Brabandere, B. Bolsens, J. Van den Keybus, A. Woyte, J. Driesen, and R. Belmans, "A voltage and frequency droop control method for parallel inverters," *IEEE Transactions on power electronics*, vol. 22, no. 4, pp. 1107–1115, 2007.

[128] J. W. Simpson-Porco, F. Dörfler, and F. Bullo, "Voltage stabilization in microgrids via quadratic droop control," *IEEE Transactions on Automatic Control*, vol. 62, no. 3, pp. 1239–1253, 2016.

[129] K. De Brabandere, B. Bolsens, J. Van den Keybus, A. Woyte, J. Driesen, and R. Belmans, "A voltage and frequency droop control method for parallel inverters," *IEEE Transactions on Power Electronics*, vol. 22, no. 4, pp. 1107–1115, July 2007.

[130] M. Su, P. Pan, X. Long, Y. Sun, and J. Yang, "An active power-decoupling method for single-phase ac–dc converters," *IEEE Transactions on Industrial Informatics*, vol. 10, no. 1, pp. 461–468, 2013.

[131] F. Luo, Y. M. Lai, K. H. Loo, C. K. Tse, and X. Ruan, "A generalized droop-control scheme for decentralized control of inverter-interfaced microgrids," in *2013 IEEE International Symposium on Circuits and Systems (ISCAS)*, May 2013, pp. 1320–1323.

[132] J. Rocabert, A. Luna, F. Blaabjerg, and P. Rodriguez, "Control of power converters in ac microgrids," *IEEE transactions on power electronics*, vol. 27, no. 11, pp. 4734–4749, 2012.

[133] B. K. Poolla, D. Groß, and F. Dörfler, "Placement and implementation of grid-forming and grid-following virtual inertia and fast frequency response," *IEEE Transactions on Power Systems*, vol. 34, no. 4, pp. 3035–3046, July 2019.

[134] Y. G. Rebours, D. S. Kirschen, M. Trotignon, and S. Rossignol, "A survey of frequency and voltage control ancillary services—part i: Technical features," *IEEE Transactions on power systems*, vol. 22, no. 1, pp. 350–357, 2007.

[135] J. S. Dohler, P. M. de Almeida, J. G. de Oliveira *et al.*, "Droop control for power sharing and voltage and frequency regulation in parallel distributed generations on ac microgrid," in *2018 13th IEEE International Conference on Industry Applications (INDUSCON)*. IEEE, 2018, pp. 1–6.

[136] N. Mahdian, A. Khorsandi, H. R. Baghaee, N. Sadati, S. S. Moghaddam, and J. M. Guerrero, "Voltage and frequency consensusability of autonomous microgrids over fading channels," *IEEE Transactions on Energy Conversion*, 2020.

[137] R. Mahmud, M. A. Hossain, and H. Pota, "Nonlinear output feedback droop control for parallel inverters in standalone microgrids," in *2019 9th International Conference on Power and Energy Systems (ICPES)*. IEEE, 2019, pp. 1–6.

[138] M. A. Mahmud, M. J. Hossain, H. R. Pota, and A. M. T. Oo, "Robust nonlinear distributed controller design for active and reactive power sharing in islanded microgrids," *IEEE Transactions on Energy Conversion*, vol. 29, no. 4, pp. 893–903, 2014.

[139] S. M. Ashabani and Y. A. I. Mohamed, "A flexible control strategy for grid-connected and islanded microgrids with enhanced stability using nonlinear microgrid stabilizer," *IEEE Transactions on Smart Grid*, vol. 3, no. 3, pp. 1291–1301, 2012.

[140] H. Cai, G. Hu, F. L. Lewis, and A. Davoudi, "A distributed feedforward approach to cooperative control of ac microgrids," *IEEE Transactions on Power Systems*, vol. 31, no. 5, pp. 4057–4067, 2015.

[141] D. Karimipour and F. R. Salmasi, "Stability analysis of ac microgrids with constant power loads based on popov's absolute stability criterion," *IEEE Transactions on Circuits and Systems II: Express Briefs*, vol. 62, no. 7, pp. 696–700, 2015.

[142] R. F. Bastos, T. Dragičević, J. M. Guerrero, and R. Q. Machado, "Decentralized control for renewable DC Microgrid with composite energy storage system and UC voltage restoration connected to the grid," in *IECON 2016 - 42nd Annual Conference of the IEEE Industrial Electronics Society*, Oct 2016, pp. 2016–2021.

[143] A. Jäger-Waldau, "Photovoltaics: Status and perspectives until 2020," *Green*, vol. 1, no. 3, pp. 277–290, 2011.

[144] G. Kavlak, J. McNerney, and J. E. Trancik, "Evaluating the causes of cost reduction in photovoltaic modules," *Energy policy*, vol. 123, pp. 700–710, 2018.

[145] M. A. Woodhouse, B. Smith, A. Ramdas, and R. M. Margolis, "Crystalline silicon photovoltaic module manufacturing costs and sustainable pricing: 1h 2018 benchmark and cost reduction road map," National Renewable Energy Lab.(NREL), Golden, CO (United States), Tech. Rep., 2019.

[146] A. H. Al-Waeli, K. Sopian, H. A. Kazem, and M. T. Chaichan, "Photovoltaic/thermal (pv/t) systems: Status and future prospects," *Renewable and Sustainable Energy Reviews*, vol. 77, pp. 109–130, 2017.

[147] M. G. Villalva, J. R. Gazoli, and E. Ruppert Filho, "Comprehensive approach to modeling and simulation of photovoltaic arrays," *IEEE Transactions on power electronics*, vol. 24, no. 5, pp. 1198–1208, 2009.

[148] A. Cupertino, J. De Resende, H. Pereira, and S. S. Júnior, "A grid-connected photovoltaic system with a maximum power point tracker using passivity-based control applied in a boost converter," in *2012 10th IEEE/IAS International Conference on Industry Applications*. IEEE, 2012, pp. 1–8.

[149] N. Drir, L. Barazane, and M. Loudini, "Comparative study of maximum power point tracking methods of photovoltaic systems," in *2014 International Conference on Electrical Sciences and Technologies in Maghreb (CISTEM)*. IEEE, 2014, pp. 1–5.

[150] D. Sera, L. Mathe, T. Kerekes, S. V. Spataru, and R. Teodorescu, "On the Perturb-and-Observe and Incremental Conductance MPPT Methods for PV Systems," *IEEE Journal of Photovoltaics*, vol. 3, no. 3, pp. 1070–1078, July 2013.

[151] D. C. Huynh and M. W. Dunnigan, "Development and Comparison of an Improved Incremental Conductance Algorithm for Tracking the MPP of a Solar PV Panel," *IEEE Transactions on Sustainable Energy*, vol. 7, no. 4, pp. 1421–1429, Oct 2016.

[152] M. G. Villalva *et al.*, "Conversor eletrônico de potência trifásico para sistema fotovoltaico conectado à rede elétrica," 2010.

[153] T. Kousksou, P. Bruel, A. Jamil, T. El Rhafiki, and Y. Zeraouli, "Energy storage: Applications and challenges," *Solar Energy Materials and Solar Cells*, vol. 120, pp. 59–80, 2014.

[154] M. Aneke and M. Wang, "Energy storage technologies and real life applications - a state of the art review," *Applied Energy*, vol. 179, pp. 350–377, 2016.

[155] N. Omar, M. A. Monem, Y. Firouz, J. Salminen, J. Smekens, O. Hegazy, H. Gaulous, G. Mulder, P. Van den Bossche, T. Coosemans *et al.*, "Lithium iron phosphate based battery–assessment of the aging parameters and development of cycle life model," *Applied Energy*, vol. 113, pp. 1575–1585, 2014.

[156] G. Sarre, P. Blanchard, and M. Broussely, "Aging of lithium-ion batteries," *Journal of power sources*, vol. 127, no. 1-2, pp. 65–71, 2004.

[157] K. Divya and J. Østergaard, "Battery energy storage technology for power systems—an overview," *Electric power systems research*, vol. 79, no. 4, pp. 511–520, 2009.

[158] O. Tremblay and L.-A. Dessaint, "Experimental validation of a battery dynamic model for ev applications," *World electric vehicle journal*, vol. 3, no. 2, pp. 289–298, 2009.

[159] C. Zhu, X. Li, L. Song, and L. Xiang, "Development of a theoretically based thermal model for lithium ion battery pack," *Journal of Power Sources*, vol. 223, pp. 155–164, 2013.

[160] N. Xu and J. Riley, "Nonlinear analysis of a classical system: The double-layer capacitor," *Electrochemistry Communications*, vol. 13, no. 10, pp. 1077–1081, 2011.

[161] W. Jing, C. H. Lai, W. S. Wong, and M. D. Wong, "Dynamic power allocation of battery-supercapacitor hybrid energy storage for standalone pv microgrid applications," *Sustainable Energy Technologies and Assessments*, vol. 22, pp. 55–64, 2017.

[162] ——, "A comprehensive study of battery-supercapacitor hybrid energy storage system for standalone pv power system in rural electrification," *Applied Energy*, vol. 224, pp. 340–356, 2018.

[163] Y. Ye and K. W. E. Cheng, "Analysis and design of zero-current switching switched-capacitor cell balancing circuit for series-connected battery/supercapacitor," *IEEE Transactions on Vehicular Technology*, vol. 67, no. 2, pp. 948–955, 2017.

[164] A. Ostadi, M. Kazerani, and S.-K. Chen, "Hybrid energy storage system (hess) in vehicular applications: A review on interfacing battery and ultra-capacitor units," in *2013 IEEE Transportation Electrification Conference and Expo (ITEC)*. IEEE, 2013, pp. 1–7.

[165] C. Abbey and G. Joos, "Supercapacitor energy storage for wind energy applications," *IEEE Transactions on Industry Applications*, vol. 43, no. 3, pp. 769–776, 2007.

[166] M. ud din Mufti, S. A. Lone, S. J. Iqbal, M. Ahmad, and M. Ismail, "Super-capacitor based energy storage system for improved load frequency control," *Electric Power Systems Research*, vol. 79, no. 1, pp. 226–233, 2009.

[167] D. Casadei, G. Grandi, C. Rossi *et al.*, "A supercapacitor-based power conditioning system for power quality improvement and uninterruptible power supply," in *Proceedings of the 2002 IEEE International Symposium on Industrial Electronics, ISIE*, 2002.

[168] S. B. Siad, "Dc microgrids control for renewable energy integration," Ph.D. dissertation, 2019.

[169] A. Verdicchio, P. Ladoux, H. Caron, and C. Courtois, "New medium-voltage dc railway electrification system," *IEEE Transactions on Transportation Electrification*, vol. 4, no. 2, pp. 591–604, June 2018.

[170] R. R. Pecharromán, A. López-López, A. P. Cucala, and A. Fernández-Cardador, "Riding the Rails to DC Power Efficiency: Energy efficiency in dc-electrified metropolitan railways." *IEEE Electrification Magazine*, vol. 2, no. 3, pp. 32–38, Sept 2014.

[171] D. Roch-Dupré, Álvaro J. López-López, R. R. Pecharromán, A. P. Cucala, and A. Fernández-Cardador, "Analysis of the demand charge in dc railway systems and reduction of its economic impact with energy storage systems," *International Journal of Electrical Power and Energy Systems*, vol. 93, pp. 459 – 467, 2017.

[172] R. Barrero, J. V. Mierlo, and X. Tackoen, "Energy savings in public transport," *IEEE Vehicular Technology Magazine*, vol. 3, no. 3, pp. 26–36, Sept 2008.

[173] A. Rufer, D. Hotellier, and P. Barrade, "A supercapacitor-based energy storage substation for voltage compensation in weak transportation networks," *IEEE Transactions on Power Delivery*, vol. 19, no. 2, pp. 629–636, April 2004.

[174] A. L. Allegre, A. Bouscayrol, P. Delarue, P. Barrade, E. Chattot, and S. El-Fassi, "Energy storage system with supercapacitor for an innovative subway," *IEEE Transactions on Industrial Electronics*, vol. 57, no. 12, pp. 4001–4012, Dec 2010.

[175] F. A. Inthamoussou, J. Pegueroles-Queralt, and F. D. Bianchi, "Control of a supercapacitor energy storage system for microgrid applications," *IEEE Transactions on Energy Conversion*, vol. 28, no. 3, pp. 690–697, Sept 2013.

[176] S. Nasr, M. Petit, M. Iordache, and O. Langlois, "Stability of DC micro-grid for urban railway systems," *International Journal of Smart Grid and Clean Energy*, vol. 4, no. 3, pp. 261–268, 2015.

[177] A. J. López-López, R. R. Pecharromán, A. Fernández-Cardador, and A. P. Cucala, "Assessment of energy-saving techniques in direct-current-electrified mass transit systems," *Transportation Research Part C: Emerging Technologies*, vol. 38, pp. 85–100, 2014.

[178] A. González-Gil, R. Palacin, and P. Batty, "Sustainable urban rail systems: Strategies and technologies for optimal management of regenerative braking energy," *Energy Conversion and Management*, vol. 75, pp. 374 – 388, 2013.

[179] S. Lu, P. Weston, S. Hillmansen, H. B. Gooi, and C. Roberts, "Increasing the regenerative braking energy for railway vehicles," *IEEE Trans. on Intelligent Transportation Systems*, vol. 15, no. 6, pp. 2506–2515, Dec 2014.

[180] J. A. Aguado, A. J. S. Racero, and S. de la Torre, "Optimal operation of electric railways with renewable energy and electric storage systems," *IEEE Trans. on Smart Grid*, vol. 9, no. 2, pp. 993–1001, March 2018.

[181] C. Mayet, L. Horrein, A. Bouscayrol, P. Delarue, J. N. Verhille, E. Chattot, and B. Lemaire-Semail, "Comparison of different models and simulation approaches for the energetic study of a subway," *IEEE Trans. on Vehicular Technology*, vol. 63, no. 2, pp. 556–565, Feb 2014.

[182] F. Perez, G. Damm, F. Lamnabhi-Lagarrigue, and P. Ribeiro, "Nonlinear control for isolated dc microgrids," *Revue Africaine de la Recherche en Informatique et Mathématiques Appliquées*, vol. 30, 2019.

[183] S. Chen, H. B. Gooi, and M. Wang, "Sizing of energy storage for microgrids," *IEEE Transactions on Smart Grid*, vol. 3, no. 1, pp. 142–151, 2011.

[184] N. Mohan, T. M. Undeland, and W. P. Robbins, *Power electronics: converters, applications, and design.* John wiley & sons, 2003.

[185] D. W. Hart, *Eletrônica de potência: análise e projetos de circuitos.* McGraw Hill Brasil, 2016.

[186] M. J. Tiburski *et al.*, "Técnicas para otimização de conversores da família boost com alto ganho de tensão e alto rendimento aplicados à célula a combustível," 2019.

[187] K. F. Krommydas and A. T. Alexandridis, "Modular Control Design and Stability Analysis of Isolated PV-Source/Battery-Storage Distributed Generation Systems," *IEEE Journal on Emerging and Selected Topics in Circuits and Systems*, vol. 5, no. 3, pp. 372–382, Sept 2015.

[188] H. K. Khalil, *Nonlinear control.* Prentice Hall, 2014.

[189] B. Charlet, J. Lévine, and R. Marino, "On dynamic feedback linearization," *Systems & Control Letters*, vol. 13, no. 2, pp. 143–151, 1989.

[190] E. D. Sontag, "Input to state stability: Basic concepts and results," in *Nonlinear and optimal control theory.* Springer, 2008, pp. 163–220.

[191] E. D. Sontag, "Smooth stabilization implies coprime factorization," *IEEE Transactions on Automatic Control*, vol. 34, no. 4, pp. 435–443, April 1989.

[192] P. Pepe and H. Ito, "On Saturation, Discontinuities, and Delays, in iISS and ISS Feedback Control Redesign," *IEEE Transactions on Automatic Control*, vol. 57, no. 5, pp. 1125–1140, May 2012.

[193] Z. Chen, A. Iovine, G. Damm, and L. Galai-Dol, "Power Management for a DC MicroGrid in a Smart Train Station including Recovery Braking," in *ECC 2019 - European Control Conference*, Jun 2019.

[194] H. J. Sira Ramirez and R. Silva-Ortigoza, *Control design techniques in power electronics devices.* Springer, 2006.

[195] Y. Chen, G. Damm, A. Benchaib, M. Netto, and F. Lamnabhi-Lagarrigue, "Control induced explicit time-scale separation to attain dc voltage stability for a vsc-hvdc terminal," in *IFAC Proceedings Volumes (IFAC-PapersOnline)*, vol. 19, 08 2014.

[196] P. Rouchon, "Necessary condition and genericity of dynamic feedback linearization," *J. Math. Systems Estim. Control*, vol. 4, no. 2, pp. 257–260, 1994.

[197] Y. Chen, "Nonlinear control and stability analysis of multi-terminal high voltage direct current networks," Ph.D. dissertation, 2015.

[198] P. W. Sauer, S. Ahmed-Zaid, and P. Kokotovic, "An integral manifold approach to reduced order dynamic modeling of synchronous machines," *IEEE transactions on Power Systems*, vol. 3, no. 1, pp. 17–23, 1988.

[199] J. W. Kimball and P. T. Krein, "Singular perturbation theory for dc–dc converters and application to pfc converters," *IEEE Transactions on Power Electronics*, vol. 23, no. 6, pp. 2970–2981, 2008.

[200] G. Oriolo, A. D. Luca, and M. Vendittelli, "Wmr control via dynamic feedback linearization: design, implementation, and experimental validation," *IEEE Transactions on Control Systems Technology*, vol. 10, no. 6, pp. 835–852, Nov 2002.

[201] R. Marino, "Static and dynamic feedback linearization of nonlinear systems," in *Perspectives in control theory.* Springer, 1990, pp. 249–260.

[202] F. Locment, M. Sechilariu, and I. Houssamo, "Dc load and batteries control limitations for photovoltaic systems. experimental validation," *IEEE Transactions on Power Electronics*, vol. 27, no. 9, pp. 4030–4038, Sept 2012.

[203] P. M. De Almeida, J. L. Duarte, P. F. Ribeiro, and P. G. Barbosa, "Repetitive controller for improving grid-connected photovoltaic systems," *IET Power Electronics*, vol. 7, no. 6, pp. 1466–1474, 2014.

[204] S. Golestan, M. Monfared, F. D. Freijedo, and J. M. Guerrero, "Performance improvement of a prefiltered synchronous-reference-frame pll by using a pid-type loop filter," *IEEE Transactions on Industrial Electronics*, vol. 61, no. 7, pp. 3469–3479, 2013.

[205] H. A. Pereira, A. F. Cupertino, C. da SG Ribeiro, and S. Silva, "Influence of pll in wind parks harmonic emissions," in *2013 IEEE PES Conference on Innovative Smart Grid Technologies (ISGT Latin America)*. IEEE, 2013, pp. 1–8.

[206] A. Iovine, G. Damm, E. De Santis, M. D. Di Benedetto, L. Galai-Dol, and P. Pepe, "Voltage Stabilization in a DC MicroGrid by an ISS-like Lyapunov Function implementing Droop Control," in *2018 European Control Conference (ECC)*, June 2018, pp. 1130–1135.

[207] E. D. Sontag and Y. Wang, "On characterizations of the input-to-state stability property," *Systems and Control letters*, vol. 24, no. 5, pp. 351–360, 1995.

[208] G. C. Konstantopoulos, Q. Zhong, B. Ren, and M. Krstic, "Bounded integral control of input-to-state practically stable nonlinear systems to guarantee closed-loop stability," *IEEE Transactions on Automatic Control*, vol. 61, no. 12, pp. 4196–4202, Dec 2016.

[209] A. Teel, L. Moreau, and D. Nešić, "Input to state set stability for pulse width modulated control systems with disturbances," *Systems & Control Letters*, vol. 51, no. 1, pp. 23 – 32, 2004.

[210] G. C. Konstantopoulos and A. T. Alexandridis, "Generalized nonlinear stabilizing controllers for hamiltonian-passive systems with switching devices," *IEEE Transactions on Control Systems Technology*, vol. 21, no. 4, pp. 1479–1488, July 2013.

[211] I. M. Mitchell, A. M. Bayen, and C. J. Tomlin, "A time-dependent hamilton-jacobi formulation of reachable sets for continuous dynamic games," *IEEE Transactions on Automatic Control*, vol. 50, no. 7, pp. 947–957, July 2005.

[212] N. Hatziargyriou, J. Milanović, C. Rahmann, V. Ajjarapu, C. Cañizares, I. Erlich, D. Hill, I. Hiskens, I. Kamwa, B. Pal *et al.*, "Stability definitions

and characterization of dynamic behavior in systems with high penetration of power electronic interfaced technologies," 2020.

[213] P. Kundur, N. J. Balu, and M. G. Lauby, *Power system stability and control*. McGraw-hill New York, 1994, vol. 7.

[214] J. Machowski, J. Bialek, and J. Bumby, *Power system dynamics: stability and control*. John Wiley & Sons, 2011.

[215] J. A. Barnes, A. R. Chi, L. S. Cutler, D. J. Healey, D. B. Leeson, T. E. McGunigal, J. A. Mullen, W. L. Smith, R. L. Sydnor, R. F. Vessot *et al.*, "Characterization of frequency stability," *IEEE transactions on instrumentation and measurement*, no. 2, pp. 105–120, 1971.

[216] A. M. Pirbazari, "Ancillary services definitions, markets and practices in the world," in *2010 IEEE/PES Transmission and Distribution Conference and Exposition: Latin America (T D-LA)*, Nov 2010, pp. 32–36.

[217] M. A. Pai, P. W. Sauer, and B. C. Lesieutre, "Static and dynamic nonlinear loads and structural stability in power systems," *Proceedings of the IEEE*, vol. 83, no. 11, pp. 1562–1572, Nov 1995.

[218] D. Karlsson and D. J. Hill, "Modelling and identification of nonlinear dynamic loads in power systems," *IEEE Transactions on Power Systems*, vol. 9, no. 1, pp. 157–166, Feb 1994.

[219] B. d. Almeida, "Análise da operação de sistemas de potência isolados para plataformas flutuantes," Ph.D. dissertation, Universidade de São Paulo, 2019.

[220] J. Dixon, L. Moran, J. Rodriguez, and R. Domke, "Reactive power compensation technologies: State-of-the-art review," *Proceedings of the IEEE*, vol. 93, no. 12, pp. 2144–2164, Dec 2005.

[221] D. Lee, "Ieee recommended practice for excitation system models for power system stability studies (ieee std 421.5-1992)," *Energy Development and Power Generating Committee of the Power Engineering Society*, vol. 95, no. 96, 1992.

[222] G. Joos, B. Ooi, D. McGillis, F. Galiana, and R. Marceau, "The potential of distributed generation to provide ancillary services," in *2000 power engineering society summer meeting (cat. no. 00ch37134)*, vol. 3. IEEE, 2000, pp. 1762–1767.

[223] T. Wu, M. Rothleder, Z. Alaywan, and A. D. Papalexopoulos, "Pricing energy and ancillary services in integrated market systems by an optimal power flow," *IEEE Transactions on power systems*, vol. 19, no. 1, pp. 339–347, 2004.

[224] Y. G. Rebours, D. S. Kirschen, M. Trotignon, and S. Rossignol, "A survey of frequency and voltage control ancillary services—part ii: Economic features," *IEEE Transactions on power systems*, vol. 22, no. 1, pp. 358–366, 2007.

[225] "Resolução normativa 822, de 26 de junho de 2018, que regulamenta a prestação e remuneração de serviços ancilares no sin," National Agency of Electrical Energy - ANEEL (Brazil), Tech. Rep., 2018.

[226] "Revisão da resolução normativa 697/2015, que regulamenta a prestação e remuneração de serviços ancilares no sin, relatório de análise de impacto regulatório 006/2019," National Agency of Electrical Energy - ANEEL (Brazil), Tech. Rep., 2019.

[227] "Technical arrangements for ancillary services - submodule 14.2," National Agency of Electrical Energy - ANEEL (Brazil), Tech. Rep., 2019.

[228] Y. V. Makarov, M. A. Elizondo, J. G. O'Brien, Q. Huang, H. Kirkham, Z. Huang, M. Chinthavali, D. Suman, N. Mohan, W. Hess *et al.*, "Models and methods for assessing the value of hvdc and mvdc technologies in modern power grids," Pacific Northwest National Lab.(PNNL), Richland, WA (United States), Tech. Rep., 2017.

[229] X. . Zhang, L. Yao, B. Chong, C. Sasse, and K. R. Godfrey, "Facts and hvdc technologies for the development of future power systems," in *2005 International Conference on Future Power Systems*, Nov 2005, pp. 6 pp.–6.

[230] D. Pattabiraman, R. H. Lasseter., and T. M. Jahns, "Comparison of grid following and grid forming control for a high inverter penetration power system," in *2018 IEEE Power Energy Society General Meeting (PESGM)*, Aug 2018, pp. 1–5.

[231] N. Grid, "Electricity ten year statement," *UK Electricity Transmission, London*, 2014.

[232] L. Jessen, S. Günter, F. W. Fuchs, M. Gottschalk, and H.-J. Hinrichs, "Measurement results and performance analysis of the grid impedance in different low voltage grids for a wide frequency band to support grid integration of renewables," in *2015 IEEE Energy Conversion Congress and Exposition (ECCE)*. IEEE, 2015, pp. 1960–1967.

[233] T. Breithaupt, B. Tuinema, D. Herwig, D. Wang, L. Hofmann, J. Rueda Torres, A. Mertens, S. Rüberg, R. Meyer, V. Sewdien *et al.*, "Migrate deliverable d1. 1 report on systemic issues," *MIGRATE Project Consortium: Bayreuth, Germany*, p. 137, 2016.

[234] G. Joos, B. T. Ooi, D. McGillis, F. D. Galiana, and R. Marceau, "The potential of distributed generation to provide ancillary services," in *2000 Power Engineering Society Summer Meeting (Cat. No.00CH37134)*, vol. 3, July 2000, pp. 1762–1767 vol. 3.

[235] U. Markovic, O. Stanojev, E. Vrettos, P. Aristidou, and G. Hug, "Understanding stability of low-inertia systems," 2019.

[236] ENTSO-E, "Documentation on controller tests in test grid configurations," European Network of Transmission System Operators for Electricity, Tech. Rep., 2013.

[237] N. Grid, "Enhanced frequency response: Invitation to tender for pre-qualified parties," 2016.

[238] S. Eirgrid, "Ds3: System services consultation–new products and contractual arrangements," 2012.

[239] E. R. C. of Texas (ERCOT), "Future ancillary services in ercot," 2013.

[240] ENTSO-E, "High penetration of power electronic interfaced power sources (hpopeips)," Guidance document for national implementation for network codes on grid connection, Tech. Rep., 2017.

[241] H. Beck and R. Hesse, "Virtual synchronous machine," in *2007 9th International Conference on Electrical Power Quality and Utilisation*, Oct 2007, pp. 1–6.

[242] K. Sakimoto, Y. Miura, and T. Ise, "Stabilization of a power system with a distributed generator by a virtual synchronous generator function," in *8th International Conference on Power Electronics-ECCE Asia*. IEEE, 2011, pp. 1498–1505.

[243] M. Torres and L. A. Lopes, "Virtual synchronous generator: A control strategy to improve dynamic frequency control in autonomous power systems," 2013.

[244] D. Shrestha, U. Tamrakar, Z. Ni, and R. Tonkoski, "Experimental verification of virtual inertia in diesel generator based microgrids," in *2017 IEEE*

International Conference on Industrial Technology (ICIT). IEEE, 2017, pp. 95–100.

[245] Q.-C. Zhong, "Virtual synchronous machines: A unified interface for grid integration," *IEEE Power Electronics Magazine*, vol. 3, no. 4, pp. 18–27, 2016.

[246] H. Bevrani, T. Ise, and Y. Miura, "Virtual synchronous generators: A survey and new perspectives," *International Journal of Electrical Power & Energy Systems*, vol. 54, pp. 244–254, 2014.

[247] X. Hou, Y. Sun, X. Zhang, J. Lu, P. Wang, and J. M. Guerrero, "Improvement of frequency regulation in vsg-based ac microgrid via adaptive virtual inertia," *IEEE Transactions on Power Electronics*, vol. 35, no. 2, pp. 1589–1602, 2019.

[248] X. Hou, H. Han, C. Zhong, W. Yuan, M. Yi, and Y. Chen, "Improvement of transient stability in inverter-based ac microgrid via adaptive virtual inertia," in *2016 IEEE Energy Conversion Congress and Exposition (ECCE)*. IEEE, 2016, pp. 1–6.

[249] Q.-C. Zhong, P.-L. Nguyen, Z. Ma, and W. Sheng, "Self-synchronized synchronverters: Inverters without a dedicated synchronization unit," *IEEE Transactions on power electronics*, vol. 29, no. 2, pp. 617–630, 2013.

[250] Z. Ma, Q.-C. Zhong, and J. D. Yan, "Synchronverter-based control strategies for three-phase pwm rectifiers," in *2012 7th IEEE conference on industrial electronics and applications (ICIEA)*. IEEE, 2012, pp. 225–230.

[251] M. Van Wesenbeeck, S. De Haan, P. Varela, and K. Visscher, "Grid tied converter with virtual kinetic storage," in *2009 IEEE Bucharest PowerTech*. IEEE, 2009, pp. 1–7.

[252] J. Svensson, "Synchronisation methods for grid-connected voltage source converters," *IEE Proceedings-Generation, Transmission and Distribution*, vol. 148, no. 3, pp. 229–235, 2001.

[253] T. Midtsund, J. Suul, and T. Undeland, "Evaluation of current controller performance and stability for voltage source converters connected to a weak grid," in *The 2nd International Symposium on Power Electronics for Distributed Generation Systems*. IEEE, 2010, pp. 382–388.

[254] C. Chang, D. Gorinevsky, and S. Lall, "Stability analysis of distributed power generation with droop inverters," *IEEE Transactions on Power Systems*, vol. 30, no. 6, pp. 3295–3303, Nov 2015.

[255] A. Mohd, E. Ortjohann, D. Morton, and O. Omari, "Review of control techniques for inverters parallel operation," *Electric Power Systems Research*, vol. 80, no. 12, pp. 1477–1487, 2010.

[256] O. Saborio Romano, "Small-signal modelling and stability analysis of a traditional generation unit and a virtual synchronous machine in grid-connected operation," Master's thesis, NTNU, 2015.

[257] M. F. M. Arani, Y. A.-R. I. Mohamed, and E. F. El-Saadany, "Analysis and mitigation of the impacts of asymmetrical virtual inertia," *IEEE Transactions on Power Systems*, vol. 29, no. 6, pp. 2862–2874, 2014.

[258] N. Soni, S. Doolla, and M. C. Chandorkar, "Improvement of transient response in microgrids using virtual inertia," *IEEE transactions on power delivery*, vol. 28, no. 3, pp. 1830–1838, 2013.

[259] S. D'Arco and J. A. Suul, "Virtual synchronous machines—classification of implementations and analysis of equivalence to droop controllers for microgrids," in *2013 IEEE Grenoble Conference*. IEEE, 2013, pp. 1–7.

[260] J. C. Gonzalez-Torres, V. Costan, G. Damm, A. Benchaib, A. Bertinato, S. Poullain, B. Luscan, and F. Lamnabhi-Lagarrigue, "Hvdc protection criteria for transient stability of ac systems with embedded hvdc links," *The Journal of Engineering*, vol. 2018, no. 15, pp. 956–960, 2018.

[261] N. G. Bretas and L. F. Alberto, "Lyapunov function for power systems with transfer conductances: extension of the invariance principle," *IEEE Transactions on Power Systems*, vol. 18, no. 2, pp. 769–777, 2003.

[262] D. Lee, "Ieee recommended practice for excitation system models for power system stability studies," *IEEE Std 421.5-2016*, pp. 1–207, Aug 2016.

[263] H. A. Alsiraji and R. El-Shatshat, "Comprehensive assessment of virtual synchronous machine based voltage source converter controllers," *IET Generation, Transmission & Distribution*, vol. 11, no. 7, pp. 1762–1769, 2017.

[264] X. Wang, Y. W. Li, F. Blaabjerg, and P. C. Loh, "Virtual-impedance-based control for voltage-source and current-source converters," *IEEE Transactions on Power Electronics*, vol. 30, no. 12, pp. 7019–7037, 2014.

[265] J. He and Y. W. Li, "Analysis, design, and implementation of virtual impedance for power electronics interfaced distributed generation," *IEEE Transactions on Industry Applications*, vol. 47, no. 6, pp. 2525–2538, 2011.

CHAPTER G

APPENDIX I

G.1. Proportional Integral (PI) Controller

The linear control of the DC Microgrid presented in Chapter 4 is designed via PI controller, which is inserted in the control input of the power converters. The controlled voltages (V_{dc}, $V_{C_{11}}$ and $V_{C_{14}}$) present a control structure with an outer control loop, that provides the reference for the inner control loop. The outer loop is designed to be slower than the inner one, where the difference between the dynamics in this case is at least ten decades, according to classical PI cascade controllers. In the other devices of the system, the currents (I_{L_6}, I_{L_9} and $I_{ld,q}$) are directly controlled. The block diagrams of the PI controllers in each converter of the system will be introduced next.

First, the block diagram for the DC bus voltage is depicted in Figure G.1, where $I_{sum} = I_{R_5} + I_{R_8} + I_{R_{12}} + I_{R_{15}} + I_{R_{17}}$. The PI controller is applied to the voltage control loop and the current loop, which is inserted in a nonlinear plant.

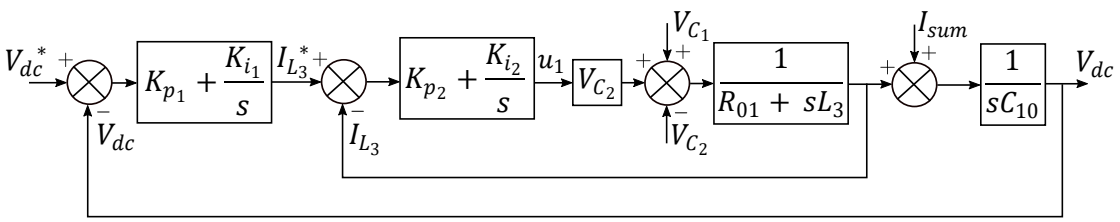

Figure G.1: Block diagram of the DC bus voltage control.

The Calculated control input for DC bus voltage control is presented in (G.1), where the current reference is provided by the voltage control loop in (G.2).

$$u_1 = -K_{p_2}(I_{L_3} - I_{L_3}^*) - K_{i_2}\int(I_{L_3} - I_{L_3}^*)dt \tag{G.1}$$

$$I_{L_3}^* = -K_{p_1}(V_{dc} - V_{dc}^*) - K_{i_1}\int(V_{dc} - V_{dc}^*)dt \tag{G.2}$$

Based on the block diagram in Figure G.1, considering the linearization of the plant and the PI controller, the closed-loop transfer function for DC bus voltage is obtained:

$$\frac{V_{dc}(s)}{V_{dc}^*(s)} = \frac{K_{p_1}s + K_{i_1}}{C_{10}s^2 + K_{p_1}s + K_{i_1}} \tag{G.3}$$

Generally, the canonical form of the transfer function is expressed as:

$$F(s) = \frac{2\xi s + \omega_n^2}{s^2 + 2\xi\omega_n s + \omega_n^2} \tag{G.4}$$

where the damping coefficient $\xi = K_{p_1}/2\omega_n C_{10}$ and the natural frequency $\omega_n = \sqrt{K_{i_1}/C_{10}}$ can be adjusted to obtain the desired dynamical behavior with proper filtering. The Wiener method defines $\xi = \sqrt{2}$ and ω_n is defined according to the controller bandwidth.

The gains of the PI controller can be calculated according to the chosen poles (p_1 and p_2) of the system, such that the voltage has the desired dynamics. Therefore, the gains of the controller are given as:

$$s^2 + \frac{K_{p_1}}{C_{10}}s + \frac{K_{i_1}}{C_{10}} = (s + p_1)(s + p_2) = s^2 + (p_1 + p_2)s + p_1p_2 \tag{G.5}$$

$$K_{p_1} = C_{10}(p_1 + p_2) \quad ; \quad K_{i_1} = C_{10}(p_1p_2) \tag{G.6}$$

The transfer function of the current control loop is provided as:

$$\frac{I_{L_3}(s)}{I_{L_3}^*(s)} = \frac{K_{p_2}s + K_{i_2}}{L_3s^2 + (R_{01} + K_{p_1})s + K_{i_1}} \tag{G.7}$$

Considering the desired poles (p_3 and p_4) for the current dynamics, the gains of the controllers are calculated as:

$$K_{p_2} = L_3(p_3 + p_4) - R_{01} \quad ; \quad K_{i_2} = L_3p_3p_4 \tag{G.8}$$

The block diagram of the battery control is depicted in Figure G.2. The PI controller is applied to the current control loop, which is inserted in a nonlinear plant.

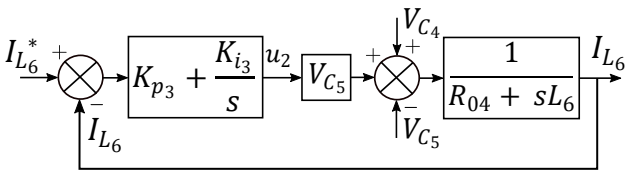

Figure G.2: Block diagram of the current battery control.

The control law for the battery's current is introduced in (G.9).

$$u_2 = -K_{p_3}(I_{L_6} - I^*_{L_6}) - \int K_{i_3}(I_{L_6} - I^*_{L_6})dt \tag{G.9}$$

Based on the block diagram in Figure G.2, considering the linearization of the plant and the PI controller, the closed-loop transfer function for battery current is obtained:

$$\frac{I_{L_6}(s)}{I^*_{L_6}(s)} = \frac{K_{p_3}s + K_{i_3}}{L_6 s^2 + (R_{04} + K_{p_3})s + K_{i_3}} \tag{G.10}$$

Considering the desired poles (p_5 and p_6) for the current dynamics, the gains of the controllers are calculated as:

$$K_{p_3} = L_6(p_5 + p_6) - R_{04} \quad ; \quad K_{i_3} = L_6 p_5 p_6 \tag{G.11}$$

The block diagram of the PV array is depicted in Figure G.3.

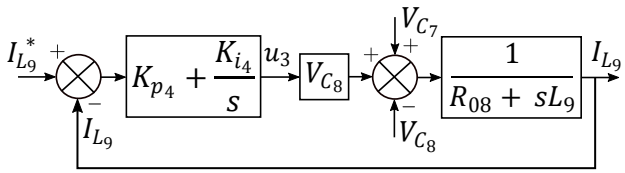

Figure G.3: Block diagram of the current PV control.

The control law of the PV array current is introduced in (G.12).

$$u_3 = -K_{p_4}(I_{L_9} - I^*_{L_9}) - K_{i_4}\int (I_{L_9} - I^*_{L_9})dt \tag{G.12}$$

The closed-loop transfer function for PV array current is obtained:

$$\frac{I_{L_9}(s)}{I^*_{L_9}(s)} = \frac{K_{p_4}s + K_{i_4}}{L_9 s^2 + (R_{08} + K_{p_4})s + K_{i_4}} \tag{G.13}$$

Considering the desired poles (p_7 and p_8) for the current dynamics, the gains of the controllers are calculated as:

$$K_{p_4} = L_9(p_7 + p_8) - R_{08} \quad ; \quad K_{i_4} = L_9 p_7 p_8 \tag{G.14}$$

The block diagram of the DC Load is depicted in Figure G.4.

The control law of the DC load voltage is given in (G.15), where the current reference is calculated in (G.16).

$$u_4 = -K_{p_6}(I_{L_{13}} - I^*_{L_{13}}) - K_{i_6}\int (I_{L_{13}} - I^*_{L_{13}})dt \tag{G.15}$$

$$I^*_{L_{13}} = K_{p_5}(V_{C_{11}} - V^*_{C_{11}}) + K_{p_5}\int (V_{C_{11}} - V^*_{C_{11}})dt \tag{G.16}$$

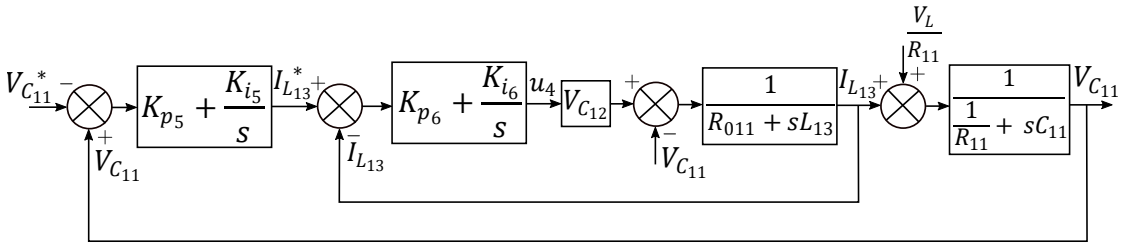

Figure G.4: Block diagram of the DC load voltage control.

The closed-loop transfer function for DC load voltage is obtained:

$$\frac{V_{C_{11}}(s)}{V_{C_{11}}^*(s)} = \frac{K_{p_5}s + K_{i_5}}{C_{11}s^2 + (\frac{1}{R_{11}} + K_{p_5})s + K_{i_5}} \tag{G.17}$$

Considering the desired poles (p_9 and p_{10}) for voltage dynamics, the gains of the controllers are calculated as:

$$K_{p_5} = C_{11}(p_9 + p_{10}) - \frac{1}{R_{11}} \quad ; \quad K_{i_5} = C_{11}p_9p_{10} \tag{G.18}$$

The transfer function of the current control loop is provided as follows:

$$\frac{I_{L_{13}}(s)}{I_{L_{13}}^*(s)} = \frac{K_{p_6}s + K_{i_6}}{L_{13}s^2 + (R_{011} + K_{p_6})s + K_{i_6}} \tag{G.19}$$

Considering the desired poles (p_{11} and p_{12}) for the current dynamics, the gains of the controllers are calculated as:

$$K_{p_6} = L_{13}(p_{11} + p_{12}) - R_{011} \quad ; \quad K_{i_6} = L_{13}p_{11}p_{12} \tag{G.20}$$

The block diagram of the regenerative braking system is depicted in Figure G.5.

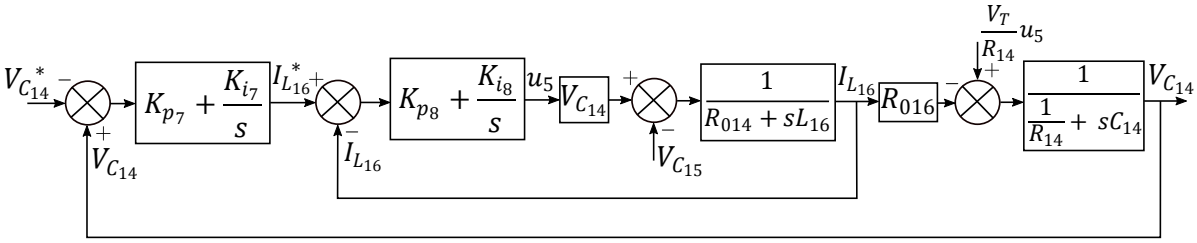

Figure G.5: Block diagram of the DC load voltage control.

In the same way, the control law of the train's regenerative braking is given in (G.21), where the current reference is computed in (G.22).

$$u_5 = -K_{p_8}(I_{L_{16}} - I_{L_{16}}^*) - K_{i_8}\int(I_{L_{16}} - I_{L_{16}}^*)dt \tag{G.21}$$

$$I_{L_{16}}^* = K_{p_7}(V_{C_{14}} - V_{C_{14}}^*) + K_{i_7}\int(V_{C_{14}} - V_{C_{14}}^*)dt \tag{G.22}$$

The closed-loop transfer function for train voltage is obtained:

$$\frac{V_{C_{14}}(s)}{V^*_{C_{14}}(s)} = \frac{K_{p_7}s + K_{i_7}}{R_{14}C_{14}s^2 + (1 + K_{p_7})s + K_{i_7}} \tag{G.23}$$

Considering the desired poles (p_{13} and p_{14}) for voltage dynamics, the gains of the controllers are computed as:

$$K_{p_7} = R_{14}C_{14}(p_{13} + p_{14}) - 1 \quad ; \quad K_{i_7} = R_{14}C_{14}p_{13}p_{14} \tag{G.24}$$

The transfer function for the current control loop is provided as follows:

$$\frac{I_{L_{16}}(s)}{I^*_{L_{16}}(s)} = \frac{K_{p_8}s + K_{i_8}}{L_{16}s^2 + (R_{014} + K_{p_8})s + K_{i_8}} \tag{G.25}$$

Considering the desired poles (p_{15} and p_{16}) for the current dynamics, the gains of the controllers are computed as:

$$K_{p_8} = L_{16}(p_{15} + p_{16}) - R_{014} \quad ; \quad K_{i_8} = L_{16}p_{15}p_{16} \tag{G.26}$$

The block diagram of the VSC control is depicted in Figure G.6. The PI controller is applied to the current control loop, which is inserted in the nonlinear plant.

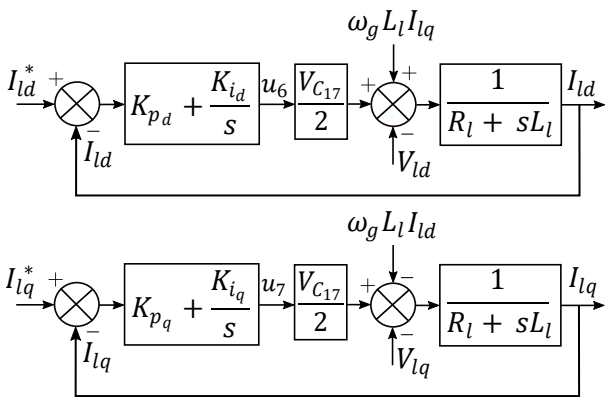

Figure G.6: Block diagram of I_{ld} and I_{lq} current control, respectively.

Finally, the modulation index of the VSC converter to inject power in the AC side of the grid are computed in (G.27) and (G.28) respectively.

$$u_6 = -K_{p_d}(I_{ld} - I^*_{ld}) - K_{i_d}\int(I_{ld} - I^*_{ld})dt \tag{G.27}$$

$$u_7 = -K_{p_q}(I_{lq} - I^*_{lq}) - K_{i_q}\int(I_{lq} - I^*_{lq})dt \tag{G.28}$$

The closed-loop transfer function for $I_{ld,q}$ currents is obtained:

$$\frac{I_{ld,q}(s)}{I^*_{ld,q}(s)} = \frac{K_{p_9}s + K_{i_9}}{L_l s^2 + (R_l + K_{p_9})s + K_{i_9}} \tag{G.29}$$

Considering the desired poles (p_{17} and p_{18}) for the current dynamics, the gains of the controllers are calculated as:

$$K_{p_9} = L_l(p_{17} + p_{18}) - R_l \quad ; \quad K_{i_9} = L_l p_{17} p_{18} \tag{G.30}$$

The poles are chosen, such that the time-constant of the current dynamics is about 50 ms and the time-constant for the voltage dynamics is about 100 ms. The parameters for the linear controllers are presented in Table G.1 and these values are used to calculate the gains for the nonlinear controllers. The fine adjustment of the control gains were made by simulation tests, in order to achieve a suitable control performance, balancing convergence speed and overshoot signals for both nonlinear and linear controllers. In practical applications and experimental tests, the tuning of gains and the parameters of the controllers may need to be readjusted, considering, unknown perturbations and deviations in the Microgrid parameters, for both nonlinear and linear controllers.

Table G.1: Parameter gains of the linear PI controller.

Supercap.	$K_{p_1} = 25$	$K_{i_1} = 2000$	$K_{p_2} = 10$	$K_{i_2} = 1000$
Battery	$K_{p_3} = 10$	$K_{i_3} = 100$		
PV array	$K_{p_4} = 10$	$K_{i_4} = 100$		
DC load	$K_{p_5} = 20$	$K_{i_5} = 500$	$K_{p_6} = 10$	$K_{i_6} = 100$
Train	$K_{p_7} = 25$	$K_{i_7} = 500$	$K_{p_8} = 10$	$K_{i_8} = 100$
VSC	$K_{p_9} = 50$	$K_{i_9} = 100$		

G.2. Park Transformation

The currents of a balanced three-phase electrical system can be written as:

$$i_a = \hat{I}\sin(\omega_g t) \tag{G.31}$$

$$i_b = \hat{I}\sin(\omega_g t - \frac{2\pi}{3}) \tag{G.32}$$

$$i_c = \hat{I}\sin(\omega_g t + \frac{2\pi}{3}) \tag{G.33}$$

where $\hat{I}$ is the peak value of current and ω_g is the grid frequency.

The Park transformation is a change of variables that implies obtaining a rotating reference frame with direct (d), quadrature (q) and zero (0) components with DC values. This transformation greatly simplifies the complexity of solving AC power system equations. In this case, the grid frequency represents the rotational speed of

the phasor. The transformation from abc frame to $dq0$ is introduced the following matrix:

$$\begin{bmatrix} i_d \\ i_q \\ i_0 \end{bmatrix} = \frac{2}{3} \begin{bmatrix} \cos(\theta) & \cos(\theta - \frac{2\pi}{3}) & \cos(\theta + \frac{2\pi}{3}) \\ -\sin(\theta) & -\sin(\theta - \frac{2\pi}{3}) & -\sin(\theta + \frac{2\pi}{3}) \\ \frac{1}{2} & \frac{1}{2} & \frac{1}{2} \end{bmatrix} \cdot \begin{bmatrix} i_a \\ i_b \\ i_c \end{bmatrix} \tag{G.34}$$

where the transformation is also applied for voltages, and the time-varying phase angle is defined as $\theta = \int \omega_g$. The zero component of the Park transformation is associated with symmetrical components, therefore under balanced circuits: $i_a + i_b + i_c = 0$, which results in $i_0 = 0$.

The inverse transformation can be written as follows:

$$\begin{bmatrix} i_a \\ i_b \\ i_c \end{bmatrix} = \frac{2}{3} \begin{bmatrix} \cos(\theta) & -\sin(\theta) & 1 \\ \cos(\theta - \frac{2\pi}{3}) & -\sin(\theta - \frac{2\pi}{3}) & 1 \\ \cos(\theta + \frac{2\pi}{3}) & -\sin(\theta + \frac{2\pi}{3}) & 1 \end{bmatrix} \cdot \begin{bmatrix} i_d \\ i_q \\ i_0 \end{bmatrix} \tag{G.35}$$

The three phase complex power of a balanced system ($i_0 = 0$) is given as:

$$S_{3\phi} = \frac{3}{2} V I^* \tag{G.36}$$

where $V = v_d + jv_q$ is the voltage phasor and $I^* = i_d - ji_q$ is the complex current phasor, with $S_{3\phi} = P + jQ$.

Therefore, the active and reactive power expression using dq components are given as:

$$P = \frac{3}{2}(i_d v_d + i_q v_q) \tag{G.37}$$

$$Q = \frac{3}{2}(i_d v_q - i_q v_d) \tag{G.38}$$

G.3. Input-to-State Stability

The definition of input to state stability is provided in [207], which is applied in this thesis to prove the stability of the DC Microgrid described in Chapter 4. The ISS definition and properties are introduced next.

Considering a nonlinear system:

$$\dot{x} = f(x, u) \tag{G.39}$$

where x is considered an extended state, $f : \mathbb{R}^n \times \mathbb{R}^m \to \mathbb{R}^n$ continuously differentiable and $u : \mathbb{R}_{\geq 0} \to \mathbb{R}^m$ is a measurable locally bounded input control.

For each $\xi \in \mathbb{R}^n$ and $u \in L_\infty^m$ one may express the trajectory of the system (G.39) as $x(t, \xi, u)$ where the initial condition is $x(0) = \xi$. Therefore, the definition is given as follows:

Definition 1. *The system (G.39) is input/state stable (ISS) if there exists a $\mathcal{KL}$-function $\beta : \mathbb{R}_{\geq 0} \times \mathbb{R}_{\geq 0} \to \mathbb{R}_{\geq 0}$ and a $\mathcal{K}$-function $\gamma : \mathbb{R}_{\geq 0} \to \mathbb{R}_{\geq 0}$ such that, for each input u and for each ξ, the following inequality holds:*

$$|x(t, \xi, u)| \leq \beta(|\xi|, t) + \gamma(||u||) \tag{G.40}$$

for each $t \geq 0$.

This is seen as a generalization in a nonlinear way of the bound $|x(t)| \leq |\xi|e^{-\alpha t}$+c||u||, which holds for a linear system ($\dot{x} = Ax + Bu$) when matrix A is asymptotically stable. From this definition, one stated that a system can be stabilized by a smooth feedback if and only if it is feedback equivalent to an ISS system as shown in [207].

Definition 2. *A smooth function $W : \mathbb{R}^n \to \mathbb{R}_{\geq 0}$ is called an ISS-Lyapunov function of system (G.39) if there exist $\mathcal{K}_\infty$-functions α_1, α_2 and $\mathcal{K}$-functions α_3 and α_4 such that:*

$$\alpha_1(|\xi|) \leq W(\xi) \leq \alpha_2(|\xi|) \tag{G.41}$$

for any ξ and

$$\nabla W(\xi).f(\xi, u) \leq -\alpha_3(|\xi|) \tag{G.42}$$

for any ξ and any μ such that $|\xi| \geq \alpha_4(|\mu|)$.

Therefore W is an ISS-Lyapunov function for (G.39), which results that it is a Lyapunov function in the usual sense. System (G.39) is ISS if it admits an ISS-Lyapunov function.

A interesting connection between ISS stability and robust stability can be done. By a time-varying feedback for system (G.39) one will mean function $k : \mathbb{R}_{\geq 0} \times \mathbb{R}^n \to \mathbb{R}^n$ for which the differential equation corresponding to using k as the feedback is given:

$$\dot{x} = f(x, k(t, x)) \tag{G.43}$$

Let ρ be a $\mathcal{K}_\infty$-function, where a feedback law will be said to be bounded by ρ if for each ξ, $|k(t, \xi)| \leq \rho(|\xi|)$ holds for almost all (recall that k is assumed to

be only measurable) $t \geq 0$. So, the system (G.39) is robustly stable if there exists a $\mathcal{K}_\infty$-function ρ, called as the stability margin, and $\mathcal{KL}$-function β such that, for every feedback law bounded by ρ it holds that:

$$|x(t)| \leq \beta(|x(0)|, t) \quad \forall t \geq 0 \tag{G.44}$$

for every solution of the system (G.43).

The main result is that the system (G.39) is ISS if and only if it is robustly stable.

One may remark from [207]:

Remark 9. *Note that ISS is not a notion of local stability with respect to small perturbations. It is a global notion, and perturbations can be arbitrarily large (since function ρ is in class $\mathcal{K}_\infty$). In some sense, this is analogous to exponential stability for linear systems, where a perturbation of the spectrum preserves global asymptotic stability.*

CHAPTER H

Appendix II - Résumé en Français

H.1. Introduction

Le réseau électrique traverse une révolution depuis les années 2000. Une telle révolution se compose d'abord d'aspects économiques tels que la libéralisation des marchés de l'électricité, le dégroupage et la privatisation de sociétés d'électricité précédemment détenues par l'État, ce qui apporte une nouvelle dynamique au marché de l'énergie. Ensuite, pour des raisons environnementales et sociétales, il y a eu le choix de réduire l'utilisation des sources fossiles, et dans une certaine mesure, même l'énergie nucléaire. Ce changement fondamental de la matrice panier énergétique a introduit des proportions toujours croissantes de sources d'énergie renouvelables. De tels changements, s'ils se poursuivent dans le futur, vont complètement remodeler le fonctionnement des réseaux électriques, en particulier parce que les deux points précédents (économique et environnemental) sont plutôt antagonistes. De plus, les énergies renouvelables introduisent une grande variabilité dans le réseau électrique, qui a besoin d'un équilibre parfait à tout moment sur la puissance électrique produite et consommée [1]. La solution pour atteindre la stabilité dans une telle production et consommation variants dans le temps a été l'introduction de nouveaux éléments des Systèmes et Technologies de l'Information et Télécommunication (ICT). Une telle intégration entre les réseaux électriques traditionnels et les ICT est maintenant connue sous le nom de *Smart-Grids* [2–4].

La modernisation du système électrique est également liée à la croissance constante de la demande d'énergie, et des charges modernes basées sur l'électronique de puissance. Par conséquent, lorsque les charges modernes et les énergies renouvelables interfacées par un convertisseur de puissance atteignent des niveaux de pénétration élevés, la planification et l'exploitation du système peuvent devenir un défi très complexe. Dans ce contexte, les Smart-Grids sont composés de plusieurs éléments qui

utilisent divers nouveaux outils de calcul et des ICT tels que le Big Data, le Machine Learning et l'Optimisation pour rendre possible l'interconnexion de technologies hétérogènes. Ainsi, la communication rapide entre les éléments avec le traitement de l'information crée une philosophie d'auto-guérison, une capacité de *black-start*, une application de comptage intelligent, etc. [5, 6].

H.1.1. Sources d'énergie renouvelables

La forte Intégration de la géneration distribuée, caractérisée par de petites unités de production à proximité des centres de consommation (connectés aux systèmes de distribution), apporte certains avantages comme la réduction des pertes de puissance, la réduction des coûts d'approvisionnement, le soulagement de la transmission, etc. La plus grande partie de géneration distribuée est composée d'énergies renouvelables. Les énergies renouvelables ont certaines caractéristiques qui les distinguent complètement des autres sources d'énergie, comme les générateurs diesel qui sont des sources dispatchables. La caractéristique la plus courante est que les énergies renouvelables ne sont pas contrôlées pour acheminer l'énergie. Le vent, le soleil, les marées et d'autres phénomènes naturels ne sont pas corrélés aux besoins des consommateurs, ce qui signifie une production d'énergie intermittente. Pour cette raison, il n'est pas possible d'avoir à tout moment la production qui correspond à la consommation; cette production intermittente est le plus grand défi que posent les énergies renouvelables et doit être envisagée soit dans le cadre de l'électricité, soit dans le cadre de l'énergie. Une deuxième caractéristique est que la plupart des énergies renouvelables ont une grande dispersion. Pour cette raison, la production électrique par des énergies renouvelables est souvent distribuée, donc beaucoup plus difficile à intégrer. Ainsi, les énergies renouvelables sont majoritairement intégrées dans des niveaux de basse et moyenne tension, ce qui est en totale contradiction avec la conception des systèmes électriques [7–9].

La diversité des énergies renouvelables comprend également la possibilité d'intégrer des sources d'énergie non conventionnelles, comme par exemple les systèmes de récupération d'énergie de freinage des chemins de fer qui régénèrent cette énergie en fournissant un couple négatif aux roues motrices des trains, des métros, des tramways, etc. Dans ce cas, le moteur devient un générateur, injectant de l'énergie dans le réseau. Étant donné que l'énergie produite lors du freinage par récupération est exempte d'émissions de polluants et de déchets, elle peut être considérée comme une source d'énergie renouvelable [10–12]. Dans une gare ferroviaire, l'énergie régénérée est généralement transférée vers le troisième rail afin de permettre aux trains voisins de l'utiliser. Dans le cas où il ne peut pas être utilisé

par d'autres trains, il est dissipé sur des résistances. Pour améliorer l'efficacité du système, l'énergie disponible peut être saisie pour être stockée ou utilisée en cas de besoin [13].

Dans le contexte du transport, les véhicules électriques et les trains peuvent être intégrés au système électrique, ce qui contribue à réduire les émissions de CO_2, augmentant ainsi l'efficacité de la conversion d'énergie. Mais dans le même temps, les véhicules électriques augmentent considérablement la demande de puissance dans le système de distribution. De plus, le freinage par récupération du train injecte une grande quantité de puissance dans le système en quelques secondes, ce qui peut entraîner des problèmes d'instabilité. Par conséquent, une stratégie de contrôle appropriée est nécessaire pour l'intégrer en raison des sursauts de puissance [14–16].

Les énergies renouvelables sont majoritairement intégrées au réseau électrique par des convertisseurs de puissance, qui présentent également des spécificités. La commutation de leurs semi-conducteurs, soit par IGBT, MOSFET ou thyristors, génère une forme d'onde synchronisée pour injecter correctement la puissance au réseau créé par un signal PWM. Le processus de commutation génère des harmoniques dans les signaux de tension et de courant, ce qui peut nuire aux indices de qualité de l'énergie. Par conséquent, des filtres passifs et des convertisseurs multiniveaux ont été étudiés pour réduire l'impact des harmoniques et améliorer la contrôlabilité de l'équipement. Les convertisseurs de puissance se distinguent également par leur absence d'inertie, car il n'y a pas de machine tournante dans la conversion d'énergie, en conséquence la forte pénétration des énergies renouvelables a un impact sur l'inertie du système dans son ensemble. Par conséquent, les réseaux à faible inertie sont de plus en plus courants, affectant directement la stabilité du système. Dans ce contexte, les Microgrids isolés représentent un défi majeur, car ils peuvent être entièrement composés de convertisseurs de puissance interconnectés [17, 18].

H.2. Microgrids

Parmi un certain nombre d'éléments, le concept de *Microgrids* est devenu une solution intéressante pour intégrer les énergies renouvelables, les charges et Système de Stockage d'Énergie (ESS) en tant que système autonome. Les Microgrids sont de petites portions du réseau électrique qui peuvent, dans une certaine mesure, s'équilibrer avec la production et la consommation d'électricité et peuvent stabiliser ses principales variables d'état. Le groupe d'échange de Microgrids du département américain de l'énergie a défini Microgrid comme [25]:

Un Microgrid est un groupe de charges interconnectées et de ressources énergétiques distribuées dans des limites électriques clairement définies qui agit comme une seule entité contrôlable par rapport au réseau. Un Microgrid peut se connecter et se déconnecter du réseau pour lui permettre de fonctionner à la fois en mode connecté au réseau ou en mode îloté.

Lorsque le Microgrid est toujours connecté au réseau principal, important et exportant ainsi des quantités d'énergie arbitraires, le Microgrid est dit en mode connecté. Dans ce cas, le Microgrid est maintenu synchronisé avec le réseau principal et, par conséquent, les phénomènes de fréquence, d'angle et d'inertie sont traités par le réseau principal. Ensuite, le Microgrid doit uniquement assurer la stabilité de la tension et l'atténuation de la congestion électrique dans les lignes, et optimiser certains modèles de consommation d'énergie. Cette optimisation peut concerner l'autoconsommation, la part des énergies renouvelables, le profit, entre autres, et sera obtenue en pilotant sa production, la quantité d'énergie importée du réseau principal, et éventuellement l'utilisation du stockage [26–28].

Mais lorsque le Microgrid peut être déconnecté (ou du moins ne pas être synchronisé) au réseau principal, le Microgrid est dit en mode îloté. Dans ce cas, le Microgrid est responsable du maintien de la stabilité dans tous les états qui le composent, c'est-à-dire la fréquence, l'angle (principalement des problèmes d'inertie), la tension, la congestion du flux d'énergie, ainsi que le profit. Ce cas est bien plus compliqué que le premier. Ensuite, s'il y a au moins un grand générateur synchrone dans le Microgrid, un générateur diesel par exemple, qui fournit la plus grande partie de la puissance consommée, alors le système dégénère au Microgrid isolé standard que l'on peut trouver dans des endroits éloignés. Mais lorsque de plus grandes parts d'énergies renouvelables sont présentes dans ces réseaux, le problème peut devenir très complexe [28–30].

Un autre aspect important est le nombre important de personnes vivant dans des communautés éloignées sans accès à l'électricité. Ces villages peuvent ne jamais être connectés au réseau pour des raisons économiques et de leur éloignement, c'est pourquoi le Microgrid est une excellente solution pour l'approvisionnement en électricité. D'autre part, de nombreuses communautés isolées, telles que les communautés africaines, brésiliennes, canadiennes ou insulaires, ont un grand potentiel pour le rayonnement solaire et le vent, mettant l'accent sur l'utilisation des énergies renouvelables. L'approvisionnement en électricité peut être considéré comme une contribution à l'inclusion sociale et à l'amélioration de la qualité de vie, où l'électricité est principalement utilisée à des fins domestiques telles que l'éclairage, le chauffage, la gestion de l'eau et autres pour répondre à la demande d'énergie

locale [31, 32]. De plus, la transition vers une consommation d'énergie basée sur l'électricité évite de consommer des ressources locales à base de carbone comme le charbon ou le bois, et contribue à améliorer la conservation des écosystèmes et l'atténuation des émissions de CO_2.

L'application de réseau autonome (mode îloté) nécessite un bon fonctionnement pour fournir une électricité fiable, continue, durable et de bonne qualité aux consommateurs, ce qui pose plusieurs défis techniques pour l'application des énergies renouvelables. La caractéristique intermittente et non dispatchable des énergies renouvelables entraîne de grands impacts liés à l'instabilité et aux fluctuations de leur production d'énergie. Dans ce contexte, l'utilisation de ESS couplée à des énergies renouvelables fonctionnant pour fournir une charge locale, a mis en évidence le concept de Microgrid, qui est une solution puissante pour atteindre les objectifs d'exploitation du réseau autonome, en améliorant la fiabilité, la résilience et la disponibilité de tout le système [33–35].

Les Microgrids peuvent en effet apporter une réponse importante à la plupart de ces problèmes et peuvent représenter à l'avenir la nouvelle norme pour les systèmes électriques. Néanmoins, il reste un problème très difficile pour garantir un fonctionnement fiable et d'atteindre la stabilité du système selon les *grid codes*.

Dans le contexte des Microgrids, ceux à Courant Continu (DC) sont considérés avec grand intérêt, car les énergies renouvelables (PV, éoliennes, piles à combustible), les charges électroniques, les véhicules électriques et le stockage (batteries, supercondensateurs) sont naturellement en DC. S'ils étaient connectés via un réseau DC, ils auraient besoin d'un plus petit nombre de convertisseurs, et ces convertisseurs seraient plus simples que s'ils étaient connectés via un réseau de Courant Alternatif (AC). Le résultat serait des matériaux moins chers et une meilleure efficacité (moins de pertes). En outre, le courant continu peut être plus efficace en raison de sa topologie plus simple; l'absence de puissance réactive et de fréquence à contrôler; la distorsion harmonique n'est plus un problème; et il n'y a pas besoin de synchronisation avec le réseau. La conséquence est une structure de contrôle plus simple basée sur l'interaction des courants entre les convertisseurs, la tension du bus DC étant la principale priorité de contrôle, c'est-à-dire que la tension est un indicateur naturel des conditions d'équilibre de puissance [36–40]. Dans le même temps, le Microgrid DC est un défi car la structure du réseau électrique actuel, les alimentations, les transformateurs, les câbles et la protection sont conçus pour le courant alternatif. Pour cette raison, le Microgrid hybride AC/DC est considéré comme un compromis entre AC et DC pour permettre une meilleure

intégration entre ces nouveaux appareils et les composants classiques du réseau électrique [41–43].

De nos jours, il existent plusieurs exemples de petits Microgrids DC, comme dans l'industrie maritime, aéronautique, automobile et manufacturière. Dans tous ces exemples, il est extrêmement important que le Microgrid soit contrôlé de manière à présenter une fiabilité et un fonctionnement correct. Pour atteindre cet objectif, de nombreuses stratégies de contrôle sont proposées pour les Microgrids. La commande linéaire est la plus répandue, en raison de sa simplicité et de sa robustesse; en outre, la commande linéaire est bien connue à la fois dans le milieu universitaire et dans l'industrie. Le contrôle linéaire est basé sur un modèle linéarisé donné par les équations du circuit électrique du Microgrid, où les non-linéarités ne sont pas prises en compte. En conséquence, ce modèle simplifié n'est valable que dans une petite région autour du point d'opération où la linéarisation a été effectuée. Il existent plusieurs approches pour concevoir une commande linéaire, par exemple dans le domaine fréquentiel via des fonctions de transfert ou par modèle par espace d'état, PID, retour d'état via le placement des pôles et l'optimisation LQR sont des stratégies courantes. Le *minor loop gain* est un autre exemple de technique linéaire qui relie l'impédance de la source et de la charge pour déterminer la stabilité dans le réseau. Cette stratégie assure la stabilité du système même lors de la connexion de plusieurs appareils tels que des filtres. L'approche basée sur l'impédance fournit une bonne perspective sur la dynamique comme la modélisation bien connue de l'espace d'états [35, 44, 45].

Le contrôle non linéaire quant à lui, est basé sur un modèle plus détaillé du système, dans le sens où la dynamique non linéaire et l'ensemble de l'espace de fonctionnement sont considérés. Ensuite, la théorie non linéaire permet une modélisation de réseau plus réaliste, une analyse de stabilité plus efficace et une plage de fonctionnement plus large. L'utilisation de techniques de contrôle non linéaires peut également améliorer les performances de flux de puissance dans le Microgrid, puisque le système n'est pas limité à un point de fonctionnement spécifique. En conséquence, il est possible de travailler dans une zone d'opération plus large, en considérant uniquement les limitations physiques du système. Un inconvénient de l'utilisation de la technique de contrôle non linéaire est la complexité accrue de l'analyse et parfois de la loi de contrôle résultante, qui est parfois plus difficile à mettre en oeuvre [36, 37, 46, 47].

H.3. Services Système

Historiquement, les systèmes électriques étaient basés sur des machines synchrones tournant en synchronisme, partageant la puissance pour alimenter la charge et fournissant une inertie naturelle (réponse en fréquence) suite à des perturbations ou simplement à des changements des conditions de fonctionnement. Ce schéma classique est de moins en moins vrai, en raison de la forte pénétration des appareils de l'électroniques de puissance comme les convertisseurs de puissance et les charges modernes.

Les convertisseurs de puissance sont inhérents à l'interconnexion des sources d'énergie renouvelables et des unités de stockage comme mentionné précédemment, mais aussi par les lignes HVDC qui sont construites pour renforcer les systèmes de transport actuels. Pour cette raison, l'inertie diminue rapidement, et dans certaines situations, il existe des réseaux principalement composés de convertisseurs de puissance où la référence de fréquence est complètement perdue [52–54]. Cette situation est un changement de paradigme par rapport au réseau électrique classique, et les praticiens des systèmes électriques ont du mal à maintenir le réseau en marche. Un exemple récent d'une telle situation est le black-out du 9 août 2019 au Royaume-Uni [55], dont la cause principale était la réduction de l'inertie, et son effet sur plusieurs convertisseurs de puissance interconnectant la génération distribuée.

Géneration distribuée sont principalement constitués de sources d'énergie renouvelables, qui ont une interface de l'électronique de puissance. Ainsi, les convertisseurs n'ont pas de réponse inertielle en raison de l'absence de masse rotative, comme le font les générateurs synchrones classiques. Les convertisseurs sont incapables de répondre naturellement à un changement de charge. Par conséquent, la réponse en fréquence s'aggrave, provoquant des oscillations et des problèmes de contraintes de fonctionnement. Ainsi, l'intégration des énergies renouvelables a une relation directe avec la réduction de l'inertie dans les systèmes électriques.

Les caractéristiques inhérentes aux systèmes principalement composés de convertisseurs de puissance sont:

1. Réponse rapide;
2. Manque d'inertie;
3. Problèmes d'harmoniques;
4. Interaction entre les les algorithmes de commande;
5. Faible capacité de surcharge.

De nombreuses études ont proposé différentes stratégies de contrôle pour maintenir la stabilité de la tension et de la fréquence dans les réseaux isolés. En effet, l'interfaçage de convertisseur de puissance à faible inertie ont tendance à rendre le système sensible aux perturbations. La stratégie la plus pertinente est la commande de statisme, où la relation entre la puissance active et la fréquence ($P-f$) ainsi que la puissance réactive et la tension ($Q-V$) sont établies pour assurer un fonctionnement stable du système. Cette technique de contrôle a été largement appliquée, permettant un fonctionnement flexible des ressources distribuées connectées, permettant de partager la charge et de maintenir la stabilité de fréquence et de tension dans le réseau. Quoi qu'il en soit, la stratégie classique de statisme $P-f$ et $Q-V$ n'agit qu'en régime stationnaire, puis le manque d'effet dans les transitoires rend le contrôle du statisme inapproprié pour améliorer la stabilité de fréquence. Mais nous avons déjà quelques variantes de contrôle de statisme qui considèrent la réponse transitoire en rajoutant un terme avec la dérivé de la fréquence. Habituellement, la commande en statisme est appliquée comme commande primaire dans une structure hiérarchique, où la commande secondaire est conçue pour atténuer les écarts de fréquence et de tension dans une échelle de temps plus lente [58–62].

Une possibilité intéressante pour résoudre ces problèmes est représentée par le concept de *synchronverters* [63], appelé VSM[1] dans [64–67], ou même VISMA dans [68]. Ceux-ci sont composés de convertisseurs de puissance qui imitent les machines synchrones. De cette façon, il est beaucoup plus facile d'intégrer de tels systèmes au réseau électrique, fournissant un cadre que les praticiens connaissent bien [57, 69, 70]. Ces convertisseurs à inertie virtuelle ont suscité beaucoup d'intérêt ces dernières années. Dans cette approche, il est proposé d'imiter l'état stationnaire et les caractéristiques transitoires des machines synchrones en insérant l'équation de rotation pour fournir une amélioration de la réponse inertielle.

De nombreuses études ont été menées concernant l'application de l'inertie virtuelle dans les convertisseurs de puissance, comme l'intégration de la génération distribuée [70–72], les améliorations des Microgrids [73, 74] et des systèmes d'alimentation isolés [75]. Dans [76], une comparaison sur la dynamique entre l'inertie virtuelle et la stratégie de contrôle du statisme est effectuée, en soulignant les similitudes et les avantages de chaque stratégie de contrôle, ainsi que la pertinence des propriétés d'inertie. Comme étape suivante, de nouvelles propositions d'inertie virtuelle ont émergé, par exemple dans [67], les paramètres des machines virtuelles synchrones peuvent être contrôlés, puis il est présenté une VSM avec un moment

[1]Notez que VSM est dit VSC fonctionnant comme une machine synchrone.

d'inertie variant dans le temps. L'effet d'amortissement du schéma d'inertie variante est étudié par une analyse d'énergie transitoire.

Dans les chapitres suivants, de nouveaux résultats seront présentés pour ces systèmes, mais en reconnaissant maintenant que si les convertisseurs de puissance agissent comme des machines synchrones, ils ne sont pas limités à ce comportement et peuvent fournir un support plus étendu que les machines physiques. De cette manière, il a été étudié la contribution que les machines synchrones virtuelles peuvent apporter à l'inertie globale d'un réseau électrique, et comment elles peuvent fournir des services systèmes, compte tenu du support de fréquence et de l'inertie synthétique. En particulier, cette approche peut contribuer à résoudre les problèmes posés par les énergies renouvelables dans les systèmes électriques modernes, et permettre une pénétration beaucoup plus large de ces énergies intermittentes.

H.4. Contribution de la Thèse

Cette thèse constitue un pas en avant dans le contrôle des Microgrids hybrides AC/DC et introduit une analyse rigoureuse de leur stabilité via les techniques de Lyapunov, en considérant le modèle dynamique non linéaire du système étudié. Dans ce même contexte, le comportement de plusieurs périphériques interconnectés est analysé en considérant une approche *System-of-Systems*, où différentes sources, charges et systèmes de stockage doivent fonctionner correctement.

Le Microgrid étudié est composé d'énergies renouvelables, telles que des panneaux PV contrôlés pour extraire la puissance maximale disponible, et la récupération de l'énergie de freinage des métros ou des tramways où l'énergie générée par le freinage est exploitée et correctement stockée pour être utilisée en cas de besoin.

Un HESS composé de batteries et de supercondensateurs est appliqué. La batterie est utilisée pour réaliser le flux de puissance à long terme, sans nuire à son cycle de vie, et le supercondensateur est utilisé pour réguler le bus DC du réseau assurant l'équilibre de puissance du système.

Différents types de charges (DC, AC et CPL) sont insérés dans le Microgrid pour comprendre les perturbations provoquées et comment le système réagit à ces variations.

Enfin, la connexion avec le réseau principal AC est établie, où le côté DC du réseau prend en charge le côté AC avec différentes stratégies de contrôle. Lorsqu'il existe un réseau principal AC puissant, l'objectif de contrôle est de fournir des services système en injectant/absorbant de la puissance active et réactive pour le

réseau principal. Lorsqu'il y a un réseau faible, ou même dans un cas isolé (pas de machine synchrone), la cible de contrôle est de contrôler la fréquence et la tension du système AC, assurant un fonctionnement correct et la stabilité du système. Par conséquent, le support de tension et de fréquence met en évidence la fourniture de services système.

Dans ce dernier cas d'interconnexion avec le réseau faible AC, on développe une approche de machine virtuelle synchrone, où l'équation différentielle d'un alternateur synchrone traditionnel est introduite dans le convertisseur AC/DC pour imiter le comportement inertiel d'une machine synchrone. Par conséquent, la stratégie de contrôle est conçue pour fournir un support inertiel, améliorant la stabilité de la tension et de la fréquence. Une étape additionnelle a été l'utilisation de la valeur d'inertie comme variable d'état pour améliorer le support de fréquence et la robustesse.

À partir du modèle Microgrid résultant, un contrôle non linéaire distribué est développé en tenant compte du fonctionnement de chaque appareil du système et de la stabilité de l'ensemble du réseau. Par conséquent, le contrôleur non linéaire proposé est capable d'intégrer les énergies renouvelables tout en alimentant correctement les charges locales. La commande du bus DC du Microgrid, et le système de freinage régénératif des trains lorsque c'est le cas, sont conçus sur la base d'une perturbation singulière induite par la commande et d'une *dynamic feedback linearization*. Les contrôleurs de l'équipement Microgrid sont conçus via des techniques de *feedback linearization* et *backstepping*, tandis qu'une fonction de Lyapunov considérant l'ensemble du système est construite pour garantir son stabilité.

Par conséquent, les perturbations du système telles que les pics d'énergie élevés dus au freinage des trains, la nature intermittente des énergies renouvelables, les variations de charge et les dynamiques non linéaires sont prises en compte dans les évaluations de la stratégie de commande non linéaire. Les performances du contrôleur proposé sont mises en évidence par des simulations détaillées et la comparaison de la stratégie de contrôle linéaire classique est effectuée pour souligner les améliorations de la réponse de contrôle et des propriétés de robustesse du contrôle non linéaire par rapport à l'approche linéaire.

Les contributions de la thèse peuvent être résumées comme:

- Conception d'un Microgrid hybride AC/DC flexible capable d'intégrer un certain nombre de générateurs distribués sans affecter la stabilité du système.

- Intégration de différents ESS dans un HESS qui peut équilibrer l'ensemble du réseau en transitoires et en régime permanent (stabilité à long terme).
- Étudiez les perturbations causées par les différentes charges connectées au Microgrid et le comportement intermittent des énergies renouvelables.
- Concevoir une stratégie de contrôle pour permettre le freinage régénératif des trains, de sorte que le sursaut de puissance soit correctement absorbé par le système de stockage.
- Modélisation du système et conception d'une stratégie de contrôle non linéaire distribuée à l'ensemble du Microgrid en fonction des caractéristiques physiques de leurs composants, de sorte que la stabilité soit garantie.
- Développer une analyse de stabilité complète et rigoureuse, de sorte que les propriétés de stabilité soient démontrées.
- Développer une stratégie de contrôle via une approche d'inertie virtuelle, de sorte que le côté DC du réseau soit capable de fournir correctement des services système au réseau AC, en considérant un réseau fort ou faible.
- Proposition d'un moment d'inertie virtuel variable pour améliorer la stabilité en fréquence et le support inertiel.

H.5. Conclusions Générales

Au cours des dernières décennies, le développement des Microgrids est devenu un sujet de recherche très important, visant à trouver un meilleur moyen d'intégrer les énergies renouvelables et d'assurer un fonctionnement plus fiable des nouveaux dispositifs de l'électroniques de puissance dans les systèmes d'alimentation. Les Microgrids fournissent une excellente solution compte tenu de la croissance constante de la demande de l'électricité et de la modernisation du réseau grâce aux concepts de Smart-Grid. L'impact de la géneration distribuée basée sur l'électronique de puissance est une préoccupation importante du système d'alimentation, car il affecte de nombreux aspects des systèmes d'alimentation, brisant la radialité des réseaux de distribution, la création de flux de courant bidirectionnel dans les départs de distribution et réduisant considérablement l'inertie et ainsi la capacité de régulation naturelle du système. Par conséquent, les réseaux DC sont considérés comme une solution pertinente dans les systèmes d'alimentation, car la nature DC des appareils de l'électroniques de puissance apporte des avantages technologiques et économiques. Par exemple, il permet de réduire les étages de conversion dans le réseau, puisque de nombreux éléments sont naturellement en courant continu, et permet un contrôle

plus facile du flux de puissance qui ne dépend pas de la phase ou de la puissance réactive.

Dans cette thèse, il est introduit la conception et le contrôle d'un Microgrid hybride DC/DC pour intégrer différentes sources renouvelables, des systèmes de stockage d'énergie et des charges pour un fonctionnement fiable et la stabilité de l'ensemble du système. La stabilisation des bus Microgrid par l'équilibre des flux de puissance et la fourniture de services système est assurée par la stratégie de contrôle proposée, où une analyse rigoureuse de la stabilité est réalisée.

Dans le chapitre 1, une brève introduction sur les Microgrids et les défis de la transition énergétique est présentée. Là, il est mentionné les impacts de la forte pénétration de géneration distribuée dans le réseau, la caractéristique intermittente des énergies renouvelables, la réduction de l'inertie due aux technologies de l'électroniques de puissance et la transformation du réseau de production centralisée en un système distribué hétérogène. En outre, l'importance du système de stockage d'énergie pour les systèmes électriques afin de réduire l'impact des énergies renouvelables équilibrant le flux d'énergie, d'améliorer la qualité et la fiabilité de l'énergie et de fournir un support au réseau sont exposés. Enfin, les nouvelles tendances dans les structures Microgrids sont présentées pour résoudre les problèmes du système électrique, où l'approche de l'inertie virtuelle est mise en évidence.

Au chapitre 2, il a été présenté une synthèse des aspects de contrôle, de fonctionnement et de stabilité des Microgrids, où des exemples d'application et des stratégies de gestion réels sont introduits. Des structures de contrôle standard liées aux modes de fonctionnement en îlotage ou connectés au réseau sont développées pour mettre en évidence les défis du fonctionnement des Microgrids. Les principaux aspects des Microgrids DC et AC sont comparés, où les simplifications et améliorations pouvant être obtenues grâce à un réseau DC sont introduites. Les problèmes de stabilité particuliers aux Microgrids sont mis en évidence, tels que les solutions de contrôle développées pour maintenir le bon fonctionnement du système, maintenir les indices de qualité de puissance et la fiabilité du système. En outre, les limites des contrôleurs conventionnels sont exposées, présentant la nécessité de développer des stratégies de contrôle fiables appropriées pour assurer le bon fonctionnement du système face aux défis du Microgrid.

Dans le chapitre 3, les composants du Microgrid sont décrits: les systèmes PV avec fonction intermittente où un algorithme MPPT permet au système de fonctionner au point de puissance maximum; différents types de systèmes de stockage d'énergie sous forme de batteries et de supercondensateurs à intégrer dans un système de stockage d'énergie hybride pour améliorer leur fonctionnement dans les

transitoires et la stabilité à long terme. La synthèse du freinage régénératif ferroviaire est également proposée, motivée par des collaborations industrielles. Comme ceux-ci introduisent une grande quantité de puissance sur de courtes périodes, l'intégration de cette énergie récupérée des trains se fait sur la base d'équipements plus spécifiques capables de résister à ce problème particulier, et par une stratégie de contrôle adaptée. Dans ce travail, un supercondensateur connecté via un convertisseur bidirectionnel, est capable d'absorber cette grande quantité de puissance lors de la reprise de coupure, et de réduire la forte fluctuation de puissance. La dernière partie du chapitre présente le Microgrid proposé où le niveau de tension et la configuration des convertisseurs de puissance sont dessinés.

Au chapitre 4, le modèle dynamique non linéaire du Microgrid est présenté, par un modèle dans l'espace d'état de l'ensemble du système. Un certain nombre d'éléments sont connectés au Microgrid: deux sources d'énergie renouvelables différentes (panneaux photovoltaïques et récupération de l'énergie de freinage des trains), deux types de stockage agissant à des échelles de temps différentes (une batterie et un supercondensateur), une charge DC et la connexion avec le réseau AC principal. Ensuite, un contrôleur non linéaire distribué de bas niveau, basé sur l'approche *System-of-Systems*, est développé pour le Microgrid DC intégré dans une gare connectée au réseau. Des approches de *feedback linearisation* et *backstepping* sont utilisées dans les dispositifs Microgrid. Pour les sous-systèmes de supercondensateurs et de trains, le problème de phase non minimale des convertisseurs boost/buck, en fonction de leur sortie de commande choisie, est résolu par une séparation d'échelle de temps explicite induite par la commande, qui est ensuite traitée par une analyse de perturbation singulière. Par conséquent, une *dynamic feedback linearisation* est appliquée en utilisant des propriétés de perturbation singulières, assurant le bon contrôle de ces sous-systèmes. Une fonction de Lyapunov pour l'ensemble du système, compte tenu des dispositifs interconnectés du Microgrid, est utilisée pour assurer la stabilité de l'ensemble. L'analyse de stabilité donne des propriétés de *Input-to-State stability* pour le Microgrid, par conséquent le système peut fonctionner correctement à l'intérieur de la région de stabilité et avoir de bonnes propriétés de robustesse à partir des résultats de ISS. Les simulations mettent en évidence les performances du contrôle proposé, avec des tests de robustesse paramétriques et une comparaison avec le contrôleur linéaire traditionnel (PI), soulignant les meilleures performances du contrôleur non linéaire proposé. Le comportement transitoire est bien meilleur et le réglage du contrôle beaucoup plus facile avec le contrôle non linéaire. Enfin, une tension de bus DC non statique est proposée pour effectuer la stabilisation du réseau, ce qui se traduit

par une loi de commande beaucoup plus simple. De plus, il a été proposé une simplification de la dynamique du courant du bus DC, en négligeant les petits termes. De cette manière, il était possible de développer une fonction de Lyapunov plus simple. Des tests de simulation des deux propositions sont effectués montrant les performances du système.

Au chapitre 5, le côté AC du Microgrid est mieux détaillé, ainsi que la fourniture de services systèmes nécessaires pour assurer sa stabilité. Le modèle dynamique du réseau AC est développé, y compris la connexion du Microgrid DC à travers un convertisseur de type VSC. Une analyse de la stabilité du réseau électrique, axé sur la stabilité de la tension et de la fréquence est proposé, mettant en évidence les problèmes de stabilité induits par l'augmentation du nombre de convertisseurs de puissance dans le réseau et la transition énergétique en général. Le manque d'inertie dans de tels systèmes est mis en évidence, où l'approche par inertie virtuelle est proposée ici pour améliorer la stabilité et le partage des responsabilités. L'inertie virtuelle est implémentée dans le Microgrid et les performances du système sont testées par des simulations, où la régulation de tension est effectuée par contrôle de statisme. De cette façon, il est assuré la fourniture de services système pour un réseau faible, comme le sont les Microgrids AC. Une comparaison avec la stratégie de contrôle de statisme est effectuée, où le support inertiel et la réponse en fréquence dynamique pour le contrôle d'inertie virtuelle sont mis en évidence dans les simulations. Par conséquent, une inertie virtuelle adaptative est proposée où la constante d'inertie devient un paramètre de commande variant dans le temps, laquelle adaptation peut être conçue pour améliorer la stabilité de fréquence et le support inertiel. Une analyse de stabilité de l'inertie virtuelle adaptative est effectuée où la stabilité asymptotique est assurée via le théorème de La Salle. Les résultats de la simulation montrent l'efficacité de l'inertie adaptative proposée, où une comparaison avec la solution de statisme et le contrôle de courant classique est effectuée.

Cette thèse vise à étudier des solutions pour les Microgrids, en tenant compte des tendances actuelles des systèmes électriques. L'utilisation de systèmes DC est proposée, mettant en évidence plusieurs caractéristiques bénéfiques, comme des topologies de convertisseur et une conception de commande plus simples, et le fait qu'il n'y a plus de variables complexes ni de régulation de la puissance réactive et de la fréquence. En outre, les tendances actuelles des réseaux AC sont exposées, en particulier l'inertie virtuelle pour améliorer le partage de puissance dans les systèmes isolés, et améliorer la stabilité de fréquence en prouvant la prise en charge de l'inertie et du contrôle primaire dans les Microgrids. De la même manière, il est discuté des

nouvelles tendances dans les services système, comme le support inertiel, en réponse à la forte pénétration de l'électronique de puissance, fournissant un cadre pour l'évolution du Microgrid dans les futures solutions Smart Grids.

H.6. Résultats Principaux

Les principales contributions de cette thèse peuvent être résumées comme suit:

1. Développement d'une stratégie de contrôle non linéaire pour chaque convertisseur du Microgrid basé sur le *backstepping* et *feedback linearization*.
2. Concevoir une stratégie de contrôle non linéaire pour résoudre le problème de phase non minimale des convertisseurs DC/DC en fonction de la sortie de contrôle choisie. La conception de la séparation temporelle induite par la commande et la *dynamic feedback linearization* sont utilisées pour développer un contrôleur pour le convertisseur élévateur pour le supercondensateur et le convertisseur abaisseur pour le système de récupération de freinage de train.
3. Intégration du système de freinage régénératif des trains, qui est une source d'énergie renouvelable originale dans un Microgrid, assurant le bon fonctionnement du système, compte tenu de la caractéristique de fluctuations de puissance de la récupération d'énergie de freinage.
4. Une analyse rigoureuse de la stabilité de l'ensemble du Microgrid en tenant compte de tous les dispositifs interconnectés, où la stabilité ISS. La preuve est formellement faite avec des fonctions constructives de Lyapunov où la stabilité de l'ensemble du système est assurée. L'analyse de stabilité garantit les performances dynamiques du système et de son exploitation.
5. Développement d'une stratégie de contrôle pour le partage de puissance et l'amélioration de la stabilité de fréquence basée sur une approche d'inertie virtuelle pour les Microgrids AC ou les réseaux faibles. La proposition d'inertie virtuelle adaptative pour améliorer la réponse inertielle des Microgrids, où la constante d'inertie est variable. Une analyse de stabilité est menée pour prouver la stabilité asymptotique de l'inertie virtuelle adaptative dans l'application des convertisseurs de puissance.
6. Une comparaison avec la stratégie de contrôle de statisme traditionnelle est effectuée via des simulations, où la réponse améliorée de l'inertie virtuelle adaptative est mise en évidence, puisque l'approche de contrôle de statisme n'est pas en mesure de fournir un support inertiel et a de mauvaises caractéristiques de réponse transitoire.

H.7. Travaux Futurs

Cette thèse a apporté plusieurs contributions liées à la commande et le support de services système par un Microgrid pour les réseaux faibles. Cependant, il existe encore de nombreux problèmes à étudier.

1. Les réseaux DC ne sont pas encore répandus dans les réseaux de distribution conventionnels. Il reste encore de nombreux problèmes de recherche à résoudre pour leur utilisation généralisée. Les schémas de protection des réseaux DC sont encore un défi technique difficile, ainsi que les problèmes de niveau de tension et le manque de solutions commerciales pour les convertisseurs de puissance DC/DC pour interconnecter facilement les systèmes DC, ouvrant la possibilité de construire des réseaux purement DC. Une étape suivante consiste à développer des schémas de protection et de contrôle mixtes dans les convertisseurs de puissance pour améliorer la faisabilité des systèmes DC. De plus, l'étude des systèmes hybrides mixtes AC/DC peut être un bon compromis entre les réseaux classiques et DC.
2. Le modèle de gare peut être plus détaillé pour inclure des aspects réels du freinage régénératif des trains. Dans ce travail, l'impédance du train est fixe, mais en application réelle, les pertes varient en fonction de la position du train. De plus, l'entraînement électrique du train pourrait être inclus pour faire correspondre le freinage d'un train avec l'accélération d'un autre comme cela se fait généralement.
3. Différents résultats peuvent être dérivés de l'analyse de stabilité par des considérations basées sur la passivité et la mise en oeuvre de schémas de contrôle adaptatif en considérant des propositions différentes de celles faite dans cette thèse.
4. L'inclusion de caractéristiques d'inductance dans les câbles du côté DC du Microgrid (non inclus dans la thèse) apportera une dynamique différente au système, où une nouvelle conception et un contrôle du système sont nécessaires. De plus, des aspects de filtrage peuvent résulter de cette analyse et une fonction de Lyapunov de la dynamique du courant d'inductance peut être considérée.
5. L'inertie virtuelle adaptative peut également être appliquée au facteur d'amortissement de l'équation d'oscillation, où des résultats plus forts peuvent être obtenus. Le choix des paramètres pour le coefficient d'inertie et le facteur d'amortissement est un sujet d'étude intéressant, où l'optimisation de ces paramètres peut être réalisée en tenant compte des marges opérationnelles de différents systèmes électriques comme les réseaux faibles ou les Microgrids.

Le paramétrage approprié de l'inertie virtuelle peut vraiment améliorer les propriétés de stabilité du système.

6. Un banc d'essai expérimental du système Microgrid proposé doit être mis en place pour la validation pratique des schémas de contrôle et le réglage du gain. Dans ce qui suit, ils seront testés dans une vraie station de métro. En outre, les problèmes de réseaux à tension déséquilibrée et de PLL peuvent être inclus pour envisager un réseau plus réaliste.
7. Enfin, des travaux futurs sur le développement d'un niveau de contrôle secondaire et tertiaire pour le Microgrid proposé sont nécessaires. Il est important de comprendre le comportement du système et l'interaction de la hiérarchie de contrôle entre les différentes couches. Cela permettra également la possibilité d'inclure des aspects économiques et de viser la durabilité en plus de la fiabilité et de la qualité de l'énergie.

ÉCOLE DOCTORALE
Sciences et technologies de l'information et de la communication (STIC)
université PARIS-SACLAY

Titre: Contrôle des microgrid AC/DC avec des énergies renouvables dans le contexte des smart grids inclus services système et la mobilité électrique

Mots clés: Microgrids, contrôle non-linéaire, stabilité du système électrique, Régulation de tension et de fréquence, méthodes de Lyapunov, inertie virtuelle, services système

Résumé: Les Microgrids sont une excellente solution aux problèmes actuels soulevés par la croissance constante de la demande de charge et la forte pénétration des sources d'énergie renouvelables, qui se traduisent par une modernisation du réseau grâce au concept de "Smart-Grids". L'impact des sources d'énergie distribuées basées sur l'électronique de puissance est une préoccupation importante pour les systèmes d'alimentation, où la régulation naturelle de la fréquence du système est entravée en raison de la réduction de l'inertie. Dans ce contexte, les réseaux à courant continu (CC) sont considérés comme une solution pertinente, car la nature CC des appareils électroniques de puissance apporte des avantages technologiques et économiques par rapport au courant alternatif (CA). La thèse propose la conception et le contrôle d'une Microgrid hybride AC/DC pour intégrer différentes sources renouvelables, y compris la récupération d'énergie solaire et de freinage des trains, aux systèmes de stockage d'énergie sous forme de batteries et de supercondensateurs et à des charges telles que les véhicules électriques ou d'autres réseaux (AC ou DC), pour un fonctionnement et une stabilité fiables. La stabilisation des tensions des bus du Microgrid et la fourniture de services systèmes sont assurées par la stratégie de contrôle proposée, où une étude de stabilité rigoureuse est réalisée. Un contrôleur non linéaire distribué de bas niveau, basé sur une approche "System-of-Systems", est développé pour un fonctionnement correct de l'ensemble du Microgrid. Un supercondensateur est appliqué pour faire face aux transitoires, équilibrant le bus CC du Microgrid et absorbant l'énergie injectée par des sources d'énergie intermittentes et possiblement très fortes comme celle provenant du freinage régénératif de trains ou metros, tandis que la batterie réalise le flux de puissance à long terme. Un contrôle de linéarisation par bouclage dynamique basé sur une analyse par perturbation singulière est développé pour les supercondensateurs et les trains. Des fonctions de Lyapunov sont construites en tenant compte des dispositifs interconnectés au Microgrid pour assurer la stabilité de l'ensemble du système. Les simulations mettent en évidence les performances du contrôle proposé avec des tests de robustesse paramétriques et une comparaison avec le contrôleur linéaire traditionnel. L'approche VSM (Virtual Synchronous Machine) est implémentée dans le Microgrid pour le partage de puissance et l'amélioration de la stabilité de fréquence. Une inertie virtuelle adaptative est proposée, puis la constante d'inertie devient une variable d'état du système qui peut être conçue pour améliorer la stabilité de fréquence et le support inertiel, où l'analyse de stabilité est effectuée. Par conséquent, le VSM est la connexion de liaison entre les côtés DC et AC du Microgrid, où la puissance disponible dans le réseau DC est utilisée pour les services système dans les Microgrids AC. Les résultats de la simulation montrent l'efficacité de l'inertie adaptative proposée, où une comparaison avec la solution de statisme et le contrôle standard est effectuée.

Title: Control of AC/DC microgrids with renewables in the context of smart grids including ancillary services and electric mobility

Keywords: Microgrids, nonlinear control, power system stability, voltage and frequency regulation, Lyapunov methods, virtual inertia, ancillary services

Abstract: Microgrids are a very good solution for current problems raised by the constant growth of load demand and high penetration of renewable energy sources, that results in grid modernization through "Smart-Grids" concept. The impact of distributed energy sources based on power electronics is an important concern for power systems, where natural frequency regulation for the system is hindered because of inertia reduction. In this context, Direct Current (DC) grids are considered a relevant solution, since the DC nature of power electronic devices bring technological and economical advantages compared to Alternative Current (AC). The thesis proposes the design and control of a hybrid AC/DC Microgrid to integrate different renewable sources, including solar power and braking energy recovery from trains, to energy storage systems as batteries and supercapacitors and to loads like electric vehicles or another grids (either AC or DC), for reliable operation and stability. The stabilization of the Microgrid buses' voltages and the provision of ancillary services is assured by the proposed control strategy, where a rigorous stability study is made. A low-level distributed nonlinear controller, based on "System-of-Systems" approach is developed for proper operation of the whole Microgrid. A supercapacitor is applied to deal with transients, balancing the DC bus of the Microgrid and absorbing the energy injected by intermittent and possibly strong energy sources as energy recovery from the braking of trains and subways, while the battery realizes the power flow in long term. Dynamical feedback control based on singular perturbation analysis is developed for supercapacitor and train. A Lyapunov function is built considering the interconnected devices of the Microgrid to ensure the stability of the whole system. Simulations highlight the performance of the proposed control with parametric robustness tests and a comparison with traditional linear controller. The Virtual Synchronous Machine (VSM) approach is implemented in the Microgrid for power sharing and frequency stability improvement. An adaptive virtual inertia is proposed, then the inertia constant becomes a system's state variable that can be designed to improve frequency stability and inertial support, where stability analysis is carried out. Therefore, the VSM is the link between DC and AC side of the Microgrid, regarding the available power in DC grid, applied for ancillary services in the AC Microgrid. Simulation results show the effectiveness of the proposed adaptive inertia, where a comparison with droop and standard control techniques is conducted.

Université Paris-Saclay
Espace Technologique / Immeuble Discovery
Route de l'Orme aux Merisiers RD 128 / 91190 Saint-Aubin, France